Variational calculations of rotational-vibrational spectra and properties of small molecules

Inaugural-Dissertation

zur Erlangung des Doktorgrades
der Mathematisch-Naturwissenschaftlichen Fakultät
der Heinrich-Heine-Universität Düsseldorf

vorgelegt von

Andrey Yachmenev
aus Iwanowo

Mülheim an der Ruhr/Düsseldorf 2011

Aus dem Institut für Theoretische Chemie und Computerchemie der Heinrich-Heine-Universität Düsseldorf

Gedruckt mit Genehmigung der Mathematisch-Naturwissenschaftlichen Fakultät der Heinrich-Heine-Universität Düsseldorf

Referent:	Prof. Dr. Walter Thiel
Korreferent:	Prof. Dr. Christel Marian

Tag der mündlichen Prüfung:

Hiermit versichere ich, die hier vorgelegte Arbeit eigenständig und ohne unerlaubte Hilfe angefertigt zu haben. Die Dissertation wurde in der vorgelegten oder in ähnlicher Form noch bei keiner Institution eingereicht. Ich habe keine erfolglosen Promotionsversuche unternommen.

Düsseldorf, den

(Andrey Yachmenev)

Acknowledgements

Foremost, I would like to thank my adviser Prof. Thiel for the continuous support of my research, open-minded suggestions, and immense knowledge. I am grateful for the opportunities to visit scientific meetings, workshops and schools and for the continuous financial support.

I am grateful to Dr. Yurchenko (Technische Universität Dresden, Germany) for his guidance in all the time of research, his patience, motivation, and enthusiasm. I would like to thank Dr. Breidung for insightful discussions and significant assistance of this work.

I would like to acknowledge the fruitful collaborations with Prof. Jensen (Bergische Universität Wuppertal, Germany), Prof. Sauer (University of Copenhagen, Denmark), and Prof. Ruud (University of Tromsø, Norway). I thank the Center for Theoretical and Computational Chemistry (Norway) for giving me opportunity to work there.

I would like to thank Dr. Barbatti, Dr. Breidung, and Dr. Weingart for proof-reading my thesis.

List of papers included in the thesis

(1) "A variationally computed $T = 300$ K line list for NH_3", S. N. Yurchenko, R. J. Barber, A. Yachmenev, W. Thiel, P. Jensen, J. Tennyson, *J. Phys. Chem. A*, **113**, 11845 (2009).
Contributions to potential energy surface refinement. Variational calculations of the rovibrational spectra of ammonia. Preparation of the astrophysical database and calculation of line profiles.

(2) "An *ab initio* calculation of the vibrational energies and transition moments of HSOH", S. N. Yurchenko, A. Yachmenev, W. Thiel, O. Baum, T. F. Giesen, V. V. Melnikov, P. Jensen, *J. Mol. Spectrosc.*, **257**, 57 (2009).
Variational calculations of the vibrational energy levels and vibrational transition moments of HSOH.

(3) "Thermal averaging of the indirect nuclear spin-spin coupling constants of ammonia (NH_3): the importance of the large amplitude inversion mode", A. Yachmenev, S. N. Yurchenko, I. Paidarova, P. Jensen, W. Thiel, S. P. A. Sauer, *J. Chem. Phys.*, **132**, 114305 (2010).
Variational calculations of the rovibrational and thermal corrections to the spin-spin coupling constants of ammonia.

(4) "A theoretical spectroscopy, *ab initio* based study of the electronic ground state of $^{121}SbH_3$", S. N. Yurchenko, M. Carvajal, A. Yachmenev, W. Thiel, P. Jensen, *J. Quant. Spec. Rad. Trans.*, **111**, 2279 (2010).
Variational calculations of the rovibrational energy levels and spectra of SbH_3.

(5) “Theoretical rotation-torsion spectra of HSOH”, A. Yachmenev, S. N. Yurchenko, P. Jensen, O. Baum, T. F. Giesen, W. Thiel, *Phys. Chem. Chem. Phys.*, **12**, 8387 (2010).
Variational calculations of the rotation-torsion energy levels and spectra for the ground and fundamental torsional states of HSOH.

(6) “A new ‘spectroscopic’ potential energy surface for formaldehyde in its ground electronic state”, A. Yachmenev, S. N. Yurchenko, P. Jensen, W. Thiel, *J. Chem. Phys.*, submitted for publication (2011).
Ab initio calculations of the potential energy surface for H_2CO. Variational calculations of the rovibrational energy levels. Contributions to potential energy surface refinement.

(7) “High level *ab initio* potential energy surface and vibrational energies of H_2CS”, A. Yachmenev, S. N. Yurchenko, T. Ribeyre, W. Thiel, *J. Chem. Phys.*, submitted for publication (2011).
High level ab initio calculations of the potential energy surface for H_2CS. Variational calculations of the vibrational energy levels.

Own tasks are specified in italics.

Abstract

The main goal of this work was the development of theoretical methods for calculating the rotational-vibrational spectra and properties of small molecules in the ground electronic state. The functionality of the computer program TROVE [S. N. Yurchenko, P. Jensen, W. Thiel, *J. Mol. Spectrosc.*, **245**, 126 (2007)], devised for variational calculations of the rotational-vibrational states, was extended in three major areas: (i) calculation of accurate potential energy surfaces (PES) by refinement against spectroscopic data, (ii) calculation of high-resolution rotational-vibrational spectra, (iii) calculation of rotational-vibrational and temperature corrections to molecular properties, as well as high-temperature partition functions and related thermodynamic properties.

PES. The PES can generally be determined either by solving the electronic structure problem using suitable quantum chemical methods, or by solving the *reverse* rotation-vibration problem, starting from a guess for the PES and refining it to reproduce accurate spectroscopic data for state energies and transition frequencies. The quantum chemical methods provide accurate solutions for molecular systems consisting of up to 10–20 electrons. They are general and predict smooth global potential energy surfaces. The latter approach can provide results of much higher (spectroscopic) accuracy, but it can usually only be applied to systems consisting of only three nuclei. Furthermore it is restricted to local parts of the potential energy surface around the equilibrium geometry. In our work we have developed, based on the variational TROVE method, an efficient method for refining an *ab initio* PES to spectroscopic data, which allows us to treat up to penta-atomic molecules. It combines the high flexibility of the quantum chemical methods in predicting global PESs with the high accuracy of the spectroscopic

methods. Using this approach we have obtained PESs for NH_3 and H_2CO of unprecedented accuracy unreachable for state-of-the-art quantum chemical methods so far.

SPECTRA. Modern spectroscopic applications require a detailed knowledge of accurate transition intensities for thousands or even millions of lines. Only relatively few programs offer the calculation of transition intensities as a routine task. Most of these programs focus on triatomic molecules. We have developed and implemented in TROVE a general method for calculating the transition line strengths and intensities for arbitrary molecules. Due to algorithmic improvements the computations have become feasible for tetra- and penta-atomic molecules and for spectra comprising millions of lines. We have applied this method for calculating the spectra of HSOH, SbH_3, and NH_3. For NH_3 we have produced an astrophysical line list consisting of 3.25 million transitions between states with energies up to $12\,000$ cm^{-1}.

PROPERTIES. When a molecule interacts with an electromagnetic field, the electronic and nuclear degrees of freedom are affected, and therefore the molecular electromagnetic properties contain both electronic and rovibrational contributions. Properties such as isotope effects, partition functions, and related thermodynamic quantities are generally solely due to rovibrational contributions. We have addressed the problem of calculating the rovibrational contributions to molecular properties and developed two such approaches. The first one treats the rovibrational and temperature contributions variationally, by averaging the corresponding electronic property over the rovibrational states. Our study of the rovibrational contributions to the indirect nuclear spin-spin coupling constants of ammonia has shown that the effects of large amplitude motion and Coriolis coupling are quite substantial and cannot be recovered even with a high-order perturbation treatment. The second approach directly deals with the spectroscopic observables, namely rovibrational energy levels, their derivatives, and the spectra of a molecule in an electromagnetic field.

Zusammenfassung

Hauptziel dieser Arbeit war die Entwicklung theoretischer Methoden zur Berechnung von Rotationsschwingungsspektren und Eigenschaften kleiner Moleküle im elektronischen Grundzustand. Die Funktionalität des Computerprogramms TROVE [S. N. Yurchenko, P. Jensen, W. Thiel, *J. Mol. Spectrosc.*, **245**, 126 (2007)], das für Variationsrechnungen an Rotationsschwingungszuständen konzipiert ist, wurde auf drei größere Anwendungsgebiete erweitert: (i) Berechnung genauer Potentialflächen (PES) durch Anpassung an spektroskopische Daten, (ii) Berechnung hochaufgelöster Rotationsschwingungsspektren, (iii) Berechnung von Rotationsschwingungskorrekturen und thermischen Korrekturen für molekulare Eigenschaften und von Zustandssummen bei hohen Temperaturen zur Bestimmung thermodynamischer Größen.

PES. Potentialflächen können allgemein bestimmt werden entweder durch Elektronenstruktur-Rechnungen mit geeigneten quantenchemischen Methoden oder durch Lösung des inversen spektroskopischen Problems, indem man von einer Abschätzung für die PES ausgeht und diese dahingehend verfeinert, dass genaue spektroskopische Daten für Zustandsenergien und Übergangsfrequenzen reproduziert werden. Die quantenchemischen Rechenverfahren liefern akkurate Lösungen für Moleküle mit 10-20 Elektronen. Sie sind allgemein verwendbar und erlauben die Vorhersage glatter globaler Potentialflächen. Der inverse Ansatz (siehe oben) kann im Prinzip Ergebnisse einer viel höheren (spektroskopischen) Genauigkeit erzielen, ist aber typischerweise nur auf Systeme mit bis zu drei Atomen anwendbar. Außerdem ist er beschränkt auf lokale Ausschnitte der PES in der Umgebung

der Gleichgewichtsgeometrie. Basierend auf der variationellen TROVE-Methode haben wir in dieser Arbeit ein effizientes Verfahren zur Anpassung einer ab initio PES an spektroskopische Daten entwickelt, mit dem Moleküle mit bis zu fünf Atomen behandelt werden können. Es kombiniert die hohe Flexibilität quantenchemischer Methoden zur Vorhersage globaler PESs mit der hohen Genauigkeit spektroskopischer Methoden. Unter Verwendung dieses Verfahrens haben wir die Potentialflächen für NH_3 und H_2CO mit beispielloser Genauigkeit erhalten, welche selbst für quantenchemische Methoden auf dem neuesten Stand der Technik bis jetzt unerreichbar ist.

Spektren. Moderne spektroskopische Anwendungen erfordern eine detaillierte Kenntnis genauer Übergangsintensitäten für Tausende oder gar Millionen von Linien. Nur relativ wenige Programme erlauben die Berechnung von Übergangsintensitäten routinemäßig. Die meisten der in Frage kommenden Programme konzentrieren sich auf dreiatomige Moleküle. Wir haben eine allgemeine Methode zur Berechnung der Stärke und Intensität von Übergangslinien beliebiger Moleküle entwickelt und in TROVE implementiert. Aufgrund algorithmischer Verbesserungen sind solche Rechnungen möglich geworden für vier- und fünfatomige Moleküle und für Spektren, die Millionen von Linien enthalten. Wir haben diese Methode zur Berechnung der Spektren von HSOH, SbH_3 und NH_3 angewendet. Für NH_3 haben wir eine Liste astrophysikalisch relevanter Linien generiert, die 3.25 Millionen Übergänge zwischen Zuständen mit Energien bis zu 12 000 cm^{-1} abdeckt.

Moleküleigenschaften. Wenn ein Molekül mit einem elektromagnetischen Feld in Wechselwirkung tritt, werden die Freiheitsgrade der Elektronen und der Kerne beeinflusst. Daher leisten sowohl die Elektronen als auch die Rotationen und Schwingungen der Kerne Beiträge zu den elektromagnetischen Eigenschaften eines Moleküls. Eigenschaften wie Isotopeneffekte, Zustandssummen und entsprechende thermodynamische Größen gehen im Allgemeinen ausschließlich auf Rotationsschwingungsbeiträge zurück. Wir

haben uns dem Problem der Berechnung von Rotationsschwingungsbeiträgen zu Moleküleigenschaften gewidmet und zwei diesbezügliche Verfahren entwickelt. Das erste behandelt die Rotationsschwingungs- und Temperaturbeiträge variationell, indem die entsprechende elektronische Eigenschaft über die Rotationsschwingungszustände gemittelt wird. Unsere Untersuchung der Rotationsschwingungsbeiträge zu den indirekten Kernspin-Kopplungskonstanten von Ammoniak hat gezeigt, dass die Effekte der Inversionsschwingung ("large amplitude motion") und der Coriolis-Kopplung überraschend groß sind und nicht einmal von einer Störungsrechnung hoher Ordnung erfasst werden können. Das zweite Verfahren befasst sich unmittelbar mit den spektroskopischen Observablen, nämlich den Rotations-Vibrations-Energieniveaus, deren Ableitungen und den Spektren eines Moleküls in einem elektromagnetischen Feld.

Contents

List of Figures

LIST OF FIGURES

List of Tables

LIST OF TABLES

1

Introduction

Molecular spectroscopy provides information on the structure, potential energy surface (PES) and internal dynamics of molecules. Such spectra require a detailed assignment and analysis based on theoretical models describing molecular motions from the quantum mechanical point of view. Due to the complexity of the multi-dimensional Schrödinger equation for molecular quantum states the *exact* quantum mechanical treatment is not possible. To solve this equation approximate methods have been developed which simplify this equation and offer approximate models of molecular motions.

A key advance for the theoretical treatment of molecular motions is the separation of nuclear and electronic degrees of freedom through the Born-Oppenheimer (BO) approximation (1, 2, 3). This approximation allows us to treat a molecular system as a set of nuclei moving over a PES created by the fast moving electrons that adjust simultaneously to any change of nuclear configuration. This approximation works extremely well for many molecular systems, although it breaks down when two electronic states strongly couple with each other at some nuclear configurations. Nevertheless, even in such a situation the PES concept is still useful: the nuclei can be imagined as moving in a manifold of coupled electronic states, each associated with a PES.

An important part of molecular spectroscopy focuses on understanding of the rotational-vibrational (ro-vibrational) spectra and properties, for which the ro-vibrational energy levels and wavefunctions associated with a PES must be determined. There are a number of steps involved in calculating the ro-vibrational spectrum of a molecule or any other property (electromagnetic, thermodynamic, etc.) from first principles.

These steps are depicted in Fig. 1.1 assuming a completely *ab initio* procedure. At first, the PESs are obtained by solving the time-independent Schrödinger equation for the electrons while treating the nuclei as static point charges. A variety of modern quantum chemistry methods (*ab initio* methods) are able to solve approximately the electronic structure problem and predict the potential (electronic) energy and electronic molecular properties, as well as their first and second geometrical derivatives for a single nuclear configuration. Given a PES the next step is solving the corresponding Schrödinger equation for the motion of nuclei. At this step the ro-vibrational energy levels and associated wavefunctions for that PES are determined. The ro-vibrational properties are then calculated as an expectation value of the corresponding operators in the ro-vibrational states of interest. After properly accounting for the parameters of the experimental measurements, e.g., temperature, pressure, absorption path length, intensity of the incident light, etc., the observables can finally be evaluated.

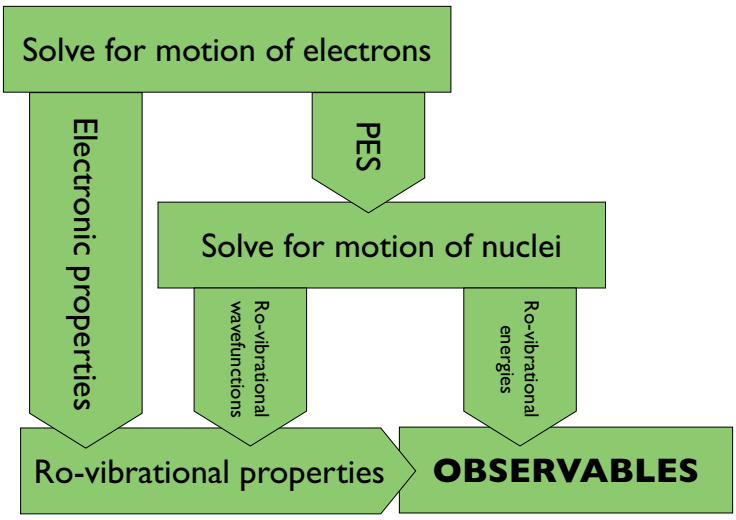

Figure 1.1: First-principles calculations of observables - Flow diagram depicting the steps involved in calculating the observables from first principles

The major step in Figure 1.1 is solving the time-independent Schrödinger equation applied to the motion of nuclei. This can be done using either perturbation theory (PT) or variational theory. The conventional methods to solve the nuclear motion problem are based on effective Hamiltonians for the ro-vibrational states under investigation

using the PT approach. The standard PT of the ro-vibrational states of semirigid molecules (4, 5, 6, 7, 8, 9), in which the nuclei execute small amplitude vibrations near the equilibrium structure, provides analytic expressions for the effective Hamiltonian parameters, called spectroscopic constants, as functions of the equilibrium structure and of the PES characteristics. The spectroscopic constants can be estimated either from the PES calculated by *ab initio* methods or, in a reverse procedure, from molecular spectra. Although PT has for a long time been the theoretical basis of high resolution molecular spectroscopy, there are many problems which cannot be solved by PT in a satisfying manner. Most standard PT treatments are based on the assumption of small amplitude vibrational motion. However there are many situations where this assumption is poor: molecules containing 'fast' hydrogen atoms and multiple minima in the PES and associated tunneling splittings are typical examples. Variational methods address directly cases for which the PT treatment is not reliable. They are able to solve both the rotational and vibrational problems within the same framework which adds considerably to their flexibility. However, these advantages have their price: variational computations are much more expensive than those based on PT. The computational expense of variational calculations is related to the size of the basis set employed which in turn depends on the coordinate system chosen. Therefore the choice of coordinates is important for the efficiency of a calculation. The optimal coordinates should satisfy several conditions: (a) span the whole configuration space accessible for the nuclei of the molecule; (b) be compatible with the symmetry of the molecule; such coordinates simplify partitioning of the Hamiltonian matrix into smaller independent sub-matrices; (c) minimize kinetic energy operator (KEO) and PES interaction terms, making the total Hamiltonian nearly separable; this also ensures faster basis set convergence. It is difficult to satisfy all of the above conditions even for small molecules. Usually coordinates that are optimal for the KEO are not acceptable for the PES. The normal coordinates, for example, do satisfy these criteria only if the internal motions are of small amplitude. However, for large amplitude vibrational motions standard straight extrapolations of normal coordinates often are not appropriate. Instead, curvilinear coordinates have to be employed for a proper description of large amplitude motion.

For a molecule composed of N nuclei, $3N$ Cartesian coordinates are needed to describe all its possible motions. Exact removal of translation leaves $3N-3$ coordinates. A further exact separation of the molecular motions is impossible. The transformation

to the molecule-fixed (MF) frame introduces three coordinates describing overall rotation and leaves $3N-6$ coordinates that describe internal nuclear motions in MF frame. The Euler angles θ, ϕ, χ are commonly used to define the rotation. More complicated nuclear motions can be viewed as a combination of rotation and internal nuclear motion. The last and most important step is the definition of $3N-6$ vibrational coordinates. These coordinates are invariant under uniform translation and rotation. The transformation from the initial Cartesian coordinates, relative to the space-fixed (SF) frame, to the translational, rotational, and vibrational coordinates, induces the transformation of the KEO and the PES. While the transformation of PES can be derived easily, due to rotational invariance (true for the field-free problem), the transformation of KEO is much more difficult. General prescriptions for the analytical derivation of MF Hamiltonians for various choices of internal coordinates were developed by Sørensen (10), Sutcliffe (11), and Webster *et al.* (12) based either upon application of the chain rule or Podolsky's trick (13). In practice, it is quite difficult to follow one of these prescriptions because the algebra can get very cumbersome. An alternative solution is the automatic numerical procedure for KEO transformation developed in recent years by Yurchenko *et al.* and implemented in the variational code TROVE (14).

The main highlights of the TROVE methodology can be summarized as following: (a) numerical construction of the ro-vibrational Hamiltonian for arbitrary molecules and arbitrarily chosen coordinates, either in the exact pointwise representation or approximated by a Taylor series expansion; (b) variational or discrete variable representation (DVR) solution for the full ro-vibrational problem; (c) possibility to compute highly excited rotational states ($J \leq 60$); the fast convergence is reached by employing the Eckart (4) conditions, that minimize the ro-vibrational coupling; (d) full utilization of the symmetry properties of a molecule (even for the non-abelian groups).

Accurate variational calculations of the ro-vibrational energies and wavefunctions are only possible for small molecular systems. Until recently most of the work using variational methods has concentrated on triatomic molecules (see, for example, (15)). The need to derive the ro-vibrational Hamiltonian (and its matrix representation) for each new molecule and each new type of the ro-vibrational coordinates hindered the straightforward extension of the variational methods to larger molecules. Substantial progress has been made in recent years towards the development of general numerical

procedures for constructing the ro-vibrational Hamiltonians (14, 16) and general variational techniques for solving the fully coupled ro-vibrational problem. Today, accurate variational calculations on tetra- and penta-atomic molecules are becoming more common. The spectroscopic data provided by the variational calculations are nowadays in much demand for atmospheric and astronomical research.

The ro-vibrational energies and wavefunctions can be used to calculate a number of different molecular properties. These include almost all of spectroscopy (transition moments, line strengths and intensities), thermally averaged and purely vibrational electromagnetic properties, as well as thermodynamic properties. Many chemical properties of a molecule can be described by an analysis of the critical points of the PES: geometries of minima and transition states, relative energies and barriers, second derivatives and harmonic frequencies, etc. Thus, the local characteristics of the PES determine much of the physics and chemistry of molecules.

Much theoretical effort was directed in the present work towards the development and implementation (in TROVE) of methods to study the aforementioned molecular properties. The work extended the functionality of TROVE in several directions: (a) fast calculation of the ro-vibrational transition matrix elements for any scalar, vector, or more general, tensor operator; (b) calculation of the ro-vibrational transition dipole line strengths and intensities in the infra-red; (c) calculation of the ro-vibrational matrix elements of the polarizability tensor and simulation of Raman activities; (d) calculation of the ro-vibrational density matrix exponential and temperature corrections to the molecular properties; calculation of partition functions and thermodynamic parameters; (e) calculation of the ro-vibrational energies and molecular properties in the presence of a homogeneous external electric field. The new developments were applied for solution of the following problems: (a) calculation of benchmark results for ro-vibrational energies, that are used for testing the accuracy of the modern *ab initio* methods; (b) refinement of highly accurate PESs through adjustment to spectroscopic data; (c) calculation of high-resolution spectra for a myriad of transitions in small molecules to provide accurate line lists for astrophysical databases; (d) calculation of thermally averaged electromagnetic properties, high-temperature partition functions, and related thermodynamic properties.

1. INTRODUCTION

In this work we focus on the following three topics: (i) calculation of ground electronic state PESs at high (spectroscopic) accuracy; (ii) calculation of high-resolution ro-vibrational spectra, and (iii) calculation of the ro-vibrational contributions to electric and magnetic properties. In Chapter 2, the *ab initio* and the *spectroscopic* methods for calculating accurate PESs are described. The performance of both methods is explored in case studies on H_2CS and H_2CO. In Chapter 3, the *ab initio* calculation of electric dipole moment surfaces and the theoretical model used for simulating the ro-vibrational spectra are described. As applications we present the theoretical simulation of the rotation-torsion spectra of HSOH and of the complete $T = 300$ K line list of NH_3. By analysing the ro-vibrational transitions and the associated energies and wavefunctions, we were able to explain the intensity anomaly observed in the rotation-torsion spectrum of HSOH. The theoretical model used for calculating the thermally averaged properties and purely vibrational electric properties is presented in Chapter 4. As example, the magnetic properties of $^{15}NH_3$ and its isotopologues are discussed, with emphasis on the effects of the large amplitude inversion motion.

2

Accurate potential energy surfaces for the ground electronic state

The concept of PESs is fundamental for the understanding of most modern branches of chemistry, including almost all of spectroscopy and kinetics (17, 18, 19, 20). Nevertheless PESs exist only within the BO separation of the electronic and nuclear motion, although adiabatic corrections relax this strict separation. Usually attention is focused on cases where a single PES is sufficiently uncoupled from the surfaces of other electronic states so that their interaction may be ignored. Most important is the PES of the ground electronic state.

Modern quantum chemical methods can be used to explore these PESs. The availability of analytical gradients and higher derivative methods for most of quantum chemical methods has substantially amplified the capability to locate and characterize crucial points and regions on the PES: determination of molecular geometries, force fields, transition structures, etc. In theoretical ro-vibrational spectroscopy, large sections of the PES around the equilibrium region need to be computed accurately as input for solving the Schrödinger equation for nuclear motion. In the reverse problem one can obtain details of the PES from an analysis of well-resolved ro-vibrational spectra. Using such a procedure to improve the purely theoretical PES results in a "spectroscopic PES". The spectroscopic methods for obtaining PESs possess one important advantage over the *ab initio* techniques: they can utilize results of higher (spectroscopic) accuracy. The spec-

troscopic determination of a PES involves the following steps: (a) collecting accurate data for ro-vibrational transitions and energies; (b) choice of a physically correct model for the description of nuclear motion, including the choice of the initial guess for the PES and of ro-vibrational coordinates; (c) application of reliable procedures to compute ro-vibrational energies with high accuracy. The accuracy and reliability of the resulting PES depends on the wealth of data covering equally well all important energy regions. If sufficient data are not available, the refinement may lead to a PES distorted to an unphysical form in the regions of configuration space which are not sampled by the experimental data. Usually this condition is never well satisfied because spectroscopic measurements of high accuracy are available only for a very narrow frequency range. Therefore spectroscopic methods can be used for modeling more or less local parts of the potential surfaces. The *ab initio* methods are more flexible in the prediction of the global potential energy hypersurface. The *ab initio* construction of a hypersurface involves: (a) choice of physically correct and robust electron correlation methodology; (b) application of highly flexible and compact basis set; (c) design of a suitable geometrical grid. A compromise between the two approaches can be reached when the potential of the *ab initio* methods in predicting the global hypersurface is combined with the high accuracy available from spectroscopic methods at least for local parts of the PES under investigation.

In the following two sections, 2.1 and 2.2, we briefly describe the *ab initio* and spectroscopic methods for determination of the ground electronic state PESs, aiming at high accuracy. Case studies on H_2CS and H_2CO serve as examples for the performance of both methods.

2.1 *Ab initio* determination

For nearly all systems of chemical interest the exact solution to the nonrelativistic time-independent electronic Schrödinger equation cannot be obtained, and thus one must introduce approximations. There are two fundamental approximations: truncation of the one- and N-particle bases. Extension of both the one-particle space (atomic basis set) and N-particle space (many-electron wavefunction) is needed to achieve results close to the nonrelativistic limit. The limiting case of the one-electron basis set is usually referred to as complete basis set limit (CBS), while the case of the complete

N-particle basis set is referred to as full configuration interaction (FCI) limit. Most of the methods in quantum chemistry can be understood in terms of convergence of the results to the CBS and FCI limits.

The simplest standard model that *ab initio* theory offers is the Hartree-Fock (HF) mean field theory. An appealing feature of HF is that it retains the notion of molecular orbitals as one-electron functions describing the motion of an electron in an average field of all other electrons. At minima, the HF method typically recovers some 99 % of the electronic energy, but its performance can deteriorate rapidly when moving away from equilibrium. The weakness of the HF model is that it does not include electron correlation effects that may vary greatly over a PES. In the wavefunction models that go beyond the HF description, techniques of various sophistication are employed to represent the long- and short-range electron-electron interactions, especially the Coulomb hole.

The most powerful methods for treating electron-electron correlation effects are based on the multi-reference configuration interaction (MRCI) expansion or utilize the more ingenious single-reference coupled-cluster (CC) representation (see for example (21)). The MRCI methods are known to offer the most accurate general treatment of the electron-correlation effects, i.e. they are well converged in the N-electron basis set. While MRCI provides an extremely accurate representation of a PES close to FCI, this approach is limited to molecules with a small number of valence electrons that can be well described by a limited number of orbitals in the active space. Single reference CC methods promise to yield accurate representations of the PES at lower cost than MRCI (22), if non-dynamical electron correlation is not overly important. One more advantage of the CC method over MRCI is that it is also size-consistent (23, 24) and thus can provide comparable accuracy for all parts of the potential investigated. More specifically, during molecular fragmentation a size-consistent method leads to a wave function which is multiplicatively separable and an energy which is additively separable. While variational calculations are size-consistent only if an exponentially growing direct-product space of the fragments is employed for their construction, nonvariational CC and PT methods are naturally designed for multiplicatively separable approximate wavefunctions.

Two approaches to obtain the correlation energy at the CBS limit have emerged in recent years. First, noting that the correlation energy converges systematically

in correlation-consistent basis sets, one can extrapolate from results with finite basis sets (25, 26, 27, 28, 29). Second, one can use wave functions that explicitly depend on the interelectronic distance when evaluating contributions from excited configurations (30, 31, 32, 33, 34). The latter approach defines the family of explicitly correlated methods that promise near-basis-set limit correlation energies using moderate size basis sets.

The CC and explicitly correlated methods are briefly described in the following two sections (Sec. 2.1.1 and 2.1.2) as the most successful approaches that offer size-consistent results close to the FCI and CBS limits, in other words, close to the exact solution. Calculation of the remaining small high level correction terms to the PES that arise from the correlation of core electrons, effects due to special relativity, nonadiabatic effects, etc., are described in Section 2.1.3.

2.1.1 Coupled-cluster method

The coupled-cluster method is an attempt to introduce interactions among electrons within clusters as well as couplings among these clusters and to permit the wavefunction to contain all possible disjoint clusters. The mechanism for introducing these cluster interactions is to write the wavefunction in terms of so-called cluster operator T acting on a reference function describing noncoupled electrons

$$|\psi\rangle_{CC} = \exp(T)|\psi_0\rangle \tag{2.1}$$

The reference function is limited, in most standard single-reference treatments, to a single Slater determinant. The cluster operator T generates one-, two-electron, etc., clusters

$$T = T_1 + T_2 + ...T_N, \tag{2.2}$$

$$T_1 = \sum_{i,a} t_i^a a^+ i, \tag{2.3}$$

$$T_2 = \frac{1}{4} \sum_{i,j,a,b} t_{ij}^{ab} a^+ b^+ ij, \text{ etc...} \tag{2.4}$$

In these equations the indices $i, j, ...$ denote spin-orbitals occupied in $|\psi_0\rangle$, $a, b, ...$ denote unoccupied spin-orbitals. The cluster amplitudes $t_{ij...}^{ab...}$ are determined by insisting that $\exp(T)|\psi_0\rangle$ satisfies the Schrödinger equation

$$H \exp(T)|\psi_0\rangle = E \exp(T)|\psi_0\rangle, \tag{2.5}$$

which upon premultiplying by $\exp(-T)$ gives

$$\exp(-T)H\exp(T)|\psi_0\rangle = E|\psi_0\rangle. \tag{2.6}$$

The above exponential series gives when the Hausdorff expansion is employed

$$\begin{aligned}\Big(H &+ [H,T] + \frac{1}{2!}[[H,T],T] + \frac{1}{3!}[[[H,T],T],T] \\ &+ \frac{1}{4!}[[[[H,T],T],T],T]\Big)|\psi_0\rangle = E|\psi_0\rangle.\end{aligned} \tag{2.7}$$

The series truncates exactly after fourth-order terms regardless of the level at which T is truncated. This exact truncation is a result of the fact that H contains at most two-electron operators, which involve four, particle or hole, operators. A closed set of equations for the amplitudes is obtained by insisting that the final Schrödinger equation 2.7, when projected against a set of low-order excitations out of $|\psi_0\rangle$, yields zero. If the particular excitations are chosen to include up through n-fold excitations the resulting set of equations will then be equal in number to the number of amplitudes $t_{ij\ldots}^{ab\cdots}$ in T_n. Once these amplitudes are obtained by solving the resulting nonlinear equations, the total electronic energy is computed by projecting Eq. 2.7 onto $|\psi_0\rangle$.

It should be noted that the energy expression obtained from Eq. 2.7 is not variational in the sense that it is not given as an expectation value of the Hamiltonian. The quantity

$$E = \frac{\langle\psi_0|\exp(T^\dagger)H\exp(T)|\psi_0\rangle}{\langle\psi_0|\exp(T^\dagger)\exp(T)|\psi_0\rangle} \tag{2.8}$$

would give rise to a variational energy expression. Another way to arrive at variational coupled-cluster theory is to apply a unitary transformation to the Hamiltonian of the form (35)

$$E = \langle\psi_0|\exp(T^\dagger - T)H\exp(T - T^\dagger)|\psi_0\rangle. \tag{2.9}$$

Unfortunately, the Hausdorff commutator expansion of exponential operators in Eqs. 2.8 and 2.9 is infinite. The expansion of the operator in Eq. 2.9, however, converges faster than the expansion of Eq. 2.8 (35).

The highlights of CC theory are as follows: (a) at any order of truncation, CC methods are size-extensive; (b) the exponential form ensures that all higher excitations are included in the wavefunction; (c) CC wavefunctions are not variational, one of the consequences is that calculation of energy derivatives requires the setup and solution of

additional linear response equations. In the usual applications of coupled-cluster theory, only certain excitation operators are included in the cluster operator. Restricting T just to T_2 results in the CCD method. Inclusion of T_1 and T_2 gives the widely employed CCSD method. Inclusion of T_3 defines the CCSDT method. The well-balanced CCSD(T) (36) approach, which includes a noniterative perturbative correction for the effect of connected triple excitations, is able to provide relative electronic energies of chemical accuracy as well as excellent results for a wide range of molecular properties (37, 38, 39).

2.1.2 Explicitly correlated methods

The Coulomb potential in the usual electronic Hamiltonian becomes singular when any two particles coalesce. In order to fulfill the requirements that the wavefunctions satisfy the Schrödinger equation and remain bounded at these poles, certain cusp conditions need to be satisfied. Particularly, one must consider the nuclear cusp, when electrons and nuclei coincide, and the electronic (Coulomb) cusp, when electrons coincide. The nuclear cusp condition is satisfied when the wavefunction exhibits, close to the nucleus, a simple exponential dependence on the electronic coordinate. This can be achieved by using Slater-type basis functions. The Coulomb cusp conditions lead to a wavefunction that is continuous but not smooth at $r_{12} = 0$, the wavefunction has discontinuous first derivatives

$$\left(\frac{\partial\Psi(r_{12})}{\partial r_{12}}\right)_{r_{12}\to 0} = \frac{1}{2}\Psi(r_{12}=0) \tag{2.10}$$

It is also well known that the deviation between exact and approximate wavefunctions is most significant at short electron-electron distances. However, it has been argued for quite some time that the actual contribution to the energy from the configuration space around the coalescence point is negligible (40). In fact it is not the cusp condition that is important for energies, but rather the overall shape of the Coulomb hole.

Methods that explicitly introduce the interelectronic coordinates in the wavefunction are known as explicitly correlated methods. If the term $|\Phi\rangle$ dominates in the conventional expansion of the wavefunction, one can write

$$|\Psi\rangle = \frac{1}{2}\hat{r}_{12}|\Phi\rangle + \hat{C}|\Phi\rangle \tag{2.11}$$

where $\hat{C}$ transforms $|\Phi\rangle$ to a conventional configuration expansion and $\hat{r}_{12}$ introduces explicit dependence of the wavefunction $|\Psi\rangle$ on the interelectronic distance r_{12}. Such methods, which employ a simple reference configuration multiplied linearly by the interelectronic distances, are referred to as R12 methods (41). If other functions of $\hat{r}_{12}$ are used instead of $\hat{r}_{12}$ itself, the so-called F12 methods are obtained. Three-, and four-electron integrals over linear r_{12}-dependent functions appear in the R12 theory. In practice, these many-electron intergrals are eliminated in linear R12 theory by inserting into them an approximate resolution of identity in terms of an orbital basis. Further improvements in computational efficiency are possible due to improved RI techniques (42, 43, 44), density fitting (45), and local correlation (46, 47). Linear R12 techniques (41) have been implemented within the frameworks of CI, CC, and PT theory. Recently proposed more approximate and less expensive CCSD(T)-F12x ($x = a, b$) methods (48, 49) have been used in our studies.

2.1.3 Small high level corrections

The high level (HL) correction terms tacitly neglected in most quantum chemical calculations of PESs include: core-electron correlation, usually divided into core-core and core-valence parts, high-order excitation contributions to electron correlation, adiabatic and nonadiabatic corrections, and effects due to special relativity. The corrections to PESs arising from these effects are generally small but if we aim at high, nearly spectroscopic, accuracy they should be considered. It has been shown that for many diatomic systems, spectroscopic accuracy can be obtained by combining the valence-only CCSD(T) results at the one-particle basis set limit with various HL correction terms that are evaluated with smaller basis sets (29, 50, 51, 52, 53, 54, 55). Computational savings are obtained by exploiting different basis set convergence rates of these terms. Relatively few studies have considered such HL corrections in the calculation of multidimensional PES (56, 57, 58, 59, 60, 61). The lack of analytical derivatives for most of the HL correction terms implies that a large number of well-converged single point calculations must be performed to construct an accurate PES. This restricts routine application of such methods for construction of PESs of polyatomic molecules.

One of the most common assumptions in quantum chemistry concerns inner-shell orbitals. It is assumed that the energetics and structures of most molecular species are determined by interactions of valence electrons, spatially much more extended than

the tight inner shell orbitals. The core-correlation energy is defined as the difference between the all-electron correlation energy and the valence-valence correlation energy. The core-core correlation energy arises from double and higher excitations out of the core orbitals, the core-valence correlation energy results from single excitations out of the core orbitals together with excitations from the valence orbitals. The core-valence (CV) correlation energy is sensitive to the changes in the geometry of molecule, and thus it affects substantially the calculation of the PES (force constants).

High order electron correlation corrections (HO) need to be included for an accurate treatment of electron correlation. They are usually considered as a correction beyond the standard CCSD(T) treatment. They can be estimated using high order single-reference CC approaches, CCSDT, CCSDTQ, and CCSDTQP or MRCI-based methods. They are usually smaller than the CV corrections, although in some cases both are comparable and almost cancel each other.

The diagonal Born-Oppenheimer correction (DBOC) to the potential function

$$\langle \Psi_{\text{elec}}| - \sum_A \frac{\hbar^2}{2M_A} \nabla_{\text{A}}^2 |\Psi_{\text{elec}}\rangle \tag{2.12}$$

represents an attempt to improve on the BO approximation. The BO energy plus DBOC provides the best energy possible using a single PES. The addition of DBOC to the BO energy constitutes the adiabatic approximation. The DBOC is mass-dependent (62, 63) and usually quite small. Its calculation is straightforward if analytical derivatives are available (64). Usually, rather accurate estimates for the DBOC can be obtained already at the HF level of theory (65, 66). However, the more hydrogen atoms are present in the chemical system the more important becomes the DBOC, and in such cases an accurate calculation of this correction requires correlated methods. For highly accurate PES prediction the DBOC cannot be neglected, especially if hydrogen or other light atoms are present in the molecular system.

Relativistic effects are defined as the difference in an observable property that arises from the true velocity of light as opposed to the assumed infinite velocity in conventional treatments of quantum chemistry. Fully relativistic calculations solve the four-component Dirac-Hartree-Fock equation (67, 68, 69). The Dirac equation, which is difficult to handle computationally in its four-component spinor form, can be brought into a two-component form by an appropriate transformation (70). Widely used among

the two-component methods are the Douglas-Kroll-Hess (DKH) approach (71, 72) and the ZORA scheme (73). At the nonrelativistic limit the most important terms in the first-order expression include the one-electron mass-velocity (MV) term, the one- and two-electron Darwin terms (D1, D2), and the spin-spin and spin-orbit coupling terms. For light atoms the spin-orbit coupling terms are small and usually neglected in the calculations of PESs. The size of the MVD corrections to the PES in light molecules may be quite substantial, contributing, for example, more than 20 cm^{-1} to the inversion barrier of ammonia.

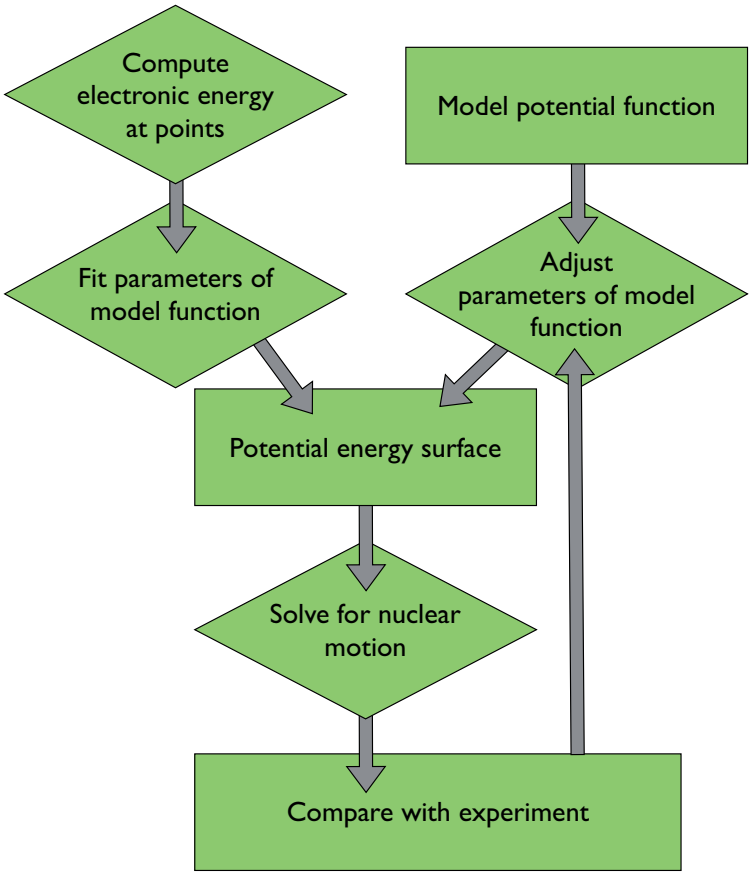

Figure 2.1: PES fitting procedure - Flow diagram depicting the steps involved in the adjustment of a theoretical PES to experimental data

2.2 Spectroscopic determination

The realization that it is not possible to calculate *ab initio* PESs of many-electron molecules to spectroscopic accuracy has led to an alternative strategy. Comparisons between calculated and experimental data, usually either transition frequencies or energy levels, are used to refine the PES. This procedure, which results in a spectroscopically determined effective PES, is summarized in Fig. 2.1. Spectroscopically determined potentials usually rely on high accuracy *ab initio* calculations as starting point. These calculations give a PES at grid points, so these are normally interpolated by fitting to some suitable function. The fitted potentials are then used as a starting guess for variational calculations, the results of which can be compared with experiment. The potential is then adjusted and the procedure repeated until convergence is achieved. The usual technique to optimize potentials is least-squares (LSQ) fitting. In practice it is desirable for the fitting procedure not to take too many iterations since each step is computationally fairly expensive. This goal can be achieved by making use of the derivatives of the potential with respect to the parameters being optimized. These derivatives can be obtained at modest computational cost using the Hellmann-Feynman theorem

$$\frac{\partial E_i}{\partial F_k} = \langle i|\frac{\partial V}{\partial F_k}|i\rangle, \tag{2.13}$$

for each state i of interest. In Eq. 2.13 V is the present approximation for the PES and F_k is any parameter that we wish to vary. The derivatives of the KEO are assumed to be zero since the exact KEO is parameter free. However, if the KEO is approximated by a power series expansion at the equilibrium geometry, variations of the parameters will affect kinetic energy as well.

In the PESs fittings, the parameters selected for refinement and the physical nature of the available observed transitions are strongly interrelated. An unrestricted optimization of the parameters may lead to unphysical behavior of the resulting PES, especially if there are large variations in parameters that are of little or no relevance for the transitions used in the refinement. In order to prevent the refined surface from distorting into unrealistic/unphysical shapes in regions that are not well characterized by the experimental data we have developed a restraining technique that forces the

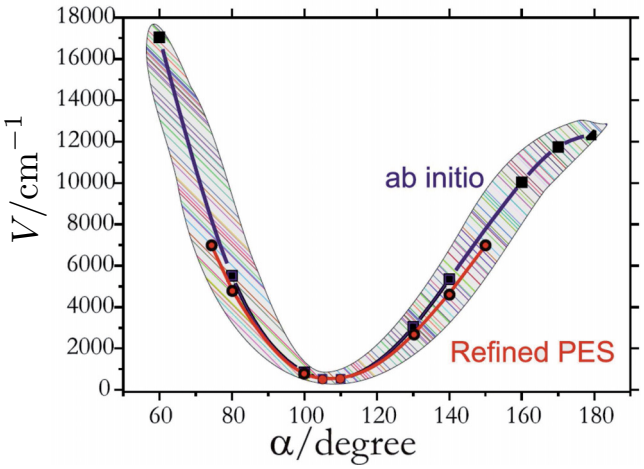

Figure 2.2: Schematic representation of the PES restraint refinement - The adjusted potential (red curve) reproduces experimental data in the vicinity of the equilibrium well and resembles the *ab initio* potential (blue) in the remote parts. The accessible potential range during refinement is shown by the shaded area; it is tight at equilibrium and broadens at large displacements

refined PES to stay relatively close to the *ab initio* PES. This is schematically shown in Fig. 2.2.

The PES refinement is a very time consuming procedure: at each Newton step the $N_E \times N_F$ derivatives of N_E energies with regard to N_F parameters need to be estimated. This makes PES refinement even for a triatomic molecule a hard and resource consuming task.

The procedure may, however, be simplified when recognizing that the initial *ab initio* PES is already quite accurate in reproducing experiment. Therefore the required corrections to the PES may be considered as small perturbations that are easily treated by a PT approach. Denoting this correction to the initial *ab initio* PES by ΔV, the corresponding Hamiltonian is given by

$$H = T + V_0 + \Delta V = H_0 + \sum_{klm...} \Delta F_{klm...} \xi_1^k \xi_2^l \xi_3^m ..., \tag{2.14}$$

where H_0 is an *ab initio* Hamiltonian, ξ_r $(r = 1, 2, ..3N-6)$ are internal vibrational coordinates, and $\Delta F_{klm...}$ are perturbations to the *ab initio* PES expansion parameters. The Hamiltonian H is diagonalized in the basis constructed from the eigenfunctions of the *ab initio* Hamiltonian H_0. This significantly simplifies the evaluation of the

corresponding matrix elements

$$\langle i|H|i'\rangle = E_0^{(i)}\delta_{ii'} + \sum_{klm...} \Delta F_{klm...}\langle i|\xi_1^k\xi_2^l\xi_3^m...|i'\rangle \tag{2.15}$$

with

$$H_0|i\rangle = E_0^{(i)}|i\rangle. \tag{2.16}$$

Hence, in the refinement procedure we need to compute and store all the matrix elements $\langle i|\xi_1^k\xi_2^l\xi_3^m...|i'\rangle$ only once. The derivatives for the LSQ fitting are calculated utilizing the Hellmann-Feynman theorem

$$\frac{\partial E^{(j)}}{\partial \Delta F_{klm...}} = \langle j|\xi_1^k\xi_2^l\xi_3^m...|j\rangle = \sum_{ii'} C_i^{(j)}C_{i'}^{(j)}\langle i|\xi_1^k\xi_2^l\xi_3^m...|i'\rangle, \tag{2.17}$$

where $|j\rangle$ is an eigenfunction of H

$$|j\rangle = \sum_i C_i^{(j)}|i\rangle, \tag{2.18}$$

$$H|j\rangle = E^{(j)}|j\rangle. \tag{2.19}$$

The spectroscopic data selected for the fitting usually contain energy levels that correspond to low values of quantum number of the total angular momentum, $J = 0 - 8$. This is enough to obtain a PES that is able to produce accurate results for high-J energy levels. It should be noted that the results of the fitting are generally quite sensitive to the size of the basis set employed, and therefore the adjusted PES is normally just an effective PES, i.e. it can guarantee the stated accuracy only when utilized in conjunction with the approach (type of coordinates, KEO and PES operators, basis set) used in the fitting.

Further computational savings can be obtained if accurate vibrational band centers ($J = 0$) are known from experiment. The idea comes from standard ro-vibrational PT and is based on the fact that PES parameters mainly determine positions of $J = 0$ band origins whilst $J > 0$ energies are mainly governed by the equilibrium parameters. Therefore, in order to obtain accurate rotational spectra we adjust only the equilibrium constants (this usually requires only one Newton step), using the microwave spectra as reference data. Solving the vibrational ($J = 0$) problem

$$H_{\rm vib}|n\rangle \;=\; E_{\rm vib}^{(n)}|n\rangle \tag{2.20}$$

we obtain the vibrational energies $E_{\mathrm{vib}}^{(n)}$ and vibrational functions $|n\rangle$. The full ro-vibrational problem is then formulated in the basis of these functions $|n\rangle$ multiplied by the rotational functions $|J,k,m\rangle$:

$$\begin{aligned}\langle n';J,k',m|H_{\mathrm{vib}}+H_{\mathrm{ro-vib}}|n;J,k,m\rangle &= E_{\mathrm{vib}}^{(n)}\delta_{n,n'}\delta_{k,k'} \\ &+ \langle n';J,k',m|H_{\mathrm{ro-vib}}|n;J,k,m\rangle.\end{aligned} \tag{2.21}$$

In Eq. 2.21 the purely vibrational Hamiltonian is diagonal in the basis of vibrational eigenfunctions, and the total Hamiltonian can be viewed as an effective Hamiltonian with $E_{\mathrm{vib}}^{(n)}$ as parameters. Since the vibrational wavefunctions are not overly sensitive to the quality of the PES (less so than the energies according to PT), we expect that the second matrix in Eq. 2.21 can be computed with significant accuracy by using the vibrational wavefunctions from the *ab initio* PES and refining the equilibrium constants only. Therefore, in order to improve substantially the description of the ro-vibrational energy levels, only the vibrational energies $E_{\mathrm{vib}}^{(n)}$ must be refined. If the experimental numbers $E_{\mathrm{obs.}}^{(n)}$ are available, the corresponding energies in Eq. 2.21 may be replaced with the exact ones, $E_{\mathrm{vib}}^{(n)} \leftarrow E_{\mathrm{obs.}}^{(n)}$.

This procedure offers a fast and efficient way to improve the theoretical description of ro-vibrational spectra of molecules and to reach the spectroscopic accuracy for a given *ab initio* PES. The ro-vibrational energies, obtained as eigenvalues of the effective Hamiltonian in Eq. 2.21, are usually in very good agreement with experiment.

2.3 High level *ab initio* PES of H_2CS

Here we review the *ab initio* calculation of the six-dimensional ground electronic state PES of H_2CS (74). The available high-resolution spectroscopic data for H_2CS is very scarce which hinders the construction of a globally accurate spectroscopic PES. For example, the refined force constants from Carter and Handy (75) provide the reasonably accurate results for their fitting set covering the pure rotational, fundamental, $2\nu_2$, and $\nu_2+\nu_3$ bands, but they fail for other transitions outside their fitting set. Thus the calculation of an accurate *ab initio* PES is the only resort. Our goal was to generate such PES for H_2CS by combining the highest level of modern *ab initio* theory with variational calculations (14) of the vibrational energies for this molecule.

2. ACCURATE POTENTIAL ENERGY SURFACES FOR THE GROUND ELECTRONIC STATE

Towards this end we employ the recently proposed explicitly correlated F12 singles and doubles coupled cluster method including a perturbational estimate of connected triple excitations, CCSD(T)-F12b (48) in conjunction with the corresponding F12-optimized correlation consistent basis set cc-pVQZ-F12 (76). The F12 methods have the advantage of providing the near-basis-set-limit accuracy even with basis sets of moderate size (34). Since the perturbative triples (T) contributions to the correlation energies CCSD(T)-F12b are not treated in an explicitly correlated manner in this work, we extrapolated them using the standard X^{-3} expression (77) (where $X = 3, 4$ denotes the cardinal quantum number of the basis sets cc-pVTZ-F12 and cc-pVQZ-F12 respectively). Henceforth these F12 coupled cluster calculations will be referred to as VQZ-F12*.

We also include high-level (HL) additive corrections comprising the core-valence (CV), scalar relativistic (SR), high-order electron correlation (HO), and diagonal Born-Oppenheimer (DBOC) corrections, which are expected to contribute significantly to the molecular (ro-)vibrational energies. It has been shown, for example, that the HL corrections evaluated using small basis sets in conjunction with valence-only CCSD(T) methods at the one-particle basis set limit can provide spectroscopic accuracy in case of diatomic closed-shell molecules (29, 50, 51, 52, 53, 54, 55). The importance of the HL corrections for accurate construction of multidimensional PESs for polyatomic molecules has also been recognized (see, for example, Refs. (56, 57, 58, 59, 60, 61)). Different HL corrections are expected to contribute differently to the vibrational energies. In order to investigate this effect in detail we constructed a set of 6D PESs, in which each of the HL corrections was included independently, and utilized them in variational calculations of vibrational term values of H_2CS below 5000 cm^{-1}.

Inspection of Table 2.1 shows that CV has a large effect on all vibrational term values, raising the values by up to 15 cm^{-1}, but is largely compensated by negative HO and SR values. The HO correction appears to lower the vibrational term values, especially for all bands involving the ν_3 mode associated with the C-S stretch. The out-of-plane mode ν_4 is also significantly affected by this correction with a change of the fundamental term value by 3 cm^{-1}. The impact from the SR contribution also appears mostly in the term values associated with the ν_3 mode, for example, with a change of 4.42 cm^{-1} in case of $3\nu_3$, whereas the effect on other modes is minimal, within 1-2 cm^{-1}. Only the ν_1 and ν_5 modes are affected by the DBOC correction, whose influence

is however generally rather small (about 0.5 cm^{-1} for the fundamentals). In case of the CH vibrational modes, the large positive CV contributions are not well compensated by the negative HO and SR corrections, which leads to a significant combined effect on the corresponding term values ν_1 and ν_5, 2.99 cm^{-1} and 3.42 cm^{-1}, respectively. By contrast, the net effect of all HL corrections on the C-S stretching is smaller, only -1.20 cm^{-1} for ν_3, due to fortuitous cancellation.

We now consider our two best *ab initio* PESs of H_2CS, VQZ-F12^{*HL} and VQZ-F12*. The latter is calculated at the specified theoretical level (i.e., CCSD(T) at the near-CBS limit), which is expected to provide accurate results due to the cancellation of different HL contributions. The former PES, VQZ-F12^{*HL}, is generated from VQZ-F12* by adding all HL = CV+HO+SR+DBOC corrections. In Table 2.2 we collect the fundamental term values obtained from these two PESs, and compare them to the available experimental data (78, 79). The VQZ-F12* surface provides vibrational term values in fairly good agreement with experiment: the maximum error is 2.60 cm^{-1} for ν_3, the deviations are less than 2 cm^{-1} for the other fundamentals, and the mean absolute deviation for all six fundamentals amounts to 1.22 cm^{-1}. In spite of the significantly higher computational effort, the VQZ-F12^{*HL} surface yields similar errors: the wavenumbers of the C-H stretching modes ν_1 and ν_5 are overestimated by 1.43 and 3.12 cm^{-1}, respectively, the description of ν_3 is slightly improved (overestimate of 1.40 rather than 2.60 cm^{-1}), and the mean absolute deviation for all six fundamentals is 1.13 cm^{-1}. These data indicate that it is very difficult to get beyond wavenumber accuracy by a purely *abinitio* approach for molecules such as H_2CS, in spite of a dedicated attempt to include the dominant HL corrections in a converged manner.

In the future we plan to perform an empirical optimization of our *ab initio* PESs through least-squares fittings to the available (78, 79) experimental energies of H_2CS. Since the amount of experimental data is very limited, the accuracy of the *ab initio* PES is of special importance. We believe that both of our *ab initio* PESs are equally well suited as initial guesses for the refinement process. The refined PES will then be used for simulating the high-resolution rotational-vibrational spectra in the infra-red region.

mode	$\Gamma^{(\mathbf{C}_{2v})}$	VQZ-F12*	CV	HO	SR	DBOC	Total HL
ν_6	B_2	989.59	2.71	-1.19	-0.35	0.09	1.26
ν_4	B_1	990.59	3.64	-3.01	-0.56	-0.03	0.04
ν_3	A_1	1061.81	4.94	-4.61	-1.48	-0.05	-1.20
ν_2	A_1	1454.50	2.89	-1.28	-0.19	-0.20	1.22
$2\nu_6$	A_1	1965.56	6.03	-3.84	-0.89	0.10	1.40
$\nu_4+\nu_6$	A_2	1988.41	6.33	-4.22	-0.92	0.08	1.27
$2\nu_4$	A_1	1991.73	6.50	-4.45	-0.93	0.01	1.13
$\nu_3+\nu_4$	B_1	2047.29	7.65	-6.15	-2.03	-0.09	-0.62
$\nu_3+\nu_6$	B_2	2047.92	8.63	-7.43	-1.84	0.04	-0.60
$2\nu_3$	A_1	2113.97	9.88	-9.25	-2.95	-0.12	-2.44
$\nu_2+\nu_6$	B_2	2429.00	5.49	-2.45	-0.54	-0.12	2.38
$\nu_2+\nu_4$	B_1	2438.82	6.63	-4.47	-0.79	-0.23	1.14
$\nu_2+\nu_3$	A_1	2511.92	7.84	-5.92	-1.66	-0.26	0.00
$2\nu_2$	A_1	2875.24	5.71	-2.25	-0.46	-0.44	2.56
$3\nu_6$	B_2	2946.96	8.40	-4.52	-1.12	0.26	3.02
$3\nu_4$	B_1	2954.65	9.94	-7.55	-1.52	0.02	0.89
ν_1	A_1	2969.47	6.11	-2.04	-0.52	-0.56	2.99
$2\nu_4+\nu_6$	B_2	2997.92	9.32	-6.06	-1.35	0.06	1.97
$2\nu_6+\nu_4$	B_1	3000.08	9.70	-6.66	-1.40	0.04	1.68
$2\nu_6+\nu_3$	A_1	3018.97	10.69	-8.30	-2.38	0.05	0.06
ν_5	B_2	3024.32	6.54	-2.28	-0.50	-0.34	3.42
$\nu_3+\nu_4+\nu_6$	A_2	3041.58	11.32	-8.99	-2.40	0.03	-0.04
$2\nu_4+\nu_3$	A_1	3044.92	11.47	-9.18	-2.42	-0.03	-0.16
$2\nu_3+\nu_6$	B_2	3095.45	13.60	-11.61	-3.31	-0.02	-1.34
$2\nu_3+\nu_4$	B_1	3095.51	12.56	-11.36	-3.51	-0.14	-2.45
$3\nu_3$	A_1	3156.42	14.81	-13.89	-4.42	-0.16	-3.66
$2\nu_6+\nu_2$	A_1	3393.66	8.42	-4.35	-0.95	-0.06	3.06
$\nu_2+\nu_4+\nu_6$	A_2	3422.46	9.23	-5.64	-1.16	-0.12	2.31
$2\nu_4+\nu_2$	A_1	3429.48	9.92	-6.82	-1.31	-0.24	1.55
$\nu_2+\nu_3+\nu_6$	B_2	3482.65	10.43	-7.15	-2.02	-0.17	1.09
$\nu_2+\nu_3+\nu_4$	B_1	3491.57	11.62	-9.20	-2.28	-0.29	-0.15
$2\nu_3+\nu_2$	A_1	3559.70	12.77	-10.58	-3.13	-0.32	-1.26
$2\nu_2+\nu_6$	B_2	3839.77	8.26	-3.52	-0.78	-0.34	3.62
$2\nu_2+\nu_4$	B_1	3855.66	9.50	-5.56	-1.07	-0.46	2.41
$2\nu_2+\nu_3$	A_1	3930.76	10.64	-6.92	-1.93	-0.49	1.30
$3\nu_2$	A_1	4283.46	8.50	-3.43	-0.70	-0.63	3.74

Table 2.1: The effect of the high-level *ab initio* corrections on the vibrational term values (in cm^{-1}) of H_2CS.

Mode	$\Gamma^{(C_{2v})}$	VQZ-F12*	VQZ-F12*^{HL}	Exp. (78)	VQZ-F12*–Exp.	VQZ-F12*^{HL}–Exp.
ν_1	A_1	2969.47	2972.46	2971.03	-1.56	1.43
ν_2	A_1	1454.50	1455.72	1455.50	-1.00	0.22
ν_3	A_1	1061.81	1060.61	1059.21	2.60	1.40
ν_4	B_1	990.59	990.63	990.18	0.41	0.45
ν_5	B_2	3024.32	3027.74	3024.62	-0.30	3.12
ν_6	B_2	989.59	990.85	991.02	-1.43	-0.17
$2\nu_2$	A_1	2875.24	2877.80	2877.11	-1.87	0.69
$\nu_2+\nu_3$	A_1	2511.92	2511.92	2511.60	0.32	0.32

Table 2.2: Best theoretical estimates of the vibrational wavenumbers of H_2CS (in cm^{-1}) compared with the available experimental data.

2.4 Spectroscopic PES of H_2CO

In this section we review the determination of an accurate spectroscopic PES for H_2CO in the ground electronic state (80). The initial guess for the PES was computed *ab initio* using the CCSD(T) level of theory and the augmented correlation-consistent basis set aug-cc-pVQZ. The calculations were done for thousands of geometries, covering energies up to 40 000 cm^{-1} above equilibrium. This *ab initio* PES leads to uncertainties in vibrational term values below 7200 cm^{-1} of less than 4 cm^{-1}. The purely rotational energy levels for $J \leq 5$ are produced very well, with an rms error of 0.095 cm^{-1}. This implies that *ab initio* equilibrium geometry is also quite accurate.

The analytical representation of the *ab initio* PES for H_2CO was further refined by fitting to 319 ro-vibrational energies with $J = 0, 1, 2, 5$. The *ab initio* data were used as a restraint to prevent unphysical behavior of the resulting refined PES, and to allow all potential parameters to be varied irrespective of the amount of the experimental data available for particular vibrational excitations. This latter goal is achieved by simultaneously fitting the potential parameters to the *ab initio* points and to the experimental energy levels. The calculated spectroscopic PES reproduces the available experimental data for the ro-vibrational energies of H_2CO with unprecedented accuracy. The total rms error for all energy levels used in the fitting is 0.04 cm^{-1}. A graphical overview of the fitting accuracy is presented in Figs. 2.3 and 2.4. In Fig. 2.4 the residuals are also shown for the vibrational band centers which were not used for the PES refinement due to their relatively high experimental uncertainties (standard deviation of 1.7 cm^{-1}).

We are planning to use the spectroscopic PES of H_2CO in comprehensive line list calculations. Another possible application is the detailed assignment of experimental

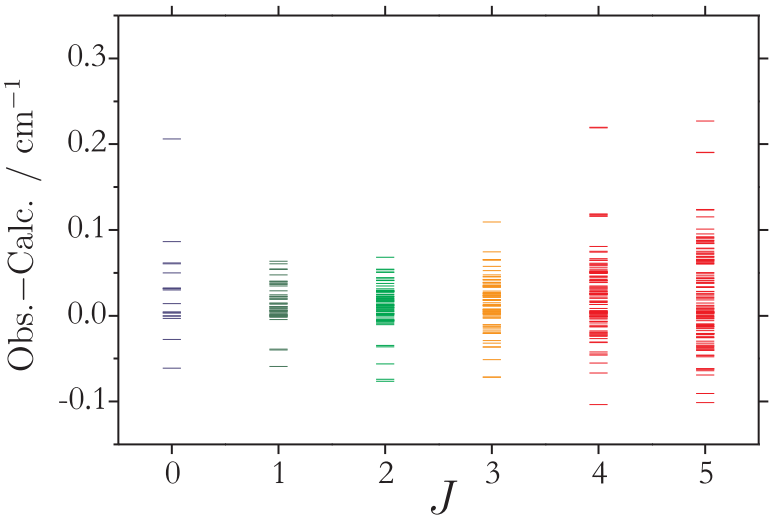

Figure 2.3: Results of H_2CO PES adjustment (I) - Residuals (Obs.-Calc.) obtained for $J \geq 0$ term values with the refined PES of H_2CO

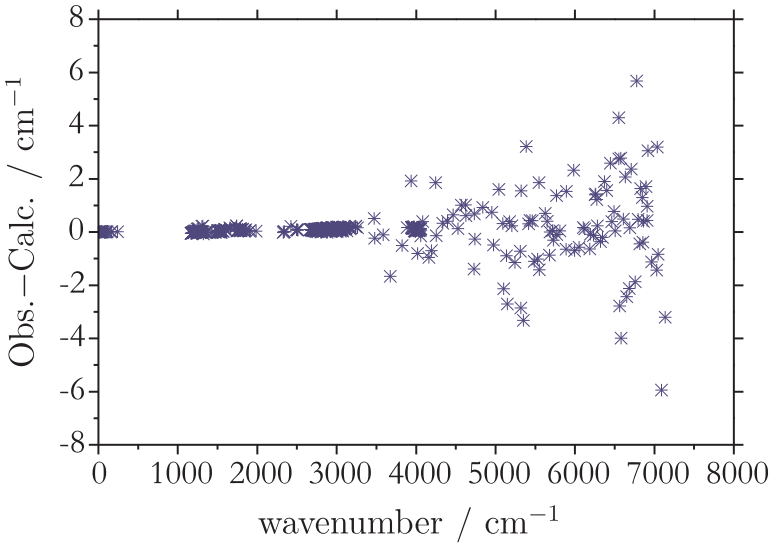

Figure 2.4: Results of H_2CO PES adjustment (II) - Residuals (Obs.-Calc.) obtained for $J \geq 0$ term values with the refined PES of H_2CO. Also shown are the residuals for the experimental energies that were excluded from the fitting due to their low accuracy.

transitions in the 1.5 μm region, which have been extensively investigated by high-resolution spectroscopy (81).

2. ACCURATE POTENTIAL ENERGY SURFACES FOR THE GROUND ELECTRONIC STATE

3

Ro-vibrational spectra

One of the most important aims of theoretical spectroscopy is to assist in the interpretation and understanding of high resolution spectroscopy experiments. To provide theoretical support for such experiments, it is not sufficient to calculate only the ro-vibration energies, but one also needs to predict theoretical transition intensities so that spectra can be simulated.

In nearly all cases of interest, transitions involving changes in ro-vibrational state are driven by electric dipoles. To calculate the probability of such transitions using the wavefunctions derived from variational calculations, it is also necessary to know the dipole moment as a function of internal coordinates. These dipole moment surfaces can be computed by most quantum chemical methods, usually in the form of a separate surface for each Cartesian component (Sec. 3.1). The computation of dipole transition moments and intensities is relatively straightforward given a set of ro-vibrational functions and an appropriate dipole moment surface (Sec. 3.3). However, only relatively few programs offer the calculation of transition intensities as a routine task. The topic has not received much attention, perhaps because many experiments are not suitable for measuring either absolute or relative intensities. However, many actual applications of spectroscopy require detailed knowledge of accurate transition intensities, and theory remains the one major source of such data.

3.1 *Ab initio* dipole moment surface

The dipole moment, as other molecular properties, may be described as the response of the molecular system to an external perturbation. The dipole moment may be identified with the first derivative of the electronic energy E with respect to the external electric field ϵ_α ($\alpha = x, y, z$):

$$\mu_\alpha = -\left(\frac{dE}{d\epsilon_\alpha}\right)_{\epsilon_\alpha=0}. \tag{3.1}$$

These derivatives can be calculated either numerically, using finite differences (finite-field calculations), or analytically. The finite differentiation technique is straightforward and may be immediately applied to any method of quantum chemistry. The dipole moment can thus be calculated as:

$$\frac{dE}{d\epsilon_\alpha} \approx \frac{E(\epsilon_\alpha) - E(-\epsilon_\alpha)}{2\epsilon_\alpha}. \tag{3.2}$$

One disadvantage of this numerical scheme is the high computational cost, since six additional energy computations must be performed to compute all three Cartesian components. There are further disadvantages of the numerical approach, especially for higher derivatives, which will be discussed later (Sec. 4.1).

The alternative to numerical differentiation is analytical differentiation, which requires the derivation of suitable analytical expressions for the corresponding derivatives and their implementation within a computer code for actual calculations. Since the electronic energy may depend on the perturbation parameter ϵ explicitly through the Hamiltonian operator and implicitly through the wavefunction parameters c (molecular orbitals, CI coefficients, etc.), the differentiation of the general energy expression yields:

$$\frac{dE}{d\epsilon} = \frac{\partial E}{\partial \epsilon} + \frac{\partial E}{\partial c}\frac{\partial c}{\partial \epsilon}. \tag{3.3}$$

The first term represents the explicit dependence on the perturbation and can normally be handled easily (82). A straightforward computation of the second term, implicitly dependent on the perturbation parameter, is often not possible, since the derivatives $\partial c/\partial \epsilon$ are not known. The second term, however, vanishes for coefficients c that are determined variationally, $\partial E/\partial c = 0$. The situation is more complicated for non-variational parameters, but it is still possible in this case to eliminate $\partial c/\partial \epsilon$ from the gradient expression. The most elegant way to do so is to use the method of the Lagrange

multipliers. Suppose that we have a set of equations $g(\epsilon, c(\epsilon)) = 0$ that determine the wavefunction parameters c. Then, the energy functional can be written as

$$\tilde{E}(\epsilon, c(\epsilon), \lambda(\epsilon)) = E(\epsilon, c(\epsilon)) + \lambda(\epsilon) g(\epsilon, c(\epsilon)), \tag{3.4}$$

where $\lambda(\epsilon)$ are Lagrangian multipliers. Now, to obtain an equation for the coefficients c, we require $\tilde{E}$ to be stationary with respect to λ, i.e. $d\tilde{E}/d\lambda = 0$. The equations for the Lagrangian multipliers $\lambda(\epsilon)$ can be obtained by making $\tilde{E}$ stationary with respect to the coefficients c, $d\tilde{E}/dc = 0$. The solution of these additional sets of equations is required to make $\tilde{E}$ stationary with respect to $\lambda(\epsilon)$. The equation for the derivative with respect to the perturbation ϵ can then be written as

$$\frac{d\tilde{E}}{d\epsilon} = \frac{\partial \tilde{E}}{\partial \epsilon} = \frac{\partial E}{\partial \epsilon} + \lambda \frac{\partial g}{\partial \epsilon}. \tag{3.5}$$

Therefore there is no need to compute $\partial c/\partial \epsilon$ derivatives, instead an additional set of equations $d\tilde{E}/dc = 0$ needs to be solved. Whenever analytical derivatives are available, they are the preferred choice due to their high accuracy and fast evaluation.

The application of analytical differentiation techniques is not straightforward, it requires complicated implementations including substantial programming efforts and theoretical work for derivation of appropriate equations. Analytical first and second derivatives are nowadays available for HF, DFT, MCSCF, MPn ($n = 2, 3, 4$), CISD, MRCI, CCSD, CCSD(T), and CCSDT-n quantum chemical methods.

3.2 Line strengths

The intensity of an electric dipole transition in absorption or emission is determined by parameters particular to the experimental measurement, (temperature and pressure, absorption path length and intensity of the incident light, etc.) and a factor that is independent of the experimental parameters. This factor, the line strength $S(f \leftarrow i)$, determines the probability that the molecule makes a transition $f \leftarrow i$ from the initial state i to the final state f. The line strength is given by:

$$S(f \leftarrow i) = \sum_{A=X,Y,Z} |\langle \Phi_f | \mu_A | \Phi_i \rangle|^2, \tag{3.6}$$

where μ_A is the component of the electric dipole moment along the axis $A = X, Y, Z$ in the SF (laboratory) frame. In our approach the total internal wavefunction is given by:

$$|\Psi^{(k)}_{\text{tot}}\rangle = |\Psi^{(k)}_{\text{ns}}\rangle|\Psi^{(k)}_{\text{elec}}\rangle|\Psi^{(k)}_{\text{rovib}}\rangle. \tag{3.7}$$

The nuclear spin wavefunction $|\Psi^{(k)}_{\text{ns}}\rangle$ can be separated out if the hyperfine interaction term in the Hamiltonian is neglected. The remaining factorization of the wavefunction into an electronic part $|\Psi^{(k)}_{\text{elec}}\rangle$ and a nuclear part $|\Psi^{(k)}_{\text{rovib}}\rangle$ follows from the BO approximation. Inserting the wavefunction from Eq. 3.7 in the equation 3.6 we obtain:

$$S(f \leftarrow i) = g_{\text{ns}} \sum_{m_i, m_f} \sum_{A=X,Y,Z} |\langle \Psi^{(f)}_{\text{rovib}} \Psi^{(f)}_{\text{elec}} | \mu_A | \Psi^{(i)}_{\text{elec}} \Psi^{(i)}_{\text{rovib}} \rangle|^2, \tag{3.8}$$

where the factor g_{ns} accounts for the degeneracy of both initial and final states with respect to the quantum number of the total nuclear spin. Furthermore, in the absense of an external electric field, the states are degenerate with respect to the quantum number of projection of the total angular momentum on the Z axis; summation over m_i and m_f accounts for this degeneracy.

As pointed out above, we distinguish between rotational and vibrational motions of a molecule by introducing the xyz MF frame, defined in terms of Eckart conditions (4). The orientation of the MF frame, relative to the XYZ SF system, is defined by the three standard Euler angles θ, ϕ, χ. The electronic wavefunction is defined in the MF frame and parametrically dependent on the internal coordinates. The ro-vibrational wavefunction is written as product of vibrational and rotational wavefunctions,

$$|\Psi^{(k)}_{\text{rovib}}\rangle = \mathbf{C}^{(k)} |\boldsymbol{\psi}_{\text{vib}}(\xi_1, ...\xi_{3N-6})\rangle \otimes |\boldsymbol{\psi}_{\text{rot}}(\theta, \phi, \chi)\rangle, \tag{3.9}$$

where ξ_i are internal (vibrational) coordinates.

Therefore, to compute the matrix elements in Eq. 3.8, the dipole moment function μ_A, defined in SF coordinate system, must be expressed in the MF frame, i.e., as a function of internal coordinates and Euler angles. This transformation is most easily done using the algebra of spherical tensor operators (83). The transformation properties of spherical tensor operators under rotation are determined by the Wigner rotation matrices $\mathbf{D}(\theta, \phi, \chi)$ (83). The spherical tensor operator of rank ω along the SF axes,

$U_{\rm sf}^{(\omega,A)}$, can be viewed as a rotated version of this operator in the MF frame, $U_{\rm mf}^{(\omega,\alpha)}$, so the relation can be written as:

$$U_{\rm sf}^{(\omega,A)} = \sum_{\alpha=-\omega}^{\omega} [D_{A\alpha}^{(\omega)}(\theta,\phi,\chi)]^* U_{\rm mf}^{(\omega,\alpha)}. \tag{3.10}$$

This relation may be employed to link dipole moment spherical tensor operators in two coordinate systems. The SF dipole moment components in terms of spherical tensor operators $\mu_{\rm sf}^{(1,A)}$ can be obtained from the corresponding Cartesian components via Eq. 3.11, and an analogous expression, Eq. 3.12, holds for the MF frame:

$$\mu_{\rm sf}^{(1,-1)} = (\mu_X + i\mu_Y)/\sqrt{2}, \quad \mu_{\rm sf}^{(1,0)} = \mu_Z, \quad \mu_{\rm sf}^{(1,1)} = (-\mu_X + i\mu_Y)/\sqrt{2}, \tag{3.11}$$

$$\mu_{\rm mf}^{(1,-1)} = (\mu_x + i\mu_y)/\sqrt{2}, \quad \mu_{\rm mf}^{(1,0)} = \mu_z, \quad \mu_{\rm mf}^{(1,1)} = (-\mu_x + i\mu_y)/\sqrt{2}. \tag{3.12}$$

Taking into account Eqs. 3.10-3.12 and inserting them into Eq. 3.8 we obtain the following expression for the line strength:

$$\begin{aligned} S(f \leftarrow i) &= g_{\rm ns} \sum_{m_i,m_f} \sum_{A=-1}^{1} \left| \langle \Psi_{\rm rovib}^{(f)} \Psi_{\rm elec}^{(f)} | \mu_{\rm sf}^{(1,A)} | \Psi_{\rm elec}^{(i)} \Psi_{\rm rovib}^{(i)} \rangle \right|^2 \\ &= g_{\rm ns} \sum_{m_i,m_f} \sum_{A=-1}^{1} \left| \sum_{\alpha=-1}^{1} \langle \Psi_{\rm rovib}^{(f)} \Psi_{\rm elec}^{(f)} | [D_{A\alpha}^{(1)}(\theta,\phi,\chi)]^* \mu_{\rm mf}^{(1,\alpha)}(\xi_1,...\xi_{3N-6}) | \Psi_{\rm elec}^{(i)} \Psi_{\rm rovib}^{(i)} \rangle \right|^2 . \end{aligned} \tag{3.13}$$

Inserting the ro-vibrational wavefunctions given by Eq. 3.9 and separating rotational and vibrational variables in integrals we obtain:

$$\begin{aligned} S(f \leftarrow i) = g_{\rm ns} \sum_{m_i,m_f} \sum_{A=-1}^{1} \Big| \mathbf{C}^{(f)*} \mathbf{C}^{(i)} \sum_{\alpha=-1}^{1} \Big(& \langle \boldsymbol{\psi}_{\rm rot} | [D_{A\alpha}^{(1)}(\theta,\phi,\chi)]^* | \boldsymbol{\psi}_{\rm rot} \rangle \\ & \otimes \langle \boldsymbol{\psi}_{\rm vib} | \langle \Psi_{\rm elec}^{(f)} | \mu_{\rm mf}^{(1,\alpha)}(\xi_1,...\xi_{3N-6}) | \Psi_{\rm elec}^{(i)} \rangle | \boldsymbol{\psi}_{\rm vib} \rangle \Big) \Big|^2 . \end{aligned} \tag{3.14}$$

The rotational basis set is built from the rigid-rotor wavefunctions $|\psi_{\rm rot}\rangle = |J,k,m\rangle$ and matrix elements of the rotational matrix in Eq. 3.14 are easily evaluated using the Clebsch-Gordan series:

$$\begin{aligned} \langle J',k',m' | [D_{A\alpha}^{(1)}(\theta,\phi,\chi)]^* | J,k,m \rangle &= (-1)^{k'+m'} \sqrt{(2J'+1)(2J+1)} \\ &\times \begin{pmatrix} J & 1 & J' \\ k & \alpha & -k' \end{pmatrix} \begin{pmatrix} J & 1 & J' \\ m & A & -m' \end{pmatrix}. \end{aligned} \tag{3.15}$$

These matrix elements, containing the $3j$-symbols $\begin{pmatrix} J & 1 & J' \\ k & \alpha & -k' \end{pmatrix}$, determine rigorous selection rules for J and k quantum numbers of the total angular momentum and its

projection on z axis, respectively. Since the molecular energy does not depend on m quantum numbers, the summations over the degeneracies in the initial and final states evaluated together with the sum over A give unity. The general properties of $3j$-symbols in Eq. 3.15 ensure that the line strength will vanish unless

$$\Delta J = 0, \pm 1. \tag{3.16}$$

For individual matrix elements not to vanish, Δk must satisfy the condition:

$$\Delta k = 0, \pm 1. \tag{3.17}$$

The electronic matrix elements of the operators μ_α can be obtained by electronic structure calculations (Sec. 3.1). In our work, we are only concerned with transitions within one electronic state, so $\Psi^{(f)}_{\rm elec} = \Psi^{(i)}_{\rm elec}$. The vibrational matrix element of $\bar{\mu}_\alpha$ is nonzero only if it belongs to the molecular symmetry group of the molecule:

$$\Gamma^{(i)}_{\rm vib} \otimes \Gamma^{(f)}_{\rm vib} \supset \Gamma(\bar{\mu}_\alpha), \tag{3.18}$$

where Γ denotes the respective symmetries of the vibrational functions and of the dipole moment operator integrated over electronic coordinates.

To speed up the calculations, we have optimized the strategy for calculating the line strength in TROVE. The evaluation of the dipole moment matrix elements $\langle \Psi^{(f)}_{\rm rovib} | \mu_A | \Psi^{(i)}_{\rm rovib} \rangle$ can be regarded as a unitary transformation of the dipole moment matrix elements from the representation of primitive (basis) functions $|\psi^{(r)}_{\rm vib}\rangle \otimes |\psi^{(s)}_{\rm rot}\rangle$ to the representation of the eigenfunctions $\Psi^{(k)}_{\rm rovib}$, $(k = i, f)$ by means of Eq. 3.9. Such a transformation involves nested loops and results in N^4 operations (N is the size of primitive basis set). An N^3 efficiency can be reached if this operation is performed in two steps. First, the effective half-transformed line strength is evaluated for the lower state as:

$$\mathbf{S}^{(i)}_A = \langle \Psi^{(i)}_{\rm rovib} | \mu_A (|\psi_{\rm vib}\rangle \otimes |\psi_{\rm rot}\rangle). \tag{3.19}$$

In the second step, the line strength is calculated as:

$$S(f \leftarrow i) = g_{\rm ns} \sum_{m_i, m_f} \sum_{A=X,Y,Z} \left| \mathbf{C}^{(f)} \mathbf{S}^{(i)}_A \right|^2. \tag{3.20}$$

The effective half-transformed line strength calculated for a given J is then used to compute the line strength involving transitions with angular momentum quantum numbers $J' = J$ and $J' = J + 1$.

3.3 Physical conditions and intensities

In an absorption experiment where a parallel beam of light with wavenumber ν and intensity $I_0(\nu)$ passes through a length l of a gas at a concentration c, the intensity of the transmitted light $I(\nu)$ is given by the Lambert-Beer law:

$$I(\nu) = I_0(\nu) \exp(-lc\epsilon(\nu)), \tag{3.21}$$

where $\epsilon(\nu)$ is an absorption coefficient. If we assume the absorbing molecules to be in thermal equilibrium at absolute temperature T, the integral absorption coefficient for an electric dipole transition from an initial state with energy E_i to a final state with energy E_f is given by (84)

$$\begin{aligned} I(f \leftarrow i) &= \int_{\text{Line}} \epsilon(\nu) d\nu \\ &= \frac{8\pi^3 N_a \nu_{fi} \exp(-E_i/kT)[1 - \exp(-hc\nu_{fi}/kT)]}{(4\pi\epsilon_0)3hcQ} S(f \leftarrow i), \end{aligned} \tag{3.22}$$

where $hc\nu_{fi} = E_f - E_i$, N_A is the Avogadro constant, h is Planck's constant, c is the speed of light in vacuum, k is the Boltzmann constant, ϵ_0 is the permittivity of free space, $S(f \leftarrow i)$ is the line strength defined in Eq. 3.6, and Q is the partition function defined as:

$$Q = \sum_i g_i \exp(-E_i/kT), \tag{3.23}$$

where g_i is the degeneracy of the state with energy E_i and the sum runs over all energy levels of a molecule.

In Eq. 3.22, we define the intensity of a transition as a function of temperature. We characterize each transition by a specific wavelength and intensity, which implies that absorption and emission spectra should look like a batch of lines with characteristic position and height. However, we only have to look, for example, at an astronomical spectrum to realize that spectral lines have a definite width, i.e., they spread out across a range of wavelengths. Spectral lines are clearly not just infinitely narrow, but have profiles.

One source of broadening is associated with the uncertainty principle, which states that the product of the uncertainty in the measurement of energy and time is $\Delta E \Delta t \geq h/2\pi$, where h is Planck's constant. Therefore the longer an excited state exists, the

narrower the line width. Some decay processes prevent the molecule from staying in a specified energy state for longer than a time interval Δt on average, and hence the line width is $\gamma \sim 1/\Delta t$. The principal contributions to γ in gases are: collisional broadening, which is proportional to the pressure; saturation broadening, which depends upon the rate at which the molecules are transferred between the upper and lower energy states by the radiation field; and radiative decay of the excited state level. The shape function $f(\nu - \nu_0)$ of homogeneously broadened line has the Lorentz form:

$$f(\nu) = \frac{\gamma/4\pi^2}{(\nu - \nu_0)^2 + (\gamma/4\pi)^2}, \tag{3.24}$$

where γ is a half-width at half-height.

Another, heterogeneous, source of broadening in gases is associated with the Doppler effect. If a moving molecule emits radiation, the emitted frequency is shifted by an amount which depends on the component of molecular velocity in the direction of emitted radiation. Many molecules moving in different directions with different speeds will produce a line blend with significant width. If the molecules are in thermal equilibrium at some temperature T, with a Maxwell distribution of velocities, this gives rise to a Gaussian line shape of the form:

$$f(\nu) = \frac{1}{\Delta\nu_D\sqrt{\pi}} e^{-(\nu-\nu_0)^2/(\Delta\nu_D)^2}, \tag{3.25}$$

where

$$\Delta\nu_D = \frac{\nu_0}{c}\sqrt{\frac{2kT}{m}}, \tag{3.26}$$

and the half-width and half-height are related to $\Delta\nu_D$ by $\Delta\nu_D\sqrt{\ln 2}$. The overall line shape may be considered as being made up from a large number of Lorenzian curves, for various broadening contributions, and convoluted with a Gaussian profile. This results in a Voigt line shape.

By measuring the amount of broadening, one can determine such properties as the temperature and density of a gas, or even the presence of magnetic field. Careful studies of broadened spectral lines contain much information about physical processes, for example taking place in Earth's atmosphere or in distant astrophysical objects.

3.4 Spectra of HSOH from first principles

The HSOH molecule has received substantial attention in recent years as a long-missing link between the better known molecules HOOH and HSSH. Each of these molecules has a skew-chain equilibrium geometry (Fig. 3.1), and particularly interesting features of their spectra originate in the energy splittings resulting from the torsional motion of the OH or SH moieties around the axis connecting two heavy atoms (a-axis). The torsional

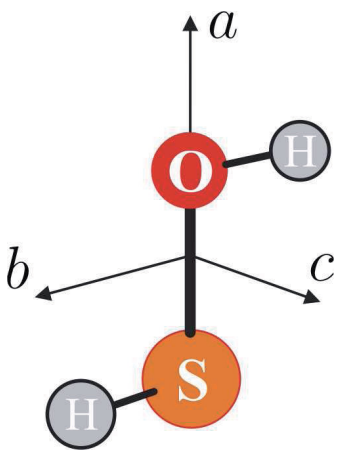

Figure 3.1: HSOH molecule - The *abc* principal axes

motion (Fig. 3.2) couples significantly with the over-all rotation of the molecule around the a-axis, and the torsional splittings depend strongly on the rotational excitation. For HSOH this dependence was found to be quite anomalous (85), giving rise to a complicated variation of the splittings with K_a rotational quantum numbers. The anomaly was also seen in the ($b-$type-transition)/($c-$type-transition) intensity ratio in the vibrational-ground-state ${}^{r}Q_{K_a}$ branches of HSOH (86). The experimentally observed torsional splittings for the vibrational ground state were successfully analyzed by means of the TROVE program based on an *ab initio* PES (87).

The main purpose of our study was to calculate the PES and DMS of HSOH using high-level *ab initio* methods, to compute the rotation-torsion term values and splittings, with particular emphasis on the experimentally available term values associated with the OH-stretch and SH-stretch, and to perform the first theoretical simulation of the high-resolution spectra of HSOH. The details of the *ab initio* and variational TROVE calculations can be found in Refs. (88) and (89). One dimensional cuts through the calculated PES and DMS along the torsional minimum energy path are shown in Figs. 3.2

and 3.3. The theoretical results for the ro-vibrational energy levels and torsional

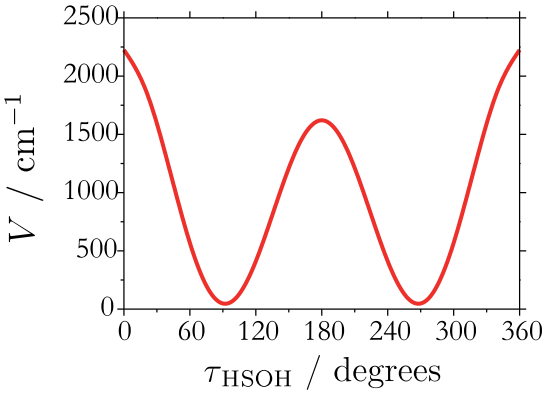

Figure 3.2: Potential energy surface of HSOH - One dimensional cut through the potential energy function of HSOH for torsional motion (remaining five coordinates taken at their equilibrium values)

splittings are generally in good agreement with experimental data available for HSOH (Table 3.1). They allow us to explain extensive perturbations found experimentally in the SH-stretch fundamental band. The calculations suggest that the torsional splittings in the fundamental levels are significantly larger than that in the vibrational ground state. This is consistent with the experimental observation for the SH-stretch fundamental band (90).

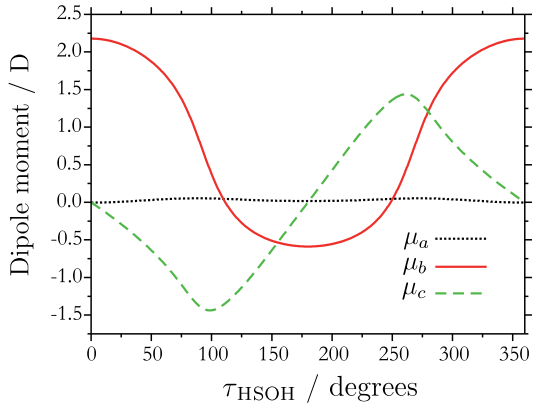

Figure 3.3: Electric dipole moment of HSOH - Dipole moment components for HSOH, computed along the torsional minimum energy path

We have simulated rotation-torsion spectra for the ground vibrational state, the first

Mode	Theory	Exp. [gas phase] (90, 91)	Exp. [Ar matrix] (92)
Vibrational term values			
ν_{OH}	3625.9	3625.59260(20)	3608.3
ν_{SH}	2544.4	2537.9869(12)	2550.1
ν_{HOS}	1174.0		1175.7
ν_{OSH}	1007.7		
ν_{SO}	760.0		762.5
ν_{HSOH}	443.0		445.3
Torsional splittings			
g.s.	0.00215	0.00214	
ν_{OH}	0.0036	<0.01	
ν_{SH}	-0.0775	0.024(2)	
ν_{HOS}	-0.0335		
ν_{OSH}	0.0255		
ν_{SO}	0.0546		
ν_{HSOH}	0.1279		

Table 3.1: Vibrational term values and torsional splittings (in cm^{-1}) for the vibrational ground state and the fundamental levels of HSOH

torsion fundamental state, and torsion fundamental band at $T = 300$ K (89). Since HSOH is a near prolate rotor molecule, the rotational band is characterized by a perpendicular type spectrum with strong R-type and Q-type transitions, the P-branches are comparatively weak. Figure 3.4 shows the $J \leq 40$ simulated rotational spectrum for the ground vibrational state of HSOH. The principal axis a with the smallest moment of inertia is approximately parallel to the SO bond, and so HSOH has a relatively small 'parallel' dipole moment component μ_a, and large 'perpendicular' components μ_b and μ_c (Fig. 3.3). Strong transitions whose intensity originates predominantly in the μ_b or μ_c dipole moment components are classified as being of b-type or c-type, respectively. This normally allows the observed lines to be identified according to their intensities: the ratio between intensities of b-type and c-type transitions is roughly equal to the ratio between the squares of dipole moment components μ_b and μ_c:

$$\frac{I_b}{I_c} = \frac{\bar{\mu}_b^2}{\bar{\mu}_c^2} \tag{3.27}$$

If this relation is satisfied, the observed transitions can be recognized as being of b-type or c-type. From *ab initio* calculations of the dipole moment at the equilibrium geometry, we obtain $I_b/I_c \approx 0.29$. The experimentally derived intensity ratios (Fig. 3.5) have been reported to be very close to this value; $I_b/I_c = 0.22(4)$ and $0.23(2)$ for ${}^rQ_0$ and ${}^rQ_1$ branches (86). For ${}^rQ_2$ and ${}^rQ_3$ branches the ratios were found to be 0.58(11)

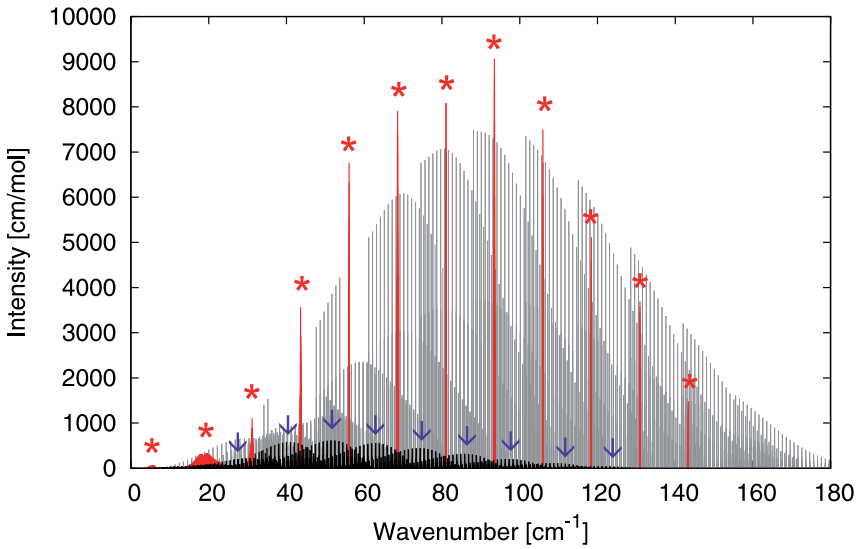

Figure 3.4: Simulated rotational spectrum of HSOH at $T = 300$ K - All prominent transitions have $\Delta k = 1$. The ${}^rP$ and ${}^rQ$ branches are indicated by arrows and asterisks, the strongest transitions are found in the ${}^rR$ branches

and below 0.02 respectively, which is not compatible with Eq. 3.27. In Ref. (86), this 'intensity anomaly' was attributed to a mixing of states. Our variational calculations predict the intensity ratio 1/3 for ${}^rQ_0$, ${}^rQ_1$, and ${}^rQ_2$ branches (Fig. 3.6), in accord with Eq 3.27. However, in agreement with experimental findings, the ${}^rQ_3$ branch has hardly any b-type transitions at all.

To understand this intensity anomaly, we analyzed the eigenfunctions for the rotation-torsion states involved. We found that four eigenfunctions associated with certain values of J and K_a ($K_a > 0$) can be modeled by the following expressions

$$\psi_1^{(A')} \approx c_{JK_a}|J, K_a, \tau_{\rm rot} = 0\rangle|\tau_{\rm tor} = 0\rangle + s_{JK_a}|J, K_a, \tau_{\rm rot} = 1\rangle|\tau_{\rm tor} = 1\rangle, \quad (3.28)$$

$$\psi_2^{(A')} \approx -s_{JK_a}|J, K_a, \tau_{\rm rot} = 0\rangle|\tau_{\rm tor} = 0\rangle + c_{JK_a}|J, K_a, \tau_{\rm rot} = 1\rangle|\tau_{\rm tor} = 1\rangle, \quad (3.29)$$

$$\psi_1^{(A")} \approx c_{JK_a}|J, K_a, \tau_{\rm rot} = 0\rangle|\tau_{\rm tor} = 1\rangle + s_{JK_a}|J, K_a, \tau_{\rm rot} = 1\rangle|\tau_{\rm tor} = 0\rangle, \quad (3.30)$$

$$\psi_2^{(A")} \approx -s_{JK_a}|J, K_a, \tau_{\rm rot} = 0\rangle|\tau_{\rm tor} = 1\rangle + c_{JK_a}|J, K_a, \tau_{\rm rot} = 1\rangle|\tau_{\rm tor} = 0\rangle, \quad (3.31)$$

where $c_{JK_a} = \cos(\theta_{JK_a})$ and $c_{JK_a} = \sin(\theta_{JK_a})$ with the mixing angle $0 \leq \theta_{JK_a} \leq \pi/4$, $\tau_{\rm rot}$ determines rotational parity and $\tau_{\rm tor}$ determines torsional parity. In Eq. 3.28, $|\tau_{\rm tor}\rangle$ stands for torsional basis. For simplicity, the vibrational quantum numbers are skipped.

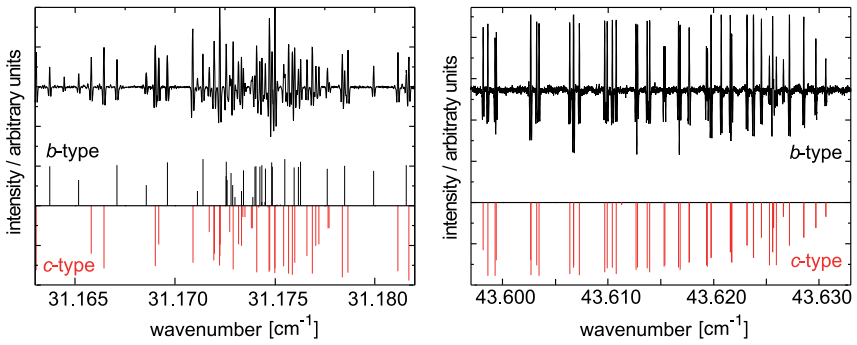

Figure 3.5: Observed $^rQ_2$ and $^rQ_3$ branches in the rotational spectrum of HSOH - Below the experimental spectra, the assignments to *b*-type or *c*-type are indicated by stick spectra

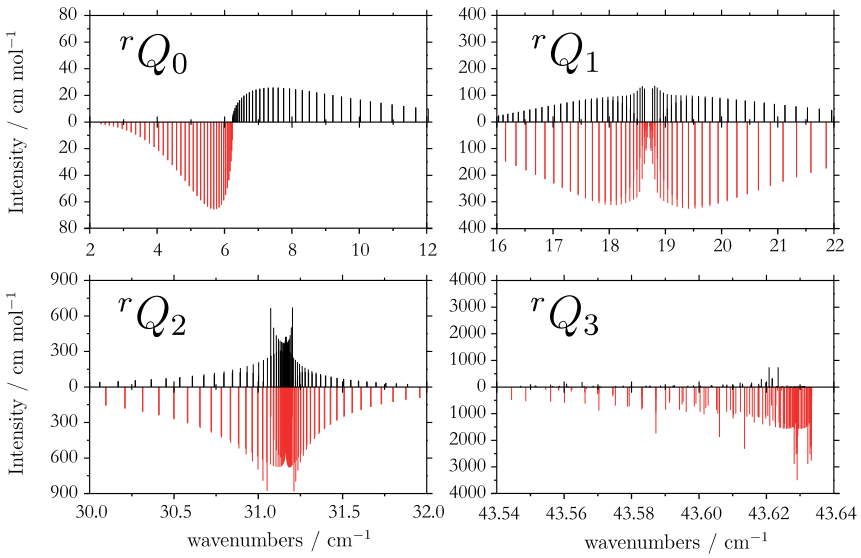

Figure 3.6: Calculated $^rQ_{K_a}$ ($K_a = 0, 1, 2, 3$) branches in the rotational spectrum of HSOH - Transitions assigned as *b*-type transitions are drawn in black, and *c*-type transitions are drawn upside-down in red.

Assuming that non-vanishing vibrational matrix elements of the dipole moment operators μ_b and μ_c are independent of τ_{tor}, we obtain eight non-vanishing transitions for a given J value in a ${}^rQ_{K_a}$ branch:

$$\begin{aligned} S_{A'(1)\leftrightarrow A''(1)} = S_{A'(2)\leftrightarrow A''(2)} &\sim \cos^2(\theta_{J,K_a+1} - \theta_{J,K_a})\langle\bar{\mu}_b\rangle^2 + \\ &+ \sin^2(\theta_{J,K_a+1} + \theta_{J,K_a})\langle\bar{\mu}_c\rangle^2, \end{aligned} \tag{3.32}$$

$$\begin{aligned} S_{A'(1)\leftrightarrow A''(2)} = S_{A'(2)\leftrightarrow A''(1)} &\sim \cos^2(\theta_{J,K_a+1} + \theta_{J,K_a})\langle\bar{\mu}_c\rangle^2 + \\ &+ \sin^2(\theta_{J,K_a+1} - \theta_{J,K_a})\langle\bar{\mu}_b\rangle^2, \end{aligned} \tag{3.33}$$

where $\langle\bar{\mu}_b\rangle$ and $\langle\bar{\mu}_c\rangle$ is a short-hand notation for $\langle 0|\bar{\mu}_b|0\rangle$ and $\langle 0|\bar{\mu}_c|1\rangle$ vibrational matrix elements, respectively. For small $K_a > 0$, analyses of ro-vibrational calculations show that $\theta_{J,K_a} \approx 0$. That is, for small $K_a = 0, 1, 2$ we can approximate $\theta_{J,K_a} = 0$ and so for ${}^rQ_0$ and ${}^rQ_1$ transitions $\theta_{J,K_a} = \theta_{J,K_a+1} = 0$. Eqs. 3.32 and 3.33 then simplify to

$$S_{A'(1)\leftrightarrow A''(1)} = S_{A'(2)\leftrightarrow A''(2)} \sim \langle\bar{\mu}_b\rangle^2, \tag{3.34}$$

$$S_{A'(1)\leftrightarrow A''(2)} = S_{A'(2)\leftrightarrow A''(1)} \sim \langle\bar{\mu}_c\rangle^2. \tag{3.35}$$

Equation 3.34 defines b-type transition, while Eq. 3.35 defines c-type transition. We found that at higher K_a-values, the rotation-torsion wavefunctions become equal mixtures of $|J, K_a, 0\rangle$ and $|J, K_a, 1\rangle$ basis functions. In the limit $K_a \to \infty$, $\theta_{J,K_a} = \pi/4$ and equations 3.32 and 3.33 simplify to

$$S_{A'(1)\leftrightarrow A''(1)} = S_{A'(2)\leftrightarrow A''(2)} \sim \langle\bar{\mu}_b\rangle^2 + \langle\bar{\mu}_c\rangle^2, \tag{3.36}$$

$$S_{A'(1)\leftrightarrow A''(2)} = S_{A'(2)\leftrightarrow A''(1)} \sim 0. \tag{3.37}$$

In this situation, the assignment of transition as being of b-type or c-type is meaningless. This is consistent with the fact that for the ${}^rQ_3$ branch I_b/I_c is experimentally determined to be below 0.002 (86). We made the following observations: (a) b/c-type assignments become ambiguous for $K_a \geq 3$, since for many transitions in the corresponding ${}^rQ_{K_a}$ branches, the contributions to intensities from μ_b and μ_c are roughly equal; (b) in the limit $k \to \infty$ we find transitions for which the b-type and c-type intensity contributions cancel each other according Eq. 3.37. We also find 'hybrid' transitions for which the two contributions interfere, Eq. 3.36. The detailed analysis of the rotation-torsion wavefunctions and contributions to the intensity from μ_a, μ_b

and μ_c components for ${}^rQ_{K_a}$ branches in the vibrational ground state are reported in Ref. (89).

The simulations of ro-vibrational spectra for ground state, fundamental torsional state and fundamental torsional band reproduce the observed intensity patterns very well, including the intensity anomalies in the ${}^rQ_{K_a}$ branches, which are caused by large amplitude torsional motion; these anomalies can be understood qualitatively by analysis of the variational results. The complete list of ro-vibrational energies and intensities for the vibrational ground state, the torsional fundamental state, and the torsional fundamental band has been published (89). We hope that our results will support future spectroscopic research on HSOH.

3.5 Spectroscopic line list for NH_3

The ammonia molecule can be found in a wide range of astrophysical environments and, because of the richness and intensity of its spectrum, it is easily observed from the Earth. Many of the NH_3 spectral lines are known and assigned, and frequently used to determine physical conditions in distant objects. However, the vast majority of lines in the NH_3 spectrum are not yet known experimentally, which impedes identification and interpretation of NH_3 features in the spectra of astrophysical objects. The absence of a satisfactory ammonia line list means that it is not possible to model accurately the atmospheres of late brown dwarfs or the cooler classes of exoplanets - environments where ammonia is a major source of opacity (93, 94, 95, 96).

Our aim is to provide line list for NH_3 that will fill this important gap. Three elements are required for its generation: accurate PES, accurate DMS, and accurate solution of the ro-vibrational problem for a large number of highly excited ro-vibrational molecular states. The spectroscopically adjusted PES (Sec. 2.2) and an *ab initio* calculated DMS have been employed in variational (TROVE) calculations. We have developed intensity and symmetrization tools specific to the NH_3 problem, and introduced a number of algorithmic improvements to make the calculations more tractable. Using these techniques we have produced a cool $T = 300$ K line list for NH_3.

The details of the *ab initio* and variational calculations, and of the PES refinement can be found in Ref. (97). Figure 3.7 shows the overall simulated ($T = 300$ K) ab-

sorption spectrum (TROVE) and compares it with experimental absorption spectrum (HITRAN) (98) of NH_3.

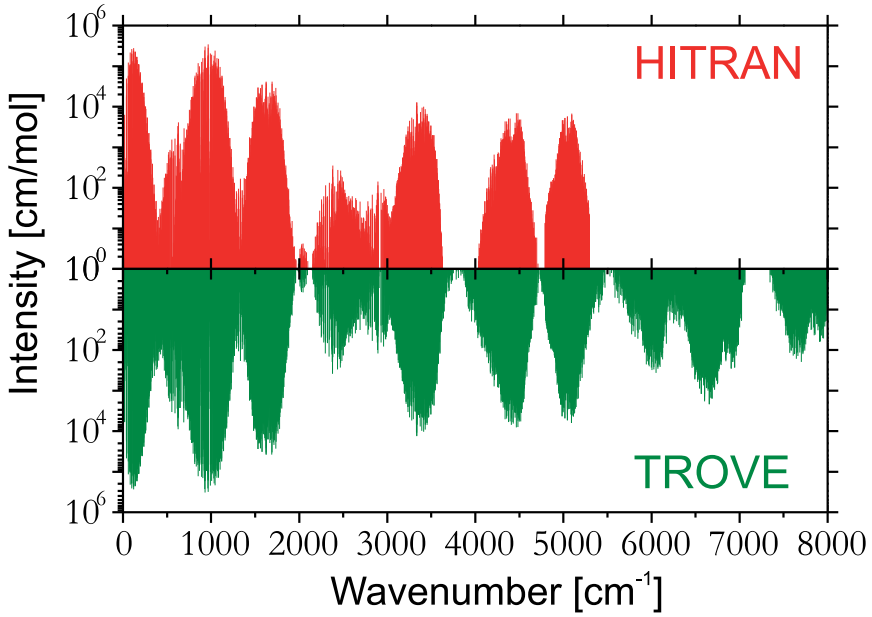

Figure 3.7: Calculated absorption spectrum of NH_3 (I) - Overview of the simulated ($T = 300$ K) spectrum (TROVE) of NH_3 compared to experiment (HITRAN)

We have produced an ammonia line list consisting of 3.25 million transitions between 184 400 energy levels for the ro-vibrational states up to $J_{max} \leq 20$ and energies up to 12 000 cm^{-1}. Detailed comparisons with observed room-temperature spectra show excellent agreement for the position and intensity of the transitions (Fig. 3.8). These comparisons indicate that the HITRAN database is rather incomplete in its coverage of the infrared spectrum of ammonia. The line list can be used to produce synthetic NH_3 spectra that agree well with observation at room temperature.

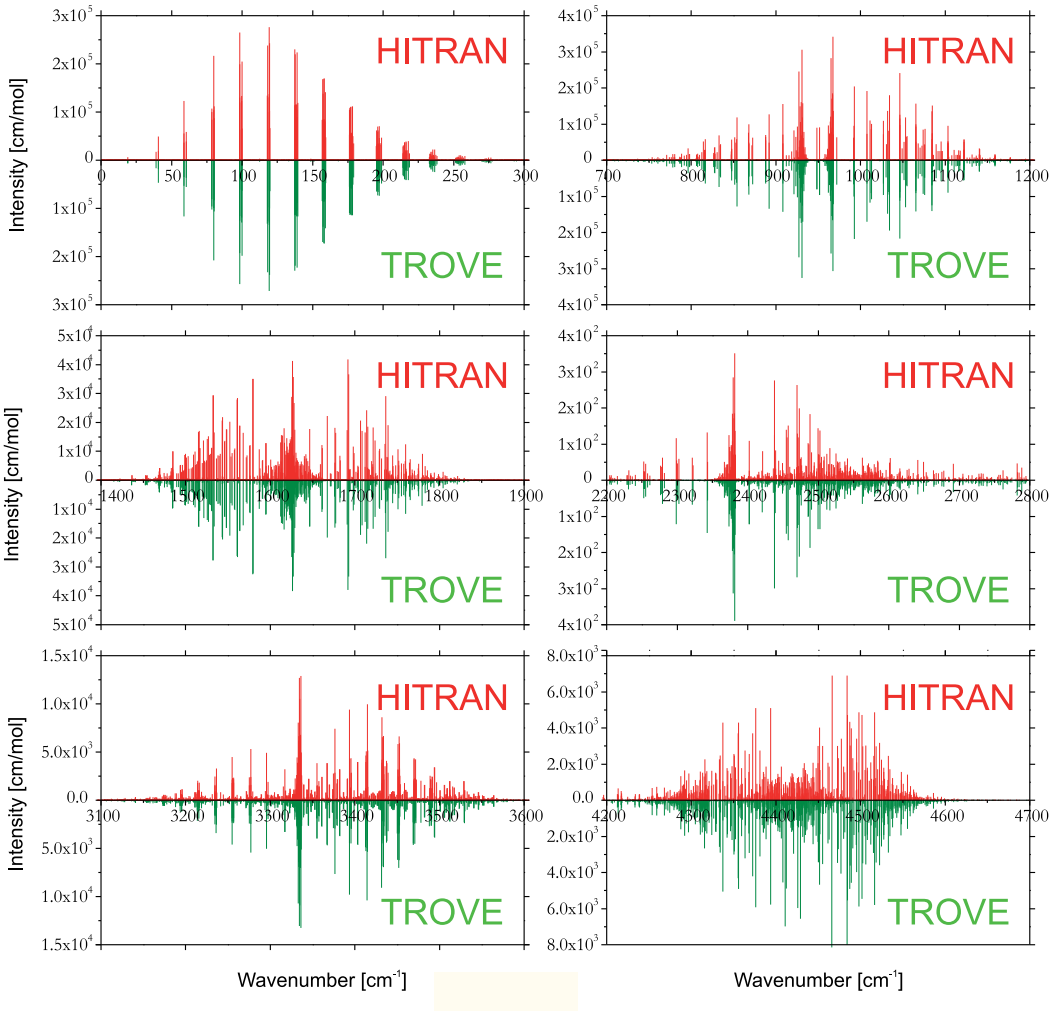

Figure 3.8: Calculated absorption spectrum of NH_3 (II) - Comparison of the simulated (TROVE) and observed (HITRAN) spectra of NH_3 at $T = 300$ K for several low-lying band systems.

4

Ro-vibrational properties

The effects that arise from the interaction of a molecule with an external electromagnetic field, or from electromagnetic interactions within a molecule, are usually described in terms of so called molecular properties, which are intrinsic to an electronic or ro-vibrational state of the molecule and independent from the strength of external fields or internal moments. They play an important role in the interpretation of phenomena such as the refractive index, the Stark effect, the Kerr effect and the nuclear magnetic resonance spectra.

Molecular properties are naturally formulated as a response of a molecule to an external perturbation induced by an electromagnetic field. If the interaction with the electromagnetic field is weak, the situation can be analyzed by expanding the energy E of the system in a Taylor series about the energy in the absence of the field. In a static uniform electric field $\mathbf{F}$ the energy can be written as:

$$\begin{aligned} E(\mathbf{F}) &= E_0 + \left(\frac{\partial E}{\partial F_\alpha}\right)_0 F_\alpha + \frac{1}{2}\left(\frac{\partial^2 E}{\partial F_\alpha \partial F_\beta}\right)_0 F_\alpha F_\beta \\ &+ \frac{1}{6}\left(\frac{\partial^3 E}{\partial F_\alpha \partial F_\beta \partial F_\gamma}\right)_0 F_\alpha F_\beta F_\gamma + ... \end{aligned} \tag{4.1}$$

Since the potential energy of a system of charges in a static electric field is given in multipole form by

$$E = E_0 - \mu_\alpha F_\alpha - \frac{1}{3}\Theta_{\alpha\beta} F_{\alpha\beta} + ..., \tag{4.2}$$

and

$$\mu_\alpha = -\frac{\partial E}{\partial F_\alpha}, \quad \Theta_{\alpha\beta} = -3\frac{\partial E}{\partial F_{\alpha\beta}}, \tag{4.3}$$

we can associate the derivatives in Eq. 4.1 with the derivatives of the electric dipole moment μ_α,

$$\mu_\alpha = \mu_{0\alpha} + \alpha_{\alpha\beta}F_\beta + \frac{1}{2}\beta_{\alpha\beta\gamma}F_\beta F_\gamma + ..., \tag{4.4}$$

where

$$\mu_{0\alpha} = -\left(\frac{\partial E}{\partial F_\alpha}\right)_0 \tag{4.5}$$

$$\alpha_{\alpha\beta} = -\left(\frac{\partial^2 E}{\partial F_\alpha \partial F_\beta}\right)_0 \tag{4.6}$$

$$\beta_{\alpha\beta\gamma} = -\left(\frac{\partial^3 E}{\partial F_\alpha \partial F_\beta \partial F_\gamma}\right)_0 . \tag{4.7}$$

The permanent electric dipole moment, $\mu_{0\alpha}$, the electric polarizability, $\alpha_{\alpha\beta}$, and the first electric hyperpolarizability, $\beta_{\alpha\beta\gamma}$, describe properties of a molecule placed in a static uniform electric field. A similar expansion of the molecular electric quadrupole moment $\Theta_{\alpha\beta}$ in the presence of a static gradient electric field gives the permanent electric quadrupole moment and the electric quadrupole polarizability.

For a molecule in a static uniform magnetic field, the energy can be expanded similarly to Eq. 4.1. The potential energy of a system of charges immersed in an external magnetic induction is expressed in terms of magnetic moments, analogously to the electric field case. The properties arising from the first and second derivatives are the permanent magnetic dipole moment and the magnetic susceptibility. The interaction of nuclear magnetic moment with the molecular magnetic induction gives rise to properties such as the nuclear magnetic shielding tensor and the indirect spin-spin coupling tensor.

When discussing molecular properties it is usually assumed that only the electronic wavefunction is directly affected by a perturbation, which gives rise to the electronic properties (see Sec. 4.1). The nuclear motion affects molecular properties through the parametric dependence of the electronic wavefunction on the coordinates of the nuclei. Usually the electronic property is calculated at a set of nuclear geometries first, and the resulting property function is then averaged over ro-vibrational wavefunctions for molecular states of interest. Finally a summation over thermally accessible states with appropriate Boltzmann factors describes the temperature dependence of the molecular property (see Sec. 4.2).

There are, however, cases when the effect of a perturbation on the nuclear motion is quite significant, sometimes comparable or even larger than the electronic contribution, and thus cannot be neglected. The ro-vibrational contributions to molecular properties are sometimes called 'pure vibrational' ones, due to Bishop (99). They can be formulated in the same manner as the electronic properties, i.e., as partial derivatives of the ro-vibrational energy with respect to a perturbation. The ro-vibrational energies and wavefunctions are obtained from the solution of an eigenvalue problem for the field-perturbed ro-vibrational Hamiltonian (see Sec. 4.3).

4.1 *Ab initio* property surface

Similar to the electric dipole moment (Sec. 3.1), the *ab initio* molecular properties may be described in terms of derivatives of the electronic energy with respect to a perturbation parameter. The derivatives can be calculated either numerically or analytically.

The numerical differentiation method (or finite field method) involves numerical evaluation of derivatives of electronic energy or first- and higher-order properties in the presence of a perturbation operator, $P_\alpha F_\alpha$. Calculations are performed for various values of field strength F_α, and the desired derivative can be obtained either by finite difference or by fitting to a Taylor expansion in the field strength F_α (Eq. 4.1). The finite field method has some disadvantages, they are: (a) limited accuracy, especially for high derivatives, where the results may be strongly affected by rounding errors; (b) high computational cost, since numerical differentiation requires for each derivative two additional energy computations; (c) there is no straightforward extension to the computation of frequency dependent properties. The finite field method is so far the easiest method to implement as long as the perturbation operators are real, and any program for the calculation of a property can be used. Handling magnetic properties by the finite field method is less straightforward since the corresponding perturbation operators are complex. Nevertheless finite field approaches to the calculation of magnetic shielding constants and spin-spin coupling constants have been developed (100).

The analytic derivative method is generally more difficult to implement for any new type of wavefunction (Sec. 3.1), since specific expressions for analytical derivatives have to be derived and implemented. The general expression for the first-order properties

is given in Eq. 3.5, and expressions for higher derivatives can be obtained by differentiating the gradient expressions with respect to further perturbations. The analytical expressions for first- and second-order properties have been derived and implemented for many methods of quantum chemistry (101). The analytical approach can be extended to the case of time-dependent perturbations using the pseudo-energy derivative method (102) and the quasi-energy derivative method (103). The advantages of the analytical derivative method are: (a) higher accuracy for the calculated derivatives; (b) less computational effort relative to numerical procedure; (c) complex numbers, and therefore magnetic properties, can be easily handled; (d) frequency-dependent properties can be treated by response theory.

In applications, the computed properties will often be fitted by an appropriate analytical function. The model function should be chosen with special care in order to satisfy all symmetry properties of a molecular property function in the molecular symmetry group. For symmetric molecules, it is sometimes helpful to represent molecular properties of a vector or tensor form in terms of projections on molecular bonds. The molecular bond representation has the advantage that it is independent of the definition of the Cartesian frame, and its components obey symmetry relations, which can easily be established from the permutation symmetry of the molecule.

4.2 Ro-vibrationally averaged properties

If the ro-vibrational energy levels are not directly affected by a perturbation, the nuclear motion contributes to molecular properties only through ro-vibrational averaging. Most commonly evaluated is the zero-point vibrational correction (ZPVC) which is the matrix element of an electronic property operator, $P_{\mathrm{el}}(\xi_1, ...\xi_{3N-6})$, taken with the ground state vibrational wavefunctions:

$$P_{\mathrm{ZPVC}} = \langle \psi^{(0)}_{\mathrm{vib}} | P_{\mathrm{el}}(\xi_1, ...\xi_{3N-6}) | \psi^{(0)}_{\mathrm{vib}} \rangle - P(\xi_1^{(\mathrm{eq})}, ...\xi_{3N-6}^{(\mathrm{eq})}). \tag{4.8}$$

The effect of temperature, T, can be modelled by Boltzmann averaging of the operator over the accessible ro-vibrational states of energy $E^{(i)}_{\mathrm{rovib}}$:

$$P_T = \frac{1}{Q} \sum_i P^{(i)}_{\mathrm{rovib}} \exp\left(-\frac{E^{(i)}_{\mathrm{rovib}}}{kT} \right), \tag{4.9}$$

where

$$P^{(i)}_{\text{rovib}} = \langle \Psi^{(i)}_{\text{rovib}} | P_{\text{el}}(\xi_1, ...\xi_{3N-6}) | \Psi^{(i)}_{\text{rovib}} \rangle, \tag{4.10}$$

and Q is the partition function given by Eq. 3.23. The required matrix elements in Eq. 4.10 depend solely on the vibrational coordinates and can be written with the ro-vibrational wavefunction $\Psi^{(i)}_{\text{rovib}}$, taken from Eq. 3.9, as:

$$P^{(i)}_{\text{rovib}} = \mathbf{C}^{(i)} \cdot (\langle \boldsymbol{\psi}_{\text{vib}} | P_{\text{el}}(\xi_1, ...\xi_{3N-6}) | \boldsymbol{\psi}_{\text{vib}} \rangle \otimes \langle \boldsymbol{\psi}_{\text{rot}} | \boldsymbol{\psi}_{\text{rot}} \rangle) \cdot \mathbf{C}^{(i)}. \tag{4.11}$$

The rotational functions are symmetric rigid-rotor wavefunctions, $|\psi_{\text{rot}}\rangle = |j, k, m\rangle$, satisfying $\langle \boldsymbol{\psi}_{\text{rot}} | \boldsymbol{\psi}_{\text{rot}} \rangle = (\boldsymbol{\delta}_{jj'} \boldsymbol{\delta}_{kk'})_{jk,j'k'}$. In Eq. 4.11 the coefficients $\mathbf{C}^{(i)}$ are obtained from the solution of the "fully coupled" rotation-vibration problem, thus taking into account all rotation-vibration interactions such as Coriolis effects. Therefore rotational motions may contribute to molecular properties indirectly through coupling with vibrational motions. The effects of rotation-vibration interactions are commonly disregarded, although for some molecules, especially for those possessing large amplitude vibrational motion, contributions from rotation-vibration coupling may be as large as those from vibrations (see Sec. 4.4).

The evaluation of Eqs. 4.9 and 4.10 requires knowledge of eigenvalues $E^{(i)}_{\text{rovib}}$ and eigenfunctions $\Psi^{(i)}_{\text{rovib}}$ which are usually obtained variationally, that is by matrix diagonalization. We have introduced an alternative approach based on the matrix exponential technique, in which we avoid a time-consuming diagonalization procedure. It is based on the observation that Eq. 4.9 represents the trace of a matrix product

$$P_T = \text{tr}(\rho^{(T)}_{i,i} P^{(i)}_{\text{rovib}}), \tag{4.12}$$

involving the diagonal density matrix

$$\rho^{(T)}_{i,i} = \frac{1}{Q} \exp(-\beta E^{(i)}_{\text{rovib}}) = \frac{1}{Q} \langle \Psi^{(i)}_{\text{rovib}} | \exp(-\beta H_{\text{rovib}}) | \Psi^{(i)}_{\text{rovib}} \rangle, \tag{4.13}$$

where $\beta = 1/kT$. Since the trace does not depend on the choice of the representation, Eq. 4.13 can be evaluated in any representation we find suitable. The obvious choice is to work with the representation of basis functions, which are given by

$$|\psi^{(njkm)}_{\text{rovib}}\rangle = |\psi^{(n)}_{\text{vib}}\rangle |j, k, m\rangle. \tag{4.14}$$

The non-diagonal density matrix $\rho^{(T)}_{njk,n'j'k'}$ is constructed by expanding the matrix exponential as a Taylor series in the representation of basis functions as:

$$\begin{aligned}\rho^{(T)}_{njk,n'j'k'} &= \frac{1}{Q}\langle\psi^{(njk)}_{\text{rovib}}|\exp(-\beta H_{\text{rovib}})|\psi^{(n'j'k')}_{\text{rovib}}\rangle \\ &= \frac{1}{Q}\sum_{l\geq 0}^{L}\frac{1}{l!}\langle\psi^{(njk)}_{\text{rovib}}|(-\beta H_{\text{rovib}})^l|\psi^{(n'j'k')}_{\text{rovib}}\rangle\end{aligned} \tag{4.15}$$

Thus the problem of diagonalizing the Hamiltonian matrix $\langle\boldsymbol{\psi}_{\text{rovib}}|H_{\text{rovib}}|\boldsymbol{\psi}_{\text{rovib}}\rangle$ is replaced by the problem of evaluating the matrix products in Eq. 4.15. The thermally averaged property P_T can be calculated as

$$P_T = \text{tr}(\rho^{(T)}_{njk,n'j'k'}P^{(njk,n'j'k')}_{\text{rovib}}), \tag{4.16}$$

where

$$P^{(njk,n'j'k')}_{\text{rovib}} = \langle\psi^{(n)}_{\text{vib}}|P(\xi_1,...\xi_{3N-6})|\psi^{(n')}_{\text{vib}}\rangle\delta_{jj'}\delta_{kk'}. \tag{4.17}$$

The computational merit of the method depends on the matrix argument. The Taylor series gives a convergent result with a small number of expansion terms only if the argument is close to the null matrix. However, even when this is not the case, the computation can still be done efficiently when scaling and squaring techniques are employed (104). The method exploits a fundamental property unique to the exponential function:

$$\exp(-\beta H) = \exp(-\frac{1}{2}\beta H)\exp(-\frac{1}{2}\beta H). \tag{4.18}$$

As a result, $\exp(-\beta H)$ can be computed recursively from $\exp(-\beta H/2^N)$ by repeated squaring (N times). Depending on the norm of βH, N can be chosen such that the norm of $\beta H/2^N$ becomes sufficiently small. The term $\exp(-\beta H/2^N)$ can then be evaluated accurately and efficiently by Taylor series expansion. The performance of this technique depends upon the values of N and L (Eq. 4.15) being used. The larger the value of N the smaller the norm and, as a result, the faster the convergence of Taylor expansion and vice versa. We have performed tests on small molecules and found that a matrix norm of 0.1 is the optimal choice for $N + L$ to be minimal. Figure 4.1 compares CPU times used for evaluation of the matrix exponential and for diagonalization as a function of basis set size. It is obvious that the matrix exponential technique is very efficient. It can be used for fast computation of thermally averaged molecular properties, partition functions, and thermodynamic parameters.

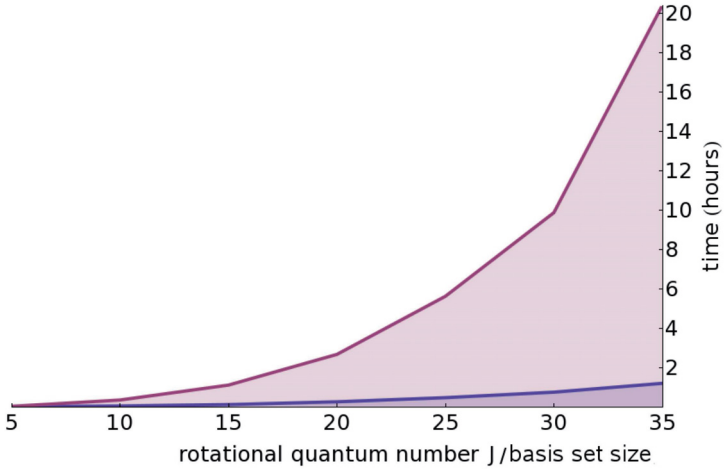

Figure 4.1: Efficiency of the matrix exponential technique - CPU time used for Hamiltonian matrix diagonalization (red line) and for calculation of its exponent (blue line) plotted against basis set size.

4.3 'Pure' vibrational properties

At the molecular level both electronic and nuclear degrees of freedom can interact with an electromagnetic light wave and, as a result, electromagnetic properties contain both electronic and ro-vibrational contributions. The ro-vibrational effects are known to be the most pronounced for nonlinear optical properties (first and second hyperpolarizabilities), where their contribution is often comparable in magnitude, or even larger, than that due to electronic motions. Various approaches have been proposed to treat nuclear motion contributions to electric properties using either perturbation theory (105, 106, 107) or analytical response theory (108, 109). All of these approximations employ the model of a non-rotating molecule being aptly oriented in the laboratory frame. The uniform electric field Hamiltonian has the following form:

$$H'(\mathbf{F}) = -\mu_\alpha^{(\mathrm{el})} F_\alpha - \frac{1}{2}\alpha_{\alpha\beta}^{(\mathrm{el})} F_\alpha F_\beta - \frac{1}{6}\beta_{\alpha\beta\gamma}^{(\mathrm{el})} F_\alpha F_\beta F_\gamma - \frac{1}{24}\gamma_{\alpha\beta\gamma\delta}^{(\mathrm{el})} F_\alpha F_\beta F_\gamma F_\delta, \qquad (4.19)$$

where F_α, F_β, F_γ, or F_δ are components of the electric field vector, and the quantities $\mu_\alpha^{(\mathrm{el})}$, $\alpha_{\alpha\beta}^{(\mathrm{el})}$, $\beta_{\alpha\beta\gamma}^{(\mathrm{el})}$, and $\gamma_{\alpha\beta\gamma\delta}^{(\mathrm{el})}$ are the electronic dipole moment, polarizability, first and second hyperpolarizability, respectively, which are obtained from electronic structure calculations. They are functions of the vibrational coordinates, i.e., $\mu_\alpha^{(\mathrm{el})} = \mu_\alpha^{(\mathrm{el})}(\xi_1, ...\xi_{3N-6})$, etc. The vibrational field-dependent energies, $E_{\mathrm{vib}}^{(i)}(\mathbf{F})$, are obtained

as eigenvalues of the full field-dependent Hamiltonian, $H_0 + H'(\mathbf{F})$. Taking derivatives of the resulting vibrational energies with respect to the field strength we obtain full, electronic *plus* vibrational, electric dipole moment and polarizabilities as:

$$\mu_\alpha^{(i)} = \frac{\partial E_{\rm vib}^{(i)}(\mathbf{F})}{\partial F_\alpha}, \quad \alpha_{\alpha\beta}^{(i)} = \frac{\partial^2 E_{\rm vib}^{(i)}(\mathbf{F})}{\partial F_\alpha \partial F_\beta}, \quad \beta_{\alpha\beta\gamma}^{(i)} = \frac{\partial^3 E_{\rm vib}^{(i)}(\mathbf{F})}{\partial F_\alpha \partial F_\beta \partial F_\gamma}, \quad \text{etc.} \tag{4.20}$$

The total property P given in Eq. 4.20 may be written as a sum of two terms: $P = P^{(\rm el)}(\xi_1^{(\rm eq)}, ...\xi_{3N-6}^{(\rm eq)}) + P^{(\rm vib)}$, from which the so-called 'pure vibrational' contribution, $P^{(\rm vib)}$, can be defined. It should be noted that properties obtained from Eqs. 4.19 and 4.20 depend on the definition of the laboratory coordinate system, they change under uniform rotation, although tensor traces remain unchanged.

When we refer to experiment it appears rather difficult to 'catch' a molecule appropriately oriented with respect to a laser beam or an applied electric field, since the molecule will normally be rotating. In order to simulate the real world situation, we must allow the molecule for such rotation, although one should keep in mind that the model of non-rotating molecule may be valid for 'slow' bulky macromolecules.

What would still happen if we have a molecule rotating in the applied uniform electric field, and what quantities can be associated with pure vibrational contributions? Identifying the direction of the electric field with the Z direction in the SF frame, the electric field Hamiltonian, truncated at fourth-order terms, can be written as:

$$H'(F_Z) = -\mu_Z F_Z - \frac{1}{2}\alpha_{ZZ} F_Z^2 - \frac{1}{6}\beta_{ZZZ} F_Z^3 - \frac{1}{24}\gamma_{ZZZZ} F_Z^4. \tag{4.21}$$

We aim at evaluating H' matrix elements in the basis of eigenfunctions of the field-free ro-vibrational Hamiltonian, given by Eq. 3.9. A procedure, similar to that applied in the case of the line strength (see Sec. 3.2), may be used here. First, we have to define SF Cartesian operators μ_Z, α_{ZZ}, etc., in the MF coordinate system, which are then expressed in spherical coordinates, i.e., defined in terms of spherical tensor operators. The latter are given by Eqs. 3.11 and 3.12 for electric dipole moment components in the SF and MF frames, respectively. Tensors of higher ranks can be generated from spherical tensors of lower ranks through linear combination:

$$\alpha = \mu \otimes \mu \tag{4.22}$$

$$\alpha_{\rm sf}^{(2,q)} = \sum_{q_1}\sum_{q_2} \langle 1,1;q_1,q_2|1,1;2,q\rangle \mu_{\rm sf}^{(1,q_1)} \mu_{\rm sf}^{(1,q_2)}, \tag{4.23}$$

where $\langle 1,1;q_1,q_2|1,1;2,q\rangle$ are Clebsch-Gordan coefficients. The similarity of this equation with the relationship between the direct product and total angular momentum basis sets may be appreciated:

$$|JM\rangle = \sum_{m_1}\sum_{m_1}\langle j_1,j_2;m_1,m_2|j_1,j_2;J,M\rangle|j_1,m_1\rangle|j_2,m_2\rangle. \tag{4.24}$$

For the polarizability the six spherical tensor components in the SF frame are given by:

$$\begin{aligned}
\alpha_{\rm sf}^{(0,0)} &= \frac{1}{\sqrt{3}}\left(\alpha_{XX}+\alpha_{YY}+\alpha_{ZZ}\right), && (4.25)\\
\alpha_{\rm sf}^{(2,-2)} &= \frac{1}{2}\left(\alpha_{XX}-\alpha_{YY}\right)-i\alpha_{XY}, && (4.26)\\
\alpha_{\rm sf}^{(2,-1)} &= \alpha_{XZ}-i\alpha_{YZ}, && (4.27)\\
\alpha_{\rm sf}^{(2,0)} &= \frac{1}{\sqrt{6}}\left(-\alpha_{XX}-\alpha_{YY}+2\alpha_{ZZ}\right), && (4.28)\\
\alpha_{\rm sf}^{(2,1)} &= -\alpha_{XZ}-i\alpha_{YZ}, && (4.29)\\
\alpha_{\rm sf}^{(2,2)} &= \frac{1}{2}\left(\alpha_{XX}-\alpha_{YY}\right)+i\alpha_{XY}, && (4.30)
\end{aligned}$$

with similar expressions for MF components. Eq. 4.23 can also be used to find the spherical representation for β and γ Cartesian tensor operators. Using the relations given by Eqs. 3.11 and 4.25-4.30 with similar equations for β and γ tensors, and performing a lot of algebra, we can write the electric field Hamiltonian, defined in Eq. 4.21, in the spherical basis as:

$$\begin{aligned}
H'(F_Z) = &- \mu_{\rm sf}^{(1,0)}F_Z && (4.31)\\
&- \frac{1}{6}\left(-\sqrt{3}\alpha_{\rm sf}^{(0,0)}+\sqrt{6}\alpha_{\rm sf}^{(2,0)}\right)F_Z^2\\
&- \frac{1}{60}\left(-3\sqrt{15}\beta_{\rm sf}^{(1,0)}+2\sqrt{10}\beta_{\rm sf}^{(3,0)}\right)F_Z^3\\
&- \frac{1}{1680}\left(21\sqrt{5}\gamma_{\rm sf}^{(0,0)}-30\sqrt{14}\gamma_{\rm sf}^{(2,0)}+4\sqrt{70}\gamma_{\rm sf}^{(4,0)}\right)F_Z^4.
\end{aligned}$$

The spherical tensor operators, defined in the SF coordinate system, can be easily 'rotated' to the MF frame using the Wigner rotation matrices, $\mathbf{D}(\theta,\phi,\chi)$, as given in Eq. 3.10. For example, the relation for the $\alpha_{\rm sf}^{(2,0)}$ component can be written as:

$$\alpha_{\rm sf}^{(2,0)} = \sum_{\sigma=-2}^{2}[D_{0\sigma}^{(2)}(\theta,\phi,\chi)]^*\alpha_{\rm mf}^{(2,\sigma)}, \tag{4.32}$$

where $\alpha_{\rm mf}^{(2,\sigma)}$ are the components of the polarizability tensor in the MF coordinate system. Inserting this equation, together with the similar equations for other tensor operators, the electric field Hamiltonian may finally be written in the MF frame, i.e., in terms of $3N-6$ internal (vibrational) coordinates and three Euler angles.

We build the rotational basis set from the rigid-rotor wavefunctions, $|j,k,m\rangle$. As a consequence of the Wigner-Eckart theorem, the rotation matrix elements in the basis of rigid-rotor wavefunctions $|j,k,m\rangle$ can be evaluated as

$$\begin{aligned}\langle j',k',m'|[D^{(\omega)}_{0\sigma}(\theta,\phi,\chi)]^*|j,k,m\rangle &= (-1)^{k'+m'}\sqrt{(2j'+1)(2j+1)} \\ &\times \begin{pmatrix} j & \omega & j' \\ k & \sigma & -k' \end{pmatrix}\begin{pmatrix} j & \omega & j' \\ m & 0 & -m' \end{pmatrix},\end{aligned} \tag{4.33}$$

which represents the more general form of Eq. 3.15. From the properties of Wigner $3j$-symbols it follows that non-vanishing matrix elements in Eq. 4.33 must satisfy the following conditions:

$$|j'-j| \leq \omega, \tag{4.34}$$

$$m'-m = 0, \tag{4.35}$$

$$k'-k = \sigma. \tag{4.36}$$

According to Eq. 4.35 the quantum number m of projection of the total angular momentum on the distinguished axis Z in the SF system is a good (appropriate) quantum number. Therefore the field-dependent Hamiltonian matrix can be divided into independent sub-blocks for each value of the quantum number m. The size of each m-submatrix, however, is determined by the size of the field-free ro-vibrational basis, $N_{\rm vib}\times(2j+1)$, and the maximum rank, ω, of tensor operators entering H'.

In order to identify 'pure vibrational' effects on electric properties we need to address a situation where rotational motion is not affected by the electric field, i.e., we assume the molecule to be in its ground rotational state, $|j,k,m\rangle = |0,0,0\rangle$. Inserting $|0,0,0\rangle$ rotational functions into Eqs. 4.33, 4.32, and 4.31, with similar expressions for $\mu_{\rm sf}$, $\beta_{\rm sf}$, and $\gamma_{\rm sf}$ tensors, and carrying out a significant amount of algebra, we obtain the following expression for the electric field Hamiltonian of a molecule in the ground rotational state:

$$\begin{aligned}H'(F_Z) = &- \frac{1}{2!}\frac{1}{3}\left(\alpha_{xx}+\alpha_{yy}+\alpha_{zz}\right)F_Z^2 \\ &- \frac{1}{4!}\frac{1}{5}\left(\gamma_{xxxx}+\gamma_{yyyy}+\gamma_{zzzz}+2\gamma_{xxyy}+2\gamma_{xxzz}+2\gamma_{yyzz}\right)F_Z^4.\end{aligned} \tag{4.37}$$

In this equation $\alpha_{\alpha\alpha}$ and $\gamma_{\alpha\beta}$ are the electronic tensor components in the MF coordinate system. Equation 4.37 proves that there are only few properties, for which it makes sense to speak about 'pure vibrational' contributions, namely the diagonal elements of polarizability tensor, $\alpha_{\alpha\alpha}$, and the diagonal and bi-diagonal elements of the second hyperpolarizability tensor, $\gamma_{\alpha\alpha\alpha\alpha}$ and $\gamma_{\alpha\alpha\beta\beta}$. Using Eqs. 4.19 and 4.20 to compute 'pure vibrational' contributions for other quantities, such as μ and β, is therefore meaningless.

In order to include other quantities in the H' operator we must consider rotational transitions, i.e. 'turn on' rotational motion. For example, looking at the $|1,k,0\rangle \leftarrow |0,0,0\rangle$ transition and integrating H' over the rotational degrees of freedom we obtain following expressions:

$$\begin{aligned}\langle 1,0,0|H'|0,0,0\rangle = &- \frac{1}{\sqrt{3}}\mu_z F_Z \\ &- \frac{1}{3!}\frac{\sqrt{3}}{5}\left(\beta_{xxz}+\beta_{yyz}+\beta_{zzz}\right)F_Z^3\end{aligned} \tag{4.38}$$

$$\begin{aligned}\langle 1,\pm 1,0|H'|0,0,0\rangle = &- \frac{1}{3\sqrt{2}}\left(\pm\mu_x \pm i\mu_y\right)F_Z \\ &- \frac{1}{3!}\frac{1}{5\sqrt{2}}\left(\pm[\beta_{xxx}+\beta_{xyy}+\beta_{xzz}] \mp i[\beta_{xxy}+\beta_{yyy}+\beta_{yzz}]\right)F_Z^3.\end{aligned} \tag{4.39}$$

We note again that these quantities cannot be associated with 'pure vibrational' effects, since rotational transitions have been considered.

In the TROVE program, we construct the electric field Hamiltonian and integrate it analytically over rotational coordinates in the basis of symmetry-adapted $|j,k,m\rangle$ functions (9, 15). The resulting Hamiltonian matrix is huge, of dimension $N_{\text{vib}} \times (2J_{\max}+1) \times (2m+1)$ (where N_{vib} and $2J_{\max}+1$ are the size of the vibrational and rotational basis sets, respectively). It contains imaginary numbers, which puts an additional burden on the computational resources. After analysis of the matrix elements corresponding to various $\Delta k > 0$ transitions we find that all even-σ matrix elements of operators $U_{\text{mf}}^{(\omega,\sigma)}$, i.e. $\alpha_{\text{mf}}^{(2,\pm 2)}$, $\beta_{\text{mf}}^{(3,\pm 2)}$, $\gamma_{\text{mf}}^{(4,\pm 4)}$, and $\gamma_{\text{mf}}^{(4,\pm 2)}$, are real, while all odd-σ matrix elements, $\mu_{\text{mf}}^{(1,\pm 1)}$, $\alpha_{\text{mf}}^{(2,\pm 1)}$, $\beta_{\text{mf}}^{(3,\pm 3)}$, $\beta_{\text{mf}}^{(3,\pm 1)}$, $\gamma_{\text{mf}}^{(4,\pm 3)}$, $\gamma_{\text{mf}}^{(4,\pm 1)}$, are imaginary. For $\Delta k = 0$, all matrix elements are real. Therefore the time and memory required for calculating H' matrix elements can be significantly reduced when computing and storing real and imaginary parts of the Hamiltonian independently, i.e. $H' = H'\delta_{\text{mod}(k,2),0} + iH'\delta_{\text{mod}(k,2),1}$.

Frequency dependent properties may be calculated by introducing the time dependence in the field strength function, i.e. $F_Z = F_Z(t)$, and solving the time-dependent Schrödinger equation, with the stationary wavefunction, $\psi^{(0)}$, perturbed by a small harmonic frequency, $\psi = \psi^{(0)} e^{-i\omega t}$. The derivation of explicit equations for frequency dependent properties is discussed, for example, in Ref. (110).

The behavior of molecules in the presence of an external electric field is still an open area both for theoretical and experimental studies, for example, with regard to the laser manipulation and orientation of molecules, Raman optical activity, and various processes of nonlinear optics. When a molecule interacts with an electromagnetic wave, both the electronic and nuclear degrees of freedom are affected, and as a result the molecular optical properties contain both electronic and vibrational contributions (111, 112, 113). Surprisingly, for many optical processes the nuclear motion contribution is often comparable in magnitude, or even larger, than that due to electronic motion. In the future we plan to study the (nonlinear) optical properties of small nonrigid molecules for which the accurate treatment of nuclear motion is of great importance. To our knowlege, variational full-dimensional treatments of molecular nonlinear optical properties are still novel. Another interesting topic for future work is the direct calculation of the spectroscopic observables of a molecule in an electromagnetic field, in particular, the optical activity of rotationally induced chiral states.

4.4 Thermally averaged magnetic properties of ammonia

Accurate calculations of nuclear magnetic resonance (NMR) constants have for a long time been a challenge for theoretical chemistry. Modern *ab initio* methods are capable of producing magnetic properties of experimental accuracy, however absolute agreement with experimental values is hampered by the fact that the ro-vibrational corrections are ignored (see Sec. 4.2). The influence of molecular ro-vibrational motion on magnetic properties, such as magnetizability, shielding, spin-spin, and spin-rotational tensors, has therefore been the topic of several studies (114, 115, 116, 117, 118, 119). Small changes in the magnetic constants such as isotope effects or the temperature dependence can only be reproduced by taking into account the ro-vibrational contributions (117,

119). Such calculations require values of the magnetic constants for particular ro-vibrational states. This implies that the magnetic constants as functions of internal coordinates have to be averaged over the corresponding ro-vibrational wavefunction. The vibrational wavefunctions have normally been obtained by first order perturbation theory and effects of ro-vibrational coupling have always been disregarded. However, perturbation theory works well only for 'rigid' molecules, vibrating in the vicinity of equilibrium, and shows poor convergence or does not converge at all for molecules possessing large amplitude anharmonic motion.

For this reason, the NH_3 molecule, with its large amplitude inversion mode, has previously not been addressed in recent ro-vibrational-averaging studies with high level *ab initio* methods. In our work, we thus decided to obtain accurate ro-vibrational corrections to the magnetic properties of $^{15}NH_3$ and its isotopologues, to analyse the effects due to ro-vibrational coupling, temperature, and isotopic substitution, and to validate more approximate models for ro-vibrational averaging, which are based on a 'rigid' representation of molecular motion in ammonia. We have reinvestigated the ro-vibrational corrections to spin-spin coupling constants (120), magnetizablity, shielding constants, and spin-rotation constants (121) in ammonia using state-of-the-art *ab initio* methods. Contrary to earlier studies, we have not employed perturbation theory in the calculation of the vibrational corrections, but have for the first time directly averaged the multidimensional surfaces for coupling constants obtained at the SOPPA(CCSD) level (122, 123) using accurate rovibrational wave functions. The latter were determined by means of the variational TROVE code (14) in conjunction with a highly accurate potential energy surface of ammonia from Ref. (124). For the averaging, the matrix exponential technique was utilized (see Sec. 4.2). Details of the *ab initio* calculations and the analytical representation for the spin-spin coupling constants of $^{15}NH_3$ are presented in Ref. (120). The same approach has been utilized in calculations of other magnetic constants (121).

The results of thermal averaging ($T = 300$ K) for $^{15}NH_3$ and its deuterated isotopologues are listed in Table 4.1. The values in parenthesis are the thermal corrections, defined as the difference between the averaged and the equilibrium values:

$$\Delta P = \langle P \rangle - P_{\mathrm{eq}}. \tag{4.40}$$

	$^{15}NH_3$	$^{15}ND_3$	$^{15}NH_2D$	$^{15}NHD_2$
$\langle J_{NH} \rangle$	61.947 (0.361)		61.884 (0.425)	61.823 (0.486)
$\langle J_{ND} \rangle$		62.083 (0.226)	62.284 (0.025)	62.216 (0.093)
$\langle J_{HH} \rangle$	10.681 (0.555)		10.671 (0.565)	
$\langle J_{HD} \rangle$			10.734 (0.502)	10.721 (0.515)
$\langle J_{DD} \rangle$		10.806 (0.430)		10.795 (0.441)
$\langle \xi \rangle$	-3.717 (-0.032)	-3.709 (-0.025)	-3.714 (-0.030)	-3.712 (-0.027)
$\langle \sigma_N \rangle$	263.527 (-7.332)	265.618 (-5.241)	264.154 (-6.705)	264.814 (-6.045)
$\langle \sigma_H \rangle$	30.841 (-0.652)		30.869 (-0.624)	30.931 (-0.562)
$\langle \sigma_D \rangle$		31.011 (-0.482)	30.978 (-0.515)	30.980 (-0.513)
$\langle C_N \rangle$	-6.715 (-0.587)	-6.548 (-0.420)	-6.669 (-0.541)	-6.619 (-0.491)
$\langle C_H \rangle$	18.160 (-1.140)		18.217 (-1.083)	18.367 (-0.933)
$\langle C_D \rangle$		18.442 (-0.858)	18.368 (-0.932)	18.366 (-0.934)

Table 4.1: Calculated thermally averaged spin-spin coupling constants, J_{NH} and J_{HH} (in Hz), isotropic magnetizability, ξ (in a.u.), shielding constants, σ_N and σ_H (in ppm), and spin-rotation constants, C_N and C_H (in kHz), of ammonia isotopologues. Values in parenthesis are the corresponding thermal ($T = 300$ K) corrections.

In TROVE we solve the 'fully coupled' rotational-vibrational problem, and thus take into account all rotation-vibration interactions. This allows us to investigate the importance of the rotation-vibration coupling effects for thermal averaging and thus to assess the accuracy of the pure vibrational approach in which rotation is ignored. In our approach, pure vibrational averaging corresponds to $\langle P \rangle$ values obtained from averaging over the vibrational wave functions only, $j = 0$. The resulting values will be labelled as $\langle P \rangle_{j=0}$; they differ from the $T = 0$ K (ZPVA) values, $\langle P \rangle_{T=0K}$. In Fig. 4.2 we demonstrate that rotational contributions are almost as large as, or even larger than vibrational ones. Figure 4.2 depicts thermal corrections to the magnetic constants, $\Delta P_{T=300K}$, defined as

$$\Delta P_{T=300K} = \langle P \rangle_{T=300K} - \langle P \rangle_{T=0K} \tag{4.41}$$

and computed for different values of the maximum rotational quantum number j_{max}. For the spin-spin coupling constants we can see that the thermal correction increases as j increases and then converges to a small value. Thus the final thermal correction for the spin-spin coupling constants is small, but only when it is properly evaluated.

For the magnetizability, shielding and spin-rotation coupling constants, the situation is different: at $j = 0$ the thermal correction is marginal, but when j increases the correction also grows, and so almost the whole thermal effect is due to rotational motion.

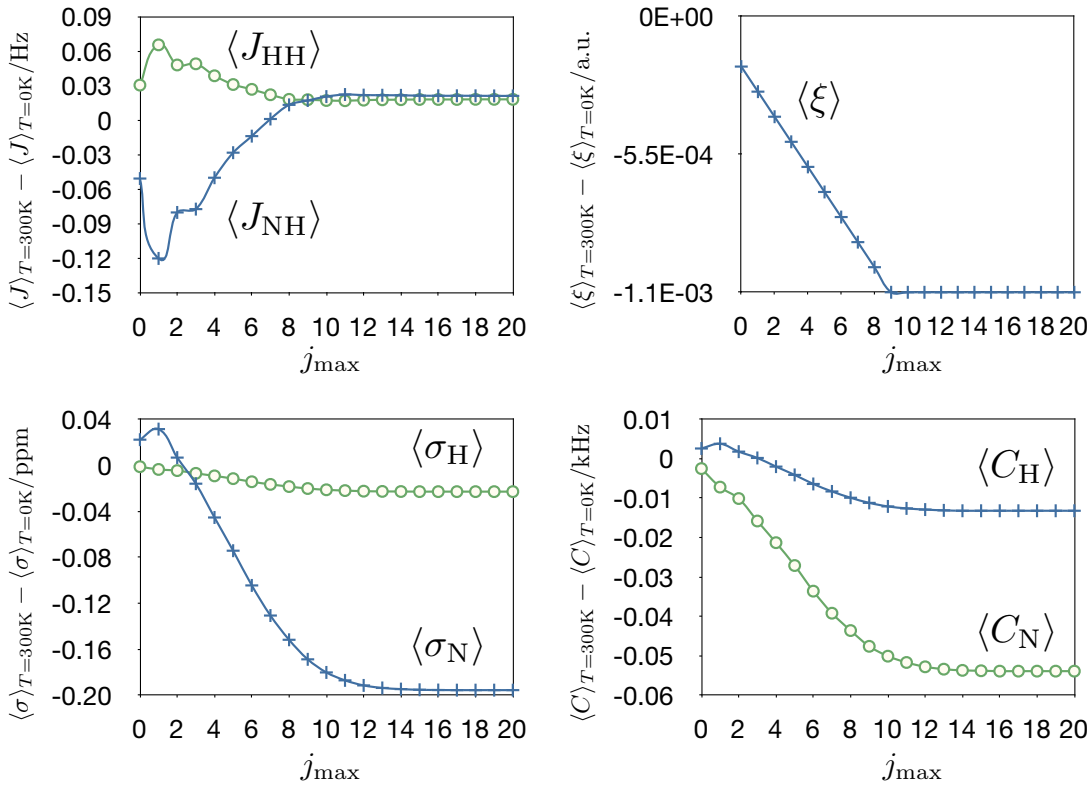

Figure 4.2: Convergence of thermal corrections to magnetic constants of $^{15}NH_3$ vs rotational excitation j_{max} - The thermal corrections (as defined along the ordinate) were calculated for j_{max} and are plotted (relative to the corresponding $T = 0$ K values) for the spin-spin coupling constants, J_{NH} and J_{HH}, the isotropic magnetizability, ξ, the shielding constants, σ_{N} and σ_{H}, and the spin-rotation constants, C_{N} and C_{H}.

Our approach of thermal averaging explicitly takes into account the nonrigid character of the umbrella inversion mode and correctly describes the tunneling through the low inversion barrier of ammonia. However, the vast majority of studies of thermal and ZPVA corrections to magnetic constants utilize first and second order vibrational perturbation theory. To test the effects of large amplitude motion on the thermal corrections we have recomputed the averages by employing the 'rigid' approach, i.e., by

treating ammonia as a single minimum rigid $\mathbf{C}_{3v}$ system. We have computed averaged constants variationally for different truncation orders in the kinetic energy (N_{KEO}) and potential energy (N_{PES}) expansions, thus imitating perturbation theory models. In Fig. 4.3 we show the discrepancies between spin-spin coupling constants obtained with the $N_{\mathrm{KEO}}/N_{\mathrm{PES}}$ 'rigid' approach and those obtained with the 'true' model, i.e. by taking into account nonrigid character of umbrella motion. The results converge very fast with N_{KEO} so that a second-order expansion is sufficient for the kinetic energy, while the potential requires at least $N_{\mathrm{PES}} = 6$. The 'rigid' results, however, tend to converge to values quite different from the 'true' values with increasing N_{PES}. Both the $\langle J_{\mathrm{NH}} \rangle$ and $\langle J_{\mathrm{HH}} \rangle$ constants are finally overestimated by 0.4−0.5 Hz, which is comparable to the thermal correction itself. It is also impossible to propose some universal 'intermediate' model, which could benefit from error cancelation. While for $\langle J_{\mathrm{NH}} \rangle$ the $N_{\mathrm{KEO}}/N_{\mathrm{PES}}$=2/4 'rigid' approach yields excellent results, it overestimates $\langle J_{\mathrm{HH}} \rangle$ by 0.7 Hz. The other magnetic constants appear to be reproduced quite well by the 'rigid' approach, see Fig. 4.4. Deviations from the 'true' results are quite small, with the only exception of the σ_{N} constant. Excellent results for all constants can be obtained already with the $N_{\mathrm{KEO}}/N_{\mathrm{PES}}$=2/6 expansions. The 'rigid' approach also shows correct, or almost correct, convergence to the 'true' results for the magnetizability, shielding, and spin-rotational coupling constants.

Therefore we can recommend the $N_{\mathrm{KEO}}/N_{\mathrm{PES}}$=2/6 'rigid' approach to obtain satisfactory results for all magnetic constants except for spin-spin coupling constants. The latter are more affected by tunneling (large amplitude motion) effects and cannot be treated by the 'rigid' model, or equivalently, by perturbation theory at all. It should be noted, that most standard quantum chemistry packages use a perturbation theory approach that resembles the $N_{\mathrm{KEO}}/N_{\mathrm{PES}}$=0/4 model, which unfortunately shows the worst results. The 0/4 model can be significantly improved by taking into account kinetic anharmonicity effects at second order.

Comparison with previous theoretical calculations (115, 125, 126) shows that only one study (115) has results close to ours, although the reported vibrational corrections from second-order perturbation theory (0/4 'rigid' model) are too large compared to our variational results. Figure 4.5 shows the effects of isotopic substitution on the thermal corrections for J_{NH} and J_{HH} spin-spin coupling constants. We compare our results for spin-spin coupling constants with measured isotopic shifts. Experimentally the

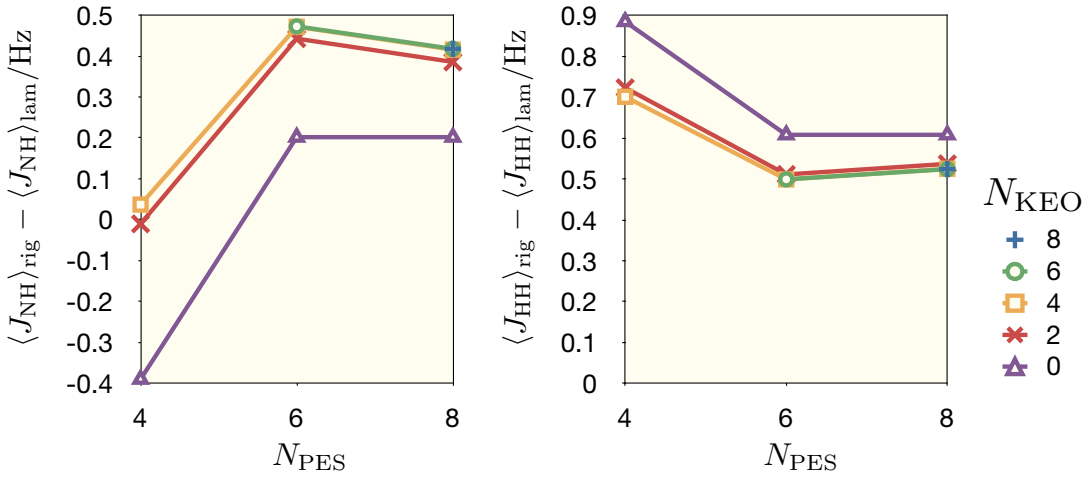

Figure 4.3: Validation of the 'rigid' approach in the calculation of the spin-spin coupling constants of $^{15}NH_3$ - Shown are deviations between the values calculated by treating NH_3 molecule as rigid $\mathbf{C}_{3v}$ system ($\langle\rangle_{\mathrm{rig}}$), and those obtained by taking into account the large amplitude character of umbrella motion, ($\langle\rangle_{\mathrm{lam}}$). Various expansion orders for kinetic energy (N_{KEO}) and potential energy (N_{PES}) operators have been employed in the 'rigid' approach.

primary isotopic shift for the one-bond coupling is -0.46±0.13 Hz, while the secondary isotope shift is 0.07±0.02 Hz (127). Our theoretical values are -0.33 Hz for the primary and 0.06−0.07 Hz for the secondary isotope effects in $^{15}NH_2D$ and $^{15}NHD_2$, in a very good agreement with experiment. The J_{NH} coupling constant measured in a liquid phase (128) with the vapor-to-liquid shift recently reported in Ref. (129) is -61.95 Hz which is also in excellent agreement with our thermally averaged value of -61.97 Hz.

In summary, we have presented state-of-the-art calculations of magnetic constants of ammonia and its isotopologues. Compared with our full variational treatment of nuclear motion, the standard perturbation-theory approach underestimates the nuclear motion corrections significantly. Comparison with the available experimental data reveals excellent agreement for the absolute values and their primary and secondary isotope effects.

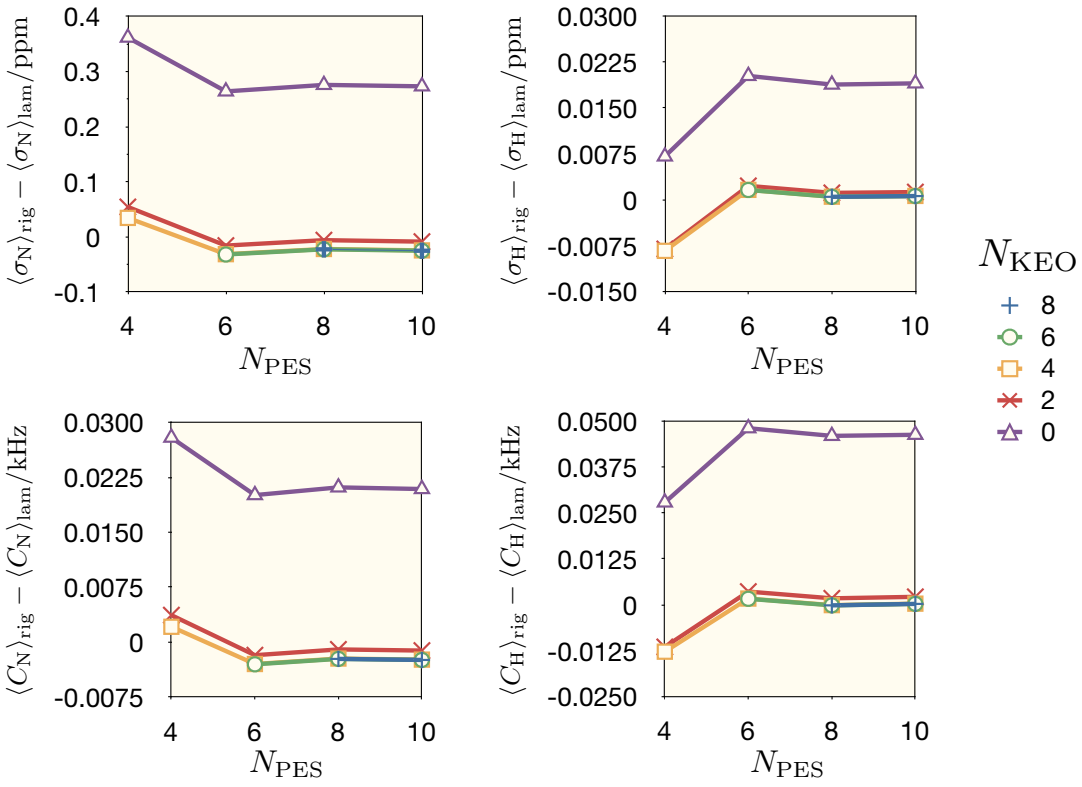

Figure 4.4: Validation of the 'rigid' approach in the calculation of the nitrogen and hydrogen shielding constants and spin-rotation coupling constants of $^{15}NH_3$ - Shown are deviations between the values calculated by treating NH_3 molecule as rigid $\mathbf{C}_{3v}$ system ($\langle\rangle_{rig}$), and those obtained by taking into account the large amplitude character of umbrella motion, ($\langle\rangle_{lam}$). Various expansion orders for kinetic energy (N_{KEO}) and potential energy (N_{PES}) operators have been employed in the 'rigid' approach.

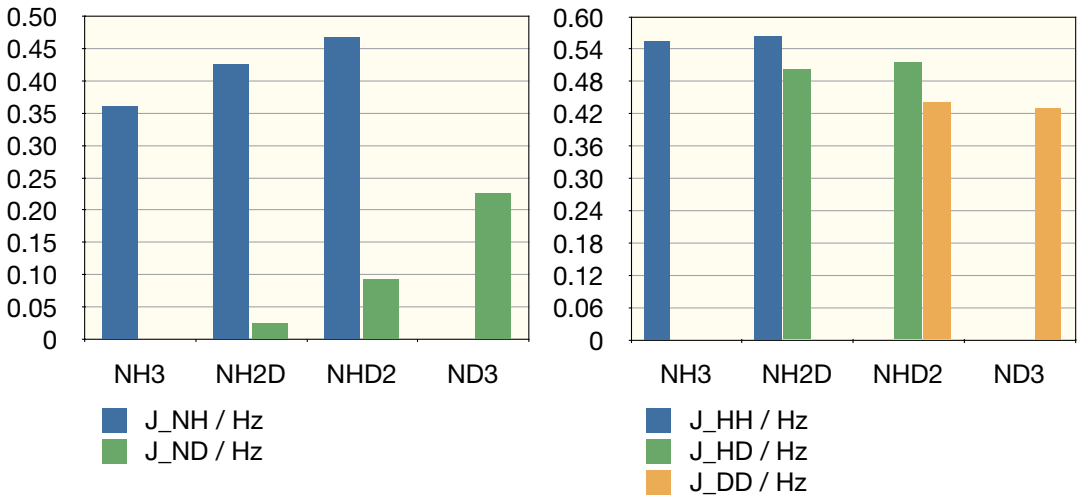

Figure 4.5: Effect of isotopic substitution on the J_{NH} and J_{HH} spin-spin coupling constants of $^{15}\mathbf{NH_3}$ - The thermal (T = 300 K) corrections to the spin-spin coupling constants are plotted for various ammonia isotopologues in order of increasing H/D substitution.

5

Conclusions and outlook

We have presented new efficient and flexible methods for calculating ro-vibrational spectra and properties of small molecules. These methods extend the functionality of the computer program TROVE, developed in our group in recent years and intended for a general variational treatment of the nuclear motion problem. Flexibility means that there are no limitations on the type of molecule, ro-vibrational state or transition for which spectra or other electric or magnetic properties are calculated. All computational procedures are formulated and implemented in a general rather than a molecule-specific manner. The program can compute the complete ro-vibrational spectrum in a selected frequency region reproducing all features due to the ro-vibrational coupling and tunneling effects observable in experiment. It has modular structure making it relatively easy to exchange property-specific parts when implementing a new property function. The new efficient procedure for PES refinement (Sec. 2.2) has been developed in this way, i.e., by combining already existing parts of the program. The efficiency of the code in the computation of molecular properties and spectra is achieved by optimization of the two most resource and time consuming tasks. First, the procedures for computing the ro-vibrational transition probabilities, driven by the electric dipole moment and electric polarizability, have been optimized. This is accomplished by deriving explicit formulas for the ro-vibrational transition matrix elements of the electric dipole and polarizability operators for all possible kinds of Δj, Δk, and Δm transitions (Sec. 3.2). This allows one to avoid the use of complex numbers and to employ efficient integral prescreening techniques to reduce the number of integrals that need to be computed. Explicit formulas have also been derived for matrix elements of the first and second hyperpo-

larizabilities which enter the external electric field Hamiltonian (Sec. 4.3). To compute temperature corrections to the properties we have proposed a new method which uses the thermally averaged ro-vibrational density matrix rather than the ro-vibrational energies and wavefunctions (Sec. 4.2). This method does not solve an eigenvalue problem that becomes unfeasible when high temperatures and thus highly excited states are involved, but computes the temperature-weighted Hamiltonian matrix exponential. It is up to 100 times faster than matrix diagonalization (with LAPACK), scales very well with the number of CPUs, and consumes two times less RAM memory.

There are several directions in which the present implementation work can be extended or improved. The TROVE strategy is to develop and implement general methods for the variational treatment of the ro-vibrational problem that enable us to calculate spectra and properties for arbitrary molecules and arbitrarily chosen coordinates. Going beyond dipole and polarizability transition probabilities, a possible extension is to include other quantities entering the electric field multipole expansion, such as, for example, the quadrupole moment and quadrupole polarizability. Being able to treat a molecule in a non-uniform electric field, future applications can address the nuclear motion of molecules placed in a crystal or any other macromolecular (nano) environment. Another task is to optimize and enhance the flexibility of the procedures for solving the pure vibrational problem by implementing the discrete-variable-representation technique.

We have applied the TROVE program for simulating the high-resolution spectra of HSOH and NH_3, for calculating the PESs of H_2CO and NH_3 with spectroscopic accuracy, and for determining benchmark values for magnetic constants and isotopic shifts of $^{15}NH_3$.

In case of HSOH we have simulated the ro-vibrational spectra for the ground state and the fundamental torsional state. The theoretical results reproduce the observed intensity patterns very well, including the intensity anomalies in the ${}^rQ_{K_a}$ branches, which are caused by large amplitude torsional motion; these anomalies can be understood qualitatively by analysis of the variational results. For NH_3 we have produced a complete astrophysical line list for $T = 300$ K consisting of 3.25 million transitions between states with energies up to 12 000 cm^{-1}.

Using the new efficient procedure for PES refinement, we have obtained PESs for NH_3 and H_2CO of unprecedented accuracy (with rms deviations of 0.1 and 0.04 cm^{-1},

respectively) unreachable for state-of-the-art quantum chemical methods. We plan to apply this method for refining the PES of H_2CS, which was calculated using high level *ab initio* methods. Accurate theoretical predictions of spectra for overtone and combination bands of H_2CS are in much demand. We plan to compute such spectra to support recent experimental studies on this molecule.

We have applied the new method for calculating thermally averaged properties to produce benchmark results for the magnetic constants of $^{15}NH_3$ and its isotopologues. We also showed for the ro-vibrational contributions to the magnetic constants of ammonia that the effects of large amplitude motion and Coriolis coupling are quite substantial and cannot be recovered even with a high-order perturbation treatment. In the future we plan to study the (nonlinear) optical properties of small nonrigid molecules for which the accurate treatment of nuclear motion is of great importance. To our knowlege, variational full-dimensional treatments of molecular nonlinear optical properties are still missing. Another interesting topic for future work is the direct calculation of the spectroscopic observables of a molecule in an electromagnetic field, in particular, the optical activity of rotationally induced chiral states.

References

[1] M. Born and W. Heisenberg. *Ann. Phys.*, **74**:1–31, 1924.

[2] M. Born and J. R. Oppenheimer. *Ann. Phys.*, **84**:457–484, 1927.

[3] M. Born and K. Huang. *Dynamical Theory of Crystal Lattices*. Clarendon Press, Oxford, 1954.

[4] C. Eckart. *Phys. Rev*, **47**:552–558, 1935.

[5] B. T. Darling and D. M. Dennison. *Phys. Rev*, **57**:128–139, 1940.

[6] E. B. Wilson Jr., J. C. Decius, and P. Cross. *Molecular Vibrations*. McGraw-Hill, New York, 1955.

[7] J. K. G. Watson. *Mol. Phys.*, **15**:479–490, 1968.

[8] A. R. Hoy, I. M. Mills, and G. Strey. *Mol. Phys.*, **24**:1265–1290, 1972.

[9] D. Papousek and M. R. Aliev. *Molecular Vibrational Rotational Spectra*. Academia, Prague, 1982.

[10] G. O. Sørensen. In M. J. S. Dewar, editor, *Topics in Current Chemistry*, **82**, page 97. Springer-Verlag, Berlin, 1979.

[11] B. T. Sutcliffe. In R. Carbo, editor, *Current Aspects of Quantum Chemistry*, **21**, page 9. Elsevier, Amsterdam, 1982.

[12] F. Webster, M.-J. Huang, and M. Wolfsberg. *J. Chem. Phys.*, **75**:2306–2313, 1981.

[13] B. Podolsky. *Phys. Rev.*, **32**:812, 1928.

[14] S. N. Yurchenko, W. Thiel, and P. Jensen. *J. Mol. Spectrosc.*, **245**:126–140, 2007.

[15] P. R. Bunker and P. Jensen. *Molecular Symmetry and Spectroscopy*. NRC Research Press, Ottawa, 2 edition, 1998.

[16] E. Mátyus, G. Czakó, and A. G. Császár. *J. Chem. Phys.*, **130**:134112, 2009.

[17] J. N. Murrell, S. Carter, S. C. Farantos, P. Huxley, and A. J. C. Varandas. *Molecular Potential Energy Surfaces*. Wiley, New York, 1984.

[18] D. M. Hirst. *Potential Energy Surfaces*. Taylor & Francis, London, 1985.

[19] D. G. Truhlar, R. Steckler, and M. S. Gordon. *Chem. Rev.*, **87**:217–236, 1987.

[20] C. M. Western. *Chem. Soc. Rev.*, **24**:299–307, 1995.

[21] T. Helgaker, P. Jørgensen, and J. Olsen. *Molecular Electronic-Structure Theory*. Wiley, Chichester, 2000.

[22] T. Helgaker, W. Klopper, and D. Tew. *Mol. Phys.*, **106**:2107, 2008.

[23] J. A. Pople, J. Binkley, and R. Seeger. *Int. J. Quant. Chem. Symp.*, **10**:11–19, 1976.

[24] T. D. Crawford and H. F. Schaefer III. *Rev. Comput. Chem.*, **14**:33–136, 1999.

[25] D. Feller. *J. Chem. Phys.*, **96**:6104, 1992.

[26] R. J. Gdanitz. *J. Chem. Phys.*, **113**:5145, 2000.

[27] A. Karton, P. R. Taylor, and J. M. L. Martin. *J. Chem. Phys.*, **127**:064104, 2007.

[28] P. Barletta, S. V. Shirin, N. F. Zobov, O. L. Polyansky, J. Tennyson, E. F. Valeev, and A. G. Császár. *J. Chem. Phys.*, **125**:204307, 2006.

[29] D. Feller and K. A. Peterson. *J. Chem. Phys.*, **131**:154306–154316, 2009.

[30] J. Noga, W. Kutzelnigg, and W. Klopper. *Chem. Phys. Lett.*, **199**:497, 1992.

[31] W. Klopper. *J. Chem. Phys.*, **102**:6168, 1995.

REFERENCES

[32] J. Rychlewski (Ed.). *Explicitly Correlated Wave Functions in Chemistry and Physics*. Kluwer Academic Publishers, Dordrecht, 2000.

[33] J. Yang and C. Hättig. *J. Chem. Phys.*, **130**:124101, 2009.

[34] G. Rauhut, G. Knizia, and H.-J. Werner. *J. Chem. Phys.*, **130**:054105, 2009.

[35] W. Kutzelnigg. *Mol. Phys*, **94**:65–71, 1998.

[36] K. Raghavachari, J. A. Pople, E. S. Replogle, and M. Head-Gordon. *J. Phys. Chem.*, **94**:5579–5586, 1990.

[37] D. R. Yarkony (Ed.). *Modern Electronic Structure Theory*. World Scientific, Singapore, 1995.

[38] R. J. Bartlett (Ed.). *Recent Advances in Coupled-Cluster Methods*. World Scientific, Singapore, 1995.

[39] A. G. Császár, W. D. Allen, and H. F. Schaefer III. *J. Phys. Chem.*, **108**:9751–9764, 1998.

[40] D. Prendergast, M. Nolan, C. Filippi, S. Fahy, and J. C. Greer. *J. Chem. Phys.*, **115**:1626, 2001.

[41] W. Kutzelnigg. *Theor. Chim. Acta*, **68**:445, 1985.

[42] W. Klopper and C. C. M. Samson. *J. Chem. Phys.*, **116**:6397, 2002.

[43] E. F. Valeev. *Chem. Phys. Lett.*, **395**:190, 2004.

[44] S. Ten-no. *J. Chem. Phys.*, **121**:117, 2004.

[45] S. Ten-no and F. R. Manby. *J. Chem. Phys.*, **119**:5358, 2003.

[46] H.-J. Werner and F. R. Manby. *J. Chem. Phys.*, **124**:054114, 2006.

[47] F. R. Manby, H.-J. Werner, T. B. Adler, and A. J. May. *J. Chem. Phys.*, **124**:094103, 2006.

[48] T. B. Adler, G. Knizia, and H.-J. Werner. *J. Chem. Phys.*, **127**:221106, 2007.

[49] G. Knizia, T. B. Adler, and H.-J. Werner. *J. Chem. Phys.*, **130**:054104, 2009.

[50] T. A. Ruden, T. Helgaker, P. Jørgensen, and J. Olsen. *J. Chem. Phys.*, **121**(12):5874–5884, 2004.

[51] D. P. Tew, W. Klopper, M. Heckert, and J. Gauss. *J. Phys. Chem. A*, **111**(44):11242–11248, 2007.

[52] C. Puzzarini, J. F. Stanton, and J. Gauss. *Int. Rev. Phys. Chem.*, **29**(2):273–367, 2010.

[53] W. Klopper, R. A. Bachorz, C. Hättig, and D. P. Tew. *Theor. Chem. Acc.*, **126**(5-6):289–304, 2010.

[54] K. Kahn, B. Kirtman, J. Noga, and S. Tenno. *J. Chem. Phys.*, **133**(7):74106–74118, 2010.

[55] A. Karton and J. M. L. Martin. *J. Chem. Phys.*, **133**(14):144102, 2010.

[56] O. L. Polyansky, A. G. Császár, S. V. Shirin, N. F. Zobov, P. Barletta, J. Tennyson, D. W. Schwenke, and P. J. Knowles. *Science*, **299**:539, 2003.

[57] T. Rajamäki, A. Miani, and L. Halonen. *J. Chem. Phys.*, **118**:6358, 2003.

[58] T. Rajamäki, A. Miani, and L. Halonen. *J. Chem. Phys.*, **118**:10929, 2003.

[59] X. Huang and T. J. Lee. *J. Chem. Phys.*, **129**:44312, 2008.

[60] X. Huang, D. W. Schwenke, and T. J. Lee. *J. Chem. Phys.*, **129**:214304, 2008.

[61] X. Huang, D. W. Schwenke, and T. J. Lee. *J. Chem. Phys.*, **134**:044320, 2011.

[62] P. R Bunker. *J. Mol. Spectrosc.*, **35**:306–313, 1970.

[63] W. Kutzelnigg. *Mol. Phys.*, **90**:909–916, 1997.

[64] N. C. Handy, Y. Yamaguchi, and H. F. Schaefer. *J. Chem. Phys.*, **84**:4481, 1986.

[65] E. F. Valeev and C. D. Scherrill. *J. Chem. Phys.*, **118**:3921, 2003.

[66] J. Gauss, A. Tajti, M. Kállay, J. F. Stanton, and P. G. Szalay. *J. Chem. Phys.*, **125**:144111, 2006.

[67] D. F. Mayers. *Proc. Roy. Soc. London, Ser. A*, **241**:93–109, 1957.

[68] I. P. Grant. *Adv. Phys.*, **19**:747–811, 1970.

[69] J. P. Desclaux. *Comp. Phys. Commun.*, **9**:31, 1975.

[70] L. L. Foldy and S. A. Wouthuysen. *Phys. Rev.*, **78**:29–36, 1950.

[71] M. Douglas and N. M. Kroll. *Ann. Phys.*, **82**:89, 1974.

[72] B. A. Hess. *Phys. Rev. A*, **33**:3742, 1986.

[73] A. J. Sadlej and J. G. Snijders. *Chem. Phys. Lett.*, **229**:435–438, 1994.

[74] A. Yachmenev, S. Yurchenko, T. Ribeyre, and W. Thiel. *J. Chem. Phys., submitted*, 2011.

[75] S. Carter and N. C. Handy. *J. Molec. Spectrocs.*, **192**(2):263–267, 1998.

[76] K. A. Peterson, T. B. Adler, and H.-J. Werner. *J. Chem. Phys.*, **128**(8):084102, 2008.

[77] T. Helgaker, W. Klopper, H. Koch, and J. Noga. *J. Chem. Phys.*, **106**:9639, 1997.

[78] D. J. Clouthier and D. A. Ramsay. *Ann. Rev. Phys. Chem.*, **34**:31–58, 1983.

[79] J.-M. Flaud, W. J. Lafferty, A. Perrin, Y. S. Kim, H. Beckers, and H. Willner. *J. Quant. Spectr. Rad. Trans.*, **109**(6):995–1003, 2008.

[80] A. Yachmenev, S. N. Yurchenko, P. Jensen, and W. Thiel. *J. Chem. Phys., submitted*, 2011.

[81] M. Staak, E. Gash, D. Venables, and A. Ruth. *J. Mol. Spectrosc.*, **229**:115, 2005.

[82] P. Pulay. *Mol. Phys.*, **17**:197, 1969.

[83] R. N. Zare. *Angular Momentum*. Wiley, New York, 1988.

[84] M. A. H. Smith, C. P. Rinsland, B. Fridovich, and K. Narahari Rao. In K. Narahari Rao, editor, *Molecular Spectroscopy: Modern research*, **III**, page 112. Academic Press, Orlando, 1985.

[85] K. M. T. Yamada, G. Winnewisser, and P. Jensen. *J. Mol. Struct.*, **695-696**:323–337, 2004.

[86] O. Baum, M. Koerber, O. Ricken, G. Winnewisser, S. N. Yurchenko, S. Schlemmer, K. M. T. Yamada, and T. F. Giesen. *J. Chem. Phys.*, **129**:224312, 2008.

[87] R. I Ovsyannikov, V. V. Melnikov, W. Thiel, P. Jensen, O. Baum, T. F. Giesen, and S. N. Yurchenko. *J. Chem. Phys.*, **129**:154314, 2008.

[88] S. N. Yurchenko, A. Yachmenev, W. Thiel, O. Baum, T. F. Giesen, V. V. Melnikov, and P. Jensen. *J. Mol. Spectrosc.*, **257**:57–65, 2009.

[89] A. Yachmenev, S. N. Yurchenko, P. Jensen, O. Baum, T. F. Giesen, and W. Thiel. *Phys. Chem. Chem. Phys.*, **12**:8387, 2010.

[90] O. Baum, T. F. Giesen, and S. Schlemmer. *J. Mol. Spectrosc.*, **247**:25–29, 2007.

[91] G. Winnewisser, F. Lewen, S. Thorwirth, M. Behnke, J. Hahn, J. Gauss, and E. Herbst. *Chem. Eur. J.*, **9**:5501–5510, 2003.

[92] H. Beckers, S. Esser, T. Metzroth, M. Behnke, H. Willner, J. Gauss, and J. Hahn. *Chem. Eur. J.*, **12**:832–844, 2006.

[93] A. Burrows, M. Marley, W. B. Hubbard, J. I. Lunine, T. Guillot, D. Saumon, R. Freedman, D. Sudarsky, and C. Sharp. *Astrophys. J.*, **491**:856, 1997.

[94] C. M. Sharp and A. Burrows. *Astrophys. J. Suppl.*, **168**:140, 2007.

[95] A. Burrows, D. Sudarsky, and J. I. Lenine. *Astrophys. J.*, **596**:587, 2003.

[96] D. Sudarsky, A. Burrows, and I. Hubeny. *Astrophys. J.*, **588**:1121, 2003.

[97] S. N. Yurchenko, R. J. Barber, A. Yachmenev, W. Thiel, P. Jensen, and J. Tennyson. *J. Phys. Chem. A*, **113**:11845, 2009.

[98] L. S. Rothman, I. E. Gordon, A. Barbe, D. Chris Benner, P. E. Bernath, M. Birk, V. Boudon, L. R. Brown, A. Campargue, J. P. Champion, K. Chance, L. H. Coudert, V. Dana, V. M. Devi, S. Fally, J. M. Flaud, R. R. Gamache, A. Goldman, D. Jacquemart, I. Kleiner, N. Lacome, W. J. Lafferty, J. Y. Mandin, S. T. Massie, S. N. Mikhailenko, C. E. Miller, N. Moazzen-Ahmadi, O. V. Naumenko, A. V. Nikitin, J. Orphal, V. I. Perevalov, A. Perrin, A. Predoi-Cross, C. P. Rinsland, M. Rotger, M. Simeckova, M. A. H. Smith, K. Sung, S. A. Tashkun, J. Tennyson, R. A. Toth, A. C. Vandaele, and J. Van Der Auwera. The HITRAN 2008 molecular spectroscopic database. *J. Quant. Spectrosc. Radiat. Transf.*, **110**:533, 2009.

[99] D. M. Bishop. In I. Prigogine and S. A. Rice, editors, *Advances in Chemical Physics*, **104**, page 1. John Wiley & Sons, Inc., 1998.

[100] H. Fukui, K. Miura, H. Matsuda, and T. Baba. *J. Chem. Phys.*, **97**:2299–2303, 1992.

[101] J. Gauss and D. Cremer. *Adv. Quant. Chem.*, **23**:205–299, 1992.

[102] J. E. Rice and N. C. Handy. *J. Chem. Phys.*, **94**:4959–4971, 1991.

[103] K. Sasagane, F. Aiga, and R. Itoh. *J. Chem. Phys.*, **99**:3738–3778, 1993.

[104] C. Moler and C. Van Loan. *SIAM Rev.*, **45**:3, 2003.

[105] D. M. Bishop and B. Kirtman. *J. Chem. Phys.*, **95**:2646, 1991.

[106] D. M. Bishop and B. Kirtman. *J. Chem. Phys.*, **97**:5255, 1992.

[107] D. M. Bishop, J. M. Luis, and B. Kirtman. *J. Chem. Phys.*, **108**:10013, 1998.

[108] O. Christiansen. *J. Chem. Phys.*, **122**:194105, 2005.

[109] O. Christiansen, J. Kongsted, M. J. Paterson, and J. M. Luis. *J. Chem. Phys.*, **125**:214309, 2006.

[110] L. D. Barron. *Molecular Light Scattering and Optical Activity*. Cambridge University Press, New York, 2 edition, 2004.

[111] A. J. Thorvaldsen, K. Ruud, and M. Jaszunski. *J. Phys. Chem. A*, **112**:11942, 2008.

[112] E. Santiago, M. A. Castro, T. L. Fonseca, and P. K. Mukherjee. *J. Chem. Phys.*, **128**:064310, 2008.

[113] O. Loboda, R. Zalesny, A. Avramopoulos, J. M. Luis, B. Kirtman, N. Tagmatarchis, H. Reis, and M. G. Papadopoulos. *J. Phys. Chem. A*, **113**:1159, 2009.

[114] J. Vaara, J. Lounila, K. Ruud, and T. Helgaker. *J. Chem. Phys.*, **109**:8388, 1998.

[115] T. A. Ruden, O. B. Lutnæs, and T. Helgaker. *J. Chem. Phys.*, **118**:9572, 2003.

[116] K. Ruud, P. O. Åstrand, and P. R. Taylor. *J. Chem. Phys.*, **112**:2668, 2000.

[117] R. D. Wigglesworth, W. T. Raynes, S. P. A. Sauer, and J. Oddershede. *Molec. Phys.*, **94**:851–862, 1998.

[118] J. Casanueva, J. San Fabián, E. Díez, and A. L. Esteban. *J. Mol. Struct.*, **565**:449–454, 2001.

[119] P. F. Provasi and S. P. A. Sauer. *Phys. Chem. Chem. Phys.*, **11**:3987–3995, 2009.

[120] A. Yachmenev, S. N. Yurchenko, Í. Paidarova, P. Jensen, W. Thiel, and S. P. A. Sauer. *J. Chem. Phys.*, **132**:114305, 2010.

[121] A. Yachmenev, S. N. Yurchenko, W. Thiel, and S. P. A. Sauer. *unpublished results*.

[122] S. P. A. Sauer. *J. Phys. B*, **30**:3773, 1997.

[123] T. Enevoldsen, J. Oddershede, and S. P. A. Sauer. *Theor. Chem. Acc.*, **100**:275, 1998.

[124] S. N. Yurchenko, J. J. Zheng, H. Lin, P. Jensen, and W. Thiel. *J. Chem. Phys.*, **123**:134308–14, 2005.

[125] J. Kowalewski and B. Roos. *Chem. Phys.*, **11**:123–128, 1975.

[126] P. Solomon and J. M Schulman. *J. Am. Chem. Soc.*, **99**:7776–7779, 1977.

[127] R. E. Wasylishen and J. O. Friedrich. *Can. J. Chem.*, **65**:2238, 1987.

[128] M. Alei, A. E. Florin, W. M. Litchman, and J. F. O'Brian. *J. Phys. Chem.*, **75**:932, 1971.

[129] R. M. Gester, H. C. Georg, S. Canuto, M. C. Caputo, and P. F. Provasi. *J. Phys. Chem. A*, **113**:14936, 2010.

A variationally computed T = 300 K line list for NH_3

S. N. Yurchenko, R. J. Barber, A. Yachmenev, W. Thiel, P. Jensen, J. Tennyson

J. Phys. Chem. A, **113**, 11845 (2009)

A Variationally Computed $T = 300$ K Line List for NH_3[†]

Sergei N. Yurchenko,[||] Robert J. Barber,[‡] Andrey Yachmenev,[¶] Walter Thiel,[¶] Per Jensen,[§] and Jonathan Tennyson*[,‡]

Institut für Physikalische Chemie und Elektrochemie, Technische Universität Dresden, D-01062 Dresden, Germany, Department of Physics and Astronomy, University College London, London WC1E 6BT, U.K., Max-Planck-Institut für Kohlenforschung, Kaiser-Wilhelm-Platz 1, D-45470 Mülheim an der Ruhr, Germany, and FBC, Theoretische Chemie, Bergische Universität, D-42097 Wuppertal, Germany

Received: March 31, 2009; Revised Manuscript Received: June 9, 2009

Calculations are reported on the rotation−vibration energy levels of ammonia with associated transition intensities. A potential energy surface obtained from coupled cluster CCSD(T) calculations and subsequent fitting against experimental data is further refined by a slight adjustment of the equilibrium geometry, which leads to a significant improvement in the rotational energy level structure. A new accurate ab initio dipole moment surface is determined at the frozen core CCSD(T)/aug-cc-pVQZ level. The calculation of an extensive ammonia line list necessitates a number of algorithmic improvements in the program TROVE that is used for the variational treatment of nuclear motion. Rotation−vibration transitions for $^{14}NH_3$ involving states with energies up to 12000 cm^{-1} and rotational quantum number $J = 20$ are calculated. This gives 3.25 million transitions between 184400 energy levels. Comparisons show good agreement with data in the HITRAN database but suggest that HITRAN is missing significant ammonia absorptions, particularly in the near-infrared.

1. Introduction

Polyatomic molecules with large-amplitude motions have complex spectra, and some of these are well-suited to probing the physical conditions of astrophysical objects. $^{14}NH_3$ (henceforth referred to as ammonia or NH_3) is the best tetratomic example of such a molecule. It is present in a wide range of astrophysical environments, and because of the richness and intensity of its spectrum, it is easily observed from Earth. The positions of many of the stronger NH_3 lines have been measured and the transitions assigned. Some of these lines are regularly used to determine temperatures and molecular number densities in distant objects.

For example, ammonia is the main nitrogen-containing molecule observable in the spectra of cometary coma, and its number density in this region is typically ∼0.5% of that of gaseous H_2O.[1] The atmosphere of Jupiter also contains ammonia,[2,3] and a notable feature during the impact of Comet Shoemaker−Levy 9 with Jupiter in 1994 was an enhancement in the concentration of NH_3 gas in the planet's stratosphere over the impact sites.[4] Ortho−para ratio measurements have been used to measure the nuclear spin temperature of gaseous NH_3 in the comas of C/2001 Neat,[5] 9P/Tempel 1,[6] and other comets.

The spectra of M- and L-type brown dwarfs are dominated by H_2O. CH_4 becomes more important in the atmospheres of later-type dwarfs, and by the mid T-type, NH_3 absorption is significant, particularly in the 10.5 μm region.[7,8] Modeling suggests that ammonia will be an even more important source of opacity in the yet-to-be discovered Y-dwarfs,[9] and consequently, it is anticipated that NH_3 absorption bands will be the signature of this new class of ultracool dwarf.

Ammonia is also predicted to be observable in the atmospheres of extrasolar giant planets (EGPs).[10] The reactions by which N_2 and H_2 are converted into ammonia in the atmospheres of brown dwarfs and planets are complex and outside of the scope of this paper. However, the equilibrium between N_2 and NH_3 favors NH_3 at lower temperatures as (to a lesser extent) do higher pressures. These temperature and pressure dependencies suggest that the outer atmospheres of EGPs at large orbital distances will contain significant quantities of ammonia.[10] Unlike CH_4, which is also predicted to be present in the outer atmospheres of EGPs and which has been inferred in HD 189733b,[11] NH_3 has not yet been detected in the atmosphere of any exoplanet.

One impediment to identifying and interpreting NH_3 features in the spectra of astrophysical objects is the fact that the vast majority of lines in the NH_3 spectrum are not known. The HITRAN database[12] encapsulates the knowledge of ammonia rotation−vibration spectra, yet about half of the transitions in the database remain unassigned, and as we demonstrate below, many important frequency regions are simply absent. For simulations of hot spectra, the situation is even worse, and it is not realistic to expect this situation to be resolved experimentally. Accurate first-principles quantum mechanical calculations would therefore appear to be the solution to this problem. However, since such calculations are extremely challenging, no line list currently exists that is complete or accurate enough to be used to model and interpret NH_3 data from any environment where the temperature is above 400 K.

Previous studies[13−20] have solved the nuclear motion problem for NH_3 on high-level ab initio coupled cluster potential energy surfaces and compared the resulting energy levels against experimental data. In some cases,[21,22] the corresponding wave functions for nuclear motion have been employed, in conjunction

[†] Part of the "Walter Thiel Festschrift".

* To whom correspondence should be addressed. E-mail: j.tennyson@ucl.ac.uk. Fax: +(44) 20 7679 7145.
[||] Technische Universität Dresden.
[‡] University College London.
[¶] Max-Planck-Institut für Kohlenforschung.
[§] Bergische Universität.

10.1021/jp9029425 CCC: $40.75
Published on Web 07/27/2009

with ab initio dipole moment surfaces, to calculate the intensity of some of the lines in a small number of rovibrational bands. However, in every case, such work has been performed within very constrained parameters. The energy levels computed are numbered in the hundreds, giving rise to a few thousand transitions between these levels. The present state of the work on the ammonia problem prior to the current paper has recently been summarized in more detail by Huang et al.[20] After submission of this paper, vibrational term values were reported[23] for NH_3 using an exact variational nuclear motion treatment in combination with one of our previously published potential energy surfaces.[19]

From an astrophysical perspective, the absence of a satisfactory ammonia line list means that it is not possible to model accurately the atmospheres of late brown dwarfs or the cooler classes of exoplanets, environments where ammonia is a major source of opacity. Our aim is to provide a 1500 K line list for NH_3 (henceforth referred to as the high-temperature line list) that will fill this important gap. There are three elements in the generation of an ab initio line list, accurate potential energy and dipole moment surfaces (PES and DMS, respectively) and a computer program to generate accurate wave functions and eigenvalue solutions for the nuclear Schrödinger equation and associated transition intensities. Here, we test these three elements to produce an actual ammonia line list, albeit one that is less complete and accurate than our eventual goal. However, this list will be useful for generating room-temperature spectra. It is this shorter NH_3 line list (subsequently referred to as a cool line list) that we present in the current paper, together with the implications of this work for the subsequent production of a high-temperature, or hot, line list.

We adopt a variational approach to solving the nuclear motion Schrödinger equation. Our initial calculations used the program XY3[21,24] to compute spectral line intensities for a number of pyramidal molecules[21,22,25,26] and to simulate their rovibrational bands, for example, in the NH_3 absorption spectra at 300 K.[22] The theoretical results were generally in very good agreement with experiment. However, these XY3 computations proved to be quite demanding in terms of both processor time and memory requirements, and it was clear that a more efficient computational tool would be required for the hot line list. Here, we therefore employ the recently developed program TROVE,[27] which implements a general variational approach for calculating the rovibrational spectra of small polyatomic molecules. We develop intensity and symmetrization tools specific to the NH_3 problem and introduce a number of algorithmic improvements that make the calculations more tractable. We present extracts from the cool ammonia line list produced using TROVE and discuss their accuracy and the associated computational costs.

2. The Ammonia Molecule and Its Quantum Numbers

Ammonia is a symmetric top molecule. Its equilibrium geometry is a regular pyramid; the three hydrogen nuclei are at the corners of an equilateral triangle, and the nitrogen nucleus is located on the axis of symmetry, which is perpendicular to the plane of the hydrogen nuclei. The molecule is capable of inversion, that is to say, the nitrogen nucleus is able to take up positions on either side of the plane of the hydrogen nuclei.

Nine parameters are required to define the internal rovibrational motion of a tetratomic molecule. There are six vibrational modes (of which, in the case of NH_3, two are doubly degenerate). The standard Herzberg convention[28] labels the symmetric stretch and symmetric bend as ν_1 and ν_2, respectively, and the asymmetric stretch and asymmetric bend as ν_3 and ν_4, respectively. These last two are degenerate and consequently carry additional quantum numbers in the form of the suffixes l_3 and l_4, respectively. The total angular momentum is J, and K is its projection on the molecular symmetry axis. The ninth quantum number Γ is the total symmetry in the molecular symmetry group[29] D_{3h}(M), to which NH_3 belongs. The rigorous selection rules which determine the allowed electric dipole transitions of NH_3 are $\Delta J = J' - J'' = 0, \pm 1$ ($J'' + J' \geq 1$), with symmetry selection rules $A_1' \not\leftrightarrow A_1''$, $A_2' \leftrightarrow A_2''$, and $E' \leftrightarrow E''$.

We use a unique "local mode" representation that is particularly suited to our choice of internal coordinates for the primitive 1D basis functions $\phi_{n_i}(\xi)$. Apart from the general quantum numbers associated with the molecular group symmetry Γ and total angular momentum J, our quantum numbers are Γ_{rot}, K, τ_{rot}, Γ_{vib}, n_1, n_2, n_3, n_4, n_5, and n_6. Here, J, K, and Γ are as above, and n_1, n_2, n_3 are stretching local mode quantum numbers[30] which correlate with the normal mode notation as $n_1 + n_2 + n_3 = \nu_1 + \nu_3$; n_4 and n_5 are deformational bending quanta, and n_6 is the inversion quantum number equivalent to $2\nu_2 + \tau_{inv}$, where ν_2 is the normal mode quantum number and $\tau_{inv} = n_6 \bmod 2$ is the inversion parity.[24] Finally, Γ_{rot} and Γ_{vib} are the rotational and vibrational symmetry in D_{3h}(M).

Our deformational band quantum numbers n_4 and n_5 are not the standard ν_4 and l_4 quantum numbers (because of the way the basis is constructed, they are more local mode); the correlation of ν_4 is straightforward, $n_4 + n_5 = \nu_4$, while assigning l_4 values is more tricky since there is no separate, identifiable vibrational symmetry to start with. This leads to the same ν_4 quantum numbers as an experimentalist would have assigned from looking at regularities in the spectrum. Therefore, most of the time, one obtains a labeling that makes it easy to communicate with experimentalists. When there is strong interaction between basis states, the labeling becomes problematic, but it is a question of whether such states really have defined ν_4 and l_4 quantum numbers.

In the approximation that the vibration and rotation motions are entirely separated, simple arguments can be used to rationalize the molecular spectra. In this case, the states having different values of K are not mixed, which gives rise to the concept of a good quantum number K[29] and approximate dipole selection rules $\Delta K = 0$ through the component of the electric dipole moment parallel to the symmetry axis. This, for example, results in rapid decay of the states with higher values of K (typically in less than $\sim$100 s) via $\Delta J = 1$ transitions, while states with lower K values, so-called metastable states, decay very slowly (typically having a lifetime of $\sim 10^9$ s) as they rely on small dipole moments perpendicular to the symmetry axis that arise due to the interaction of rotational and vibrational motions.

The vibrational ground state of ammonia is split into two states, the lowest-energy 0^- state lying 0.793 cm^{-1} above the lowest 0^+ state. Therefore, the (almost) uniformly spaced pure rotational lines (which are in the submillimeter and far-IR regions) have two components, separated by the energy difference between the 0^- and 0^+ states. Transitions can also occur between the + and − rotational states. These are governed by approximate selection rules, $\nu^+ \leftrightarrow \nu^-$, $\Delta J = 0$, and $\Delta K = 0$ ($K \neq 0$), and give rise to a large number of lines in the 1.25 cm^{-1} (24 GHz) region. These have been seen experimentally,[31,32] and observations at 23.6 GHz of the NH_3 $J = 1$, $K = 1$ inversion transition[33] resulted in ammonia being the first polyatomic molecule to be recorded in the interstellar medium.

Because of the different relative spin orientations of the three hydrogen nuclei, the NH_3 molecule has two distinct species,

ortho and para. *ortho*-NH_3 has all three hydrogen spins parallel, a consequence of which is that the angular momentum quantum number K can only take on values equal to $3n$, where n is an integer. *para*-NH_3 has one antiparallel hydrogen spin, which gives rise to all other values of K.

Our variational calculations do not use approximate quantum numbers or approximate selection rules. However we employ the concept of near quantum numbers,[29] which is based on the idea of assigning the calculated eigenfunctions according to the largest contribution in its expansion.[29] This is important for correlating the theoretical and experimental spectral information and is performed automatically.

3. The Dipole Moment Surface

The ab initio dipole moments employed in the present work were computed with the MOLPRO2000[34,35] package at the CCSD(T)/aug-cc-pVQZ level of theory (i.e., coupled cluster theory with all single and double substitutions[36] and a perturbative treatment of connected triple excitations[37] with the augmented correlation-consistent quadruple-ζ basis[38,39]) in the frozen core approximation. We refer to this method and basis set as the AQZfc level of theory. Dipole moments were computed in a numerical finite difference procedure with an added external dipole field of 0.005 au.

The ab initio dipole moment surface (DMS) was determined on a six-dimensional grid consisting of 4677 geometries with coordinates in the ranges of $0.9 \le r_1 \le r_2 \le r_3 \le 1.20$ Å and $80 \le \alpha_1, \alpha_2, \alpha_3 \le 120°$. Here, r_i is the instantaneous value of the internuclear distance N$-$H$_i$, $i = 1, 2, 3$, and the bond angles are given as $\alpha_1 = \angle(H_2NH_3)$, $\alpha_2 = \angle(H_1NH_3)$, and $\alpha_3 = \angle(H_1NH_2)$.

It is necessary to express the DMS analytically in terms of the internal coordinates of the molecule. Earlier work[22] used an extended version of the molecular bond (MB) representation. For NH_3, the dipole moment vector is given in the MB representation as

$$\bar{\boldsymbol{\mu}} = \bar{\mu}_1^{\mathrm{Bond}}\mathbf{e}_1 + \bar{\mu}_2^{\mathrm{Bond}}\mathbf{e}_2 + \bar{\mu}_3^{\mathrm{Bond}}\mathbf{e}_3 \tag{1}$$

Here, each unit vector $\mathbf{e}_i$ lies along one of the N$-$H$_i$ bonds

$$\mathbf{e}_i = \frac{\mathbf{r}_i - \mathbf{r}_4}{|\mathbf{r}_i - \mathbf{r}_4|} \tag{2}$$

with $\mathbf{r}_i$ as the position vector of nucleus i (the protons are labeled as 1, 2, 3, and the nitrogen nucleus is labeled 4). The functions $\bar{\mu}_i^{\mathrm{Bond}}$, $i = 1, 2, 3$, in eq 1 depend on the vibrational coordinates and are expressed[22] in terms of the dipole moment projections $(\bar{\mu}\cdot\mathbf{e}_j)$ onto the bonds of the molecule.

A disadvantage of the MB representation is the ambiguity at and near planar geometries when the three vectors $\mathbf{e}_i$ become linearly dependent, or nearly linearly dependent, and singularities appear in the determination of the $\bar{\mu}_i^{\mathrm{Bond}}$ functions. We have overcome this problem by reformulating the $\bar{\mu}_i^{\mathrm{Bond}}$ functions in terms of symmetry-adapted combinations of the MB projections $(\bar{\mu}\cdot\mathbf{e}_j)$

$$\bar{\mu}_{\mathrm{A}_1''}^{\mathrm{SMB}} = (\bar{\mu}\cdot\mathbf{e}_{\mathrm{N}}) \tag{3}$$

$$\bar{\mu}_{\mathrm{E}_a'}^{\mathrm{SMB}} = \frac{1}{\sqrt{6}}[2(\bar{\mu}\cdot\mathbf{e}_1) - (\bar{\mu}\cdot\mathbf{e}_2) - (\bar{\mu}\cdot\mathbf{e}_3)] \tag{4}$$

$$\bar{\mu}_{\mathrm{E}_b'}^{\mathrm{SMB}} = \frac{1}{\sqrt{2}}[(\bar{\mu}\cdot\mathbf{e}_2) - (\bar{\mu}\cdot\mathbf{e}_3)] \tag{5}$$

where we have introduced an additional reference MB vector $\mathbf{e}_{\mathrm{N}} = \mathbf{q}_{\mathrm{N}}/|\mathbf{q}_{\mathrm{N}}|$ defined by means of the trisector

$$\mathbf{q}_{\mathrm{N}} = (\mathbf{e}_1 \times \mathbf{e}_2) + (\mathbf{e}_2 \times \mathbf{e}_3) + (\mathbf{e}_3 \times \mathbf{e}_1) \tag{6}$$

This symmetrized molecular bond representation (denoted as SMB) has been used by Yurchenko et al.[22] to resolve a similar issue encountered in connection with representing the polarizability tensor of NH_3^+ in terms of analytical functions. The subscripts of the $\bar{\mu}_\Gamma^{\mathrm{SMB}}$ functions ($\Gamma = \mathrm{A}_1''$, E_a', E_b') in eqs 3$-$5 refer to irreducible representations[29] of D_{3h}(M); $\bar{\mu}_{\mathrm{A}_1''}^{\mathrm{SMB}}$ has A_1'' symmetry in D_{3h}(M), and $(\bar{\mu}_{\mathrm{E}_a'}^{\mathrm{SMB}}, \bar{\mu}_{\mathrm{E}_b'}^{\mathrm{SMB}})$ transform as the E′ irreducible representation. The symmetrized vectors

$$\mathbf{e}_{\mathrm{A}_1'} = \mathbf{e}_{\mathrm{N}} \tag{7}$$

$$\mathbf{e}_{\mathrm{E}_a''} = \frac{1}{\sqrt{6}}(2\mathbf{e}_1 - \mathbf{e}_2 - \mathbf{e}_3) \tag{8}$$

$$\mathbf{e}_{\mathrm{E}_b''} = \frac{1}{\sqrt{2}}(\mathbf{e}_2 - \mathbf{e}_3) \tag{9}$$

have A_1' and E″ symmetry in the same manner.

The dipole moment vector $\bar{\boldsymbol{\mu}}$ vanishes at symmetric, planar configurations of D_{3h} geometrical symmetry. Also, the $\bar{\mu}_{\mathrm{A}_1''}^{\mathrm{SMB}}$ component is antisymmetric under the inversion operation E^*[29] and vanishes at planarity, which leaves only two independent components of $\bar{\boldsymbol{\mu}}$ at planarity.

The advantage of having a DMS representation in terms of the projections $(\bar{\boldsymbol{\mu}}\cdot\mathbf{e}_j)$ is that it is body-fixed in the sense that it relates the dipole moment vector directly to the instantaneous positions of the nuclei (i.e., to the vectors $\mathbf{r}_i$). These projections are well-suited to being represented as analytical functions of the vibrational coordinates.[21] For intensity simulations, however, we require the Cartesian components $\bar{\mu}_\alpha$, $\alpha = x, y, z$, of the dipole moment along the molecule-fixed xyz axes. These can be obtained by inverting the linear equations

$$\bar{\mu}_\Gamma^{\mathrm{SMB}} = \sum_{\alpha=x,y,z} A_{\Gamma,\alpha}\bar{\mu}_\alpha \tag{10}$$

where $A_{\Gamma,\alpha}$ is the α-coordinate ($\alpha = x, y, z$) of the vector $\mathbf{e}_\Gamma$ ($\Gamma = \mathrm{A}_1'$, E_a, E_b) in eqs 7$-$9. When the molecule is planar, $\bar{\mu}_{\mathrm{A}_1''}^{\mathrm{SMB}}$ is zero, as is the corresponding right-hand side in eq 10. Thus, at planar configurations, the system of linear equations in $\bar{\mu}_\alpha$ contains two nontrivial equations only. At near-planar configurations, $\bar{\mu}_{\mathrm{A}_1''}^{\mathrm{SMB}}$ is not exactly zero and cannot be neglected, and therefore, eq 10 becomes near-linear-dependent. The symmetry-adapted representation of eqs 3$-$5 appears to be well-defined even for these geometries, at least in connection with the LAPACK solver DGELSS, which can handle such rank-deficient equation systems in a least-squares approach.[40]

In the SMB theory, the functions $\bar{\mu}_\Gamma^{\mathrm{SMB}}$ (henceforth referred to as $\bar{\mu}_\Gamma$) are now represented as expansions

$$\bar{\mu}_{A_1''} = \cos\bar{\rho}[\mu_0^{(A_1'')} + \sum_k \mu_k^{(A_1'')}\xi_k + \sum_{k,l}\mu_{k,l}^{(A_1'')}\xi_k\xi_l + \sum_{k,l,m}\mu_{k,l,m}^{(A_1'')}\xi_k\xi_l\xi_m + ...] \quad (11)$$

$$\bar{\mu}_{E_a'} = \mu_0^{(E_a')} + \sum_k \mu_k^{(E_a')}\xi_k + \sum_{k,l}\mu_{k,l}^{(E_a')}\xi_k\xi_l + \sum_{k,l,m}\mu_{k,l,m}^{(E_a')}\xi_k\xi_l\xi_m + ... \quad (12)$$

$$\bar{\mu}_{E_b'} = \mu_0^{(E_b')} + \sum_k \mu_k^{(E_b')}\xi_k + \sum_{k,l}\mu_{k,l}^{(E_b')}\xi_k\xi_l + \sum_{k,l,m}\mu_{k,l,m}^{(E_b')}\xi_k\xi_l\xi_m + ... \quad (13)$$

in terms of the variables

$$\xi_k = (r_k - r_e)\exp[-\beta(r_k - r_e)^2] \qquad k = 1, 2, 3 \quad (14)$$

which describe the stretching motion

$$\xi_4 = \frac{1}{\sqrt{6}}(2\alpha_1 - \alpha_2 - \alpha_3) \quad (15)$$

$$\xi_5 = \frac{1}{\sqrt{2}}(\alpha_2 - \alpha_3) \quad (16)$$

which describe the "deformation" bending, and

$$\xi_6 = \sin\bar{\rho}_e - \sin\bar{\rho} \quad (17)$$

which describes the out-of-plane bending motion. In eq 17

$$\sin\bar{\rho} = \frac{2}{\sqrt{3}}\sin[(\alpha_1 + \alpha_2 + \alpha_3)/6] \quad (18)$$

and $\sin(\bar{\rho}_e)$ is the equilibrium value of $\sin(\bar{\rho})$. The factor $\cos\bar{\rho} = \pm(1 - \sin^2\bar{\rho})^{1/2}$ in eq 11 ensures that the dipole moment function $\bar{\mu}_{A_1''}$ changes sign when $\bar{\rho} = 0, ..., \pi$ is changed to $\pi - \bar{\rho}$. Following Marquardt et al.,[41] we have introduced the factor $\exp[-\beta(r_k - r_e)^2]$ in eq 14 in order to keep the expansion in eq 13 from diverging at large r_i.

Because of the symmetry requirements, not all of the expansion parameters $\mu_{k,l,m,...}^{(\Gamma)}$ are independent. The two E′ symmetry components $\bar{\mu}_{E_a'}$ and $\bar{\mu}_{E_b'}$ have related parameter values, while $\bar{\mu}_{A_1''}$ is "independent" of them. Yurchenko et al.[21] define a set of independent parameters $\mu_{k,l,m,...}^{(\Gamma)}$ and derive symmetry relations determining the remaining parameter values; we use these results in the present work. The expansions in eqs 11−13 are truncated after the fourth-order, which corresponds to 109 independent parameters for $\bar{\mu}_{A_1''}$ and 146 independent parameters for $(\bar{\mu}_{E_a'}, \bar{\mu}_{E_b'})$. We were able to usefully vary 176 parameters $\mu_{k,l,m,...}^{(\Gamma)}$ in a least-squares fitting to the ab initio dipole moment data, and the resulting root-mean-square (rms) error was 0.00035 D. The parameters $\mu_{k,l,m,...}^{(\Gamma)}$ together with the Fortran routine for calculating the dipole moment components are provided as Supporting Information. The new ab initio dipole moment function will be referred to as AQZfc.

For the "equilibrium" dipole moment, we obtained $\mu_e = -\bar{\mu}_{A_1''} = 1.5148$ D, based on the ab initio equilibrium geometry of $r_1 = r_2 = r_3 = r_e = 1.0103$ Å and $\alpha_1 = \alpha_2 = \alpha_3 = \alpha_e = 106.72°$.[14] This is very similar to the ATZfc DMS value of 1.5198 D.[22] The experimental value for μ_e is usually quoted as (1.561 ± 0.005) D.[42] The large discrepancy between this experimental value and high-level ab initio results has been noted before.[43] It has been attributed to uncertainties in the conversion of the measured dipole moments of specific rovibrational states to an equilibrium value which may have led to an overestimate.[43] This view has been corroborated by a recent extensive ab initio study[44] which reported a best equilibrium dipole moment of 1.5157 D at the CCSD(T)/CBS+CV level (with complete basis set extrapolations and inclusion of core−valence corrections) and a zero-point-corrected ground-state dipole moment of 1.4764 D, close to the directly measured ground-state value of 1.471932(7) D.[45] Our AQZfc value for the vibrationally averaged ground-state dipole moment is 1.4638 D. This clearly indicates that the true equilibrium dipole moment of ammonia should be closer to 1.51 than 1.56 D.

4. The Intensity Simulations with TROVE

4.1. General Formulas. We require the line strengths (from which Einstein coefficients and absorption intensities can be computed) for all transitions between the rovibrational energy levels that satisfy the selection rules using the standard methodology.[46]

We consider a transition from an initial state i with rotation−vibration wave function $|\Phi_{rv}^{(i)}\rangle$ to a final state f with rotation−vibration wave function $|\Phi_{rv}^{(f)}\rangle$. The line strength[21,29,47] $S(f \leftarrow i)$ of the rotation−vibration transition f ← i (neglecting hyperfine structure) is obtained from[21]

$$S(f \leftarrow i) = g_{ns}\sum_{m_f,m_i}\sum_{A=X,Y,Z}|\langle\Phi_{rv}^{(f)}|\bar{\mu}_A|\Phi_{rv}^{(i)}\rangle|^2 \quad (19)$$

where g_{ns} is the nuclear spin statistical weight factor[29,47] and $\bar{\mu}_A$ is the electronically averaged component of the molecular dipole moment along the space-fixed axis $A = X$, Y, or Z. The quantum numbers m_i and m_f are the projections of the total angular momentum J, in units of $\hbar$, on the Z axis in the initial and final states, respectively.

Assuming the absorbing molecules to be in thermal equilibrium at an absolute temperature T, the absorption line intensity is determined by

$$I(f \leftarrow i) = \int_{Line}\varepsilon(\tilde{\nu})d\tilde{\nu} = \frac{8\pi^3 N_A\tilde{\nu}_{if}}{(4\pi\varepsilon_0)3hc}\frac{e^{-E_i/kT}}{Q} \times [1 - \exp(-hc\tilde{\nu}_{if}/kT)]S(f \leftarrow i) \quad (20)$$

Here $\varepsilon(\tilde{\nu})$ is the absorption coefficient,[29,47] $\tilde{\nu}$ is the absorption wavenumber, and eq 20 refers to the transition from the state i with energy E_i to the state f with energy E_f, where $hc\tilde{\nu}_{if} = E_f - E_i$. Q is the partition function defined as $Q = \sum_j g_j\exp(-E_j/kT)$, where g_j is the total degeneracy of the state with energy E_j and the sum runs over all energy levels of the molecule and the other symbols have their usual meanings. The total degeneracy g_j is given by $(2J + 1)$ times the nuclear spin degeneracy, which is 0, 12, 6, 0, 12, and 6 for A_1', A_2', E′, A_1'', A_2'', and E″ symmetries, respectively. Experimental values of

$I(\mathrm{f} \leftarrow \mathrm{i})$ are obtained by numerical integration of experimentally determined $\varepsilon(\tilde{\nu})$ values.

A detailed expression for the line strength of an individual rovibrational transition within an isolated electronic state of an XY_3 pyramidal molecule is given in eq 21 of Yurchenko et al.[21] Provided that the population of the lower (initial) state is defined by the Boltzmann distribution, it is sufficient to consider only transitions starting from the levels below $E_i^{max}/hc = 3200\ cm^{-1}$, which corresponds in eq 20 to Boltzmann factors $\exp(-E_i/kT) > 2 \times 10^{-7}$ at $T = 300$ K. For similar reasons, the range of the rotational excitations can be safely limited by $J = 20$. The frequency range selected is $0-8000\ cm^{-1}$; the total energy limit (and the maximal energy for the final state) E^{max}/hc is 12000 cm^{-1}.

4.2. Computational Details. We use a symmetry-adapted basis set in the variational nuclear motion calculations. The Hamiltonian matrix is factorized into size-independent blocks according to $D_{3h}(M)$ symmetry, A_1', A_2', E_a', E_b', A_1'', A_2'', E_a'', and E_b''. The A_1' and A_1'' matrices are irrelevant for NH_3 as the corresponding states have zero nuclear spin statistical weights. Only one member of the pairs E_a and E_b needs to be processed as they represent doubly degenerate solutions. This provides a considerable savings in computing time since the dimensions of the E matrices are approximately twice as large as those of the A_2 matrices.

The calculation of the matrix elements $\langle\Phi_{rv}^{(f)}|\bar{\mu}_A|\Phi_{rv}^{(i)}\rangle$ in eq 19 proved to be a bottleneck. Here, the wave functions $\Phi_{rv}^{(w)}$ are expressed as linear combinations of basis functions (see eq 65 of Yurchenko et al.[24])

$$|\Phi_{rv}^{(w)}\rangle = \sum_{VK\tau_{rot}} C_{VK\tau_{rot}}^{(w)} |J_w K m_w \tau_{rot}\rangle |V\rangle \qquad w = \mathrm{i\ or\ f} \tag{21}$$

$C_{VK\tau_{rot}}^{(w)}$ are expansion coefficients, $|J_w K m_w \tau_{rot}\rangle$ is a symmetrized rotational basis function, τ_{rot} (=0 or 1) determines the rotational parity as $(-1)^{\tau_{rot}}$, and $|V\rangle$ is a vibrational basis function. In order to speed up this part of the calculations, we applied a prescreening procedure to the expansion coefficients $C_{VK\tau_{rot}}^{(f)}$.[22] All terms with coefficients less than the threshold value of 10^{-16} were excluded from the integration.

A further speedup was achieved by optimizing the strategy for calculating the line strengths, eq 19. The evaluation of the dipole moment matrix elements $\langle\Phi_{rv}^{(f)}|\bar{\mu}_A|\Phi_{rv}^{(i)}\rangle$ can be thought of as a unitary transformation of the dipole moment matrix in the representation of primitive functions $|J_w K m_w \tau_{rot}\rangle|V\rangle$ to the representation of the eigenfunctions $\Phi_{rv}^{(w)}$ by means of eq 21. Such a transformation involves nested loops and results in N^4 operations, where N is the number of expansion terms in eq 21. It is known that it is more efficient ($\sim N^3$ operations) to perform this transformation in two steps. First, for a given lower state i, the following effective line strength is evaluated

$$S_{i,VK}^{A} = \langle\Phi_{rv}^{(i)}|\bar{\mu}_A|\phi_{VK}\rangle \tag{22}$$

where we introduce a short-hand notation ϕ_{VK} for the primitive basis function $|J_w K m_w \tau_{rot}\rangle|V\rangle$. Once all $S_{i,VK}$ are computed, in the second step, the line strength $S(\mathrm{f} \leftarrow \mathrm{i})$ is evaluated as

$$S(\mathrm{f} \leftarrow \mathrm{i}) = g_{ns} \sum_{m_i,m_f} \sum_{A=X,Y,Z} \left| \sum_{V,K} C_{VK\tau_{rot}}^{(f)} S_{i,VK}^{A} \right|^2 \tag{23}$$

The large number of transitions that had to be evaluated was another computational bottleneck. In order to take advantage of our multiprocessor computing facility, we performed the calculation in "batches" involving states with angular momentum quantum numbers J and $J + 1$. This is the smallest grouping that is consistent with the application of the total angular momentum selection rules. The eigenvalue solutions generated for each J were ordered by increasing energy. The program then computed the line strengths for all of the allowed transitions with $J \rightarrow J$ and $J \leftrightarrow J + 1$. The $J + 1 \rightarrow J + 1$ transitions were not computed in order to avoid double counting. This also meant that $\Delta J = J = 0$ transitions, which are not permitted by the selection rules, were not calculated.

4.3. The $J = 0$ Contraction. TROVE[27] uses a variational approach to solve the nuclear Schrödinger equation. It calculates rotation−vibration energies as the eigenvalues of matrix blocks obtained by constructing the matrix representation of the rotation−vibration Hamiltonian in terms of suitable basis functions. The TROVE basis set for $J > 0$ rovibrational calculations employs vibrational eigenfunctions (solutions to the $J = 0$ problem). We call this a $J = 0$ contraction. The vibrational matrix elements of the vibrational parts of the Hamiltonian, which are required for constructing the Hamiltonian matrix at any $J > 0$ are precalculated and stored to disk in order to save memory.

The procedure for constructing the $J = 0$ Hamiltonian is as follows. In the case of NH_3, a flexible molecule with a double-well potential surface, the primitive basis functions are formed from the one-dimensional (1D) vibrational functions $\phi_{n_1}(r_1^1)$, $\phi_{n_2}(r_2^1)$, $\phi_{n_3}(r_3^1)$, $\phi_{n_4}(\xi_4^1)$, $\phi_{n_5}(\xi_5^1)$, and $\phi_{n_6}(\bar{\rho})$. Here, n_i are corresponding principal quantum numbers, and the five coordinates $(r_1^1, r_2^1, r_3^1, \xi_4^1, \xi_5^1)$ are linearized versions[24] of the coordinates $(r_1, r_2, r_3, \xi_4, \xi_5)$ introduced in connection with eqs 14−17. The $\phi_{n_i}(\xi)$ functions are generated in numerical solutions to the corresponding 1D Schrödinger equations.[27] In the present TROVE calculations, the Hamiltonians (i.e., both the kinetic energy operator and the potential energy function) are expressed as expansions (of sixth and eighth order, respectively) around the nonrigid reference configuration[48] defined by the "umbrella" coordinate, $\bar{\rho}$. The errors introduced by these truncations have been discussed in detail for H_2S and CH_3^+ previously.[27] In the present case of NH_3, we have checked the convergence of the computed vibrational term values by performing additional calculations where the expansions of the kinetic energy operator and the potential energy functions were extended by two orders (to 8th and 10th order, respectively); the corresponding rms changes in the vibrational term values (see Table 2 below) amount to 0.05 and 0.04 cm^{-1}, respectively.

We could diagonalize the Hamiltonian matrix directly in the representation of the primitive functions ϕ_{n_i}, as described by Yurchenko et al.[27] However, this basis set is not symmetry-adapted, and therefore, it does not factorize the Hamiltonian matrix into smaller symmetry blocks. A more serious problem associated with basis functions that are not symmetry-adapted relates to the intensity simulation, where symmetry plays a crucial role through the nuclear spin statistical weights. Therefore, we prepare from ϕ_{n_i} a set of symmetry-adapted vibrational basis functions ϕ_i^Γ (the details of the symmetrization approach will be reported elsewhere) and diagonalize the vibrational Hamiltonian ($J = 0$) in this basis. Here, $\Gamma = A_1'$, A_2', E', A_1'', A_2'', and E''. The resulting eigenfunctions $\Psi_{J=0,i}^\Gamma$ are then multiplied by the rotational factor $|J,K,m,\tau_{rot}\rangle$ and then symmetrized again, which results in our final basis functions $\Psi_{J,K,i}^\Gamma$. These form the $J = 0$ contracted basis set mentioned above.

It is reasonable to assume that our $J = 0$ representation will reduce the nondiagonal elements of the Hamiltonian matrix, making the $J = 0$ contracted basis set more compact than the primitive basis functions from which it is constructed and hence simplifying the calculation of the Hamiltonian matrix.

The Hamiltonian operator can be written in the following general form[27]

$$H = H_{\text{vib}} + \frac{1}{2}\sum_{\alpha\beta} J_\alpha G_{\alpha\beta} J_\beta + \frac{1}{2}\sum_{\alpha\lambda} (p_\lambda G_{\lambda\alpha} + G_{\lambda\alpha} p_\lambda) J_\alpha \tag{24}$$

where J_α ($\alpha = x, y, z$) and p_λ are the rotational and vibrational momentum operators, respectively, and H_{vib} is a pure vibrational ($J = 0$) Hamiltonian

$$H_{\text{vib}} = \frac{1}{2}\sum_{\lambda\mu} p_\lambda G_{\lambda\mu} p_\mu + V + U \tag{25}$$

used in computing the $J = 0$ eigenfunctions. $G_{\alpha\beta}$, $G_{\lambda\alpha}$, and $G_{\lambda\mu}$ are the kinetic energy factors, U is the pseudopotential,[27] and V is the molecular potential energy function. The vibrational part H_{vib} is diagonal in our $J = 0$ basis set functions $\Psi^{\Gamma}_{J=0,\text{i}}$

$$\langle \Psi^{\Gamma}_{J=0,\text{i}} | H_{\text{vib}} | \Psi^{\Gamma}_{J=0,\text{i}'} \rangle = E^{\text{vib}}_{\text{i}} \delta_{\text{i},\text{i}'} \tag{26}$$

and thus its matrix elements do not need to be calculated. The evaluation of the Hamiltonian matrix can be further simplified by precomputing the matrix elements of all vibrational parts in eq 24

$$G^{\Gamma,\Gamma',\text{i},\text{i}'}_{\alpha,\beta} = \langle \Psi^{\Gamma}_{J=0,\text{i}} | G_{\alpha,\beta} | \Psi^{\Gamma'}_{J=0,\text{i}'} \rangle \tag{27}$$

$$G^{\Gamma,\Gamma',\text{i},\text{i}'}_{\lambda,\alpha} = \langle \Psi^{\Gamma}_{J=0,\text{i}} | p_\lambda G_{\lambda\alpha} + G_{\lambda\alpha} p_\lambda | \Psi^{\Gamma'}_{J=0,\text{i}'} \rangle \tag{28}$$

The left-hand side of these equations is given in the representation of the $J = 0$ contracted functions, while the right-hand side is computed in terms of the primitive basis functions ϕ^{Γ}_k, which appear in the variational expansions of $\Psi^{\Gamma}_{J=0,\text{i}}$. All terms with contribution from the expansion coefficient of less than 10^{-16} are excluded. This speeds up the computation of $G^{\Gamma,\Gamma',\text{i},\text{i}'}_{\alpha,\beta}$ and $G^{\Gamma,\Gamma',\text{i},\text{i}'}_{\lambda\alpha}$. Equations 27 and 28 represent the last stage where the bulky primitive basis set is utilized. The rest of the computation is performed in terms of the contracted basis functions $\Psi^{\Gamma}_{J,K,\text{i}}$. These are used to evaluate the Hamiltonian matrix for all nonzero values of J. The following equation illustrates the process

$$\begin{aligned}\langle \Psi^{\Gamma}_{J,K,\text{i}} | H | \Psi^{\Gamma}_{J,K',\text{i}'} \rangle = {} & E^{\text{vib}}_{\text{i}} \delta_{\text{i},\text{i}'} \delta_{K,K'} + \\ & \frac{1}{2}\sum_{\tau'_{\text{rot}},\tau''_{\text{rot}},\Gamma',\Gamma''} \sum_{\alpha\beta} \langle JKm\tau'_{\text{rot}} | J_\alpha J_\beta | JK'm\tau''_{\text{rot}} \rangle \otimes G^{\Gamma',\Gamma'',\text{i},\text{i}'}_{\alpha,\beta} + \\ & \frac{1}{2}\sum_{\tau'_{\text{rot}},\tau''_{\text{rot}},\Gamma',\Gamma''} \sum_{\lambda,\alpha} \langle JKm\tau'_{\text{rot}} | J_\alpha | JK'm\tau''_{\text{rot}} \rangle \otimes G^{\Gamma,\Gamma',\text{i},\text{i}'}_{\lambda,\alpha}\end{aligned} \tag{29}$$

where the sign $\otimes$ represents the reduction of the product $\Psi^{\Gamma}_{J=0,\text{i}}|J,K,\tau_{\text{rot}}\rangle$ to the irreducible representation $\Psi^{\Gamma}_{J,K,n}$. The computation of the matrix elements of H according to eq 29 in the $J = 0$ representation becomes very quick. Utilizing "diagonal" vibrational basis functions is in the spirit of the efficient discrete variable representation (DVR) applied in conjunction with the Gauss−Legendre technique.[49]

Along with the matrix elements $G^{\Gamma,\Gamma',\text{i},\text{i}'}_{\alpha,\beta}$ and $G^{\Gamma,\Gamma',\text{i},\text{i}'}_{\lambda,\alpha}$, we also compute the $J = 0$ contracted matrix elements of the dipole moment components $\bar{\mu}_\alpha$ appearing in eq 10. This simplifies the calculations of line strength (eq 19). We also utilize the fact that the matrix elements $\langle \Psi^{\Gamma}_{J,K,\text{i}} | H | \Psi^{\Gamma}_{J,K',\text{i}'} \rangle$ are nonzero only for $|K - K'| \leq 2$, and the Hamiltonian matrix can thus be arranged as a rectangular array, thereby reducing memory requirements, particularly in the case of high J values.

The routine selected for diagonalization depends on the size of the matrix. For less-demanding applications, we use the LAPACK[40] routine DSYEVR, which is fast and accepts restrictions for the eigenvalues to be found. For large matrices ($J > 12$ rovibrational calculations), we choose the iterative diagonalizer DSAUPD from the ARPACK package.[50]

5. Results

5.1. Refinement of the Potential Energy Surface. For the present study, we start from a published "spectroscopic" PES (referred to as PES-1) of NH_3.[19] This PES-1 surface was obtained by refining the CBS**-5 potential parameters of an ab initio CCSD(T)/CBS surface through least-squares fittings to the experimental vibrational band centers below 6100 cm^{-1} available in the literature.[19] The analytic form of PES-1 contains the ab initio AQZfc values of the equilibrium constants r_e and α_e of NH_3. Here, as a further refinement, we also optimize these equilibrium constants to improve the description of the interband rotational energy distribution. Toward this end, we first tested the following three choices: (I) the AQZfc ab initio values $r_e = 1.010313$ Å and $\alpha_e = 106.723°$;[19] (II) the most recent spectroscopic values of Huang et al.,[20] $r_e = 1.0107$ Å and $\alpha_e = 106.75°$; and (III) the semiempirical values $r_e = 1.01139$ Å and $\alpha_e = 107.17°$ obtained from a combination of theory and experiment.[51] The variationally computed rotational energies $E_{J,\nu=0}$ of NH_3 ($J \leq 5$) corresponding to (I), (II), and (III) are listed in Table 1, where we compare them to experimental rotational term values of NH_3.[52] The results for (II)[20] are close to the experiment. We further optimized the equilibrium constants (using the ab initio values (I) as starting parameters) through a nonlinear fit to the experimental values for $J \leq 5$ given in Table 1. One iteration was enough to reduce the rms deviation to 0.0020 cm^{-1} (see the last column of Table 1), with the equilibrium constants $r_e = 1.010772$ Å and $\alpha_e = 106.730°$, which further improve on the values (II).[20] The improvements by this adjustment are significant and reflect the decisive influence of the equilibrium constants on the molecular rotational spectrum. The results of the fit for PES-1 will depend on the approximations made in the TROVE calculations during the refinement; tests with different truncations for the kinetic energy operator, the potential energy function, and the vibrational basis set indicate that the corresponding uncertainties in the adjusted equilibrium bond length and angle are less than 10^{-5} Å and 0.001°, respectively.

We thus adopt these optimized values of the equilibrium constants. All results presented in the remainder of this article are based on the analytical potential energy function which contains the optimized potential parameters from PES-1[19] and the adjusted equilibrium constants (see above). This PES will be referred to as PES-2. We note that PES-1 is given as part of the Supporting Information of Yurchenko et al.,[19] and PES-2 is obtained from PES-1 by substituting the new equilibrium parameters given in footnote d of Table 1.

TABLE 1: Theoretical Rotational Term Values ($J \leq 5$) of NH_3 Computed with TROVE Using Different Equilibrium Structure Constants

states			term values (cm^{-1})				
J	K	τ_{rot}	obs.	obs.-I[a]	obs.-II[b]	obs.-III[c]	obs.-IV[d]
1	1	0	16.1730	−0.0158	−0.0022	0.0245	−0.0001
1	0	1	19.8899	−0.0190	−0.0060	−0.0423	−0.0002
2	2	0	44.7960	−0.0443	−0.0027	0.1404	−0.0003
2	1	0	55.9387	−0.0539	−0.0142	−0.0600	−0.0006
3	3	0	85.8616	−0.0854	−0.0016	0.3474	−0.0006
3	2	0	104.4221	−0.1015	−0.0208	0.0136	−0.0010
3	1	0	115.5366	−0.1111	−0.0322	−0.1861	−0.0013
3	0	1	119.2379	−0.1144	−0.0360	−0.2526	−0.0014
4	4	0	139.3581	−0.1391	0.0012	0.6454	−0.0008
4	3	0	165.3311	−0.1618	−0.0257	0.1781	−0.0016
4	2	0	183.8291	−0.1781	−0.0448	−0.1543	−0.0021
4	1	0	194.9063	−0.1878	−0.0562	−0.3533	−0.0024
5	5	0	205.2692	−0.2053	0.0057	1.0341	−0.0010
5	4	0	238.6527	−0.2348	−0.0291	0.4331	−0.0022
5	3	0	264.5166	−0.2579	−0.0559	−0.0317	−0.0030
5	2	0	282.9372	−0.2744	−0.0749	−0.3625	−0.0035
5	1	0	293.9683	−0.2843	−0.0862	−0.5604	−0.0038
5	0	1	297.6418	−0.2876	−0.0900	−0.6263	−0.0039

[a] PES-1: Using $r_e = 1.010313$ Å and $\alpha_e = 106.723°$.[19] [b] Obtained using $r_e = 1.0107$ Å and $\alpha_e = 106.75°$.[20] [c] Obtained using $r_e = 1.01139$ Å and $\alpha_e = 107.17°$.[51] [d] PES-2: Obtained using $r_e = 1.010772$ Å and $\alpha_e = 106.730°$ (this work).

To illustrate the effect of this refinement, we show part of the rotational spectrum of NH_3 as a "stick" diagram on the left panel of Figure 1. The upper half represents the experimental lines as collected in the HITRAN 2004 database,[12] while the lower half gives the theoretical transitions computed with the TROVE approach. Lines computed with the refined equilibrium structure (PES-2, solid sticks) show excellent agreement with experiment, while the lines obtained utilizing the ab initio values (PES-1, dashed sticks) are skewed toward larger wavenumbers.

5.2. Basis Set Convergence and Empirical Adjustment of the Vibrational Band Centers. The size of the Hamiltonian matrix is an important factor that influences the accuracy with which high rovibrational states can be computed, and consequently, it is important to derive by empirical methods the smallest basis set that is consistent with the required eigenvalue accuracy (that is to say, the optimum size for "convergence").

TROVE employs polyad number truncation[24,27] to control the size of the vibrational basis set, with the polyad number P given by

$$P = 2(n_1 + n_2 + n_3) + n_4 + n_5 + \frac{n_6}{2} \qquad (30)$$

where n_i are the quantum numbers connected with the primitive functions ϕ_{n_i}. That is, we include in the primitive basis set only those functions ϕ_n for which $P \leq P_{max}$. We find that in order to achieve convergence to within 0.1 cm^{-1}, P_{max} must be in the range of 14−16.

A full rovibrational calculation with truncation at $P_{max} = 16$ is very expensive, and it is thus desirable to devise a procedure where these calculations can be done with a smaller basis set (e.g., truncated at $P_{max} = 12$) without much loss of accuracy. We recall that the vibrational part of the Hamiltonian is diagonal in the $J = 0$ basis set and that the Hamiltonian matrix in eq 29 is formed using the vibrational energies E_i^{vib} obtained as eigensolutions of eq 26. When constructing the full Hamiltonian matrix in a given basis, we can thus substitute these energies with more converged values E_i^{vib} that have been precomputed using a larger $J = 0$ basis with a higher P_{max} value. More specifically, we compute the rotational part of the Hamiltonian matrix in eq 29 using the small $P_{max} = 12$ basis set $\Psi^{\Gamma}_{J,K,n}$, while the vibrational part (given by the diagonal terms E_i^{vib}) is evaluated with the large $P_{max} = 16$ vibrational basis set. This procedure leads to reasonable convergence, that is, to results very close to those from the full $P_{max} = 16$ treatment. The reason why this approach works well is related to the separation between the vibrational and rotational degrees of freedom achieved through the $J = 0$ contraction. The vibrational motion is most difficult to converge, and this can only be achieved by using the extended $P_{max} = 16$ vibrational basis set. The Coriolis interaction is less demanding because of the use of the Eckart−Sayvetz coordinate system[27,53,54] in TROVE, and the required degree of accuracy can thus be reached with the much smaller $P_{max} = 12$ basis set in the rotational part.

The vibrational term values could be converged even more tightly by extrapolating the $P_{max} = 12$, 14, and 16 values of E_i^{vib} to the complete vibrational basis set limit.[55] However, this is not considered necessary for the purpose of generating a line list since the corrections from such an extrapolation will be small compared with the inherent errors in the term values that are caused by the imperfection of the underlying potential energy surface. Instead, if we aim for higher accuracy in a pragmatic manner, we can resort to a more empirical approach where the theoretical E_i^{vib} term values in eq 29 are replaced by accurate experimental term values, $E^{exp}_{J=0,i}$, whenever these are available in the published literature. In this case, we adjust the vibrational band centers "by hand", and by doing so, we shift the rotational energy structure toward better agreement with experiment. This procedure can be regarded as an empirical basis set correction scheme and will be denoted as the EBSC scheme.

Table 2 lists the vibrational band centers of ammonia up to 7000 cm^{-1}, as derived from experimental data and from variational calculations ($J = 0$). On the theoretical side, we quote the recent results of Huang et al.,[20] which are based on a high-level coupled cluster potential energy surface (with various corrections) that has been carefully refined against the most reliable $J = 0-2$ transitions in the HITRAN 2004 database below 5300 cm^{-1}. These results[20] are in excellent agreement with experiment (rms error of 0.023 cm^{-1} for 13 HITRAN 2004 bands below $J = 2$). The corresponding analytical potential function (with 3393 parameters) is not available to us and can thus not be used for TROVE calculations.

Our own previous refinement[19] that led to the PES-1 surface (see above) yielded rms errors of 0.4 (3.0) cm^{-1} for the vibrational band centers below 6100 (10300) cm^{-1} in variational XY3 calculations where the kinetic energy and potential energy expansions were truncated at sixth order. In the present work, we truncate the potential energy expansions at eighth order and use the PES-2 surface (see above). Both of these changes will have the effect of "detuning" the previous refinement.[19] This can be seen in the last two columns of Table 2, which list the current TROVE results for PES-2 using $P_{max} = 12$ and 16. The deviations from experiment are usually in the range of 0−3 cm^{-1}, and the rms errors amount to 1.8 and 2.4 cm^{-1}, respectively (for term values below 6100 cm^{-1} excluding those at 3462 and 4055 cm^{-1}, which are not precisely known, see Yurchenko et al.).[19] To achieve higher accuracy for the vibrational band centers, another more thorough refinement of our PES would be needed, similar in spirit to that of Huang et al.[20] A pragmatic alternative is the EBSC scheme outlined above, which, by construction, will give exact agreement with the

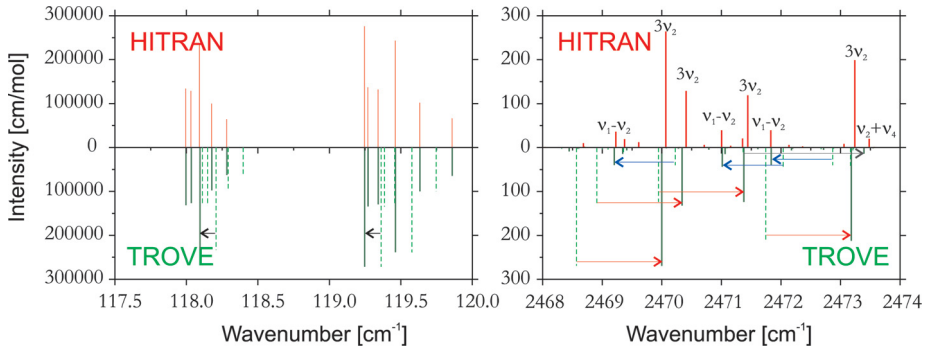

Figure 1. Comparison of the simulated and observed (HITRAN) spectra of the rotational (left panel) and the $3\nu_2/\nu_2 + \nu_4/\nu_1 - \nu_2$ band system (right panel) represented as stick diagrams. The lower plots show the effect of the empirical adjustments of the equilibrium constants (left panel) and the band centers (right panel, EBSC scheme) as a shift from the dashed to solid lines (see text).

TABLE 2: Vibrational Band Centers (cm^{-1}) of $^{14}NH_3$ Derived from Experimental Data and from Variational Calculations

Γ	state	ref.	obs.[a]	Huang et al.[b20]	$P_{max} = 12$[c]	$P_{max} = 16$[d]
A′	ν_2^+	52	932.43[e]	932.38	931.67	931.64
	$2\nu_2^+$	67	1597.47[e]	1597.44	1595.94	1595.88
	$3\nu_2^+$	68	2384.15[e]	1597.44	2382.71	2382.63
	$2\nu_4^{0,+}$	69	3216.10[e]	3215.90	3213.90	3213.52
	ν_1^+	69	3336.11[e]	3336.09	3335.63	3335.60
	$4\nu_2^+$	70	3462.00	3462.26	3461.10	3461.00
	$(\nu_2 + 2\nu_4^0)^+$	71	4115.62[e]	4115.83	4112.50	4110.94
	$(\nu_1 + \nu_2)^+$	71	4294.53[e]	4294.48	4293.46	4293.32
	$(\nu_1 + 2\nu_4)^+$	72	6520.00	6519.78	6516.34	6515.16
	$2\nu_1^+$	72	6606.00	6605.03	6600.89	6600.40
	$2\nu_3^+$	65	6795.96	6797.38	6794.60	6794.24
E′	ν_4^+	12	1626.27[e]	1626.25	1625.09	1625.02
	$(\nu_2 + \nu_4)^+$	69	2540.53[e]	2540.49	2538.50	2538.29
	$2\nu_4^{\pm 2,+}$	12	3240.16[e]	3240.14	3237.71	3237.44
	ν_3^+	12	3443.68[e]	3443.60	3443.94	3443.90
	$(\nu_2 + 2\nu_4^{\pm 2})^+$	71	4135.94[e]	4136.09	4132.67	4131.56
	$(\nu_2 + \nu_3)^+$	12	4416.92[e]	4416.90	4416.40	4416.23
	$(\nu_1 + \nu_4)^+$	12	4955.76[e]	4955.70	4953.56	4953.26
	$(\nu_3 + \nu_4)^+$	12	5052.63[e]	5052.59	5051.59	5051.21
	$(\nu_2 + \nu_3 + \nu_4)^+$	72	6012.90[e]	6012.73	6009.52	6008.64
	$(\nu_1 + 2\nu_4^{\pm 2})^+$	66	6556.42[e]	6556.66	6552.20	6551.18
	$(\nu_1 + \nu_3)^+$	66	6608.15	6609.73	6605.36	6604.32
	$(\nu_3 + 2\nu_4^2)^+$	63	6678.36	6678.48	6670.05	6669.47
	$2\nu_3^{2,+}$	72	6850.20	6850.25	6850.17	6849.94
A″	0^-	12	0.79[e]	0.80	0.81	0.80
	ν_2^-	73	968.12[e]	968.12	967.48	967.45
	$2\nu_2^-$	67	1882.18[e]	1882.14	1880.99	1880.91
	$3\nu_2^-$	68	2895.52[e]	2895.44	2894.11	2894.00
	$2\nu_4^{0,-}$	12	3217.58[e]	3217.53	3216.00	3215.27
	ν_1^-	69	3337.11[e]	3337.07	3335.63	3336.66
	$4\nu_2^-$	74	4055.00	4061.40	4060.46	4060.22
	$(\nu_1 + 2\nu_4^0)^-$	71	4173.25[e]	4173.13	4171.18	4169.58
	$(\nu_1 + \nu_2)^-$	12	4320.04[e]	4319.97	4319.16	4318.98
	$2\nu_3^{0,-}$	65	6795.46	6795.96	6793.42	6792.84
E″	ν_4^-	12	1627.37[e]	1627.35	1626.23	1626.13
	$(\nu_2 + \nu_4)^-$	12	2586.13[e]	2586.09	2584.45	2584.14
	$2\nu_4^{\pm 2,-}$	69	3241.62[e]	3241.57	3239.53	3238.98
	ν_3^-	12	3443.98[e]	3443.96	3444.36	3444.26
	$(\nu_2 + 2\nu_4^{\pm 2})^-$	71	4193.14[e]	4193.14	4190.60	4189.45
	$(\nu_2 + \nu_3)^-$	71	4435.45[e]	4435.41	4435.12	4434.90
	$(\nu_1 + \nu_4)^-$	12	4956.91[e]	4956.85	4954.94	4954.53
	$(\nu_3 + \nu_4)^-$	72	5053.24[e]	5053.19	5052.32	5051.82
	$(\nu_2 + \nu_3 + \nu_4)^-$	72	6037.12[e]	6036.33	6034.50	6032.98
	$(\nu_1 + 2\nu_4^2)^-$	66	6557.93[e]	6558.17	6554.94	6552.94
	$(\nu_1 + \nu_3)^-$	66	6609.72	6610.66	6607.78	6605.61
	$(\nu_3 + 2\nu_4^2)^-$	63	6679.15[e]	6679.17	6671.62	6670.38
	$2\nu_3^{2,-}$	72	6850.70[e]	6850.65	6850.93	6850.38

[a] Derived from experimental data. [b] $J = 0$ band centers of Huang et al.[20] computed using their refined PES. [c] Computed using the $P_{max} = 12$ basis set in conjunction with PES-2. [d] Computed using the $P_{max} = 16$ basis set in conjunction with PES-2. [e] Experimental values of band centers $E^{exp}_{J=0,i}$ used in the present EBSC scheme (see text).

available experimental band centers in $J = 0$ calculations. When generating a line list using the EBSC scheme, the imperfection of the chosen PES will thus enter only through the computed band centers of bands where reliable experimental data are missing and through the rovibrational couplings that affect the full rovibrational calculations. Another source of error is the limited accuracy of the available experimental data, for example, in the HITRAN database, and care must be exercised in selecting only reliable such data.[20]

For the remainder of this paper, we adopt the EBSC scheme in combination with PES-2. The vibrational term values used in this scheme are marked in Table 2; 37 of them are taken from experiment, and the 4401 remaining ones from the $P_{max} = 16$ calculations. The incorporation of experimental information in the EBSC scheme is obviously a departure from a purely ab initio approach, which is considered to be justified by the gain in accuracy that can be achieved when computing an extensive rovibrational line list.

As an illustration, we show in Figure 1 (right panel) a part of the simulated cool spectrum of ammonia (stick diagram) for a number of selected transitions from the band system $3\nu_2/2\nu_4/\nu_1 - \nu_2$. As before, the upper panel (HITRAN) visualizes the experimental data. The lower panel represents the $P_{max} = 12$ (dashed lines) and EBSC (solid lines) transitions, that is, spectra computed without and with the empirical adjustment of E_i^{vib} to the experimental values. All three bands that appear in the given frequency window experience different shifts of their centers such that the deviations between the HITRAN and EBSC lines drop from typically 1−2 to less than 0.1 cm^{-1}. Of course, the solid lines from the top and bottom parts should ideally coincide; the remaining slight misalignment between them is due to the limitations of the EBSC scheme that have been outlined above.

5.3. Vibrational Transition Moments. The vibrational transition moments are defined as

$$\mu_{fi} = \sqrt{\sum_{\alpha=x,y,z} \left| \langle \Psi^{\Gamma}_{J=0,f} | \bar{\mu}_{\alpha} | \Psi^{\Gamma}_{J=0,i} \rangle \right|^2} \qquad (31)$$

in terms of the vibrational wave functions $\Psi^{\Gamma}_{J=0,w}$, w = i or f, and the dipole components $\bar{\mu}_{\alpha}$ oriented along the Eckart axes.[61] For calculating the vibrational wave functions, we use the EBSC scheme with the PES-2 surface and the basis set truncated at polyad number $P_{max} = 12$. The electronically averaged dipole moment functions $\bar{\mu}_{\alpha}$ in eq 31 are derived from the AQZfc ab initio dipole moment surface by solving the linear system eq 10 as discussed above. We have computed the transition moments in eq 31 for all vibrational transitions that are relevant for the $T = 300$ K absorption spectrum. In Table 3, we list a number of selected transition moments for which experimental information is available in the literature.[42,56−60] The agreement with experiment is good.

TABLE 3: Band Centers ν_{fi} and Vibrational Transition Moments μ_{fi} for NH_3; Transitions Originating in the Vibrational Ground State

states		ν_{fi}/cm^{-1}		μ_{fi}/D		
f	i	obs.[a]	obs.[b]	ref.[c]	ATZfc[d]	AQZfc[e]
0^-	0^+	0.79	1.47193(1)	45	1.4564	1.4638
ν_2^+	0^-	931.64	0.248(7)	75	0.2445	0.2467
ν_2^-	0^+	968.12	0.236(4)	75	0.2347	0.2366
$2\nu_2^+$	0^-	1596.68	0.02036(25)	67	0.0202	0.0210
ν_4^+	0^+	1626.27	0.08408(34)	67	0.0828	0.0841
ν_4^-	0^-	1626.58	0.08408(34)	67	0.0827	0.0840
$2\nu_2^-$	0^+	1882.18	0.003256(35)	67	0.0026	0.0030
$3\nu_2^+$	0^-	2383.35	0.00496(13)	68	0.0054	0.0053
$(\nu_2 + \nu_4)^+$	0^+	2540.53	0.002358(36)	68	0.0091	0.0085
$(\nu_2 + \nu_4)^-$	0^-	2894.73	0.002182(82)	68	0.0094	0.0089
$3\nu_2^-$	0^+	2895.52	0.002856(40)	68	0.0027	0.0027
$2\nu_4^{0,+}$	0^-	3215.31	0.00920(6)[f]	70	0.0073	0.0064
$2\nu_2^{0,-}$	0^+	3217.58	0.00920(6)[f]	70	0.0074	0.0066
$2\nu_4^{\pm 2,+}$	0^+	3240.16	0.00920(6)[f]	70	0.0091	0.0089
$2\nu_4^{\pm 2,-}$	0^-	3240.82	0.00920(6)[f]	70	0.0090	0.0088
ν_1^+	0^-	3335.31	0.0262(1)	70	0.0269	0.0260
ν_1^-	0^+	3337.11	0.0262(1)	70	0.0270	0.0261
ν_3^-	0^-	3443.19	0.0182(1)	70	0.0180	0.0201
ν_3^+	0^+	3443.63	0.0182(1)	70	0.0181	0.0202
$(\nu_1 + \nu_2)^+$	0^-	4293.74	0.0079	76	0.0087	0.0088
$(\nu_1 + \nu_2)^-$	0^+	4320.04	0.0079	76	0.0083	0.0084
$(\nu_2 + \nu_3)^+$	0^+	4416.92	0.0206	76	0.0246	0.0250
$(\nu_2 + \nu_3)^-$	0^-	4434.65	0.0206	76	0.0244	0.0248

[a] Experimental data taken from Table 2. [b] Experimental uncertainties given in parentheses, in units of the last digit quoted. [c] Reference for the experimental transition moment value. [d] Taken from Yurchenko et al.,[19] XY3 calculation, PES CBS**5, ATZfc DMS. [e] Present work, TROVE calculation, EBSC scheme, PES-2, AQZfc DMS. [f] The experimental value corresponds to the total $2\nu_4^{\pm}$ transition moment and can thus not be directly compared to the separate theoretical values for $2\nu_4^{0,\pm}$ and $2\nu_4^{\pm 2,\pm}$, respectively.

The present AQZfc theoretical values are found to be very similar to the previous ATZfc results[22] (also listed in Table 3) obtained using the XY3 approach.[24] The upgrade of the ab initio dipole moment surface from CCSD(T)/aug-cc-pVTZ to CCSD(T)/aug-cc-pVQZ does not significantly affect the values of μ_{fi}, which implies that the ab initio DMS is essentially converged at this level. The complete list of theoretical transition moments is given as Supporting Information.

5.4. Intensity Simulations. In order to simulate absorption spectra at a given T and within a particular wavenumber range, the upper and lower energies and the Einstein coefficients A(f ← i) (or the line strengths) of all transitions in this range must be known; in practice, only the transitions above a certain minimum intensity are included. The simplest way to present the spectral data is a stick diagram where the height gives the integrated absorption coefficient from eq 20. In this section, we report such simulations for the NH_3 absorption bands covering the frequency range of 0−8000 cm^{-1}. The line strengths entering eq 20 are computed from eq 19 with the spin statistical weights g_{ns} from Table 2 of Yurchenko et al.[21] The simulations are carried out using the PES-2 surface and the AQZfc DMS. We used a value of 1762 for the partition function, Q, at 300 K, which was obtained by summing over all variational term values below 8000 cm^{-1}. With the limits defined above, we computed 4 943 196 transitions, of which we selected 3 249 988 with intensities >10^{-4} cm mol^{-1}.

Figure 2 shows the simulated ($T = 300$ K) absorption spectrum (TROVE) and experimental (HITRAN) absorption spectrum of NH_3 for the whole simulation range. The logarithmic scale allows almost all transitions to be displayed and

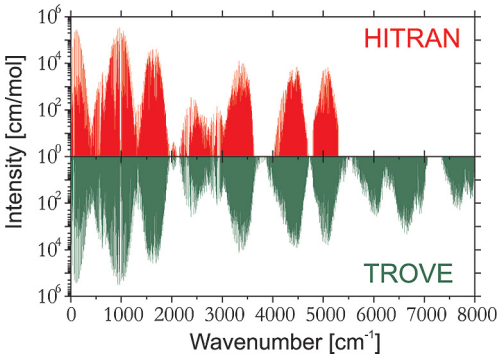

Figure 2. Overview of the simulated absorption ($T = 300$ K) spectrum (TROVE) of NH_3 compared to experiment (HITRAN).

reveals the gaps and limitations of the HITRAN 2004 database. Our intensities based on the ab initio DMS are in very good qualitative agreement with experiment. This can be better appreciated in Figure 3, where the first six band systems (0−300, 700−1200, 1400−1900, 2200−2800, 3100−3600, and 4150−4650 cm^{-1}) are shown in more detail. The largest deviation from the HITRAN 2004 intensities are observed around 4400 cm^{-1}. In general, the computed and experimental (HITRAN) rotational band intensities agree very well (see Figures 1 and 3). However, we hope that the accuracy of our theoretical spectrum will enable experimentalists to assign so-far unidentified transitions in these and other regions. It should also be noted that the region around 1.5 μm (near 6500 cm^{-1}) that is not covered in HITRAN 2004 has been the subject of a number of recent experimental studies.[62−66]

Figure 4 takes a closer look at the simulated spectrum by comparing the theoretical intensities with the available experimental data[12] in two selected wavenumber windows, 1622−1632 ($2\nu_2/\nu_4$ system) and 3333−3337 cm^{-1} ($\nu_1/4\nu_2/\nu_3/2\nu_4$ system). Not all of the experimentally known band centers have been accurately determined, and many are unknown. This is the largest source of error in our simulations with the EBSC scheme, which employs theoretical vibrational band centers in such cases (see above). The accuracy of these theoretical values for the PES-2 surface may generally not be sufficient to properly position the closely lying dark states and to capture their effects on the rovibrational structure.

As a further illustration of the quality of our simulations, we show in Figure 5 a synthetic spectrum convolved with a Gaussian profile (HWHM = 0.01 cm^{-1}) together with the observed spectrum (Kitt peak data) of NH_3 at 0.35 Torr and 295 K. It is obvious that the two spectra match very well.

Our complete cool NH_3 line list is given as Supporting Information. It details the transition energies, line strengths, and Einstein coefficients A(f ← i) and also includes the absorption intensities estimated for $T = 300$ K. A Fortran program is provided to generate synthetic spectra using this line list at other specified temperatures. However, such spectra will become increasingly inaccurate as the temperature is increased.

6. Conclusion

We have presented calculated spectra for ammonia covering a large part of the infrared region. Detailed comparisons with observed room-temperature spectra show excellent agreement for the position and intensity of the transitions. These comparisons also indicate that the HITRAN database[12] is rather incomplete in its coverage of the infrared spectrum of ammonia. A number of other problems concerning the HITRAN data for

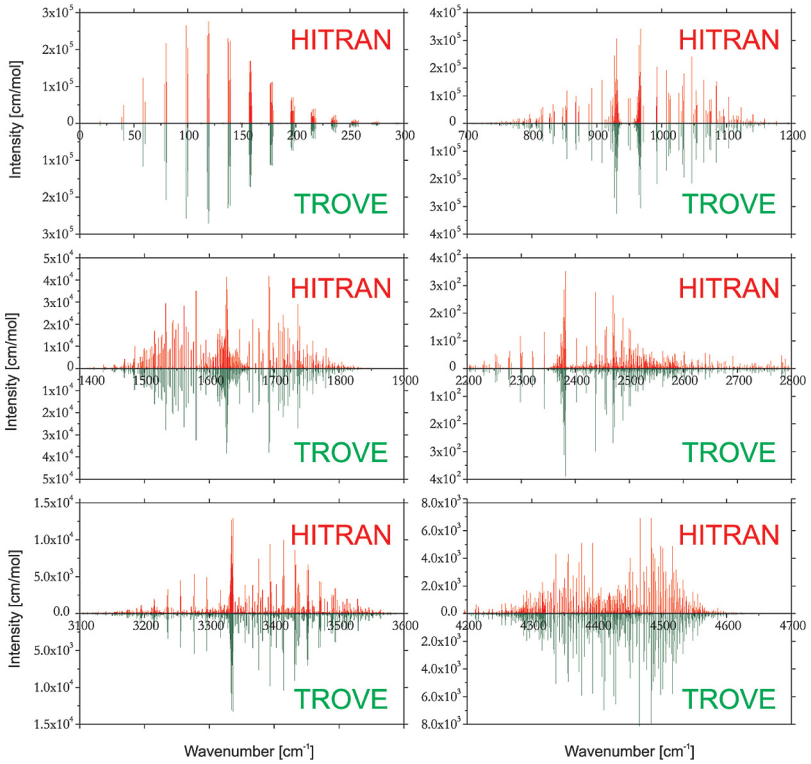

Figure 3. Comparison of the simulated (TROVE) and observed (HITRAN) spectra of NH_3 at $T = 300$ K for several low-lying band systems.

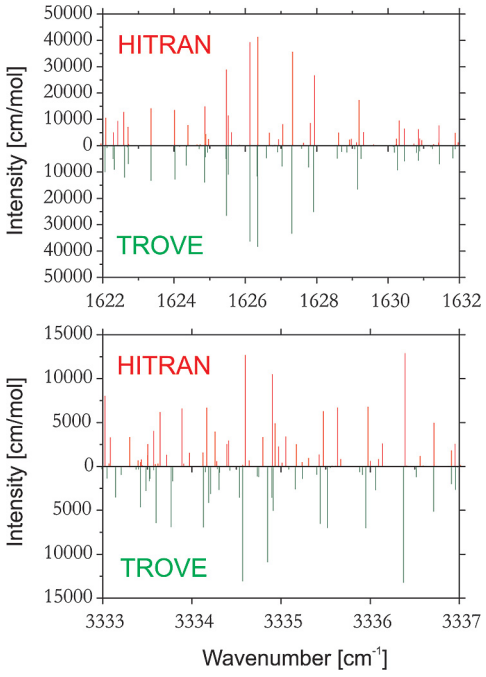

Figure 4. Comparison of the simulated (TROVE) and observed (HITRAN) spectra of NH_3 at $T = 300$ K in two selected frequency regions.

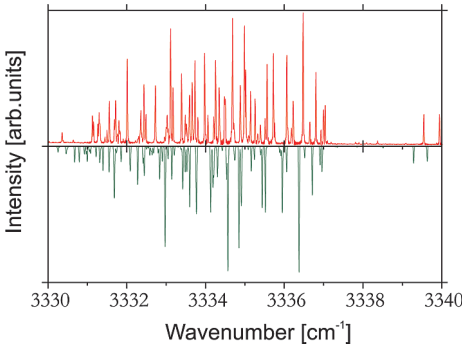

Figure 5. Comparison of the observed Kitt peak data at 0.35 Torr with a 12 m cell (upper plot) and our computed spectra of NH_3 at $T = 295$ K, convoluted with a Gaussian profile, HWHM = 0.01 cm^{-1} (lower plot).

ammonia were identified in the course of this work and will be discussed elsewhere.

Our ultimate aim is the construction of an NH_3 line list capable of replicating observed spectra at temperatures up to ~1500 K. Inter alia, this will enable a better understanding of the atmospheric signatures of brown dwarfs and exoplanets. The work presented here represents the first step toward this goal, which involves the generation, refinement, and validation of the required potential energy and dipole moment surfaces, as well as establishment of the level of accuracy that can be achieved in the variational nuclear motion calculations within our computational resources. In this initial phase, we have produced an ammonia line list consisting of 3.25 million transitions between 184 400 energy levels for rovibrational states up to $J_{max} = 20$ and energies up to 12000 cm^{-1}. This list is less complete and less accurate than ultimately desired. Nevertheless, it can be used to produce synthetic NH_3 spectra that agree well with observation at room temperature.

Acknowledgment. The authors would like to thank the Research Computing Support Team at UCL. We acknowledge support from the European Commission through Contract No. MRTN-CT-2004-512202 "Quantitative Spectroscopy for Atmospheric and Astrophysical Research" (QUASAAR). This work was supported by a grant from the Leverhulme Trust.

Supporting Information Available: The parameters $\mu^{(\Gamma)}_{k,l,m,...}$ (see eqs 11−13) together with the Fortran routine for calculating the dipole moment components; the complete cool NH_3 line list with transition energies, line strengths, and Einstein coef-

ficients $A(f \leftarrow i)$, as well as absorption intensities estimated for $T = 300$ K; and a Fortran program to generate synthetic spectra. For this material, see http://www.tampa.phys.ucl.ac.uk/ftp/astrodata/NH3/. This material is available free of charge via the Internet at http://pubs.acs.org.

References and Notes

(1) Kawakita, H.; Watanabe, J.-I. *Astrophys. J.* **2002**, *572*, L177.
(2) Lara, L.-M.; Bézard, B.; Griffith, C. A.; Lacy, J. H.; Owen, T. *Icarus* **1998**, *131*, 317.
(3) Fouchet, T.; Lellouch, E.; Bézard, B.; Encrenaz, T.; Drossart, P. *Icarus* **2000**, *143*, 223.
(4) Orton, G.; et al. *Science* **1995**, *267*, 1277.
(5) Kawakita, H.; Dello Russo, N.; Furusho, R.; Fuse, T.; Watanabe, J.-i.; Boice, D. C.; Sadakane, K.; Arimoto, N.; Ohkubo, M.; Ohnishi, T. *Astrophys. J.* **2006**, *643*, 1337.
(6) Kawakita, H.; Jehin, E.; Manfroid, J.; Hutsemékers, D. *Icarus* **2007**, *187*, 272.
(7) Burrows, A.; Marley, M.; Hubbard, W. B.; Lunine, J. I.; Guillot, T.; Saumon, D.; Freedman, R.; Sudarsky, D.; Sharp, C. *Astrophys. J.* **1997**, *491*, 856.
(8) Sharp, C. M.; Burrows, A. *Astrophys. J. Suppl.* **2007**, *168*, 140.
(9) Burrows, A.; Sudarsky, D.; Lenine, J. I. *Astrophys. J.* **2003**, *596*, 587.
(10) Sudarsky, D.; Burrows, A.; Hubeny, I. *Astrophys. J.* **2003**, *588*, 1121.
(11) Swain, M. R.; Vasisht, G.; Tinetti, G. *Nature* **2008**, *452*, 329.
(12) Rothman, L. S.; Jacquemart, D.; Barbe, A.; Benner, D. C.; Birk, M.; Brown, L. R.; Carleer, M. R.; Chackerian, C.; Chance, K.; Coudert, L. H.; Dana, V.; Devi, V. M.; Flaud, J.-M.; Gamache, R. R.; Goldman, A.; Hartmann, J.-M.; Jucks, K. W.; Maki, A. G.; Mandin, J.-Y.; Massie, S. T.; Orphal, J.; Perrin, A.; Rinsland, C. P.; Smith, M. A. H.; Tennyson, J.; Tolchenov, R. N.; Toth, R. A.; Vander, A. J.; Varanasi, P.; Wagner, G. *J. Quant. Spectrosc. Radiat. Transfer* **2005**, *96*, 139.
(13) Martin, J. M. L.; Lee, T. J.; Taylor, P. R. *J. Chem. Phys.* **1992**, *97*, 8361.
(14) Lin, H.; Thiel, W.; Yurchenko, S. N.; Carvajal, M.; Jensen, P. *J. Chem. Phys.* **2002**, *117*, 11265.
(15) Rajamäki, T.; Miani, A.; Pesonen, J.; Halonen, L. *Chem. Phys. Lett.* **2002**, *36*, 226.
(16) Rajamäki, T.; Miani, A.; Halonen, L. *J. Chem. Phys.* **2003**, *118*, 6358.
(17) Rajamäki, T.; Miani, A.; Halonen, L. *J. Chem. Phys.* **2003**, *118*, 10929.
(18) Rajamäki, T.; Kállay, M.; Noga, J.; Valiron, P.; Halonen, L. *Mol. Phys.* **2004**, *102*, 2297.
(19) Yurchenko, S. N.; Zheng, J.; Lin, H.; Jensen, P.; Thiel, W. *J. Chem. Phys.* **2005**, *123*, 134308.
(20) Huang, X.; Schwenke, D. W.; Lee, T. J. *J. Chem. Phys.* **2008**, *129*, 214304.
(21) Yurchenko, S. N.; Thiel, W.; Carvajal, M.; Lin, H.; Jensen, P. *Adv. Quantum Chem.* **2005**, *48*, 209.
(22) Yurchenko, S. N.; Carvajal, M.; Lin, H.; Zheng, J.; Thiel, W.; Jensen, P. *J. Chem. Phys.* **2005**, *122*, 104317.
(23) Mátyus, E.; Czakó, G.; Császár, A. G. *J. Chem. Phys.* **2009**, *130*, 134112.
(24) Yurchenko, S. N.; Carvajal, M.; Jensen, P.; Lin, H.; Zheng, J.; Thiel, W. *Mol. Phys.* **2005**, *103*, 359.
(25) Yurchenko, S. N.; Carvajal, M.; Thiel, W.; Jensen, P. *J. Mol. Spectrosc.* **2006**, *239*, 71.
(26) Yurchenko, S. N.; Thiel, W.; Carvajal, M.; Jensen, P. *Chem. Phys.* **2008**, *346*, 146.
(27) Yurchenko, S. N.; Thiel, W.; Jensen, P. *J. Mol. Spectrosc.* **2007**, *245*, 126.
(28) Herzberg, G. *Infrared and Raman Spectra of Polyatomic Molecules*; D. Van Nostrand Co. Inc.: New York, 1945.
(29) Bunker, P. R.; Jensen, P. *Molecular Symmetry and Spectroscopy*, 2nd ed.; NRC Research Press: Ottawa, Canada, 1998.
(30) Mills, I. M.; Robiette, A. G. *Mol. Phys.* **1985**, *56*, 743.
(31) Dennison, D. M.; Hardy, J. D. *Phys. Rev.* **1932**, *39*, 938.
(32) Cleeton, C. E.; Williams, N. H. *Phys. Rev.* **1934**, *45*, 234.
(33) Cheung, A. C.; Rank, D. M.; Townes, C. H.; Thornton, D. D.; Welch, W. J. *Phys. Rev. Lett.* **1968**, *21*, 1701.
(34) Werner, H.-J.; Knowles, P. J. *MOLPRO2000*, a package of ab initio programs; with contributions from Amos, R. D.; et al.
(35) (a) Hampel, C,; Peterson, K.; Werner, H.-J. *Chem. Phys. Lett.* **1992**, *190*, 1, and references therein. (b) The program to compute the perturbative triples corrections has been developed by Deegan, M. J. O.; Knowles, P. J. *Chem. Phys. Lett.* **1994**, *227*, 321.
(36) Purvis, G. D.; Bartlett, R. J. *J. Chem. Phys.* **1982**, *76*, 1910.
(37) Raghavachari, K.; Trucks, G. W.; Pople, J. A.; Head-Gordon, M. *Chem. Phys. Lett.* **1989**, *157*, 479.
(38) Dunning, T. H. *J. Chem. Phys.* **1989**, *90*, 1007.
(39) Woon, D. E.; Dunning, T. H. *J. Chem. Phys.* **1993**, *98*, 1358.
(40) Anderson, E.; et al. LAPACK Users' Guide, 3rd ed.; http://www.netlib.org/lapack/ (1999).
(41) Marquardt, R.; Quack, M.; Thanopulos, I.; Luckhaus, D. *J. Chem. Phys.* **2003**, *119*, 10724.
(42) Marshall, M. D.; Izgi, K. C.; Muenter, J. S. *J. Chem. Phys.* **1997**, *107*, 1037.
(43) Halkier, A.; Taylor, P. R. *Chem. Phys. Lett.* **1998**, *285*, 133.
(44) Puzzarini, C. *Theor. Chem. Acc.* **2008**, *121*, 1.
(45) Tanaka, K.; Ito, H.; Tanaka, T. *J. Chem. Phys.* **1987**, *87*, 1557.
(46) Barber, R. J.; Tennyson, J.; Harris, G. J.; Tolchenov, R. N. *Mon. Not. R. Astron. Soc.* **2006**, *368*, 1087.
(47) Bunker, P. R.; Jensen, P. *Fundamentals of Molecular Symmetry*; IOP Publishing: Bristol, U.K., 2004.
(48) Hougen, J. T.; Bunker, P. R.; Johns, J. W. C. *J. Mol. Spectrosc.* **1970**, *34*, 136.
(49) Szalay, V. *J. Chem. Phys.* **1993**, *99*, 1978.
(50) Lehoucq, R. B.; Sorensen, D. C.; Yang, C. *ARPACK Users' Guide: Solution of Large-scale Eigenvalue Problems with Implicitly Restarted Arnoldi Methods (Software, Environments and Tools)*; Society for Industrial & Applied Mathematics: Philadelphia, PA, 1998; http://www.caam.rice.edu/software/ARPACK/.
(51) Pawłowski, F.; et al. *J. Chem. Phys.* **2002**, *116*, 6482.
(52) Chen, P.; Pearson, J. C.; Pickett, H. M.; Matsuura, S.; Blake, G. A. *J. Mol. Spectrosc.* **2006**, *236*, 116.
(53) Eckart, C. *Phys. Rev.* **1935**, *47*, 552.
(54) Sayvetz, A. *J. Chem. Phys.* **1939**, *7*, 383.
(55) Ovsyannikov, R. I.; Thiel, W.; Yurchenko, S. N.; Carvajal, M.; Jensen, P. *J. Chem. Phys.* **2008**, *129*, 044309.
(56) Ueda, Y.; Iwahori, J. *J. Mol. Spectrosc.* **1986**, *116*, 191.
(57) Beckwith, P. H.; Danagher, D. J.; Reid, J. *J. Mol. Spectrosc.* **1987**, *121*, 209.
(58) Cottaz, C.; Tarrago, G.; Kleiner, I.; Brown, L. R. *J. Mol. Spectrosc.* **2001**, *209*, 30.
(59) Takami, M.; Jones, H.; Oka, T. *J. Chem. Phys.* **1979**, *70*, 3557.
(60) Sasada, S.; Hasegawa, Y.; Amano, T.; Shimizu, T. *J. Mol. Spectrosc.* **1982**, *96*, 106.
(61) Le Sueur, C. R.; Miller, S.; Tennyson, J.; Sutcliffe, B. T. *Mol. Phys.* **1992**, *76*, 1147.
(62) Li, L.; Lees, R. M.; Xu, L.-H. *J. Mol. Spectrosc.* **2007**, *243*, 219.
(63) Lees, R. M.; Li, L.; Xu, L.-H. *J. Mol. Spectrosc.* **2008**, *251*, 241.
(64) Horka, V.; Civis, S.; Xu, L.-H.; Lees, R. M. *Analyst* **2005**, *130*, 1148.
(65) Xu, L.-H.; Liu, Z.; Yakovlev, I.; Tretyakov, M. Y.; Lees, R. M. *Infrared Phys. Technol.* **2004**, *45*, 31.
(66) Berden, G.; Peeters, R.; Meijer, G. *Chem. Phys. Lett.* **1999**, *307*, 131.
(67) Cottaz, C.; Tarrago, G.; Kleiner, I.; Brown, L. R.; Margolis, J. S.; Poynter, R. L.; Pickett, H. M.; Fouchet, T.; Drossart, P.; Lellouch, E. *J. Mol. Spectrosc.* **2000**, *203*, 285.
(68) Kleiner, I.; Tarrago, G.; Brown, L. R. *J. Mol. Spectrosc.* **1995**, *173*, 120.
(69) Guelachvili, G.; Abdullah, A. H.; Tu, N.; Rao, K. N.; Urban, Š. *J. Mol. Spectrosc.* **1989**, *133*, 345.
(70) Kleiner, I.; Brown, L. R.; Tarrago, G.; Kou, Q.-L.; Picqué, N.; Guelachvili, G.; Dana, V.; Mandin, J.-Y. *J. Mol. Spectrosc.* **1999**, *193*, 46.
(71) Urban, Š.; Tu, N.; Rao, K. N.; Guelachvili, G. *J. Mol. Spectrosc.* **1989**, *133*, 312.
(72) Coy, S. L.; Lehmann, K. K. *Spectrochim. Acta* **1989**, *45A*, 47.
(73) Urban, Š.; Špirko, V.; Papoušek, D.; Kauppinen, J.; Belov, S. P.; Gershtein, L. I.; Krupnov, A. F. *J. Mol. Spectrosc.* **1981**, *88*, 274.
(74) Ziegler, L. D.; Hudson, B. *J. Phys. Chem.* **1984**, *88*, 1110.
(75) Nakanaga, T.; Kondo, S.; Saëki, S. *J. Mol. Spectrosc.* **1985**, *112*, 39.
(76) Margolis, J. S.; Kwan, Y. Y. *J. Mol. Spectrosc.* **1974**, *50*, 266.

JP9029425

An ab initio calculation of the vibrational energies and transition moments of HSOH

S. N. Yurchenko, A. Yachmenev, W. Thiel, O. Baum, T. F. Giesen, V. V. Melnikov, P. Jensen

J. Mol. Spectrosc., **257**, 57 (2009)

Journal of Molecular Spectroscopy 257 (2009) 57–65

Contents lists available at ScienceDirect

Journal of Molecular Spectroscopy

journal homepage: www.elsevier.com/locate/jms

An *ab initio* calculation of the vibrational energies and transition moments of HSOH

Sergei N. Yurchenko [a], Andrey Yachmenev [b], Walter Thiel [b], Oliver Baum [c], Thomas F. Giesen [c], Vladlen V. Melnikov [d,1], Per Jensen [d,*]

[a] *Institut für Physikalische Chemie und Elektrochemie, TU Dresden, D-01062 Dresden, Germany*
[b] *Max-Planck-Institut für Kohlenforschung, Kaiser-Wilhelm-Platz 1, D-45470 Mülheim an der Ruhr, Germany*
[c] *I. Physikalisches Institut, Universität zu Köln, Zülpicher Straße 77, D-50937 Köln, Germany*
[d] *FB C – Physikalische und Theoretische Chemie, Bergische Universität, D-42097 Wuppertal, Germany*

ARTICLE INFO

Article history:
Received 27 May 2009
In revised form 19 June 2009
Available online 28 June 2009

Keywords:
HSOH
Oxadisulfane
ab initio
Potential energy surface
Dipole moment surface
Vibrational energies
Vibrational transition moments
TROVE

ABSTRACT

We report new *ab initio* potential energy and dipole moment surfaces for the electronic ground state of HSOH, calculated by the CCSD(T) method (coupled cluster theory with single and double substitutions and a perturbative treatment of connected triple excitations) with augmented correlation-consistent basis sets up to quadruple-zeta quality, aug-cc-pV(Q+*d*)Z. The energy range covered extends up to 20000 cm^{-1} above equilibrium. Parameterized analytical functions have been fitted through the *ab initio* points. Based on the analytical potential energy and dipole moment surfaces obtained, vibrational term values and transition moments have been calculated by means of the variational program TROVE. The theoretical term values for the fundamental levels v_{SH} (SH-stretch) and v_{OH} (OH-stretch), the intensity ratio of the corresponding fundamental bands, and the torsional splitting in the vibrational ground state are in good agreement with experiment. This is evidence for the high quality of the potential energy surface. The theoretical results underline the importance of vibrational averaging, and they allow us to explain extensive perturbations recently found experimentally in the SH-stretch fundamental band of HSOH.

1. Introduction

After the first spectroscopic characterization of oxadisulfane HSOH as recently as in 2003 [1], this molecule (and its deuterated isotopologues DSOD and HSOD) has received substantial experimental and theoretical attention [2–11] as the 'long-missing link' between the better known molecules HOOH and HSSH. Each of the three molecules HOOH, HSSH, and HSOH has a skew-chain equilibrium geometry, and particularly interesting features of their spectra originate in the energy splittings resulting from the internal rotation, or torsion, of the OH or SH moieties around the axis connecting the two heavy atoms (we denote this axis as the *z* axis; see Section 3.2 below). The torsional motion couples significantly with the over-all rotation of the molecule about the *z* axis and, in consequence, the torsional splittings depend strongly on the rotational excitation, in particular on the quantum number K_a which is the absolute value of the projection, in units of ħ, of the total angular momentum onto the *z* axis. It is well known that in HOOH and HSSH, the torsional splittings 'stagger' with K_a so that, for example, states with even (odd) K_a values have larger (smaller) splittings. For HSOH, a more complicated variation of the splittings with K_a was observed experimentally [1,3]; it has an approximate periodicity with a period of three K_a-values. Initially, the unexpected splitting pattern was explained in terms of a semi-empirical model [3] based on ideas of Hougen [12] (see also Ref. [13]). The periodicity of three K_a-values in the torsional splittings was found to derive from the fact that the moments of inertia of the OH and SH moieties with respect to the *z* axis form a ratio of about 2:1; for HOOH and HSSH a periodicity of two K_a-values ensues because for these molecules, the analogous ratio is 1:1.

Quite recently [11], a slightly extended version of the Hougen-type model from Ref. [3] has been used for a successful analysis of all torsional splittings observed experimentally for HSOH. The values of the splittings were least-squares fitted to parameterized expressions derived from the model. In parallel, we have given an equally successful explanation [9] of the observed splittings using an alternative, first-principles approach in which the splittings are calculated directly from an *ab initio* potential energy surface (PES) by means of the program system TROVE [14] (Theoretical Rotation–Vibration Energies). TROVE can, in principle, calculate the rotation–vibration energies of any polyatomic molecule in an isolated electronic state, and the generally high accuracy of the rotation–vibration energies obtained has already been demonstrated in Ref. [14]. In the variational solution of the rotation–vibration Schrödinger equation for HSOH [9] we used

* Corresponding author. Fax: +49 202 439 2509.
E-mail address: jensen@uni-wuppertal.de (P. Jensen).
[1] Present address: Siberian Physical-technical Institute, Tomsk State University, Tomsk, 634050 Russia.

0022-2852/$ - see front matter © 2009 Elsevier Inc. All rights reserved.
doi:10.1016/j.jms.2009.06.010

the Hougen–Bunker–Johns (HBJ) nonrigid-reference configuration method [15]. In this method the reference geometry is chosen to minimize the vibration–torsion coupling in the kinetic energy operator. In the calculation of HSOH torsional splittings in Ref. [9] we also explored an alternative approach, akin to the semirigid bender model by Bunker and Landsberg [16], where the geometries along the torsional minimum energy path (i.e., a path where, as the torsional motion takes place, all other structural parameters than the torsional coordinate relax to minimize the potential energy) are taken as the reference configuration. In this case, the torsion–vibration coupling is minimized in the PES. It turned out that this approach provides very accurate torsional splittings as well as quite accurate values for the torsion-rotation term values.

In the present work, we describe the *ab initio* PES for the electronic ground state of HSOH, computed by the CCSD(T) *ab initio* method, which served as starting point for the calculation of the torsional splittings in Ref. [9]. Furthermore, we report the computation of an accompanying CCSD(T) *ab initio* dipole moment surface (DMS). For both the PES and the DMS, we have constructed suitable analytical-function representations of the *ab initio* points and we use these analytical representations as input for the TROVE program to calculate vibrational term values and vibrational transition moments for selected vibrational bands of HSOH.

The parameterized analytical representation of the PES has been constructed by least-squares fitting to two sets of *ab initio* energies [see Section 3 below]. One set, comprising 105 000 data points, was calculated with the aug-cc-pVTZ basis set and the other set, comprising 10 168 data points, was calculated with the aug-cc-pV(Q+*d*)Z basis set. The 10 168 geometries in the second set of data points were selected to cover in detail the energy range up to 20 000 cm^{-1} above equilibrium. The analytical function representing the PES is defined in terms of 762 parameter values.

The *ab initio* dipole moment data points were computed at the CCSD(T)/aug-cc-pV(T+*d*)Z level of theory for 8936 geometries. The finite difference scheme was employed for the dipole moment calculation. The analytical functions representing the DMS components μ_x, μ_y, and μ_z [see Section 3.2 for the definition of the *xyz* axis system] are defined in terms of 428, 382, and 420 parameter values, respectively.

The *ab initio* study of the present work is the most complete and accurate reported thus far. We have already validated the *ab initio* PES in Ref. [9] by showing that the torsional splittings and the torsion–rotation term values obtained from the PES are in excellent agreement with the available experimental values [1,3,8,11]. In the present work, we extend this validation by comparing also the remaining, experimentally available term values associated with the OH-stretch [7] and SH-stretch [7,10] fundamental levels.

The paper is structured as follows. In Section 2, we describe the *ab initio* methods employed for the electronic structure calculations. We also define in this section the grids of nuclear geometries, at which *ab initio* energies were calculated, and characterize the computed potential energy and dipole moment surfaces of HSOH. The analytical representations of the PES and DMS are introduced in Section 3. The variational nuclear-motion calculations are reported in Section 4 together with the computed theoretical values for the vibrational term values and transition moments of HSOH. In Section 5, we discuss the theoretical description of the OH-stretch and SH-stretch fundamental levels v_{OH} and v_{SH} while comparing the theoretical results with the experimental findings. Finally, Section 6 offers additional discussion and some conclusions.

2. *Ab initio* calculations

The *ab initio* calculations of the present work have been made with the MOLPRO2002 package [17,18], employing the CCSD(T) (coupled cluster theory with all single and double substitutions from the Hartree–Fock reference determinant [19] augmented by a perturbative treatment of connected triple excitations [20,21]) method.

2.1. Potential energy surface

The CCSD(T) energy calculations have been carried out in the frozen-core approximation with three different combinations of basis sets: (a) aug-cc-pVDZ basis sets for H, O, and S; (b) aug-cc-pVTZ basis sets for H, O, and S; and (c) cc-pVQZ, aug-cc-pVQZ, and aug-cc-pV(Q+*d*))Z basis sets for H, O, and S, respectively [22–25]. In the largest basis set (c), we adopt the *d*-corrected basis for S from Wilson and Dunning [25], and we do not augment the cc-pVQZ basis for H since we do not expect the corresponding diffuse functions to play a significant role. The basis set combinations (a), (b), and (c) are referred to as ADZ, ATZ, and A(Q+*d*)Z, respectively.

The CCSD(T) calculations with the three basis sets ADZ, ATZ, and A(Q+*d*)Z have very different computer-resource requirements. We used the relatively modest level of theory associated with the ADZ basis set for a preliminary scan of the PES and computed about a million *ab initio* points on a regular 6D grid. This provided us with a very detailed, albeit qualitative, survey of the PES and made it possible to determine the range of geometries necessary to describe the PES of HSOH up to 20 000 cm^{-1} above equilibrium. Exploring the potential energy surface further we have computed about 105 000 energies at the ATZ level of *ab initio* theory, covering the energy range up to 20 000 cm^{-1} above equilibrium. This strategy for choosing the grid of geometries is similar to that used in Ref. [26]. Then, finally, we run more expensive A(Q+*d*)Z calculations at 10 168 geometries. Because of the high computational demands at the A(Q+*d*)Z level of theory, it was especially important to select appropriate molecular geometries for the A(Q+*d*)Z calculations from the results of the lower-level calculations.

In order to describe the geometry of HSOH we introduce six internal coordinates: The S–O distance r_{SO}, the S–H distance r_{SH}, the O–H distance r_{OH}, $\alpha_{HOS} = \angle(H–O–S) \in [0,\pi]$, $\alpha_{OSH} = \angle(O–S–H) \in [0,\pi]$, and the torsional angle $\tau_{HSOH} \in [0,2\pi]$ (the dihedral angle between the HOS and OSH planes). Fig. 1 shows six one-dimensional (1D) cuts through the PES, visualizing the variation of the PES with each of these coordinates. In each case, the five remaining coordinates are set equal to their equilibrium values.

The equilibrium values of r_{SO}, r_{SH}, r_{OH}, α_{HOS}, α_{OSH}, and τ_{HSOH} are listed in Table 1 and compared with CCSD(T)/cc-pCVQZ values from Ref. [1], with very recent CCSD(T,full)/cc-pwCVQZ *ab initio* results by Denis [27] and with the empirical structural parameters derived by Baum et al. [5]. The table also gives the calculated *cis* and *trans* barriers to torsional motion; these values are compared with the CCSD(T)/cc-pCVQZ values from Ref. [1] and with MP2/aug-cc-pVTZ values from Ref. [28]. The top of the *cis*(*trans*) barrier is the maximum obtained for $\tau_{HSOH} = 0°$ (180°) and all other structural parameters relaxed to minimize the potential energy.

We have also computed the barrier values corresponding to a path between the two equivalent minima of the PES where one of the angles α_{HOS} or α_{OSH} reaches 180° (that is, either the HOS moiety or the OSH moiety becomes linear). We find these barriers at the MP2/aug-cc-pV(T+*d*)Z level of theory by using constrained optimization. The barrier for $\alpha_{HOS} = 180°$ is 11 780 cm^{-1}, while the barrier for $\alpha_{OSH} = 180°$ is much higher, 37 524 cm^{-1} (see Fig. 1). The lowest-energy linear configuration of the molecule is found approximately 55 424 cm^{-1} above equilibrium at the MP2/aug-cc-pV(T+*d*)Z level of theory.

2.2. Dipole moment surfaces

The *ab initio* dipole moment values were computed with MOLPRO2002 at the CCSD(T)/A(T+*d*)Z level of theory [19–25] in

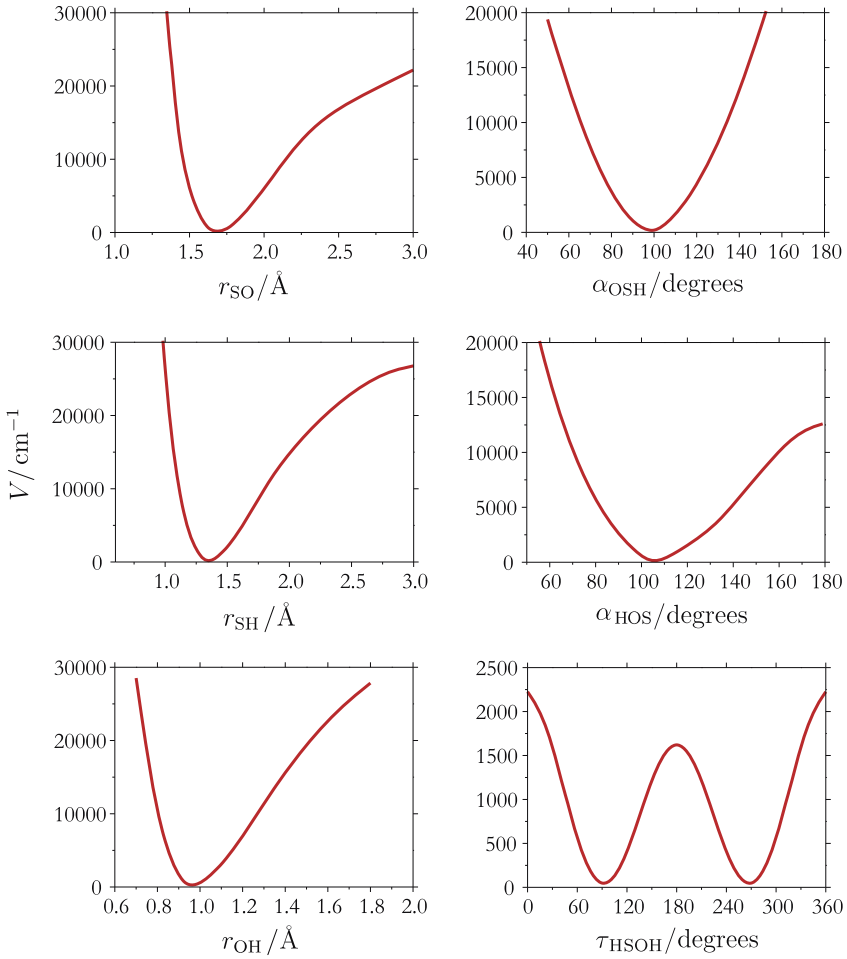

Fig. 1. Six one-dimensional (1D) cuts through the potential energy function for HSOH (one for each degree of freedom) with the remaining five coordinates taken at their equilibrium values.

Table 1
Equilibrium and transition geometries of HSOH.

	Equilibrium geometry				Transition states[a]	
	A(Q+*d*)Z[a]	Ref. [1][b]	Ref. [27][c]	Ref. [5][d]	*cis*	*trans*
r_{SO} (Å)	1.66725	1.6616	1.6614	1.6616(1)	1.687	1.690
r_{SH} (Å)	1.34431	1.3414	1.3413	1.3420(2)	1.341	1.337
r_{OH} (Å)	0.96178	0.9601	0.9601	0.9606(3)	0.960	0.962
α_{HOS} (°)	107.141	107.01	107.0	107.19(3)	108.911	105.564
α_{OSH} (°)	98.424	98.55	98.6	98.57(5)	99.411	93.325
τ_{HSOH} (°)	91.431	91.29	91.3	90.41(11)	0	180
V_{opt} (cm^{-1})					2163.3[e]	1520.9[f]

[a] Present work, obtained by geometry optimization carried out with MOLPRO2002 [17,18].
[b] CCSD(T)/cc-pCVQZ *ab initio*.
[c] CCSD(T,full)/cc-pwCVQZ *ab initio*; see Ref. [27] for further details.
[d] Empirical equilibrium geometry derived from experimental values of A_0, B_0, and C_0 in conjunction with CCSD(T)/cc-pCVQZ *ab initio* values of the α_r constants for HSOH, $H^{34}SOH$, HSOD, and DSOD. See Ref. [5] for details. Numbers in parentheses are quoted uncertainties in units of the last digit.
[e] *cis*-barrier for torsional motion. The CCSD(T)/cc-pCVQZ value from Ref. [1] is 2216 cm^{-1} and the aug-cc-pVTZ/MP2 value from Ref. [28] is 2164 cm^{-1}.
[f] *trans*-barrier for torsional motion. The CCSD(T)/cc-pCVQZ value from Ref. [1] is 1579 cm^{-1} and the aug-cc-pVTZ/MP2 value from Ref. [28] is 1473.5 cm^{-1}.

the frozen-core approximation. For these calculations we selected 8936 geometries with energies less than 12 000 cm^{-1} above equilibrium. The dipole moment components along the molecule-fixed axes were obtained as derivatives of the electronic energy with respect to the components of an external electric field. The field derivatives were computed for each geometry by means of the central finite difference scheme; for each of the *x*, *y*, and *z* molecule-fixed axes, the molecule was subjected to external electric fields with components of +0.005 a.u. and −0.005 a.u., respectively, along the axis in question.

3. Fitting of the surfaces

3.1. Potential energy surface

Fig. 1 shows that the vibrational modes of HSOH, with the exception of the torsional mode, can be viewed as oscillations around a single minimum on the PES. The torsional motion, on the other hand, involves tunneling between two equivalent minima on the PES through the *cis* and *trans* barriers whose heights are given in Table 1. We employ a cosine-type expansion to repre-

sent the dependence of the PES on the torsional angle τ_{HSOH}. We choose this expansion with a view to the fact that the PES is invariant under the inversion operation E^* [29] which causes the coordinate change $\tau_{HSOH} \rightarrow 2\pi - \tau_{HSOH}$. The dependence of the PES on the three stretching coordinates is described by expansions in Morse-type variables $y = 1 - \exp(-a[r - r_e])$, while for the bending coordinates we use the displacements $\Delta\alpha = \alpha - \alpha_e$. The expansion of the PES thus becomes

$$\begin{aligned} V(\xi_{OH}, \xi_{OS}, \xi_{SH}, \xi_{HOS}, \xi_{OSH}, \xi_{HSOH}) &= V_e + \sum_j F_j \xi_j + \sum_{j\leqslant k} F_{jk} \xi_j \xi_k + \sum_{j\leqslant k\leqslant l} F_{jkl} \xi_j \xi_k \xi_l \\ &+ \sum_{j\leqslant k\leqslant l\leqslant m} F_{jklm} \xi_j \xi_k \xi_l \xi_m + \sum_{j\leqslant k\leqslant l\leqslant m\leqslant n} F_{jklmn} \xi_j \xi_k \xi_l \xi_m \xi_n \\ &+ \sum_{j\leqslant k\leqslant l\leqslant m\leqslant n\leqslant o} F_{jklmno} \xi_j \xi_k \xi_l \xi_m \xi_n \xi_o \end{aligned} \quad (1)$$

The expansion variables are

$$\xi_k = 1 - \exp(-a_k(r_k - r_k^{ref})), \quad k = SO, SH, \text{or } OH \quad (2)$$

$$\xi_{HOS} = \alpha_{HOS} - \alpha_{HOS}^{ref}, \quad (3)$$

$$\xi_{OSH} = \alpha_{OSH} - \alpha_{OSH}^{ref}, \quad (4)$$

$$\xi_{HSOH} = \cos\tau_{HSOH} - \cos\tau_{HSOH}^{ref}, \quad (5)$$

where r_k^{ref} and α_k^{ref} are reference values of the structural parameters, the a_k are molecular parameters, V_e is the value of the PES at equilibrium, and the quantities $F_{jk\ldots}$ are the expansion coefficients. Since $\cos(2\pi - \tau_{HSOH}) = \cos\tau_{HSOH}$, the function in Eq. (1) automatically satisfies the symmetry requirement mentioned above so that there are no symmetry relations between the potential parameters, i.e., all $F_{jk\ldots}$ are independent. We take the reference values as $r_{SO}^{ref} = 1.69031$ Å, $r_{SH}^{ref} = 1.33653$ Å, $r_{OH}^{ref} = 0.96229$ Å, $\alpha_{HOS}^{ref} = 105.56^\circ$, $\alpha_{OSH}^{ref} = 93.32^\circ$, and $\tau_{HSOH}^{ref} = 180^\circ$.

Our highest-quality *ab initio* surface A(Q+*d*)Z is based on 10168 *ab initio* points covering, for the most part, the region below 12000 cm^{-1}. That is, the highest-quality *ab initio* points cover a limited region of configuration space. The less accurate ATZ PES covers in great detail the region up to 20000 cm^{-1} with almost 105000 points. In order to prevent the fitted, analytical PES from having a significantly wrong behavior in regions of configuration space not sampled by the A(Q+*d*)Z data points, we use both the ATZ and the A(Q+*d*)Z data sets as input for the least-squares fitting producing the optimized values of the potential energy parameters $F_{jkl\ldots}$. In this fitting, the points in the large ATZ data set are given weight factors typically 10^4 times smaller than those of the A(Q+*d*)Z data points. In this way the geometries, for which A(Q+*d*)Z *ab initio* energies exist, are greatly favored because of the large weight factors. However outside the A(Q+*d*)Z grid the fit is controlled by the points of the vast data set ATZ. The ratio of 10^4 between the weight factors used for the A(Q+*d*)Z and ATZ points was found by numerical experiments. We needed 762 fitting parameters to reproduce the A(Q+*d*)Z electronic energies with the root-mean-square (rms) error of 2.8 cm^{-1}. The analytical PES obtained by combination of the ATZ and A(Q+*d*)Z *ab initio* data sets is denoted A(Q+*d*)Z*. This analytical PES is assumed to be of A(Q+*d*)Z quality in the lower energy region up to 12000 cm^{-1} above equilibrium (since this is where the A(Q+*d*)Z *ab initio* data exist) and to have a qualitative correct behavior, at least of ATZ quality, at higher energy up to 20000 cm^{-1}.

In order to establish the quality of the ATZ *ab initio* energies, we have also fitted the 105000 ATZ data points without the A(Q+*d*)Z points. In this fitting, we could usefully vary 898 parameters that describe the ATZ energies with rms errors of 4.4 cm^{-1}, 13 cm^{-1}, and 32 cm^{-1} below 10000 cm^{-1}, 15000 cm^{-1}, and 20000 cm^{-1}, respectively.

The *ab initio* energy values and the parameter values obtained from the fits of the potential energy function in Eq. (1) are available as Supplementary material together with FORTRAN routines for evaluating the corresponding potential energy values at arbitrary geometries. The A(Q+*d*)Z* potential energy surface, obtained by combination of the ATZ and A(Q+*d*)Z *ab initio* data sets as described above, is expected to provide a good description of the electronic ground state of HSOH at energies up to 20000 cm^{-1} above equilibrium.

3.2. Dipole moment surfaces

Towards obtaining analytical representations of the electronically averaged dipole moment components for HSOH we introduced an axis system as follows. The *z* axis is aligned along the SO bond, pointing from S to O, and the *x* axis lies in the plane containing the SO and SH bonds and is oriented such that the H nucleus in the SH moiety has a positive *x* value. The *y* axis is oriented such that the *xyz* axis system is right-handed. This *xyz* axes are not exactly principal axes, but the *xyz* axis system is close to the principal axis system *abc* shown in Fig. 2 with the *z* axis being close to the *a* axis which has the smallest moment of inertia. With the chosen axes, the *y* component of the dipole moment is antisymmetric with respect to inversion E^* [29] (that is, it has A'' symmetry in the $\mathbf{C}_s$(M) group [29]), while the *x* and *z* component are totally symmetric (i.e., they have A' symmetry). The three dipole components are represented by the following analytical functions:

$$\begin{aligned} \bar{\mu}_\alpha(\zeta_{OH}, \zeta_{SO}, \zeta_{SH}, \zeta_{HOS}, \zeta_{OSH}, \zeta_{HSOH}) &= \mu_0^{(\alpha)} + \sum_j \mu_j^{(\alpha)} \zeta_j + \sum_{j\leqslant k} \mu_{jk}^{(\alpha)} \zeta_j \zeta_k + \sum_{j\leqslant k\leqslant l} \mu_{jkl}^{(\alpha)} \zeta_j \zeta_k \zeta_l \\ &+ \sum_{j\leqslant k\leqslant l\leqslant m} \mu_{jklm}^{(\alpha)} \zeta_j \zeta_k \zeta_l \zeta_m \end{aligned} \quad (6)$$

with $\alpha = x$ or *z*, and

$$\begin{aligned} \bar{\mu}_y(\zeta_{OH}, \zeta_{SO}, \zeta_{SH}, \zeta_{HOS}, \zeta_{OSH}, \zeta_{HSOH}) &= \sin\tau_{HSOH} \left[\mu_0^{(y)} + \sum_j \mu_j^{(y)} \zeta_j + \sum_{j\leqslant k} \mu_{jk}^{(y)} \zeta_j \zeta_k + \sum_{j\leqslant k\leqslant l} \mu_{jkl}^{(y)} \zeta_j \zeta_k \zeta_l \right. \\ &\left. + \sum_{j\leqslant k\leqslant l\leqslant m} \mu_{jklm}^{(y)} \zeta_j \zeta_k \zeta_l \zeta_m \right]. \end{aligned} \quad (7)$$

The dipole moment components are expanded in the variables

$$\zeta_k = r_k - r_k^{ref}, \quad k = OH, SO, \text{or } SH, \quad (8)$$

$\zeta_{HOS} = \xi_{HOS}$, $\zeta_{OSH} = \xi_{OSH}$, and $\zeta_{HSOH} = \xi_{HSOH}$, where ξ_{HOS}, ξ_{OSH}, and ξ_{HSOH} are given in Eqs. (3)–(5).

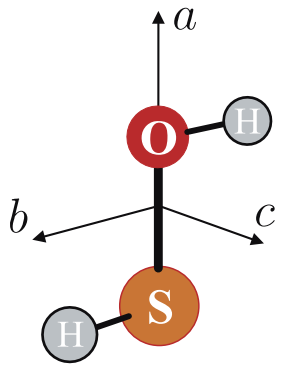

Fig. 2. The *abc* axes for the HSOH molecule.

We have determined the values of the expansion parameters of Eqs. (6) and (7) in three least-squares fittings, each of them to 8936 *ab initio* dipole moment components $\bar{\mu}_\alpha$, $\alpha = x,y,z$. In the three final fittings, we could usefully vary 428 ($\bar{\mu}_x$), 382 ($\bar{\mu}_y$), and 420 ($\bar{\mu}_z$) parameters, obtaining rms deviations of 0.0022, 0.0023, and 0.0149 D, respectively. In the lower energy region (below 8000 cm^{-1}) these deviations are smaller, 0.0005, 0.0004, and 0.0016 D, respectively. The optimized parameters are given as Supplementary material together with a FORTRAN routine for calculating the dipole moment values from Eqs. (6) and (7). We refer to the level of theory used for computing the electric dipole moment as A(T+*d*)Z.

For comparison with experimentally derived dipole moments, we must transform the dipole moment so as to obtain the components $\bar{\mu}_a$, $\bar{\mu}_b$, and $\bar{\mu}_c$ along the principal axes *abc* shown in Fig. 2. The dependence of $\bar{\mu}_a$, $\bar{\mu}_b$, and $\bar{\mu}_c$ for HSOH on the torsional angle τ_{HSOH} is depicted in Fig. 3, where we plot the dipole moment components obtained when the values of the structural parameters r_{SO}, r_{SH}, r_{OH}, α_{HOS}, α_{OSH} are determined by the torsional minimum energy path geometries of HSOH [9]. For the equilibrium values of the *ab initio* dipole moment we obtain $\bar{\mu}_a = 0.053$D, $\bar{\mu}_b = 0.744$D, and $\bar{\mu}_c = 1.399$D. These values can be compared to the corresponding CCSD(T)/cc-pCVQZ values of 0.0441, 0.7729, and 1.4329 D from Ref. [1]. The component $\bar{\mu}_a$ is close to zero for all torsional angles due to cancellation between the contributions from the SO bond dipole and the sulfur lone pairs. The two components $\bar{\mu}_b$ and $\bar{\mu}_c$ from Fig. 3 vary strongly with τ_{HSOH} and, because of this, the vibrational transition moments (see below) resulting from these components are very different from the corresponding equilibrium dipole moment values.

4. Variational calculations: vibrational term values and transition moments of HSOH

As outlined in Section 1, we employ for the variational calculations the newly developed program TROVE [14]. TROVE is a program suite designed for calculating the rotation–vibration energies of an arbitrary polyatomic molecule in an isolated electronic state. We intend TROVE to be a 'universal black-box' which anyone can use for rotation–vibration calculations. The calculation is variational in that the rotation–vibration Schrödinger equation is solved by numerical diagonalization of a matrix representation of the rotation–vibration Hamiltonian, constructed in terms of a suitable basis set. We describe the rotation–vibration motion of HSOH by means of Hougen–Bunker–Johns (HBJ) theory [15]. That is, we introduce a flexible reference configuration that follows the torsional motion and is defined in terms of the torsional coordinate τ_{HSOH}. The remaining vibrations are viewed as displacements from the reference configuration; they are described by linearized coordinates r^ℓ_{SO}, r^ℓ_{SH}, r^ℓ_{OH}, α^ℓ_{HOS}, and α^ℓ_{OSH}. The linearized coordinate [29] ξ^ℓ coincides with the corresponding geometrically defined coordinate ξ(=r_{SO}, r_{SH}, r_{OH}, α_{HOS}, or α_{OSH}) in the linear approximation. TROVE uses kinetic and potential energy operators expanded as Taylor series about the reference configuration: The kinetic energy is expanded in terms of the ξ^ℓ_k coordinates, and the potential energy is expanded in terms of quantities y^ℓ_k where $y^\ell_k = 1 - \exp(-a_k[\xi^\ell_k - r^e_k])$ with a_k from Eq. (2) for k = SO, SH, or OH, while $y^\ell_k = \xi^\ell_k - \alpha^e_k$ for k = HOS or OSH. The expansions of the kinetic and potential energy operators are truncated after the fourth and eighth order terms, respectively, and test calculations have shown that with these truncations, the energies calculated in the present work are converged to better than 0.05 cm^{-1}.

The vibrational basis set functions are constructed from one-dimensional functions obtained by numerically solving the corresponding one-dimensional (1D) Schrödinger problems by means of the Numerov–Cooley method [14,30]. That is, a vibrational basis function is given as a product of six 1D functions

$$|\phi_{vib}\rangle = |v_{SO}\rangle\,|v_{SH}\rangle\,|v_{OH}\rangle\,|v_{HOS}\rangle\,|v_{OSH}\rangle\,|v_{HSOH}, \tau_{tor}\rangle, \quad (9)$$

where v_X is the principal quantum number for the vibrational mode v_X with X = SO, SH, OH, HOS, and OSH, v_{HSOH} is the principal torsional quantum number, and τ_{tor} = 0 or 1 determines the torsional parity [29] as $(-1)^{\tau_{tor}}$. The quantum numbers v_X are limited as follows: $v_{SO} \leqslant 16$, $v_{SH} \leqslant 8$, $v_{OH} \leqslant 8$, $v_{OSH} \leqslant 8$, $v_{HOS} \leqslant 8$, and $v_{HSOH} \leqslant 18$. The total basis set is also truncated by the energy cutoff E^{cutoff} = 19000 cm^{-1}. That is, in setting up the Hamiltonian matrix, we use only those basis function products in Eq. (9) for which $E_{SO}(v_{SO}) + E_{SH}(v_{SH}) + E_{OH}(v_{OH}) + E_{HOS}(v_{HOS}) + E_{OSH}(v_{OSH}) + E^{(\tau_{tor})}_{HOSH}(v_{HOSH}) \leqslant E^{cutoff}$ [14]. Here, $E_X(v_X)$ is the 1D eigenenergy associated with the wavefunction $|v_X\rangle$ (where X = SO, SH, OH, HOS, OSH); this energy is obtained in the Numerov–Cooley integration. Furthermore, $E^{(\tau_{tor})}_{HOSH}(v_{HOSH})$ is the 1D eigenenergy corresponding to the wavefunction $|v_{HSOH},\tau_{tor}\rangle$. The 1D functions $|v_{SO}\rangle$, $|v_{SH}\rangle$, $|v_{OH}\rangle$, $|v_{HOS}\rangle$, and $|v_{OSH}\rangle$ are all totally symmetric (*i.e.*, of A' symmetry) in $\mathbf{C}_s$(M) [29], whereas $|v_{HSOH},\tau_{tor}\rangle$ has A' (A'') symmetry for τ_{tor} = 0(1). In consequence, the vibrational basis function $|\phi_{vib}\rangle$ in Eq. (9) has A' (A'') symmetry for τ_{tor} = 0(1), and the matrix representation of the vibrational Hamiltonian (*i.e.*, the matrix obtained for J = 0) is block diagonal in τ_{tor}. Thus, for J = 0 we diagonalize two matrix blocks with dimensions 16359 and 14716, respectively, one corresponding to each of the two irreducible representations A' and A'' of $\mathbf{C}_s$(M) [29].

The calculated term values for the fundamental levels v_k and the corresponding values for the torsional splitting are listed in Table 2 and compared to the experimental values available and to other theoretical values. As Supplementary material, we give a more extensive list of term values. The A(Q+*d*)Z* theoretical term value for the OH-stretch fundamental level deviates by only 0.3 cm^{-1} from the experimental gas phase value [7]. For the SH stretching motion, the analogous deviation is larger (6.4 cm^{-1}) which may partly be attributed to the strong interaction between the SH-stretching mode and the torsional mode as discussed in more detail in Section 5 below.

For the OH-stretch term value, the agreement with gas-phase experiment has improved significantly relative to the cc-pVQZ [6] and cc-pV(T+*d*)Z [27] theoretical predictions (Table 2). For the SH-stretch term value, however, it is the other way around; the cc-pVQZ [6] and cc-pV(T+*d*)Z [27] values are in better agreement with experiment than the new A(Q+*d*)Z* value. For the HOS bend, the SO stretch, and the torsion, the theoretical values from the present work are very close to the matrix values [6].

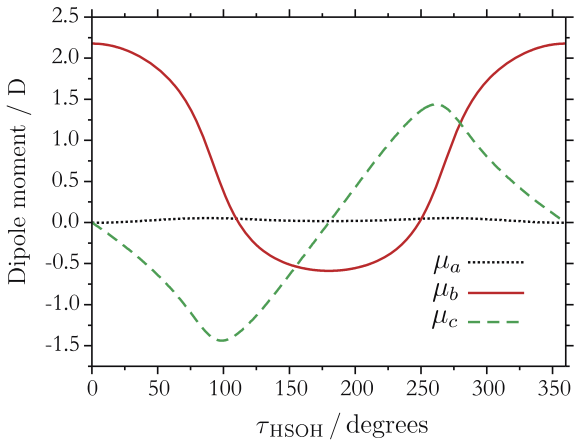

Fig. 3. Dipole moment components for HSOH, computed at the torsional minimum energy path geometries shown in Fig. 1 of Ref. [9].

Table 2
Vibrational term values, torsional splittings (in cm^{-1}) and relative band intensities for the vibrational ground state and the fundamental levels in the electronic ground state of HSOH.

State	Theory			Experiment	
	A(Q+*d*)Z*[a]	cc-pVQZ[b]	cc-pV(T+*d*)Z[c]	Gas-phase[d]	Ar matrix[e]
Vibrational term values					
ν_{OH}	3625.9	3657.2	3640	3625.59260(20)[f]	3608.3
ν_{SH}	2544.4	2536.9	2537	2537.9869(12)[g]	2550.1
ν_{HOS}	1174.0	1188.1	1192		1175.7
ν_{OSH}	1007.7	1004.6	1008		
ν_{SO}	760.0	756.7	760		762.5
ν_{HSOH}	443.0	451.7	457		445.3
State	Theory			Experiment	
	A(Q+*d*)Z*[a]	MP2/cc-pVTZ[h]		Gas-phase[d]	
Torsional splittings					
g.s.	0.00215	0.002339		0.00214[i]	
ν_{OH}	0.0036	0.002177		<0.01[f]	
ν_{SH}	−0.0775	0.001672		0.042(2)[g]	
ν_{HOS}	−0.0335	0.001849			
ν_{OSH}	0.0255	0.002995			
ν_{SO}	0.0546	0.002553			
ν_{HSOH}	0.1279	0.1473			
Band	Theory			Experiment	
	A(Q+*d*)Z*[j]	cc-pVQZ[k]	cc-pV(T+*d*)Z[l]	Ar matrix[e]	
Relative band intensities					
ν_{OH}	16	92	92	43	
ν_{SH}	4	22	21	8	
ν_{HOS}	13	54	55	53	
ν_{OSH}	0	3	3		
ν_{SO}	18	65	69	103	
ν_{HSOH}	100	100	100	54	

[a] Present work.
[b] CCSD(T)/cc-pVQZ *ab initio* calculations from Ref. [6].
[c] CCSD(T)/cc-pV(T+*d*)Z *ab initio* calculations from Ref. [27].
[d] Values derived from gas-phase spectra. Numbers in parentheses are quoted uncertainties in units of the last digit given.
[e] Values derived from Ar-matrix spectra [6].
[f] Ref. [7].
[g] Ref. [10].
[h] Ref. [28].
[i] Ref. [1].
[j] Calculated from the transition moments and transition wavenumbers in Table 3 below.
[k] CCSD(T)/cc-pVQZ harmonic calculation [6].
[l] Derived from the CCSD(T)/cc-pV(T+*d*)Z harmonic-calculation results of Ref. [27].

In comparing the fundamental-level term values obtained in the present work with the previous theoretical values [6,27] (see Table 2), we should note that the *ab initio* calculations of Ref. [6] are made with the CCSD(T)/cc-pVQZ method in an all-electron treatment, the fundamental vibrational wavenumbers being determined from the *ab initio* data by perturbation methods. Denis [27] uses the CCSD(T)/cc-pV(T+*d*)Z *ab initio* method in the frozen-core approximation and determines the fundamental vibrational wavenumbers from the *ab initio* data by perturbation methods. In the present work, we produce an analytical representation of the PES based on CCSD(T)/aug-cc-pVTZ and CCSD(T)/aug-cc-pV(Q+*d*))Z *ab initio* data obtained in the frozen-core approximation, and we determine the fundamental vibrational wavenumbers in a variational approach. The various differences in the treatment all affect the computed wavenumbers, probably easily by several cm^{-1}. Therefore, the essentially perfect agreement with experiment obtained for the OH-stretch fundamental term value in the present work, and for the SH-stretch fundamental term value in Refs. [6] and [27], is probably fortuitous in all cases.

For the torsional splitting in the vibrational ground state (experimentally derived value: 0.00214 cm^{-1}; theoretical value from the present work: 0.00215 cm^{-1}), the excellent agreement between A(Q+*d*)Z* theory and experiment may also be to some extent accidental. Experimentally, the splitting for the SH fundamental level has an absolute value of (0.042 ± 0.002) cm^{-1} [10]; the sign cannot be determined. The theoretical value from the present work is -0.0775 cm^{-1} (Table 2). The less perfect agreement for this splitting could be caused by the fact that, owing to deficiencies of the PES, one of the split energy levels may come close to another level of the same symmetry, and the resulting interaction may then significantly change the splitting by amounts on the order of 0.1 cm^{-1}. However, on the positive side we correctly predict a larger absolute value for the splitting in the SH fundamental level relative to the vibrational ground state, in qualitative agreement with experiment. By contrast, Quack and Willeke [28] predict the SH-stretch-fundamental-level splitting to be 0.001672 cm^{-1}, a value slightly lower than that for the ground state. The fact that we obtain a negative value for the SH-stretch-fundamental-level splitting cannot be confirmed (or refuted) by experiment since, at the present time, experiment provides only the absolute value of this splitting. Our theoretical value of 0.0036 cm^{-1} for the OH-stretch-fundamental-level splitting is consistent with the experimental finding that this splitting is less than 0.01 cm^{-1}.

Along with the band centers we compute also the vibrational transition moments defined as

$$\bar{\mu}_{if} = \sqrt{\sum_{\alpha=a,b,c} |\langle \Phi_{vib}^{(f)} | \bar{\mu}_\alpha | \Phi_{vib}^{(i)} \rangle|^2}, \quad (10)$$

where $|\Phi_{vib}^{(w)}\rangle$, $w = i$ or f, are vibrational wavefunctions ($J = 0$), and $\bar{\mu}_\alpha$ is the component of $\bar{\mu}$ along the molecule-fixed α(=a, b, and c) axis. The matrix elements are generated using the vibrational eigenfunctions obtained from the variational calculations in conjunction with the *ab initio* A(Q+*d*)Z* potential energy and A(T+*d*)Z dipole moment surfaces.

The transition moments $\bar{\mu}_{if}$ for the fundamental bands of HSOH and for the torsional overtones are compiled in Table 3, where we also list the individual matrix elements $\bar{\mu}_\alpha^{if} = \langle \Phi_{vib}^{(f)} | \bar{\mu}_\alpha | \Phi_{vib}^{(i)} \rangle$, $\alpha = a, b, c$, from Eq. (10). As Supplementary material, we give a more extensive list of transition moments. The expectation values of the dipole moment components in the vibrational ground state are found to be significantly smaller than the corresponding *ab initio* equilibrium dipole moment values μ_a^{eq}, μ_b^{eq}, and μ_c^{eq}. As mentioned in Section 3.2, this is a consequence of the vibrational averaging. Consequently, the 'permanent dipole moment' components μ_a^{eq}, μ_b^{eq}, and μ_c^{eq} cannot be used to estimate the line strengths [29] for rotational transitions of HSOH.

In Table 2, under the heading A(Q+*d*)Z*, we have included relative band intensities calculated from the transition moments and transition wavenumbers in Table 3. We obtain these relative intensities by calculating, for each fundamental band, the value of $\sum \tilde{\nu}_{if} \bar{\mu}_{if}^2$ (Table 3), where the sum is over the four torsional components of the band in question, and forming ratios of these quantities. These relative intensities can be roughly compared to those resulting from CCSD(T) calculations carried out at the cc-pVQZ [6] and cc-pV(T+*d*)Z [27] levels of theory, and to values obtained from the Ar-matrix spectrum [6]. These previous values are all included in Table 2. Concerning the comparison between the relative intensity results of the present work with the previous theoretical results [6,27], it should be noted that the cc-pVQZ [6] and cc-pV(T+*d*)Z [27] results are obtained under the assumption of all vibrational modes, including the torsion, being harmonic, and the intensities depending solely on the first derivatives of the DMS with respect to the vibrational coordinates. In computing the dipole moment matrix elements in Table 3 we, by contrast, use 'fully coupled', variationally determined wavefunctions and the complete DMS. We note in Table 2 that the relative intensities resulting from the cc-pVQZ [6] and cc-pV(T+*d*)Z [27] calculations are very similar but that the A(Q+*d*)Z* results of the present work deviate significantly from these previous results. We attribute the deviation to our more complete treatment of the nuclear motion, in particular of the torsion. To substantiate this assertion we have made a TROVE calculation which emulates the cc-pVQZ [6] and cc-pV(T+*d*)Z [27] calculations: In this calculation, we use the PES and DMS of the present work, but we describe the nuclear motion by means of a normal-coordinate Hamiltonian (using normal coordinates for all vibrational modes, including the torsion), and we truncate the potential energy expansion after the harmonic second-order terms and the dipole moment expansion after the linear terms. This simplified calculation gives relative-intensity ratios of $I(\nu_{OH}):I(\nu_{SH}):I(\nu_{HOS}):I(\nu_{OSH}):I(\nu_{SO}):I(\nu_{HSOH})$ = 100:14:58:3:80:100, in broad agreement with the cc-pVQZ [6] and cc-pV(T+*d*)Z [27] relative-intensity results in Table 2. The agreement demonstrates that the PES and DMS of the present work are similar to those of Refs. [6,27] and that the introduction, in TROVE, of anharmonicity, and of the correct double-minimum description of the torsional motion, significantly influences the relative intensities, leading to the A(Q+*d*)Z* results in Table 2. It is seen from the table that the most significant anharmonicity effect is a strengthening of the ν_{HSOH} band relative to the other bands.

The comparison between the theoretical intensities, which are valid for an isolated molecule in the gas phase, and the Ar-matrix results should be made with some caution since the Ar-matrix intensities are believed to be rather uncertain; they may have uncertainties of 20–30% [31]. Also, it is known from experience [31] that the band intensities of a matrix spectrum sometimes deviate very strongly from those of the corresponding gas-phase spectrum, whereas the energy shifts relative to gas-phase spectra are normally small. The Ar-matrix results in Table 2 indicate that the ν_{OH} and ν_{HOS} bands are of comparable intensity, that the ν_{SO} band is stronger than these two bands while the ν_{SH} band is somewhat weaker, and that the ν_{OSH} band is very weak. The A(Q+*d*)Z* prediction of the present work is, in fact, in keeping with these results, even though the predicted ratios of $I(\nu_{OH})/I(\nu_{SO})$ = 16/18 and $I(\nu_{HOS})/I(\nu_{SO})$ = 13/18 are much larger than the observed Ar-matrix ratios of 43/103 and 53/103, respectively. Whereas our A(Q+*d*)Z* calculation predicts the ν_{OH} and ν_{HOS} bands to be of comparable intensity (A(Q+*d*)Z* ratio 16:13, Ar-matrix ratio 43:53), the cc-pVQZ [6] and cc-pV(T+*d*)Z [27] calculations predict the ν_{OH} band to be significantly stronger than the ν_{HOS} band (predicted ratios 92:54 and 92:55, respectively). All three theoretical calculations predict the ν_{SH} band to be about four times weaker than the ν_{OH} band; this is in good agreement with a recent, accurate experimental determination (which will be discussed further in Section 5) of this intensity ratio from a gas-phase spectrum [7]. The Ar-matrix spectrum gives a ν_{OH}/ν_{SH} intensity ratio of 43/8 ≈ 5.4, in broad agreement with the accurate gas-phase result. The ν_{OSH} band is predicted to be quite weak by all theoretical calculations and, correspondingly, it is not observed in the Ar-matrix spectrum. The theoretical relative intensities in Table 2 all have in common that

Table 3
Band centers $\tilde{\nu}_{if}$ (in cm^{-1}), vibrational transition moments $\bar{\mu}_{if}$ (in D), and individual transition moment components ($\bar{\mu}_a^{if}, \bar{\mu}_b^{if}, \bar{\mu}_c^{if}$) (in D) for selected vibrational transitions of HSOH.

Vibrational state[a]				Transition moments		
i	f	$\tilde{\nu}_{if}$	$\bar{\mu}_{if}$	$\bar{\mu}_a^{if}$	$\bar{\mu}_b^{if}$	$\bar{\mu}_c^{if}$
0^+	0^+	0.000	0.699	0.040	0.698	
0^-	0^-	0.000	0.699	0.040	0.698	
0^+	0^-	0.002	1.297			−1.297
0^-	ν_{HSOH}^+	442.984	0.092			−0.092
0^+	ν_{HSOH}^+	442.986	0.527	−0.007	−0.527	
0^-	ν_{HSOH}^-	443.112	0.528	0.007	0.527	
0^+	ν_{HSOH}^-	443.114	0.092			0.092
0^-	ν_{SO}^+	759.951	0.028			0.028
0^+	ν_{SO}^+	759.953	0.173	−0.170	0.030	
0^-	ν_{SO}^-	760.006	0.173	0.170	−0.029	
0^+	ν_{SO}^-	760.008	0.028			−0.028
0^-	$2\nu_{HSOH}^+$	843.130	0.134			−0.134
0^+	$2\nu_{HSOH}^+$	843.132	0.052	−0.034	−0.039	
0^-	$2\nu_{HSOH}^-$	846.267	0.051	−0.033	−0.038	
0^+	$2\nu_{HSOH}^-$	846.269	0.135			−0.135
0^-	ν_{OSH}^+	1007.666	0.004			0.004
0^+	ν_{OSH}^+	1007.669	0.015	0.008	−0.012	
0^-	ν_{OSH}^-	1007.692	0.014	0.008	−0.012	
0^+	ν_{OSH}^-	1007.694	0.003			0.003
0^-	ν_{HOS}^-	1173.967	0.118	0.118	−0.007	
0^+	ν_{HOS}^-	1173.969	0.013			0.013
0^-	ν_{HOS}^+	1174.000	0.012			−0.012
0^+	ν_{HOS}^+	1174.002	0.117	−0.117	0.001	
0^-	ν_{SH}^-	2544.278	0.044	0.022	−0.038	
0^+	ν_{SH}^-	2544.280	0.000			
0^-	ν_{SH}^+	2544.356	0.000			
0^+	ν_{SH}^+	2544.358	0.044	0.022	−0.038	
0^-	ν_{OH}^+	3625.860	0.055			−0.055
0^+	ν_{OH}^+	3625.862	0.052	0.052	−0.005	
0^-	ν_{OH}^-	3625.863	0.052	−0.052	0.005	
0^+	ν_{OH}^-	3625.865	0.055			0.055

[a] A superscript − (+) signifies that the state in question has − (+) parity under the inversion operation E^* [29].

they predict the torsional fundamental band ν_{HSOH} to be the strongest fundamental band. This is in contrast to the Ar-matrix results where the ν_{SO} band is strongest which suggests that the intensity of the torsional band is strongly influenced by the presence of the Ar matrix.

5. The ν_{OH} and ν_{SH} fundamental bands

The rotation–torsion spectra associated with the transitions to the OH-stretch [7] and SH-stretch [7,10] fundamental levels have been experimentally recorded (see Fig. 4). Initial analysis [10] of the SH-stretch fundamental band has shown this band to be heavily perturbed. By contrast, the analogous spectra of the OH-stretch fundamental transition [6,7] appear largely "normal" and unperturbed. We discuss this in theoretical terms.

According to Table 3, the ν_{SH} band consists solely of *a*- and *b*-type transitions. In the formation of the ν_{OH} band the *a* and *c* components of the dipole moment are equally important, while the *b*-component contributes only very little.

Apart from this, we can make the rather trivial observation that the OH-stretching fundamental term value, at 3625 cm^{-1}, is significantly higher than the SH-stretching fundamental term value at 2538 cm^{-1}. At these energies, there is a significant density of excited torsional states and combination states involving bending and torsion. The wavefunctions describing such states at 3625 cm^{-1} involve more quanta of bending and torsional motion than those at 2538 cm^{-1}, so they have more nodes and are expected to produce smaller interaction matrix elements with the basis function for the OH-stretching fundamental level than the torsion/bending states around 2538 cm^{-1} do with the basis function for the SH-stretching fundamental. The 'pure' torsionally excited states found near the ν_{SH} state are $7\nu^{+}_{HSOH}$, $7\nu^{-}_{HSOH}$ $8\nu^{+}_{HSOH}$, and $8\nu^{-}_{HSOH}$ (at 2298.4, 2315.9, 2769.9, and 2730.3 cm^{-1}, respectively), whereas those closest to the ν_{OH} term value are the $9\nu^{+}_{HSOH}$, $9\nu^{-}_{HSOH}$, $10\nu^{+}_{HSOH}$, $10\nu^{-}_{HSOH}$ (at 3244.8, 3237.9, 3828.7, and 3823.7 cm^{-1}, respectively). Here, a superscript −(+) signifies −(+) parity under the inversion operation E^* [29].

Furthermore, Fig. 1 of Ref. [9] suggests that in the PES of HSOH, the SH-stretching mode is more strongly coupled to the torsion than the OH-stretching mode. The optimized value of r_{SH} as a function of a torsional angle shows a distinct variation while the analogous value of r_{OH} varies much less. In the left display of Fig. 5 we show the OH-stretch and SH-stretch harmonic vibrational wavenumbers ω_{OH} and ω_{SH}, respectively, computed from the A(Q+*d*)Z^* PES at the optimized geometries displayed in Fig. 1 of Ref. [9]. We see that ω_{SH} varies essentially more with the torsional angle than does ω_{OH}; this is in keeping with our observation that the coupling between the SH-stretching mode and the torsional mode is larger than that between the OH-stretching mode and the torsional mode. The shaded areas on this figure show the τ_{HSOH}-inter-

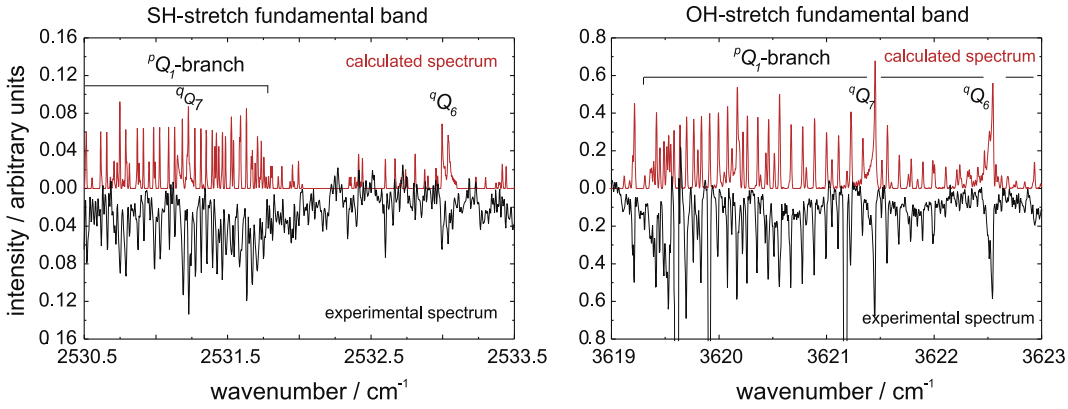

Fig. 4. Comparison of the $^pQ_1$-branch regions of the ν_{OH} and ν_{SH} fundamental stretching bands. The experimental spectra have been recorded using the Bruker IFS 120 HR Fourier transform spectrometer at the University of Wuppertal [6,7,10]. The calculated spectra are obtained at an absolute temperature of 300 K and based on molecular constants from the experimental data analyses given in Refs. [7,10]. The spectrum of the ν_{SH} band is displayed with an ordinate scale magnified 5× relative to that of the ν_{OH} band.

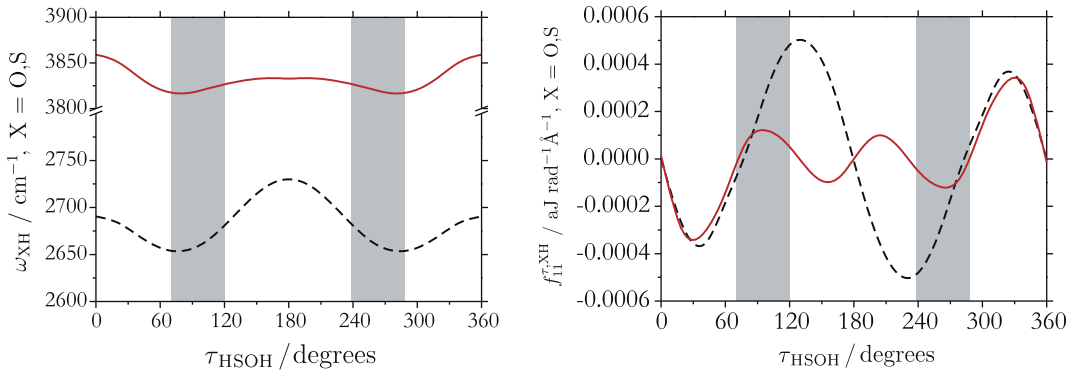

Fig. 5. (left) Harmonic vibrational wavenumbers ω_{OH} (solid curve) and ω_{SH} (dashed curve), computed from the A(Q+*d*)Z^* PES at the optimized geometries displayed in Fig. 1 of Ref. [9]. (right) Second derivatives $f^{\tau,XH}_{11} = \partial^2 V/\partial r_{XH}\partial\tau_{HSOH}$, X = O (solid curve) and S (dashed curve), computed at the optimized geometries displayed in Fig. 1 of Ref. [9]. The shaded areas in the two displays show the τ_{HSOH}-intervals where the vibrational-ground-state torsional wavefunction has an amplitude of more than 50% of the maximum amplitude.

vals where the vibrational-ground-state torsional wavefunction has an amplitude of more than 50% of the maximum amplitude. The right display of Fig. 5 shows the values of the 'mixed' second derivatives $f_{11}^{\tau,XH} = \partial^2 V/\partial r_{XH}\partial\tau_{HSOH}$, X = S and O, computed at the optimized geometries displayed in Fig. 1 of Ref. [9]. The mixed second derivatives confirm that the strongest coupling is found between the torsion and the SH-stretching mode.

As mentioned above, it has been found experimentally [7] that ν_{SH} fundamental band is 4–5 times weaker than the ν_{OH} fundamental band. This is borne out by Fig. 4 where we compare the experimentally measured ${}^pQ_1$ branches of the ν_{OH} and ν_{SH} absorption bands [7,10]. The ratio $I(\nu_{OH})/I(\nu_{SH})$ of the ν_{OH} and ν_{SH} integrated band intensities is determined experimentally [7] as 4.4 ± 0.8. According to the theoretical transition moment values from Table 3 (and the ratio of the band center wavenumbers), the ν_{OH} band is estimated to be about 4.3 times stronger than the ν_{SH} band, in good agreement with the experimental findings. The CCSD(T)/cc-pVQZ calculation from Ref. [6] gives a corresponding ratio of $92/22 \approx 4.2$ (see Table 2).

6. Summary and conclusion

We have used the coupled-cluster CCSD(T) *ab initio* method to generate a high-level potential energy surface, together with a high-level dipole moment surface, for the electronic ground state of HSOH. In the calculation of the potential energy surface, the *ab initio* points characterizing the surface in the low-energy region (up to 12 000 cm^{-1} above equilibrium) are computed using a very large basis (cc-pVQZ for H, aug-cc-pVQZ for O, and aug-cc-pV(Q+*d*)Z for S). Points in the energy region between 12 000 and 20 000 cm^{-1} above equilibrium are calculated with aug-cc-pVTZ basis sets for all nuclei. The two *ab initio* data sets were combined to produce an analytical representation of the PES as explained in Section 3. The dipole moment components were calculated by the CCSD(T)/A(T+*d*)Z method and fitted to analytical functions as explained in Section 3.2.

The analytical representations of the potential-energy and dipole-moment surfaces were used as input for the program TROVE [14] in order to calculate the vibrational energies and transition moments for selected vibrational transitions of HSOH. We find that for HSOH, the transition moment values depend significantly on the theoretical description of the nuclear motion. With our double-minimum description of the torsional motion and anharmonic treatment of the other vibrational modes, we obtain relative intensities for the fundamental bands (Table 2) that differ considerably from the results of the harmonic calculations reported in Refs. [6,27].

As discussed above, the theoretical results of the present work are generally in good agreement with the experimental data available for HSOH. The theoretical results allow us to explain, at least tentatively, extensive perturbations recently found experimentally in the SH-stretch fundamental band of HSOH. The present calculations suggest that the torsional splittings in the fundamental levels ν_{SH}, ν_{HOS}, ν_{OSH}, ν_{SO}, and ν_{HSOH} are significantly larger than that in the vibrational ground state (Table 2). As discussed above, this is consistent with the experimental observation of the SH-stretch fundamental band [7,10]. The previous MP2/aug-cc-pVTZ calculations from Ref. [28] predicted a similarly large increase of the splitting upon excitation of the ν_{HSOH} mode, but gave splittings for the other fundamental levels which are comparable to that of the vibrational ground state (Table 2). We plan an experimental study of the SO-stretch fundamental band to clarify this issue.

Acknowledgments

We are grateful to Prof. Helge Willner for helpful discussions. We acknowledge support from the European Commission (contract no. MRTN-CT-2004-512202 "Quantitative Spectroscopy for Atmospheric and Astrophysical Research" (QUASAAR)).

Appendix A. Supplementary data

Supplementary data for this article are available on ScienceDirect (www.sciencedirect.com) and as part of the Ohio State University Molecular Spectroscopy Archives (http://library.osu.edu/sites/msa/jmsa_hp.htm).

References

[1] G. Winnewisser, F. Lewen, S. Thorwirth, M. Behnke, J. Hahn, J. Gauss, E. Herbst, Chem. Eur. J. 9 (2003) 5501–5510.
[2] M. Behnke, J. Suhr, S. Thorwirth, F. Lewen, H. Lichau, J. Hahn, J. Gauss, K.M.T. Yamada, G. Winnewisser, J. Mol. Spectrosc. 221 (2003) 121–126.
[3] K.M.T. Yamada, G. Winnewisser, P. Jensen, J. Mol. Struct. 695–696 (2004) 323–337.
[4] S. Brünken, M. Behnke, S. Thorwirth, K.M.T. Yamada, T.F. Giesen, F. Lewen, J. Hahn, G. Winnewisser, J. Mol. Struct. 742 (2005) 237–242.
[5] O. Baum, S. Esser, N. Gierse, S. Brünken, F. Lewen, J. Hahn, J. Gauss, S. Schlemmer, T.F. Giesen, J. Mol. Struct. 795 (2006) 256–262.
[6] H. Beckers, S. Esser, T. Metzroth, M. Behnke, H. Willner, J. Gauss, J. Hahn, Chem. Eur. J. 12 (2006) 832–844.
[7] O. Baum, T.F. Giesen, S. Schlemmer, J. Mol. Spectrosc. 247 (2007) 25–29.
[8] O. Baum, M. Koerber, O. Ricken, G. Winnewisser, S.N. Yurchenko, S. Schlemmer, K.M.T. Yamada, T.F. Giesen, J. Chem. Phys. 129 (2008) 224312.
[9] R.I. Ovsyannikov, V.V. Melnikov, W. Thiel, P. Jensen, O. Baum, T.F. Giesen, S.N. Yurchenko, J. Chem. Phys. 129 (2008) 154314.
[10] O. Baum, Ph.D. dissertation, University of Cologne, 2008.
[11] K.M.T. Yamada, P. Jensen, S.C. Ross, O. Baum, T.F. Giesen, S. Schlemmer, J. Mol. Struct. 927 (2009) 96–100.
[12] J.T. Hougen, Can. J. Phys. 62 (1984) 1392–1402.
[13] J.T. Hougen, B. DeKoven, J. Mol. Spectrosc. 98 (1983) 375–391.
[14] S.N. Yurchenko, W. Thiel, P. Jensen, J. Mol. Spectrosc. 245 (2007) 126–140.
[15] J.T. Hougen, P.R. Bunker, J.W.C. Johns, J. Mol. Spectrosc. 34 (1970) 136–172.
[16] P.R. Bunker, B.M. Landsberg, J. Mol. Spectrosc. 67 (1977) 374–385.
[17] MOLPRO, version 2002.3 and 2002.6, a package of *ab initio* programs written by H.-J. Werner, P.J. Knowles, with contributions from R.D. Amos, A. Bernhardsson, A. Berning et al.
[18] C. Hampel, K. Peterson and H.-J. Werner, Chem. Phys. Lett. 190 (1992) 1-12 and references therein. The program to compute the perturbative triples corrections has been developed by M.J.O. Deegan and P.J. Knowles, ibid 227 (1994) 321–326.
[19] G.D. Purvis, R.J. Bartlett, J. Chem. Phys. 76 (1982) 1910–1918.
[20] M. Urban, J. Noga, S.J. Cole, R.J. Bartlett, J. Chem. Phys. 83 (1985) 4041–4046.
[21] K. Raghavachari, G.W. Trucks, J.A. Pople, M. Head-Gordon, Chem. Phys. Lett. 157 (1989) 479–483.
[22] T.H. Dunning, J. Chem. Phys. 90 (1989) 1007–1023.
[23] D.E. Woon, T.H. Dunning, J. Chem. Phys. 98 (1993) 1358–1371.
[24] R.A. Kendall, T.H. Dunning, R.J. Harrison, J. Chem. Phys. 96 (1992) 6796–6806.
[25] A.K. Wilson, T.H. Dunning, J. Chem. Phys. 119 (2003) 11712–11714.
[26] S.N. Yurchenko, H. Lin, J.J. Zheng, P. Jensen, W. Thiel, J. Chem. Phys. 123 (2005) 134308.
[27] P.A. Denis, Mol. Phys. 106 (2008) 2557–2567.
[28] M. Quack, M. Willeke, Helv. Chim. Acta 86 (2003) 1641–1652.
[29] P.R. Bunker, P. Jensen, Molecular Symmetry and spectroscopy, second ed., NRC Research Press, Ottawa, 1998.
[30] J.W. Cooley, Math. Comp. 15 (1961) 363–374.
[31] H. Willner, private communication.

Thermal averaging of the indirect nuclear spin-spin coupling constants of ammonia (NH_3): the importance of the large amplitude inversion mode

A. Yachmenev, S. N. Yurchenko, I. Paidarova, P. Jensen, W. Thiel, S. P. A. Sauer

J. Chem. Phys., **132**, 114305 (2010)

Thermal averaging of the indirect nuclear spin-spin coupling constants of ammonia: The importance of the large amplitude inversion mode

Andrey Yachmenev,[1] Sergei N. Yurchenko,[2] Ivana Paidarová,[3] Per Jensen,[4] Walter Thiel,[1] and Stephan P. A. Sauer[5,a)]

[1]*Max-Planck-Institut für Kohlenforschung, Kaiser-Wilhelm-Platz 1, D-45470 Mülheim an der Ruhr, Germany*
[2]*Physikalische Chemie, Technische Universität Dresden, Mommsenstr. 13, D-01062 Dresden, Germany*
[3]*J. Heyrovský Institute of Physical Chemistry, Academy of Sciences of the Czech Republic, Dolejškova 3, CZ 182 23 Praha 8, Czech Republic*
[4]*Fachbereich C-Theoretische Chemie, Bergische Universität, D-42097 Wuppertal, Germany*
[5]*Department of Chemistry, University of Copenhagen, Universitetsparken 5, DK-2100 Copenhagen Ø, Denmark*

(Received 25 January 2010; accepted 22 February 2010; published online 18 March 2010)

Analytic internal-coordinate representations are reported for two accurate *ab initio* spin-spin coupling surfaces of the ammonia molecule, ^1J (^{15}N,H) and ^2J(H,H). Calculations were carried out at the level of the second-order polarization propagator approximation involving coupled-cluster singles and doubles amplitudes (CCSD) and using a large specialized basis set, for a total of 841 different geometries corresponding to 2523 distinct points on the ^1J (^{15}N,H) and ^2J(H,H) surfaces. The results were fitted to power series expansions truncated after the fourth-order terms. While the one-bond nitrogen-hydrogen coupling depends more on the internuclear distance, the geminal hydrogen-hydrogen coupling exhibits a pronounced dependence on the bond angle. The spin-spin parameters are first vibrationally averaged, using vibrational wave functions obtained variationally from the TROVE computer program with a CCSD(T) based potential energy surface, for ammonia and its various deuterated isotopologues. The vibrationally averaged quantities are then thermally averaged to give values of the couplings at absolute temperatures of 300 and 600 K. We find that the nuclear-motion corrections are rather small. The computed one-bond couplings and their minute isotope effects are in excellent agreement with the experimental values. © *2010 American Institute of Physics*. [doi:10.1063/1.3359850]

I. INTRODUCTION

Accurate calculations of nuclear magnetic resonance indirect nuclear spin-spin coupling constants J have long been a challenge for theoretical chemistry.[1–3] The form of the one-electron operators for the interaction between the nuclear spin and the electrons—in particular the Fermi contact (FC) operator, which measures the spin density at the position of the nucleus, and the paramagnetic nuclear spin–electronic orbit (PSO) operator, which includes the electronic angular momentum operator—makes it necessary to use specially optimized basis sets.[4–14] Furthermore the FC and spin-dipolar (SD) contributions are obtained, in principle, as sums over excited triplet states for a closed shell molecule, and this requires a considerable amount of electron correlation to be included in the calculation. Self-consistent-field (SCF) linear response calculations often suffer from triplet instabilities or quasi-instabilities,[6,8,15–22] which renders SCF results for J unreliable. This happens in particular for systems with many lone-pairs or π-electrons, but can be overcome in sufficiently correlated wave function methods. Also density functional theory (DFT) with standard functionals has problems with reproducing spin-spin coupling constants for atoms with several lone-pairs such as fluorine.[23–26]

Nevertheless, with appropriate basis sets and correlated methods such as the second order polarization propagator approximation with coupled cluster singles and doubles amplitudes [SOPPA(CCSD)] method,[6,27] multiconfigurational self-consistent field linear response theory (MCSCF-LR)[28,29] using wave functions with sufficiently large active spaces or coupled cluster methods,[30–35] the calculations become sufficiently accurate that minor effects such as relativistic corrections and the influence of nuclear motion determine the remaining errors. The influence of molecular vibrations on the spin-spin coupling constants has therefore been the topic of several studies using SOPPA(CCSD),[36–49] MCSCF-LR,[29,44,50–52] or even DFT.[53–55] Zero-point vibrational corrections to one-bond X–H (X=C, O, F, Si) coupling constants amount typically to 5% whereas the corrections to geminal H–H coupling constants can be even larger. Small changes in the coupling constants of CH_4,[42,56,57] H_2O,[43,52,57] HF,[51] C_2H_2,[45,47] and SiH_4 (Refs. 49 and 57) such as isotope effects or temperature dependence can be reproduced in this way.

These calculations require the value of the spin-spin coupling constants not only for a single nuclear conformation, but for a particular vibrational state, and this implies that the

a)Author to whom correspondence should be addressed. Electronic mail: sauer@kiku.dk.

spin-spin coupling constant as a function of the internal nuclear coordinates has to be averaged over the corresponding vibrational wave function. This can be done either directly by numerically averaging the coupling constant surface over numerical vibrational wave functions[36,44] or by first performing a Taylor expansion of the coupling constant surface around the equilibrium geometry to a given order in internal[37,42,43,45,47,49] or normal coordinates[29,50–54] to facilitate the averaging over the vibrational wave functions. The Taylor expansion is typically truncated after the quadratic terms such that only first and second derivatives of the coupling constants at the equilibrium geometry are needed. The vibrational wave functions are normally obtained by first order perturbation theory with the exception of one recent study[55] which employed several variational methods.

NH_3 is obviously missing in the list of recent vibrational-averaging calculations employing high level wave function methods. It differs from most of the other molecules studied so far in having a large amplitude inversion mode that cannot be treated appropriately by perturbation theory. The two symmetric isotopologues NH_3 and ND_3 can be handled by the nonrigid invertor method of Špirko and co-workers.[58,59] Using this approach, vibrationally averaged values of several other molecular properties of ammonia have been obtained,[60–65] but the spin-spin coupling constants have not been calculated. However, the nonrigid invertor method was employed in the calculation of vibrationally averaged spin-spin coupling constants of the oxonium ion.[44]

On the other hand, the perturbation-theory approach was applied to the spin-spin coupling constants of ammonia in a recent DFT study[53] and in two older studies.[66,67] Kowalewski and Roos[66] employed a configuration interaction singles and doubles wave function with a basis set of double zeta plus polarization quality and studied only corrections to the geminal H–H coupling constant from the two totally symmetric vibrational modes. As vibrational wave functions for the two symmetric modes, they used linear combinations of products of Hermite functions. They observed that the geminal hydrogen coupling constant becomes increasingly negative upon inclusion of vibrational corrections. Solomon and Schulman[67] studied the N–H as well as the H–H coupling but only at the semi-empirical intermediate neglect of differential overlap (INDO) level. In the vibrational averaging, they considered all normal modes and expressed the vibrational wave functions as products of harmonic oscillator wave functions apart from the inversion mode, which they treated numerically. This implies that they neither included the couplings between the modes nor the contributions from the anharmonic force constants. They found that the calculated zero-point vibrational corrections depend strongly on the kind of wave function used for the inversion mode. Employing harmonic oscillator wave functions they obtained a zero-point vibrational correction for the geminal hydrogen coupling similar to that of Kowalewski and Roos,[66] whereas treating the inversion mode numerically reduces the zero-point vibrational correction by more than 50%. For the nitrogen-hydrogen one-bond coupling, they observed a similar strong dependence on the chosen treatment of the inversion mode, but here the zero-point vibrational correction more than doubles when the inversion mode is treated numerically. In any case, they find that the one-bond nitrogen-hydrogen coupling constant also becomes increasingly negative upon inclusion of vibrational corrections. Finally, Ruden *et al.*[53] employed not only zeroth order vibrational wave functions expressed as products of harmonic oscillator wave functions, but also the first order wave functions which account for couplings between vibrational modes and contributions from the anharmonic force constants. The inversion mode, however, was treated like the other vibrational modes. The necessary spin-spin coupling constant geometrical derivatives as well as the force constants were calculated at the DFT level employing the B3LYP functional and a basis set optimized for the calculation of coupling constants. Contrary to the previous studies Ruden *et al.*[53] found that the zero-point vibrational corrections to both couplings are positive and that in the case of the one-bond nitrogen-hydrogen coupling, the zero-point vibrational correction is an order of magnitude smaller than the value of Solomon and Schulman.[67]

In view of the above, we have reinvestigated the vibrational corrections to the coupling constants in ammonia using state-of-the-art correlated wave function methods. Contrary to earlier studies, we have not employed perturbation theory in the calculation of the vibrational corrections, but have for the first time directly averaged the multidimensional coupling constant surfaces obtained at the SOPPA(CCSD) level using accurate rovibrational wave functions. The latter were determined by means of the variational approach TROVE[68] in conjunction with a highly accurate potential energy surface of ammonia by Yurchenko *et al.*[69] For the averaging, the matrix exponential technique[70] was implemented in TROVE and utilized. In the following, the averaging over rovibrational states will be referred to as "thermal averaging," indicating that we use all rovibrational states populated according to the Boltzmann distribution at $T=300$ and 600 K. In the present work we have only considered the spin-spin coupling constant, i.e., the trace of the spin-spin coupling tensor. However, the same approach could be applied to all tensor elements in order to obtain the thermally averaged anisotropy of the coupling constants.

Finally, we note that the vapor-to-liquid shift of the coupling constants in NH_3 has been studied very recently by Gester *et al.*[71] employing a sequential QM/MM approach at the DFT(B3LYP) level of theory. For the experimentally inaccessible $^2J(\mathrm{H},\mathrm{H})$ parameter in NH_3, a shift of -2.5 Hz was predicted, whereas the shift for ^1J $(^{15}\mathrm{N},\mathrm{H})$ was computed to be 0.5 Hz, i.e., very small when compared to the results of a similar recent study on water.[72]

The paper is structured as follows. In Sec. II we discuss first the values of the spin-spin coupling constants at the equilibrium geometry before we consider the effects of averaging in Sec. III.

II. ELECTRONIC STRUCTURE CALCULATIONS

A. Computational details

It has been described many times (see, for example, Refs. 1 and 73) how to calculate the four Ramsey[74] contributions (FC, SD, paramagnetic, and diamagnetic spin-orbit) to the indirect nuclear spin-spin coupling constants using response theory methods.[73,75] The linear response functions employed in the present work were either based on MCSCF wave functions,[28,29] or they were obtained from Møller–Plesset perturbation theory as implemented in the SOPPA(CCSD) method[6,27] and in its parent method, the SOPPA.[6,76–79] The MCSCF wave functions were either of the complete active space (CAS) type[80] or of the restricted active space (RAS) type.[81] The choice of active orbitals (2–6 a_1 and 1–4 e) in the CAS calculation and (2–10 a_1 and 1–4 e in RAS 2, 11–13 a_1, and 5–7 e in RAS 3 with singles and doubles excitations from RAS 2 to RAS 3) in the RAS calculation was based on the natural orbital occupation numbers of a second order Møller–Plesset (MP2) calculation.[82,83] Both MCSCF calculations were started from the MP2 natural orbitals calculated with the inactive orbitals of the MCSCF calculation kept frozen. In all calculations, the diamagnetic spin-orbit (DSO) contribution was obtained not as a linear response function[84] but as a ground state average value. At the SOPPA and SOPPA(CCSD) level of theory, this involves the same unrelaxed one-density matrix as used elsewhere in the SOPPA and SOPPA(CCSD) approaches.[27,85] All electronic structure calculations were carried out with the 2.0 version of the DALTON program package.[6,27,29,78,86–88]

Accurate calculations of spin-spin coupling constants require either very large standard basis sets or smaller, specially optimized basis sets. We have used the second option in this work, as we need to calculate a whole coupling constant surface. The coupling constants in ammonia are similar to those of water and methane in that they are dominated by the Fermi-contact contribution, which can only be calculated accurately with extra tight s-type functions in the basis set. The basis set for hydrogen was taken from the previous study of the spin-spin coupling constants of H_2O,[43] whereas a new nitrogen basis set was devised, corresponding to the oxygen basis set used in Ref. 43. The chosen basis set consists of 17s-, 7p-, 5d-, and 2f-type primitive spherical Gaussian functions for nitrogen and of 11s-, 2p-, and 2d-type primitive spherical Gaussian functions for hydrogen. The s-type functions for nitrogen were taken from van Duijneveldt's[89] 13s8p basis set and were augmented by one diffuse (with exponent ζ_s=0.055 555) and three tight functions (with exponents ζ_s=502 471.053 087, 3 377 091.588 02, and 22 697 322.6095), whereas the p-type functions are from van Duijneveldt's[89] 13s7p basis set. The polarization functions for nitrogen are from Dunning's[90] 3d2f basis set augmented by two tight d-type functions with exponents ζ_d=2.837 and 8.315. The s-type functions for hydrogen are van Duijneveldt's[89] 7s basis set augmented by four tight s-type functions with exponents ζ_s=1258.122 088, 8392.099 358, 55 978.137 820, and 373 393.090 348. The polarization functions for hydrogen are Dunning's[90] 2p and 2d basis sets.

B. Calculations at equilibrium geometry

Tables I and II give values for ^1J (^{15}N,H) and ^2J(H,H), and for the various terms contributing to them, for the ammonia molecule at equilibrium geometry. Our MCSCF, SOPPA, and SOPPA(CCSD) values are compared with results from a selection of earlier papers.[1,9,30,34,53,57,66,67,71,91–97] We note that there is perfect agreement between the results of our SOPPA(CCSD) and the computationally much more demanding $^{10}RAS^{94}_{33SD}$ calculations for both coupling constants. This is in line with earlier findings[43–45] and supports our choice of SOPPA(CCSD) for calculating the coupling constant surfaces. Furthermore, the SOPPA results are in closer agreement with the SOPPA(CCSD) and $^{10}RAS^{94}_{33SD}$ results than the $^{10}CAS^{54}$ results. This underlines the importance of dynamical correlation effects involving many more orbitals than the ones normally included in the CAS approach for the calculation of spin-spin coupling constants.

Finally, we find that in general, our results compare well with the results of earlier correlated calculations. Some of the differences can be attributed to differences in the chosen geometry. This is, for example, the case when we compare the present results with those from earlier SOPPA calculations.[34] Many calculations, including the present ones, were done at the experimental equilibrium geometry [r_{NH}=1.0124 Å, ∠(HNH)=106.67°][98] while some of the earlier studies employed a slightly shorter bond length (1.0116–1.012 Å)[34,66,71] and a wider bond angle [∠(HNH)=107.10° or ∠(HNH)=108.067°].[34,71] Other calculations were done at optimized geometries.[53,94,96,97] Another more important reason for the deviations is the difference in basis sets. Specialized basis sets were only employed in some of the more recent studies.[9,53,57,71,94–96] Generally speaking, however, there is very good agreement between the best previous and present results (keeping in mind the subtle differences in geometry).

Tables I and II show that both couplings are dominated by the FC contribution. However, in order to calculate the one-bond ^1J (^{15}N,H) coupling constant accurately, it is necessary to include also the PSO contribution, which amounts to about 5% of the total coupling constant. Similarly, the sum of the PSO and DSO terms contributes about 10% of the geminal ^2J(H,H) coupling constant. In this respect, ammonia behaves like the other second row hydrides.[42,43] Electron correlation reduces the FC contribution to ^1J (^{15}N,H) and ^2J(H,H) by ~21% and ~54%, respectively, while the changes in the other contributions are negligible.

To generate the vibrational wave functions used in the vibrational averaging (see below) we employ the CCSD(T)-based spectroscopic potential energy surface of $^{14}NH_3$ from Ref. 69, with the equilibrium geometry at r_{NH}=1.0103 Å and ∠(HNH)=106.72°. The nuclear eigenfunctions are obtained as the variational solution of the rovibrational Schödinger equation on this potential energy surface. The corresponding equilibrium values of ^1J (^{15}N,H) and ^2J(H,H), also given in Tables I and II, serve as reference points for calculating the vibrational and thermal effects on these properties. It should be noted that the choice of the equilibrium geometry does affect the one-bond ^1J (^{15}N,H) coupling constant: the change from the experimental to the

TABLE I. Calculated nitrogen-proton coupling constants, ^1J (^{15}N,H), of ammonia at equilibrium geometry. All values are in Hz and are presented in order of the date of publication.

Method	Basis set	Ref.	r_{NH} (Å)	∠(HNH)	$^1J^{FC}_{eq}$	$^1J^{SD}_{eq}$	$^1J^{DSO}_{eq}$	$^1J^{PSO}_{eq}$	$^1J_{eq}$
INDO	n/a	67	1.0136	106.67°	⋯	⋯	⋯	⋯	−35.01
SOS-CI	6–31G	91	Not specified		−72.28	0.08	−0.19	−2.51	−74.91
SCF	6–311G**	92	1.0124	106.67°	−63.60	0.03	−0.10	−2.86	−66.54
EOM	6–311G**	92	1.0124	106.67°	−54.10	−0.02	−0.10	−2.47	−56.68
SCF	Varying[a]	93	1.012 395	106.67°	−63.29	0.07	−0.10	−2.57	−65.89
FF-MBPT[2]	Varying[a]	93	1.012 395	106.67°	−57.54	0.04	−0.11	−2.44	−60.07
SCF	Nonstandard[b]	30	1.012 395	106.67°	−71.53	0.04	−0.10	−2.45	−74.04
EOM-CCSD	Nonstandard[b]	30	1.012 395	106.67°	−56.38	−0.10	−0.11	−2.06	−58.65
^{10}CAS^{94} SCF	HuzIV	1	Experimental		−56.25	⋯	⋯	⋯	−59.27
DFT/B3LYP	HuzII-su3	94	Optimized		⋯	⋯	⋯	⋯	−63.70
^{10}RAS$^{52}_{14,8SD}$ SCF	HuzIII-su4	95	1.0124	106.67°	−58.05	−0.13	−0.08	−2.86	−61.15
^{10}CAS^{94} SCF	aug-cc-pVQZ-su1	96	Optimized		⋯	⋯	⋯	⋯	−61.70
^{10}CAS^{52} SCF	aug-cc-pVTZ	97	Optimized		⋯	⋯	⋯	⋯	−61.84
DFT/B3LYP	HuzIII-su3	53	Optimized		⋯	⋯	⋯	⋯	−64.10
DFT/B3LYP	cc-pCV5Z-sd+t	9	1.0124	106.67°	−60.7	−0.3	0.0	−3.2	−64.4
SOPPA	qzp/qz2p	34	1.0117	108.067°	⋯	⋯	⋯	⋯	−63.9
EOM-CCSD	qzp/qz2p	34	1.0117	108.067°	⋯	⋯	⋯	⋯	−61.5
SOPPA(CCSD)	aug-cc-pVTZ-Juc	57	1.0124	106.67°	⋯	⋯	⋯	⋯	−61.59
DFT/B3LYP	aug-cc-pVTZ-J	71	1.012	107.10°	−60.75	−0.24	−0.07	−3.10	−64.37
SCF	This work		1.0124	106.67°	−75.22	−0.02	−0.06	−3.07	−78.37
^{10}CAS^{54} SCF	This work		1.0124	106.67°	−60.8	−0.17	−0.07	−2.91	−63.95
^{10}RAS$^{94}_{33SD}$ SCF	This work		1.0124	106.67°	−58.98	−0.18	−0.07	−2.93	−62.17
SOPPA	This work		1.0124	106.67°	−59.28	−0.15	−0.07	−2.94	−62.43
SOPPA(CCSD)	This work		1.0124	106.67°	−58.87	−0.18	−0.07	−2.97	−62.09
SOPPA[c]	This work		1.0103	106.72°	⋯	⋯	⋯	⋯	−62.31

[a]Basis set: 6–311G** (FC), 6–31G (SD), 6–31G** (OP, OD).
[b]Basis set: N: (10s6p1d)→[6s3p1d], H: (6s1p)→[4s1p].
[c]SOPPA(CCSD) value at the reference equilibrium geometry (see text).

CCSD(T) equilibrium geometry results in a difference of 0.22 Hz which, as will be seen below, is almost as large as the vibrational correction.

C. Spin-spin coupling surfaces

Taking into account the symmetry of NH_3, it can be shown that the six spin-spin coupling constant surfaces ^1J (^{15}N,H$_i$), $i=1,2,3$ and ^2J(H$_i$,H$_j$), $i<j=1,2,3$ can be given in terms of two single functions $^1\bar{J}^{N1}(r_1,r_2,r_3,\alpha_{23},\alpha_{13},\alpha_{12})$ and $^2\bar{J}^{23}(r_1,r_2,r_3,\alpha_{23},\alpha_{13},\alpha_{12})$,

$$^1J(^{15}\mathrm{N},\mathrm{H}_1) = {}^1\bar{J}^{N1}(r_1,r_2,r_3,\alpha_{23},\alpha_{13},\alpha_{12}) = {}^1\bar{J}^{N1}(r_1,r_3,r_2,\alpha_{23},\alpha_{12},\alpha_{13}), \quad (1)$$

$$^1J(^{15}\mathrm{N},\mathrm{H}_2) = {}^1\bar{J}^{N1}(r_2,r_3,r_1,\alpha_{13},\alpha_{12},\alpha_{23}) = {}^1\bar{J}^{N1}(r_2,r_1,r_3,\alpha_{13},\alpha_{23},\alpha_{12}), \quad (2)$$

$$^1J(^{15}\mathrm{N},\mathrm{H}_3) = {}^1\bar{J}^{N1}(r_3,r_1,r_2,\alpha_{12},\alpha_{23},\alpha_{13}) = {}^1\bar{J}^{N1}(r_3,r_2,r_1,\alpha_{12},\alpha_{13},\alpha_{23}), \quad (3)$$

and

$$^2J(\mathrm{H}_2,\mathrm{H}_3) = {}^2\bar{J}^{23}(r_1,r_2,r_3,\alpha_{23},\alpha_{13},\alpha_{12}) = {}^2\bar{J}^{23}(r_1,r_3,r_2,\alpha_{23},\alpha_{12},\alpha_{13}), \quad (4)$$

$$^2J(\mathrm{H}_1,\mathrm{H}_3) = {}^2\bar{J}^{23}(r_2,r_3,r_1,\alpha_{13},\alpha_{12},\alpha_{23}) = {}^2\bar{J}^{23}(r_2,r_1,r_3,\alpha_{13},\alpha_{23},\alpha_{12}), \quad (5)$$

$$^2J(\mathrm{H}_1,\mathrm{H}_2) = {}^2\bar{J}^{23}(r_3,r_1,r_2,\alpha_{12},\alpha_{23},\alpha_{13}) = {}^2\bar{J}^{23}(r_3,r_2,r_1,\alpha_{12},\alpha_{13},\alpha_{23}). \quad (6)$$

These functions $^1\bar{J}^{N1}$ and $^2\bar{J}^{23}$ are expressed as expansions

$$^{1/2}\bar{J}^{N1/23} = {}^{1/2}\bar{J}^{N1/23}_0 + \sum_k^6 F_k\xi_k + \sum_{k\le l}^6 F_{k,l}\xi_k\xi_l + \sum_{k\le l\le m}^6 F_{k,l,m}\xi_k\xi_l\xi_m + \sum_{k\le l\le m\le n}^6 F_{k,l,m,n}\xi_k\xi_l\xi_m\xi_n \quad (7)$$

in the variables

$$\xi_k = \Delta r_k = r_k - r_e, \quad k=1,2,3, \quad (8)$$

$$\xi_4 = \Delta\alpha_{23} = \alpha_{23} - \alpha_e, \quad (9)$$

TABLE II. Calculated proton-proton coupling constants, $^2J(\mathrm{H,H})$, of ammonia at equilibrium geometry. All values are in Hz and are presented in order of the date of publication.

Method	Basis set	Ref.	r_{NH} (Å)	∠(HNH)	$^2J_{eq}^{FC}$	$^2J_{eq}^{SD}$	$^2J_{eq}^{DSO}$	$^2J_{eq}^{PSO}$	$^2J_{eq}$
CISD	Nonstandard[a]	66	1.0116	106.7°	⋯	⋯	⋯	⋯	−6.83
INDO	n/a	67	1.0136	106.67°	⋯	⋯	⋯	⋯	−7.88
SOS-CI	6–31G	91	Not specified		−28.92	1.39	−5.12	1.98	−30.33
SCF	6–311G**	92	1.0124	106.67°	−23.91	0.69	−5.2	5.06	−23.37
EOM	6–311G**	92	1.0124	106.67°	−14.78	0.49	−5.2	4.71	−14.78
SCF	Varying[b]	93	1.012 395	106.67°	−23.93	1.05	−5.25	4.46	−23.67
FF-MBPT[2]	Varying[b]	93	1.012 395	106.67°	−20.05	0.95	−5.2	4.39	−19.9
SCF	Nonstandard[c]	30	1.012 395	106.67°	−23.6	0.78	−5.22	4.49	−23.55
EOM-CCSD	Nonstandard[c]	30	1.012 395	106.67°	−11.72	0.55	−5.13	4.21	−12.09
^{10}CAS^{94} SCF	HuzIV	1	Experimental		−11.21	⋯	⋯	⋯	−9.77
DFT/B3LYP	HuzII-su3	94	Optimized		⋯	⋯	⋯	⋯	−9.8
^{10}RAS$^{52}_{14,8SD}$ SCF	HuzIII-su4	95	1.0124	106.67°	−12.51	0.62	−5.19	5.74	−11.33
^{10}CAS^{94} SCF	aug-cc-pVQZ-su1	96	Optimized		⋯	⋯	⋯	⋯	−11.4
^{10}CAS^{52} SCF	aug-cc-pVTZ	97	Optimized		⋯	⋯	⋯	⋯	−15.45
DFT/B3LYP	HuzIII-su3	53	Optimized		⋯	⋯	⋯	⋯	−10.1
DFT/B3LYP	cc-pCV5Z-sd+t	9	1.0124	106.67°	−11.8	0.7	−5.3	6.4	−10.0
DFT/B3LYP	aug-cc-pVTZ-J	71	1.012	107.10°	−11.82	0.6	−5.25	6.15	−10.32
SCF	This work		1.0124	106.67°	−26.3	0.91	−5.29	6.24	−24.44
^{10}CAS^{54} SCF	This work		1.0124	106.67°	−13.76	0.7	−5.23	6.17	−12.11
^{10}RAS$^{94}_{33SD}$ SCF	This work		1.0124	106.67°	−12.82	0.68	−5.23	6.19	−11.18
SOPPA	This work		1.0124	106.67°	−13.54	0.68	−5.25	6.26	−11.86
SOPPA(CCSD)	This work		1.0124	106.67°	−12.94	0.67	−5.24	6.24	−11.27
SOPPA[d]	This work		1.0103	106.72°	⋯	⋯	⋯	⋯	−11.24

[a]Basis set: N: (9s5p1d)→[4s2p1d], H: (5s1p)→[3s1p].
[b]Basis set: 6–311G** (FC), 6–31G (SD), 6–31G** (OP, OD).
[c]Basis set: N: (10s6p1d)→[6s3p1d], H: (6s1p)→[4s1p].
[d]SOPPA(CCSD) value at the reference equilibrium geometry (see text).

$$\xi_5 = \Delta\alpha_{13} = \alpha_{13} - \alpha_e, \tag{10}$$

$$\xi_6 = \Delta\alpha_{12} = \alpha_{12} - \alpha_e. \tag{11}$$

Here, r_i is the instantaneous value of the distance between the central N nucleus and H_i, where H_i is the proton labeled i (=1, 2, or 3); α_{ij} denotes the bond angle $\angle(H_iNH_j)$. The quantities r_e=1.0103 Å and α_e=106.72° (Ref. 69) are the equilibrium values of the r_i and α_{ij}, respectively, chosen as expansion centers for the series expansions representing ^1J (^{15}N,H) and ^2J(H,H).

The expansion coefficients $F_{k,l,m,\ldots}$ in Eq. (7) obey the following permutation rules:

$$F_{k',l',m',\ldots} = F_{k,l,m,\ldots}, \tag{12}$$

when the indices $k',l',m',\ldots$ are obtained from $k,l,m,\ldots$ by replacing all indices 2 by 3, all indices 3 by 2, all indices 5 by 6, and all indices 6 by 5. All six coupling constants were calculated at the SOPPA(CCSD) level of theory for 841 different nuclear arrangements of $^{15}NH_3$, which gave 2523 points on the $^1\bar{J}^{N1}$ and $^2\bar{J}^{23}$ surfaces. The values of the expansion parameters in Eq. (7) were obtained in a least-squares fitting to the points on the two coupling surfaces. For the $^1\bar{J}^{N1}$ and $^2\bar{J}^{23}$ functions we could usefully vary 75 and 79 parameters, respectively, which had root-mean-square (rms) deviations of 0.08 and 0.06 Hz. Tables III and IV list the optimized parameter values. Parameters, whose absolute values were determined to be less than their standard errors in initial fittings, were constrained to zero in the final fitting and omitted from the table. Furthermore, we give in the tables only one member of each parameter pair related by Eq. (12). The optimized parameters are given as supplementary material together with a FORTRAN routine for evaluating the $^1\bar{J}^{N1}$ and $^2\bar{J}^{23}$ values at arbitrary geometries.[99]

Analyzing the linear and quadratic coefficients, we find that the one-bond nitrogen-hydrogen couplings $^1\bar{J}^{N1}$ depend more strongly on the length of the bond between the two coupled atoms ($^1J_r^{NH}$=81.2396 Hz Å^{-1}) than on any of the other bond lengths ($^1J_s^{NH}$=−9.6375 Hz Å^{-1}). This confirms that unlike methane and silane,[42,46,48,49,56,57] ammonia does not exhibit an unusual differential sensitivity.[38] Furthermore, the expansion coefficients for the one-bond nitrogen-hydrogen couplings, $^1\bar{J}^{N1}$, are quite large for the "associated" bond lengths ($^1J_r^{NH}$=81.2396 Hz Å^{-1} and $^1J_{rr}^{NH}$=81.22 Hz Å^{-2}) but somewhat smaller for the angle to the neighboring H atom ($^1J_\alpha^{NH}$=−45.4271 Hz rad^{-1} and $^1J_{\alpha\alpha}^{NH}$=−61.878 Hz rad^{-2}). The opposite is true for the geminal hydrogen-hydrogen couplings, $^2\bar{J}^{23}$, where geometry dependence is dominated by the bond angle terms involving the parameters $^2J_\alpha^{HH}$ and $^2J_{\alpha\alpha}^{HH}$. A similar behavior was previously observed for other magnetic properties of ammonia[62,64] and of the isoelectronic H_3O^+ ion.[44,100]

TABLE III. Expansion coefficients of the calculated nitrogen-proton coupling constant surface, ^1J (^{15}N,H), of the ammonia molecule defined in Eq. (7). Derivatives involving the bond length changes Δr_i have been obtained with these coordinates in Å. Derivatives involving the angular variations $\Delta\alpha_{ij}$ have been obtained with these coordinates in radians. Coupling constants are in Hz.

Parameter	Value	Parameter	Value	Parameter	Value
$^1\bar{J}_0^{N1}$	−62.308 62	F_{135}	86.0	F_{1146}	−396.
$F_1=^1J_r^{NH}$	81.2396	F_{144}	−18.5	F_{1155}	88.
$F_3=^1J_s^{NH}$	−9.6375	F_{146}	9.7	F_{1156}	−48.0
$F_4=^1J_\gamma^{NH}$	−9.5986	F_{155}	−83.7	F_{1222}	−64.0
$F_5=^1J_\alpha^{NH}$	−45.4271	F_{156}	−248.8	F_{1225}	52.
$F_{11}=\frac{1}{2}{}^1J_{rr}^{NH}$	40.61	F_{223}	26.03	F_{1233}	−19.
$F_{13}=^1J_{rs}^{NH}$	44.05	F_{226}	49.11	F_{1234}	114.
$F_{14}=^1J_{r\gamma}^{NH}$	−46.57	F_{234}	68.7	F_{1244}	−178.3
$F_{16}=^1J_{r\alpha}^{NH}$	−61.51	F_{245}	−148.40	F_{1445}	−590.
$F_{23}=^1J_{st}^{NH}$	10.82	F_{255}	−9.78	F_{1456}	170.
$F_{33}=\frac{1}{2}{}^1J_{ss}^{NH}$	31.854	F_{333}	12.76	F_{1466}	122.
$F_{34}=^1J_{s\gamma}^{NH}$	−22.02	F_{444}	2.64	F_{2222}	−13.8
$F_{35}=^1J_{s\alpha}^{NH}$	25.71	F_{445}	−12.85	F_{2224}	12.
$F_{36}=^1J_{s\beta}^{NH}$	−12.28	F_{456}	−59.98	F_{2225}	17.2
$F_{44}=\frac{1}{2}{}^1J_{\gamma\gamma}^{NH}$	−6.879	F_{466}	−20.10	F_{2244}	14.0
$F_{46}=^1J_{\alpha\gamma}^{NH}$	−24.624	F_{555}	−18.89	F_{2334}	76.
$F_{55}=\frac{1}{2}{}^1J_{\alpha\alpha}^{NH}$	−30.939	F_{556}	−33.39	F_{2444}	−353.7
$F_{56}=^1J_{\alpha\beta}^{NH}$	−33.154			F_{3666}	−13.4
		F_{1111}	604.5	F_{4445}	−1.45
F_{111}	−272.61	F_{1112}	−21.4	F_{4456}	−24.3
F_{112}	40.60	F_{1114}	−58.	F_{4466}	−21.8
F_{114}	−68.6	F_{1115}	39.8	F_{4555}	−13.1
F_{115}	−11.89	F_{1122}	11.5	F_{4556}	−43.2
F_{123}	60.9	F_{1123}	53.	F_{5566}	−39.6
F_{124}	−55.2	F_{1126}	82.	F_{5666}	−11.5
F_{133}	10.78	F_{1144}	−30.1		

III. THERMAL AVERAGING

A. Theory

We have used the variational program TROVE[68] for vibrational and thermal averaging of the spin-spin constants of 15-ammonia and its isotopologues $^{15}ND_3$, $^{15}NH_2D$, and $^{15}NH_2D$. The TROVE Hamiltonian is defined by the expansions of its kinetic-energy and potential-energy parts in terms of the internal coordinates. The coordinates and the expansion orders used presently are the same as in Ref. 101. The expansions of $G_{\lambda\mu}$ and U (see Ref. 68) around the nonrigid reference configuration are truncated after the sixth-order terms while the expansion of V is truncated after the eighth-order terms. The size of the basis set is controlled by the polyad number

$$P = 2(n_1 + n_2 + n_3) + n_4 + n_5 + n_6/2, \tag{13}$$

where the quantum numbers n_i are defined in connection with the primitive basis functions ϕ_{n_i}.[68] They are essentially the principal quantum numbers associated with the local-mode vibrations of NH_3. The basis set contains only products of primitive functions ϕ_{n_i} for which $P \le P_{max}$. We found that the thermal averages were converged to better than 0.002% when using $P_{max}=10$. In the TROVE calculations, we used the spectroscopic potential energy surface of $^{14}NH_3$ from Ref. 69, which was generated by refining a CCSD(T) surface by fitting to available experimental vibrational energies.

For an ensemble of molecules in thermal equilibrium at absolute temperature T, the thermal average of an operator P is given by

$$\langle P\rangle_T = \frac{1}{Q}\sum_i g_i \exp\left(-\frac{E_{rv}^{(i)}}{kT}\right)\langle P\rangle_i, \tag{14}$$

where g_i is the degeneracy of the ith state with the energy $E_{rv}^{(i)}$ relative to the ground state energy, k is the Boltzmann constant, Q is the internal partition function defined as

$$Q = \sum_i g_i \exp\left(-\frac{E_{rv}^{(i)}}{kT}\right), \tag{15}$$

and $\langle P\rangle_i$ is an expectation value of the operator P in a rovibrational state i

$$\langle P\rangle_i = \langle \Phi_{rv}^{(i)}|P|\Phi_{rv}^{(i)}\rangle. \tag{16}$$

The calculation of the quantities in Eqs. (14)–(16) requires the eigenvalues $E_{rv}^{(i)}$ and eigenvectors $\Phi_{rv}^{(i)}$ which are usually obtained variationally, that is, by matrix diagonalization. Here we explore an alternative approach based on the matrix exponent technique,[70] in which we avoid a time-consuming diagonalization procedure. This approach is based on the realization that Eq. (14) represents the trace of a matrix product,

TABLE IV. Expansion coefficients of the calculated proton-proton coupling constant surface, $^2J(\mathrm{H},\mathrm{H})$, of the ammonia molecule defined in Eq. (7). Derivatives involving the bond length changes Δr_i have been obtained with these coordinates in Å. Derivatives involving the angular variations $\Delta\alpha_{ij}$ have been obtained with these coordinates in radians. Coupling constants are in Hz.

Parameter	Value	Parameter	Value	Parameter	Value
$^2\bar{J}_0^{23}$	−11.236 05	F_{144}	10.94	F_{1222}	−34.7
$F_1=^2J_t^{\mathrm{HH}}$	3.9149	F_{146}	43.7	F_{1233}	−14.8
$F_3=^2J_r^{\mathrm{HH}}$	0.8634	F_{155}	−11.75	F_{1234}	−103.
$F_4=^2J_\alpha^{\mathrm{HH}}$	48.3273	F_{156}	−2.8	F_{1244}	56.4
$F_5=^2J_\beta^{\mathrm{HH}}$	−0.4534	F_{223}	−24.67	F_{1444}	17.9
$F_{11}=\frac{1}{2}{}^2J_{tt}^{\mathrm{HH}}$	−0.080	F_{225}	19.86	F_{1445}	487.
$F_{13}=^2J_{rt}^{\mathrm{HH}}$	7.109	F_{226}	88.10	F_{1456}	−473.
$F_{14}=^2J_{t\alpha}^{\mathrm{HH}}$	13.67	F_{234}	−54.4	F_{1466}	−189.
$F_{16}=^2J_{t\beta}^{\mathrm{HH}}$	11.96	F_{245}	114.71	F_{2222}	−35.6
$F_{23}=^2J_{rs}^{\mathrm{HH}}$	−20.72	F_{255}	2.89	F_{2224}	−33.7
$F_{33}=\frac{1}{2}{}^2J_{rr}^{\mathrm{HH}}$	−18.622	F_{333}	−41.75	F_{2225}	15.1
$F_{34}=^2J_{r\alpha}^{\mathrm{HH}}$	13.66	F_{444}	−23.09	F_{2233}	−49.9
$F_{35}=^2J_{r\beta}^{\mathrm{HH}}$	15.28	F_{445}	15.85	F_{2244}	300.2
$F_{36}=^2J_{r\gamma}^{\mathrm{HH}}$	6.286	F_{456}	57.77	F_{2255}	8.2
$F_{44}=\frac{1}{2}{}^2J_{\alpha\alpha}^{\mathrm{HH}}$	30.318	F_{466}	22.10	F_{2333}	−47.7
$F_{46}=^2J_{\alpha\beta}^{\mathrm{HH}}$	18.484	F_{555}	−0.729	F_{2334}	166.
$F_{55}=\frac{1}{2}{}^2J_{\beta\beta}^{\mathrm{HH}}$	1.524	F_{556}	10.88	F_{2344}	312.
$F_{56}=^2J_{\beta\gamma}^{\mathrm{HH}}$	23.217			F_{2444}	364.9
		F_{1111}	−7.2	F_{4444}	61.76
F_{111}	−0.88	F_{1112}	−6.1	F_{4445}	9.36
F_{112}	−8.54	F_{1114}	−25.2	F_{4456}	26.1
F_{114}	0.87	F_{1122}	−9.9	F_{4466}	29.0
F_{115}	2.46	F_{1124}	−71.	F_{4555}	1.39
F_{123}	−18.6	F_{1126}	60.	F_{4556}	−2.2
F_{124}	28.8	F_{1146}	642.	F_{5566}	17.8
F_{133}	−5.81	F_{1155}	−323.9	F_{5666}	6.46
F_{135}	−17.4	F_{1156}	−624.	F_{6666}	2.62

$$\langle P\rangle_T = \mathrm{tr}(\rho_{i,i}\langle P\rangle_i), \tag{17}$$

involving the (diagonal) density matrix

$$\rho_{i,i} \equiv \frac{1}{Q}\exp\left(-\frac{E_{\mathrm{rv}}^{(i)}}{kT}\right) = \frac{1}{Q}\langle\Phi_{\mathrm{rv}}^{(i)}|\exp(-\beta H_{\mathrm{rv}})|\Phi_{\mathrm{rv}}^{(i)}\rangle \tag{18}$$

and the operator P, both given in the representation of the eigenfunctions $\Phi_{\mathrm{rv}}^{(i)}$ of the rotation-vibrational Hamiltonian H_{rv}. In Eq. (18), we introduced the standard notation $\beta = 1/kT$. Since the trace does not depend on the choice of the representation, we can evaluate Eq. (18) in any representation we find suitable. The obvious choice is to work with the representation of the *basis* functions, which in TROVE are given by

$$|\phi_{\mathrm{rv}}^{(i)}\rangle = |jkm\rangle|V\rangle, \tag{19}$$

where $|jkm\rangle$ is a symmetry-adapted rotational basis function, $|V\rangle = |n_1\rangle|n_2\rangle|n_3\rangle|n_4\rangle|n_5\rangle|n_6\rangle$ (see Ref. 68) is a short-hand notation for a vibrational basis function, and i is a short-hand index numbering the basis states.

TABLE V. The molecular symmetry groups, irreducible representations Γ, and the nuclear statistical weights g_{ns} for $^{15}NH_3$, $^{15}ND_3$, $^{15}NH_2D$, and $^{15}NDH_2$.

Molecule	Symmetry	g_{ns}					
Γ		A_1'	A_2'	E'	A_1''	A_2''	E''
$^{15}NH_3$	D_{3h}	0	8	4	0	8	4
$^{15}ND_3$	D_{3h}	20	2	16	20	2	16
Γ		A_1	A_2	B_1	B_2		
$^{15}NH_2D$	C_{2v}	6	6	18	18		
$^{15}NHD_2$	C_{2v}	24	24	12	12		

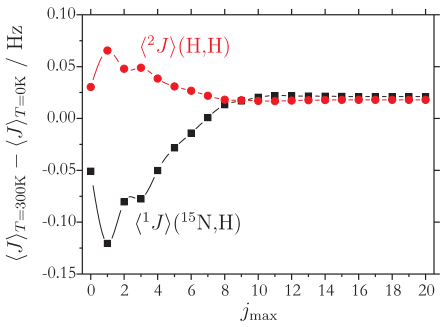

FIG. 1. Convergence of the thermally averaged N–H (squares) and H–H (circles) spin-spin coupling constants vs j_{max} plotted relative to the corresponding $T=0$ K values.

The (nondiagonal) density matrix $\rho_{l,l'}$ is constructed by expanding the matrix exponential as a Taylor series,[70]

$$\rho_{l,l'} = \frac{1}{Q}\langle\phi_{\mathrm{rv}}^{(l)}|\exp(-\beta H_{\mathrm{rv}})|\phi_{\mathrm{rv}}^{(l')}\rangle$$
$$= \frac{1}{Q}\sum_{k\geq 0}\frac{1}{k!}\langle\phi_{\mathrm{rv}}^{(l)}|(-\beta H_{\mathrm{rv}})^k|\phi_{\mathrm{rv}}^{(l')}\rangle, \quad (20)$$

in the representation of the basis functions in Eq. (19). Thus the problem of the diagonalization of the Hamiltonian matrix $\langle\phi_{\mathrm{rv}}^{(l)}|H_{\mathrm{rv}}|\phi_{\mathrm{rv}}^{(l')}\rangle$ is replaced by the problem of evaluating the matrix products in Eq. (20). In these expansions, we employed the scaling and squaring technique[70] in order to improve the convergence of the Taylor series. Usually five to ten terms in the expansion were sufficient to guarantee convergence of the average values to about 0.001 Hz. The resulting density matrix $\rho_{l,l'}$ is then utilized for averaging the spin-spin constants ^1J (^{15}N,H) and ^2J(H,H) in analogy to Eq. (17). The required matrix elements $\langle\phi_{\mathrm{rv}}^{(l)}|P|\phi_{\mathrm{rv}}^{(l')}\rangle$ depend solely on the vibrational coordinates and can be written as

$$\langle\phi_{\mathrm{rv}}^{(l)}|P|\phi_{\mathrm{rv}}^{(l')}\rangle = \langle V|P|V'\rangle\langle jkm|jk'm\rangle, \quad (21)$$

where $\langle jkm|jk'm\rangle = \delta_{k,k'}$. The integrals $\langle V|P|V'\rangle$ are computed by the technique described in Ref. 101. Before processing Eq. (20), the matrix elements $\langle\phi_{\mathrm{rv}}^{(l)}|H_{\mathrm{rv}}|\phi_{\mathrm{rv}}^{(l')}\rangle$ are transformed into a symmetry adapted representation[102] to reduce the size of the matrices. The pyramidal molecules $^{15}NH_3$ and $^{15}ND_3$ are treated in the D_{3h} (M) molecular symmetry group, while C_{2v} (M) symmetry is employed for $^{15}NH_2$ D and $^{15}NDH_2$.[102] In the case of $^{15}NH_3$, the use of symmetry is especially beneficial since the A_1' and A_1'' representations have zero nuclear weight factors and do not enter into Eq. (20). The statistical weights for the relevant states were determined following the approach of Ref. 103. They are given in Table V for easy reference. The averages could be computed for each value of the rotational quantum number (the standard notation for this quantum number is J but we denote it by j here to distinguish it from the spin-spin coupling constants) j and for each irreducible representation of the molecular symmetry group independently. The maximum value of the rotational quantum number j taken into account is different for different molecules. To ensure convergence to better than 0.001 Hz, we used $j_{max}=19$, 26, 22, and 24 for $^{15}NH_3$, $^{15}ND_3$, $^{15}NH_2$ D, and $^{15}NDH_2$, respectively. For the case of $^{15}NH_3$, the convergence with regard to j_{max} is illustrated in Fig. 1.

The partition function values [see Eq. (15)] were also computed using the matrix exponential technique in conjunction with the statistical weight factors from Table V. For $T=300$ K, we obtained $Q=1175.9$, 11 064.8, 7732.1, and 16 290.3 for $^{15}NH_3$, $^{15}ND_3$, $^{15}NH_2$ D, and $^{15}NDH_2$, respectively.

The results of the thermal averaging ($T=300$ K) for $^{15}NH_3$ and its deuterated isotopologues are listed in Table VI. The values in parentheses are the vibrational corrections ΔJ, defined as

$$\Delta J = \langle J\rangle - J_{\mathrm{eq}}. \quad (22)$$

Here and in the following, we report the three couplings to deuterium in terms of $^1J^*$ (^{15}N,D), $^2J^*$(H,D), and $^2J^*$(D,D), defined as

$$^1J^*(^{15}\mathrm{N,D}) = \frac{\gamma_{\mathrm{H}}}{\gamma_{\mathrm{D}}}{}^1J(^{15}\mathrm{N,D}), \quad (23)$$

TABLE VI. Calculated thermally averaged nitrogen-hydrogen and hydrogen-hydrogen spin-spin coupling constants of ammonia isotopologues. Values in parentheses are the corresponding vibrational (for $T=0$ K) and thermal (for $T=0$ K) corrections. All values are in Hz. The vibrational basis set is defined by $P\leq 10$ (see text).

	$^{15}NH_3$				$^{15}NH_2$ D			
	$T=0$ K [a]		$T=300$ K		$T=0$ K		$T=300$ K	
$\langle^1J(^{15}\mathrm{N,H})\rangle$	−61.968	(0.341)	−61.947	(0.361)	−61.923	(0.386)	−61.884	(0.425)
$\langle^1J^*(^{15}\mathrm{N,D})\rangle$					−62.354	(−0.045)	−62.284	(0.025)
$\langle^2J(\mathrm{H,H})\rangle$	−10.699	(0.537)	−10.681	(0.555)	−10.682	(0.554)	−10.671	(0.565)
$\langle^2J^*(\mathrm{H,D})\rangle$					−10.732	(0.504)	−10.734	(0.502)
	$^{15}NHD_2$				$^{15}ND_3$			
	$T=0$ K		$T=300$ K		$T=0$ K		$T=300$ K	
$\langle^1J(^{15}\mathrm{N,H})\rangle$	−61.785	(0.524)	−61.823	(0.486)				
$\langle^1J^*(^{15}\mathrm{N,D})\rangle$	−62.205	(0.104)	−62.216	(0.093)	−62.024	(0.285)	−62.083	(0.226)
$\langle^2J^*(\mathrm{H,D})\rangle$	−10.758	(0.478)	−10.721	(0.515)				
$\langle^2J^*(\mathrm{D,D})\rangle$	−10.825	(0.411)	−10.795	(0.441)	−10.864	(0.372)	−10.806	(0.430)

[a]Zero-point vibrational correction for $T=0$ K have been calculated for the lowest vibrational state 0^-.

$$^2J^*(H,D) = \frac{\gamma_H}{\gamma_D} {}^2J(\mathrm{H,D}), \tag{24}$$

$$^2J^*(D,D) = \left(\frac{\gamma_H}{\gamma_D}\right)^2 {}^2J(\mathrm{D,D}), \tag{25}$$

with γ_H and γ_D being the magnetogyric ratios of hydrogen and deuterium, respectively, in order to render them comparable with the corresponding couplings to hydrogen. Table VI also contains the vibrational averages of $^{1,2}J$ at $T=0$ K, calculated as expectation values for the lowest rovibrational state (i.e., the zero-point vibrational corrections). In the case of $^{15}NH_3$, the lowest rovibrational state, i.e., the only one populated at $T=0$ K, is 0^- since its symmetric counterpart 0^+ has a statistical weight factor of zero and thus does not exist according to the Pauli principle. For comparison, we have also generated the analogous values for the (nonexisting) 0^+ state, which are $\langle 0^+|{}^1J^{\mathrm{NH}}|0^+\rangle = -62.047$ Hz and $\langle 0^+|{}^2J^{\mathrm{HH}}|0^+\rangle = -10.661$ Hz.

Upon inspection of Table VI, we note first that the vibrational corrections are generally positive both for the one-bond and the geminal couplings, i.e., vibrational averaging reduces the absolute values of both coupling constants; the only exception is the one-bond N–D coupling of NH_2D at $T=0$ K with a tiny negative correction (−0.045 Hz). Second, the total thermal averaging correction obtained from Eq. (14) is rather small for the one-bond N–H coupling in $^{15}NH_3$, 0.36 Hz or 0.6%, but more significant for the geminal proton-proton coupling, 0.55 Hz or 5.2%. This is consistent with the expansion parameters from Tables I and II, which indicate that the dominant vibrational contributions to the one-bond and geminal couplings involve the rather rigid N–H and the more flexible H–N–H deformations, respectively.

The differences between the $T=0$ K and $T=300$ K $\langle J\rangle$ values (see Table VI) suggest that the temperature dependence is negligible for both couplings. This is analyzed in more detail below.

B. Contributions to the averaged coupling constants

In previous work,[42,43,45,49,104,105] we used an alternative approach to compute the coupling constants, which is in principle applicable to all molecules. We expanded the coupling surfaces in a Taylor series to second order in internal coordinates and then calculated the vibrationally and thermally averaged coupling constants $\langle J\rangle$ by averaging over the changes in the internal coordinates. For ammonia, this treatment yields

$$\begin{aligned}\langle {}^1J(^{15}N,\mathrm{H}_1)\rangle = {}& {}^1J_0^{\mathrm{NH}} + {}^1J_r^{\mathrm{NH}}\langle\Delta r_1\rangle + {}^1J_s^{\mathrm{NH}}(\langle\Delta r_2\rangle + \langle\Delta r_3\rangle) + {}^1J_\alpha^{\mathrm{NH}}(\langle\Delta\alpha_{12}\rangle + \langle\Delta\alpha_{13}\rangle) + {}^1J_\gamma^{\mathrm{NH}}\langle\Delta\alpha_{23}\rangle + \tfrac{1}{2}{}^1J_{rr}^{\mathrm{NH}}\langle\Delta r_1^2\rangle + \tfrac{1}{2}{}^1J_{ss}^{\mathrm{NH}}(\langle\Delta r_2^2\rangle \\ & + \langle\Delta r_3^2\rangle) + \tfrac{1}{2}{}^1J_{\alpha\alpha}^{\mathrm{NH}}(\langle\Delta\alpha_{12}^2\rangle + \langle\Delta\alpha_{13}^2\rangle) + \tfrac{1}{2}{}^1J_{\gamma\gamma}^{\mathrm{NH}}\langle\Delta\alpha_{23}^2\rangle + {}^1J_{rs}^{\mathrm{NH}}(\langle\Delta r_1\Delta r_2\rangle + \langle\Delta r_1\Delta r_3\rangle) + {}^1J_{st}^{\mathrm{NH}}\langle\Delta r_2\Delta r_3\rangle \\ & + {}^1J_{r\alpha}^{\mathrm{NH}}(\langle\Delta r_1\Delta\alpha_{12}\rangle + \langle\Delta r_1\Delta\alpha_{13}\rangle) + {}^1J_{r\gamma}^{\mathrm{NH}}\langle\Delta r_1\Delta\alpha_{23}\rangle + {}^1J_{s\alpha}^{\mathrm{NH}}(\langle\Delta r_2\Delta\alpha_{12}\rangle + \langle\Delta r_3\Delta\alpha_{13}\rangle) + {}^1J_{s\beta}^{\mathrm{NH}}(\langle\Delta r_2\Delta\alpha_{13}\rangle \\ & + \langle\Delta r_3\Delta\alpha_{12}\rangle) + {}^1J_{s\gamma}^{\mathrm{NH}}(\langle\Delta r_2\Delta\alpha_{23}\rangle + \langle\Delta r_3\Delta\alpha_{23}\rangle) + {}^1J_{\alpha\beta}^{\mathrm{NH}}\langle\Delta\alpha_{12}\Delta\alpha_{13}\rangle + {}^1J_{\alpha\gamma}^{\mathrm{NH}}(\langle\Delta\alpha_{12}\Delta\alpha_{23}\rangle + \langle\Delta\alpha_{13}\Delta\alpha_{23}\rangle),\end{aligned} \tag{26}$$

$$\begin{aligned}\langle {}^2J(\mathrm{H}_2,\mathrm{H}_3)\rangle = {}& {}^2J_0^{\mathrm{HH}} + {}^2J_r^{\mathrm{HH}}(\langle\Delta r_2\rangle + \langle\Delta r_3\rangle) + {}^2J_t^{\mathrm{HH}}\langle\Delta r_1\rangle + {}^2J_\alpha^{\mathrm{HH}}\langle\Delta\alpha_{23}\rangle + {}^2J_\beta^{\mathrm{HH}}(\langle\Delta\alpha_{12}\rangle + \langle\Delta\alpha_{13}\rangle) + \tfrac{1}{2}{}^2J_{rr}^{\mathrm{HH}}(\langle\Delta r_2^2\rangle + \langle\Delta r_3^2\rangle) \\ & + \tfrac{1}{2}{}^2J_{tt}^{\mathrm{HH}}\langle\Delta r_1^2\rangle + \tfrac{1}{2}{}^2J_{\alpha\alpha}^{\mathrm{HH}}\langle\Delta\alpha_{23}^2\rangle + \tfrac{1}{2}{}^2J_{\beta\beta}^{\mathrm{HH}}(\langle\Delta\alpha_{12}^2\rangle + \langle\Delta\alpha_{13}^2\rangle) + {}^2J_{rs}^{\mathrm{HH}}\langle\Delta r_2\Delta r_3\rangle + {}^2J_{rt}^{\mathrm{HH}}(\langle\Delta r_1\Delta r_2\rangle + \langle\Delta r_1\Delta r_3\rangle) \\ & + {}^2J_{r\alpha}^{\mathrm{HH}}(\langle\Delta r_2\Delta\alpha_{23}\rangle + \langle\Delta r_3\Delta\alpha_{23}\rangle) + {}^2J_{r\beta}^{\mathrm{HH}}(\langle\Delta r_2\Delta\alpha_{12}\rangle + \langle\Delta r_3\Delta\alpha_{13}\rangle) + {}^2J_{t\alpha}^{\mathrm{HH}}\langle\Delta r_1\Delta\alpha_{23}\rangle + {}^2J_{t\beta}^{\mathrm{HH}}(\langle\Delta r_1\Delta\alpha_{12}\rangle \\ & + \langle\Delta r_1\Delta\alpha_{13}\rangle) + {}^2J_{r\gamma}^{\mathrm{HH}}(\langle\Delta r_2\Delta\alpha_{13}\rangle + \langle\Delta r_3\Delta\alpha_{12}\rangle) + {}^2J_{\alpha\beta}^{\mathrm{HH}}(\langle\Delta\alpha_{12}\Delta\alpha_{23}\rangle + \langle\Delta\alpha_{13}\Delta\alpha_{23}\rangle) + {}^2J_{\beta\gamma}^{\mathrm{HH}}\langle\Delta\alpha_{12}\Delta\alpha_{13}\rangle.\end{aligned} \tag{27}$$

The expansion coefficients, $J_r, J_\alpha, \ldots$ in Eqs. (26) and (27) are almost identical to the F coefficients in Eq. (7) as seen from in Tables III and IV. In our previous work,[42,43,45,104,105] we then used first- and second-order perturbation theory to calculate average normal-coordinate displacements which were subsequently transformed to average internal-coordinate displacements, $\langle\Delta r_1\rangle$, $\langle\Delta\alpha_{23}\rangle, \ldots$. In the present work, we can obtain these average internal-coordinate displacements directly from the density matrix as given in Eqs. (17) and (18).

The mean geometrical parameters entering into Eqs. (26) and (27) for $^{15}NH_3$ and $^{15}ND_3$ are collected in Table VII. They can be utilized for averaging arbitrary properties of $^{15}NH_3$ and $^{15}ND_3$ as long as these can be represented as second-order Taylor expansions similar to Eqs. (26) and (27).

In Table VIII, we present the averaged values of the spin-spin constants $\langle J\rangle$ for $^{15}NH_3$ and $^{15}ND_3$ obtained via the second-order Taylor expansion, Eqs. (26) and (27). Compared with the full treatment, the second-order expansion only slightly overestimates the vibrational corrections to the one-bond coupling, by 0.05 Hz ($T=300$ K) for $^{15}NH_3$ and by even less for $^{15}ND_3$, while the differences are negligible for the geminal H–H or D–D couplings. The second-order treatment represented by the expansions (26) and (27) thus appears to be sufficient, at least for moderate temperatures. This might seem unexpected for a molecule such as ammo-

TABLE VII. Mean geometrical parameters of two ammonia isotopologues at 0 and 300 K compared with $H_2{}^{16}O$ (taken from Ref. 104). Bond lengths in Å and bond angles in rad.

	$^{15}NH_3$		$^{15}ND_3$		$H_2{}^{16}O$ [a]
Geometrical parameter	0 K[b]	300 K	0 K[b]	300 K	300 K
$\langle\Delta r_1\rangle$	0.019 313	0.019 945	0.014 077	0.014 768	0.017 75
$\langle\Delta r_1^2\rangle$	0.005 597	0.005 631	0.003 973	0.004 004	0.004 60
$\langle\Delta r_1\Delta r_2\rangle$	0.000 369	0.000 395	0.000 168	0.000 191	0.000 02
$\langle\Delta\alpha_{23}\rangle$	−0.000 329	−0.000 396	−0.000 938	−0.000 501	−0.004 17
$\langle\Delta\alpha_{23}^2\rangle$	0.024 070	0.024 239	0.017 739	0.018 123	0.023 89
$\langle\Delta\alpha_{23}\Delta\alpha_{13}\rangle$	−0.001 151	−0.000 953	−0.000 574	−0.000 272	
$\langle\Delta r_1\Delta\alpha_{23}\rangle$	0.000 039	0.000 022	0.000 108	0.000 071	
$\langle\Delta r_1\Delta\alpha_{13}\rangle$	−0.000 812	−0.000 831	−0.000 741	−0.000 747	−0.000 81

[a]Reference 104.
[b]Computed for the 0^- eigenstate (see text).

nia, which is known to be very anharmonic. However, one has to remember that our approach to the thermal averaging explicitly takes into account the nonrigid character of the flexible umbrella mode and correctly describes the tunneling through the low inversion barrier of ammonia. This is achieved through an appropriate construction of the basis functions $|V\rangle$ in Eq. (19). In order to demonstrate the importance of this point for the description of $\langle J\rangle$, we have recomputed the averages of the coupling constants for $^{15}NH_3$ by employing a rigid-molecule approach, i.e., by treating ammonia as a rigid C_{3v} system, with the potential function expanded up to the fourth order and the kinetic energy operator up to the second order. This should mimic the standard anharmonic approach that is commonly utilized for vibrational averaging.[29,37,42,43,45,47,49–54] Even though this rigid-molecule approach does not employ perturbation theory to generate the vibrational wave functions and our basis does not consist of the usual harmonic-oscillator functions, the analogy with the second-order perturbation treatment is close, as our internal (linearized) coordinates (see Ref. 68) are connected with the normal coordinates through a linear transformation. The computed "rigid" values of $\langle J\rangle$, −62.155 and −10.556 Hz for the nitrogen-proton and geminal H–H coupling constants, respectively, deviate substantially both from the nonrigid values (see Table VI) and from the values obtained using Eqs. (26) and (27). The vibrational correction to the geminal coupling (0.680 Hz) is significantly overestimated, while the correction to the one-bond coupling (0.154 Hz) is too small. These values can be much improved by introducing more terms into the expansions of the potential energy function (still treated as a single minimum) and the kinetic energy operator. For example, extending these up to the eighth and sixth order, respectively, we obtain $\langle {}^1J({}^{15}N,H_1)\rangle = -61.891$ Hz and $\langle {}^2J(H_2,H_3)\rangle = -10.712$ Hz, i.e., much closer to the nonrigid values. The remaining discrepancy (0.056 and −0.031 Hz, respectively) can then be attributed to the single-well character of the rigid approach.

The reasonably good agreement between the results from the second-order treatment and from the proper thermal averaging with the use of TROVE variational wave functions allows us to follow previous studies on methane, water, ethylene, and silane[42,43,45,47,49] and to analyze the thermal corrections in terms of contributions from the individual internal coordinates (Table IX). For the one-bond coupling, we find first-order and second-order stretch contributions of 1.236 and 0.626 Hz, respectively, whose sum (1.862 Hz) is almost completely canceled by the negative second-order bend contribution of −1.588 Hz. For the geminal coupling, the second-order bend contribution of 0.751 Hz is dominant and only slightly reduced by the second-order stretch contribution ${}^2J_{rs}^{HH} = -0.213$ Hz. In the rigid approach, it is mostly the bending linear contributions that are responsible for the deviations from the nonrigid results since the absolute values of

TABLE VIII. Comparison of the thermally averaged nitrogen-hydrogen and hydrogen-hydrogen spin-spin coupling constants of ammonia isotopologues calculated using the second-order Taylor expansions, see Eqs. (26) and (27). Values in parenthesis are the corresponding vibrational (for $T=0$ K) and thermal (for $T=300$ K) corrections. All values are in Hz.

Temperature	$^{15}NH_3$ [a]				$^{15}ND_3$			
(K)	$^1J(^{15}N,H)$		$^2J(H,H)$		$^1J^*(^{15}N,D)$		$^2J^*(D,D)$.	
				Based on nonrigid molecule				
0	−61.936	(0.374)	−10.692	(0.544)	−62.013	(0.297)	−10.855	(0.381)
300	−61.900	(0.409)	−10.671	(0.565)	−62.056	(0.254)	−10.802	(0.434)
				Based on (4–2) rigid C_{3v} molecule				
300	−62.155	(0.154)	−10.556	(0.680)				
				Based on (8–6) rigid C_{3v} molecule				
300	−61.891	(0.418)	−10.712	(0.524)				

[a]Zero-point vibrational correction (T=0 K) have been calculated for the lowest A_2'' vibrational state.

TABLE IX. Nuclear motion contributions to the total nitrogen-hydrogen and hydrogen-hydrogen spin-spin coupling constants of $^{15}NH_3$ at 300 and 600 K of terms involving the individual internal coordinate and the inversion mode coefficients, Eqs. (26) and (27) computed using the full nonrigid and the simplest rigid approach (see text). All values are in Hz.

	^1J (^{15}N,H)			^2J(H,H)			
	300 K		600 K		300 K		600 K
	Nonrigid	Rigid	Nonrigid		Nonrigid	Rigid	Nonrigid
$^1J_r^{NH}$	1.620	1.600	1.665	$^2J_t^{HH}$	0.078	0.077	0.080
$^1J_s^{NH}$	−0.384	−0.380	−0.395	$^2J_r^{HH}$	0.034	0.034	0.035
First order stretch	1.236	1.220	1.270		0.113	0.111	0.116
$^1J_{rr}^{NH}$	0.229	0.227	0.230	$^2J_{tt}^{HH}$	0.000	0.000	0.000
$^1J_{rs}^{NH}$	0.035	0.034	0.038	$^2J_{rr}^{HH}$	0.006	0.005	0.006
$^1J_{st}^{NH}$	0.004	0.004	0.005	$^2J_{rt}^{HH}$	−0.008	−0.008	−0.009
$^1J_{ss}^{NH}$	0.359	0.356	0.362	$^2J_{rs}^{HH}$	−0.210	−0.208	−0.211
Second order stretch	0.626	0.622	0.634		−0.213	−0.211	−0.215
Total stretch to 2nd order	1.862	1.842	1.904		−0.100	−0.100	−0.099
$^1J_{\gamma}^{NH}$	0.004	−0.015	−0.032	$^2J_{\alpha}^{HH}$	−0.019	0.073	0.162
$^1J_{\alpha}^{NH}$	0.036	−0.138	−0.304	$^2J_{\beta}^{HH}$	0.000	−0.001	−0.003
First order bend	0.040	−0.153	−0.336		−0.019	0.072	0.159
$^1J_{\gamma\gamma}^{NH}$	−0.167	−0.169	−0.184	$^2J_{\alpha\alpha}^{HH}$	0.735	0.745	0.809
$^1J_{\alpha\alpha}^{NH}$	−1.500	−1.521	−1.652	$^2J_{\beta\beta}^{HH}$	0.074	0.075	0.081
$^1J_{\alpha\gamma}^{NH}$	0.047	0.041	−0.015	$^2J_{\alpha\beta}^{HH}$	−0.035	−0.031	0.011
$^1J_{\alpha\beta}^{NH}$	0.032	0.027	−0.010	$^2J_{\beta\gamma}^{HH}$	−0.022	−0.019	0.007
Second order bend	−1.588	−1.622	−1.861		0.751	0.771	0.910
Total bend to second order	−1.548	−1.775	−2.197		0.733	0.843	1.068
$^1J_{r\gamma}^{NH}$	−0.001	−0.003	0.001	$^2J_{t\alpha}^{HH}$	0.000	0.001	0.000
$^1J_{r\alpha}^{NH}$	0.102	0.097	0.110	$^2J_{t\beta}^{HH}$	−0.020	−0.019	−0.021
$^1J_{s\gamma}^{NH}$	0.037	0.035	0.040	$^2J_{r\alpha}^{HH}$	−0.023	−0.022	−0.025
$^1J_{s\alpha}^{NH}$	−0.043	−0.041	−0.046	$^2J_{r\beta}^{HH}$	−0.025	−0.024	−0.027
$^1J_{s\beta}^{NH}$	−0.001	−0.002	0.000	$^2J_{r\gamma}^{HH}$	0.000	0.001	0.000
Second order stretch-bend	0.095	0.087	0.105		−0.067	−0.063	−0.074
Total correction to secod order	0.409	0.154	−0.188		0.565	0.680	0.895
Third and fourth orders			−0.113				0.033

$^1J_{\alpha}^{NH}$ and $^2J_{\alpha}^{HH}$ are overestimated by 0.17 and 0.09 Hz, respectively.

For the sake of comparison, we have also included in Table VII the values of the mean geometrical parameters for water,[104] which were obtained using perturbation theory. It is somewhat surprising that the mean changes in the geometrical parameters are almost the same in NH_3 and H_2O. An analysis of the computed spin-spin coupling constants of water in terms of internal coordinates[43] also concluded that the zero-point vibrational corrections reduce the absolute values of the one-bond O–H and the geminal H–H coupling constants. Compared with ammonia, the zero-point vibrational corrections for the one-bond coupling are more pronounced in water (7.6% versus 4.9%) due to the fact that the first-order stretch contribution is about three times larger and the second-order bend contribution is about half as large.

C. Rotation-vibration interaction

When averaging molecular properties, the effects of rotation-vibration interactions are commonly disregarded. Sometimes rotational effects are entirely neglected in that the required energies, matrix elements, and partition functions are constructed from vibrational contributions only. Sometimes it is assumed that in Eq. (14), $E_{rv}^{(i)}=E_{vib}^{(i)}+E_{rot}^{(i)}$ and, correspondingly, $Q=Q_{vib}Q_{rot}$, where the rotational energies $E_{rot}^{(i)}$ are taken to be those for the vibrational ground state. In the present treatment, we calculate $E_{rv}^{(i)}$ and Q using "fully coupled" rotation-vibration wave functions, and thus we take into account all rotation-vibration interactions such as Coriolis effects. This allows us to investigate the importance of the rotation-vibration coupling effects for thermal averaging and thus assess the accuracy of the pure vibrational averaging approach in which rotation is ignored. In our approach, vibrational averaging corresponds to $\langle J\rangle$ values computed from the vibrational ($j=0$) wave functions only. The resulting values of $\langle J\rangle$ will be referred to as $\langle J\rangle_{j=0}$. For $^{15}NH_3$ we obtain $\langle {}^1J\rangle_{j=0}=-62.019$ Hz and $\langle {}^2J\rangle_{j=0}=-10.669$ Hz at 300 K. These values differ from the $T=0$ K values $\langle J\rangle_{T=0\ K}$, which are also obtained from pure vibrational integrations, the deviations (−0.051 and 0.030 Hz, respectively) reflecting the temperature dependence of the purely vibrational averages. Interestingly, these differences are significantly larger than those resulting from "complete" thermal averaging with all relevant j values included, which are obtained from the $\langle J\rangle_{T=300\ K}$ and $\langle J\rangle_{T=0\ K}$ values (see Table VI). In Fig. 1 we demonstrate that the rotational contributions (from $j>0$) are almost as large as the vibrational ones, but with opposite

sign; hence, there is significant cancellation, and small thermal corrections ensue. Figure 1 depicts thermal corrections $\Delta J_{T=300\ \mathrm{K}}$ defined as

$$\Delta J_{T=300\ \mathrm{K}} = \langle J \rangle_{T=300\ \mathrm{K}} - \langle J \rangle_{T=0\ \mathrm{K}} \tag{28}$$

and computed for different values of the maximal rotational quantum number $j_{\max}$. As j increases, there is first a rather large oscillation at $j=1$ and then the total thermal correction converges to 0.021 Hz ($\langle {}^1J \rangle_{T=300\ \mathrm{K}}$) and 0.018 Hz ($\langle {}^2J \rangle_{T=300\ \mathrm{K}}$). For the rotational correction (i.e., the contributions from $j>0$ states), we obtain 0.072 and −0.012 Hz, respectively. These values are too large to be ignored. Thus the final thermal correction is small, but only when it is properly evaluated.

D. Higher temperatures

In order to gain a better understanding of the temperature effects, we have performed thermal averaging of ^1J (^{15}N,H) and ^2J(H,H) for $^{15}NH_3$ also at $T=600$ K, obtaining averages of −62.610 and −10.308 Hz, respectively. At $T=600$ K, we had to use $j_{\max}=30$ to reach convergence, with the partition function for $^{15}NH_3$ being $Q=3851.8$. The contributions to the vibrational corrections for the spin-spin coupling constants are collected in Table IX so that they can be compared with the $T=300$ K values. In contrast to the $T=300$ K results, where the bending and stretching contributions in Eqs. (26) and (27) partially cancel each other, the bending contributions exceed the stretching ones at $T=600$ K, resulting in a significant negative correction (−0.301 Hz) for the one-bond coupling and in a large positive correction (0.928 Hz) for the geminal coupling relative to the corresponding $T=0$ K values. The effect from higher (third and fourth) order terms in the Hamiltonian at $T=600$ K is now notable for the one-bond coupling (−0.113 Hz) but still rather small for the geminal coupling (0.033 Hz). The rotational effects (i.e., contributions from states with $j>0$) are less important at $T=600$ K, namely −0.056 Hz for the one-bond coupling (relative to $^1J_{j_{\max}=0}=-62.554$ Hz) and 0.074 Hz for the geminal coupling (relative to $^2J_{j_{\max}=0}=-10.382$ Hz). This is to be expected. As far as thermal averaging is concerned, the rotation at high temperature can be safely separated from the vibration, which effectively removes the rotational contributions. The vibrational thermal effect ($j=0$) is quite large at $T=600$ K for both coupling constants, with $\Delta\,{}^1J_{T=600\ \mathrm{K}}=-0.586$ Hz and $\Delta\,{}^2J_{T=600\ \mathrm{K}}=0.317$ Hz as follows from Eq. (28).

E. Comparison with experiment and earlier calculations

In Table X, we compare our present results for vibrationally averaged spin-spin coupling constants in ammonia with those from earlier calculations. We note that only the very recent DFT/B3LYP calculation by Ruden *et al.*[53] gives results comparable to ours. In two early studies,[66,67] the values for the vibrational ground states are far off the experimental values. This must be due to an insufficient basis set and/or level of correlation in these calculations. The recent DFT study[53] leads to averaged coupling constants close to our values; however, the vibrational corrections obtained by second-order perturbation theory are too large compared to our variational treatment. Our second-order rigid molecule treatment reproduces the reported correction for the two-bond hydrogen-hydrogen coupling[53] rather well, but the reported correction to the one-bond coupling remains too large even if we account for the rotational effect (about 0.07 Hz, see Fig. 1 and discussion above).

TABLE X. Results of previous calculations of the nitrogen-proton coupling, ^1J (^{15}N,H), and proton-proton coupling, ^2J(H,H), in the vibrational ground state of ammonia $^{15}NH_3$. All values are in Hz and are presented in order of the date of publication.

Method	Ref.	^1J ($^{14/15}$N,H)	^2J(H,H)
CISD[a]	66	···	−8.28
INDO[b]	67	−37.39	−9.29
INDO[c]	67	−40.34	−8.57
DFT/B3LYP[d]	53	−63.7	−9.4
SOPPA(CCSD)	This work	−61.97	−10.70

[a]Basis set: N: (9s5p1d)→[4s2p1d], H: (5s1p)→[3s1p]; vibrational averaging over the two symmetric normal modes (symmetric stretch and inversion mode) using variationally determined linear combinations of products of harmonic oscillator wave functions.
[b]Vibrational averaging over all six normal modes using perturbation theory with only zeroth order vibrational wave functions, i.e., products of harmonic oscillator functions. No contribution from the anharmonicity of the potential or the coupling of normal modes.
[c]Vibrational averaging over the inversion mode with a numerical wave function and over the other normal modes with the vibrational wave function as product of harmonic oscillator functions, i.e., no contribution from the anharmonicity of the potential other than in the inversion mode or the coupling of normal modes.
[d]Basis set: HuzIII-su3; vibrational averaging over all six normal modes using perturbation theory to second order and zeroth and first order vibrational wave functions—contribution from the anharmonicity of the potential included.

Finally, in Table XI, we have collected the available experimental values of the one- and two-bond coupling constants in different isotopologues of ammonia. A complete set of data was presented by Wasylishen and Friedrich[109] who also produced the values with the smallest error bars up to date. Unfortunately their measurements were carried out in the liquid phase and not in a vapor as e.g., in the old study by Alei *et al.*,[108] so that their data are not directly comparable to our theoretical gas-phase values. However, we can correct the measured ^1J (^{15}N,H) coupling constant in $^{15}NH_3$ with the vapor-to-liquid shift recently calculated at the B3LYP level by Gester *et al.*[71] This leads to an empirical gas phase value of −61.95 Hz for ^1J (^{15}N,H) in $^{15}NH_3$ which is in excellent agreement with our thermally averaged value of −61.97 Hz.

Furthermore we can compare with the measured isotope shifts. Experimentally the primary isotope shift for the one-bond coupling is -0.46 ± 0.13 Hz, while the secondary isotope shift is 0.07 ± 0.02 Hz.[109] Our theoretical values are −0.33 Hz for the primary and 0.06–0.07 Hz for the secondary isotope effects in $^{15}NH_2$ D and $^{15}NHD_2$, again in very good agreement with experiment. Slight deviations from experiment are encountered for the isotope effects in $^{15}ND_3$ and for the secondary isotope effects on the H–D geminal couplings (where our values are too small). However, one

TABLE XI. Experimental values of the nitrogen-proton coupling, $^1J(^{15}\mathrm{N,H})$, or nitrogen-deuterium coupling, $^1J^*(^{15}\mathrm{N,D})=(\gamma_H/\gamma_D)^1J(^{15}\mathrm{N,D})$, and proton-deuterium coupling, $^2J^*(\mathrm{H,D})=(\gamma_H/\gamma_D)^2J(\mathrm{H,D})$. All values are in Hz and are presented in order of the date of publication.

Coupling	Phase	Ref.	$^{15}NH_3$	$^{15}NH_2D$	$^{15}NHD_2$	$^{15}ND_3$
$^1J(^{15}\mathrm{N,H})$	Liquid	106	$\lvert 61.2\pm0.9\rvert$	⋯	⋯	⋯
$^1J(^{15}\mathrm{N,H})$	Liquid (room temperature)	107	$\lvert 61.8\pm0.5\rvert$	⋯	⋯	⋯
$^1J(^{15}\mathrm{N,H})$	Vapor	108	$\lvert 61.2\pm0.3\rvert$	⋯	⋯	⋯
$^1J(^{15}\mathrm{N,H})$	Liquid (20 °C)	109	-61.45 ± 0.03	-61.38 ± 0.07	-61.31 ± 0.04	⋯
$^1J^*(^{15}\mathrm{N,D})$	Liquid (20 °C)	109	⋯	-61.85 ± 0.04	-61.77 ± 0.06	-61.69 ± 0.01
$^2J^*(\mathrm{H,D})$	Liquid	106	⋯	$\lvert 10.35\pm0.80\rvert$	$\lvert 10.35\pm0.80\rvert$	⋯
$^2J^*(\mathrm{H,D})$	Liquid (20 °C)	109	⋯	-9.61 ± 0.03	-9.35 ± 0.03	⋯

should note that the solvent effect on the geminal couplings was estimated to be 2.5 Hz,[71] which is ten times larger than the isotope effect. The discrepancies between our calculated gas phase isotope shifts and the values measured in solution are therefore likely to be caused by solvent effects.

IV. SUMMARY

We have calculated point-wise surfaces of the one-bond and two-bond spin-spin coupling constants in ammonia at the level of SOPPA(CCSD) employing a specialized large one-electron basis set. Both surfaces, consisting of 2523 points each, were fitted to a fourth-order power series in the internal coordinates and subsequently thermally averaged using variational vibrational wave functions obtained from the TROVE Hamiltonian in conjunction with a CCSD(T)-based potential energy surface.

Vibrational and thermal averaging at 300 K leads to a rather small correction of 0.36 Hz or 0.6% for the one-bond nitrogen-hydrogen coupling constant in $^{15}NH_3$ and to a more notable correction of 0.56 Hz or 5.0% for the hydrogen-deuterium two-bond coupling constant in $^{15}NH_2D$. Analyzing the contributions to the nuclear-motion corrections through second order in a Taylor expansion in internal coordinates for the nonrigid ammonia molecule, we observe that the dominant contributions to the one-bond coupling are the negative second-order bending terms $\frac{1}{2}{}^1J^{\mathrm{NH}}_{\alpha\alpha}(\langle\Delta\alpha^2_{12}\rangle+\langle\Delta\alpha^2_{13}\rangle)$ and the positive first-order own-bond stretching term $^1J^{\mathrm{NH}}_r\langle\Delta r_1\rangle$. Thus, the bending motion increases the absolute value of the one-bond coupling constant whereas the stretching motion decreases it, leading to substantial cancellation and an overall slight decrease. For the two-bond coupling, the positive second-order bending term $\frac{1}{2}{}^2J^{\mathrm{HH}}_{\alpha\alpha}\langle\Delta\alpha^2_{23}\rangle$ dominates so that the vibrational correction decreases the absolute value of the coupling constant.

Compared with our full variational treatment of nuclear motion, the standard perturbation-theory approach for a rigid ammonia molecule underestimates the nuclear motion correction to $^1J(\mathrm{N,H})$ by 57% (mainly due to the inadequate treatment of the large amplitude inversion mode), while the correction to $^2J(\mathrm{H,H})$ is overestimated (by 30%).

Comparison with the available experimental data reveals excellent agreement for the absolute values of the one-bond couplings and their primary and secondary isotope effects, while there are some slight deviations for the geminal hydrogen-deuterium couplings.

ACKNOWLEDGMENTS

S.P.A.S. acknowledges grants from the Danish Center for Scientific Computing, from the Carlsberg Foundation and from the Danish Natural Science Research Council/The Danish Councils for Independent Research (Grant No. 272-08-0486). This work was supported also by Grant No. IAA 401870702 from the Grant Agency of the Academy of Sciences of the Czech Republic.

[1] T. Helgaker, M. Jaszuński, and K. Ruud, Chem. Rev. (Washington, D.C.) **99**, 293 (1999).
[2] J. Vaara, Phys. Chem. Chem. Phys. **9**, 5399 (2007).
[3] L. B. Krivdin and R. H. Contreras, Annu. Rep. NMR Spectrosc. **61**, 133 (2007).
[4] J. M. Schulman and D. N. Kaufman, J. Chem. Phys. **57**, 2328 (1972).
[5] T. Helgaker, M. Jaszuński, K. Ruud, and A. Górska, Theor. Chem. Acc. **99**, 175 (1998).
[6] T. Enevoldsen, J. Oddershede, and S. P. A. Sauer, Theor. Chem. Acc. **100**, 275 (1998).
[7] J. Guilleme and J. San Fabián, J. Chem. Phys. **109**, 8168 (1998).
[8] P. F. Provasi, G. A. Aucar, and S. P. A. Sauer, J. Chem. Phys. **115**, 1324 (2001).
[9] J. E. Peralta, G. E. Scuseria, J. R. Cheeseman, and M. J. Frisch, Chem. Phys. Lett. **375**, 452 (2003).
[10] W. Deng, J. R. Cheeseman, and M. J. Frisch, J. Chem. Theory Comput. **2**, 1028 (2006).
[11] F. Jensen, J. Chem. Theory Comput. **2**, 1360 (2006).
[12] U. Benedikt, A. A. Auer, and F. Jensen, J. Chem. Phys. **129**, 064111 (2008).
[13] Y. Y. Rusakov, L. B. Krivdin, S. P. A. Sauer, E. P. Levanova, and G. G. Levkovskaya, Magn. Reson. Chem. **48**, 44 (2010).
[14] F. Jensen, "The optimum contraction of basis sets for calculating spin-spin coupling constants," Theor. Chim. Acta, doi:10.1007/s00214-009-0699-5 (in press).
[15] G. E. Scuseria and R. H. Contreras, Theor. Chim. Acta **59**, 437 (1981).
[16] G. E. Scuseria, A. R. Engelmann, and R. H. Contreras, Theor. Chim. Acta **61**, 49 (1982).
[17] G. E. Scuseria and R. H. Contreras, Chem. Phys. Lett. **93**, 425 (1982).
[18] G. A. Aucar and R. H. Contreras, J. Magn. Reson. **93**, 413 (1991).
[19] R. H. Contreras, M. C. Ruiz de Azúa, C. G. Giribet, G. A. Aucar, and R. Loboyan de Bonczok, J. Mol. Struct.: THEOCHEM **284**, 249 (1993).
[20] R. M. Lobayan and G. A. Aucar, J. Mol. Struct.: THEOCHEM **452**, 1 (1998).
[21] R. M. Lobayan and G. A. Aucar, J. Mol. Struct.: THEOCHEM **452**, 13 (1998).

[22] P. F. Provasi, G. A. Aucar, and S. P. A. Sauer, Int. J. Mol. Sci. **4**, 231 (2003).
[23] O. Malkina, D. R. Salahub, and V. G. Malkin, J. Chem. Phys. **105**, 8793 (1996).
[24] J. E. Peralta, V. Barone, R. H. Contreras, D. G. Zaccari, and J. P. Snyder, J. Am. Chem. Soc. **123**, 9162 (2001).
[25] P. Lantto, J. Vaara, and T. Helgaker, J. Chem. Phys. **117**, 5998 (2002).
[26] V. Barone, P. F. Provasi, J. E. Peralta, J. P. Snyder, S. P. A. Sauer, and R. H. Contreras, J. Phys. Chem. A **107**, 4748 (2003).
[27] S. P. A. Sauer, J. Phys. B **30**, 3773 (1997).
[28] J. Olsen and P. Jørgensen, J. Chem. Phys. **82**, 3235 (1985).
[29] O. Vahtras, H. Ågren, P. Jørgensen, H. J. A. Jensen, S. B. Padkjær, and T. Helgaker, J. Chem. Phys. **96**, 6120 (1992).
[30] S. A. Perera, H. Sekino, and R. J. Bartlett, J. Chem. Phys. **101**, 2186 (1994).
[31] H. Sekino and R. J. Bartlett, Chem. Phys. Lett. **225**, 486 (1994).
[32] S. A. Perera, M. Nooijen, and R. J. Bartlett, J. Chem. Phys. **104**, 3290 (1996).
[33] A. A. Auer and J. Gauss, J. Chem. Phys. **115**, 1619 (2001).
[34] J. E. Del Bene, I. Alkorta, and J. Elguero, J. Chem. Theory Comput. **4**, 967 (2008).
[35] A. A. Auer and J. Gauss, Chem. Phys. **356**, 7 (2009).
[36] J. Oddershede, J. Geertsen, and G. E. Scuseria, J. Phys. Chem. **92**, 3056 (1988).
[37] J. Geertsen, J. Oddershede, W. T. Raynes, and G. E. Scuseria, J. Magn. Reson. **93**, 458 (1991).
[38] W. T. Raynes, J. Geertsen, and J. Oddershede, Chem. Phys. Lett. **197**, 516 (1992).
[39] J. Geertsen, J. Oddershede, and W. T. Raynes, Magn. Reson. Chem. **31**, 722 (1993).
[40] W. T. Raynes, J. Geertsen, and J. Oddershede, Int. J. Quantum Chem. **52**, 153 (1994).
[41] J. Geertsen, J. Oddershede, W. T. Raynes, and T. L. Marvin, Mol. Phys. **82**, 29 (1994).
[42] R. D. Wigglesworth, W. T. Raynes, S. P. A. Sauer, and J. Oddershede, Mol. Phys. **92**, 77 (1997).
[43] R. D. Wigglesworth, W. T. Raynes, S. P. A. Sauer, and J. Oddershede, Mol. Phys. **94**, 851 (1998).
[44] S. P. A. Sauer, C. K. Møller, H. Koch, I. Paidarová, and V. Špirko, Chem. Phys. **238**, 385 (1998).
[45] R. D. Wigglesworth, W. T. Raynes, S. Kirpekar, J. Oddershede, and S. P. A. Sauer, J. Chem. Phys. **112**, 3735 (2000).
[46] S. P. A. Sauer and W. T. Raynes, J. Chem. Phys. **113**, 3121 (2000).
[47] R. D. Wigglesworth, W. T. Raynes, S. Kirpekar, J. Oddershede, and S. P. A. Sauer, J. Chem. Phys. **114**, 9192 (2001).
[48] S. P. A. Sauer and W. T. Raynes, J. Chem. Phys. **114**, 9193 (2001).
[49] S. P. A. Sauer, W. T. Raynes, and R. A. Nicholls, J. Chem. Phys. **115**, 5994 (2001).
[50] S. Kirpekar, T. Enevoldsen, J. Oddershede, and W. T. Raynes, Mol. Phys. **91**, 897 (1997).
[51] P.-O. Åstrand, K. Ruud, K. V. Mikkelsen, and T. Helgaker, J. Chem. Phys. **110**, 9463 (1999).
[52] J. Casanueva, J. San Fabián, E. Díez, and A. L. Esteban, J. Mol. Struct. **565–566**, 449 (2001).
[53] T. A. Ruden, O. B. Lutnæs, and T. Helgaker, J. Chem. Phys. **118**, 9572 (2003).
[54] T. A. Ruden, T. Helgaker, and M. Jaszuński, Chem. Phys. **296**, 53 (2004).
[55] M. B. Hansen, J. Kongsted, D. Toffoli, and O. Christiansen, J. Phys. Chem. A **112**, 8436 (2008).
[56] S. P. A. Sauer and P. F. Provasi, ChemPhysChem **9**, 1259 (2008).
[57] P. F. Provasi and S. P. A. Sauer, Phys. Chem. Chem. Phys. **11**, 3987 (2009).
[58] V. Špirko, J. Mol. Spectrosc. **101**, 30 (1983).
[59] V. Špirko and W. P. Kraemer, J. Mol. Spectrosc. **133**, 331 (1989).
[60] W. Hüttner, U. E. Frank, W. Majer, K. Mayer, and V. Špirko, Mol. Phys. **64**, 1233 (1988).
[61] V. Špirko, H. J. A. Jensen, and P. Jørgensen, Chem. Phys. **144**, 343 (1990).
[62] S. P. A. Sauer, V. Špirko, and J. Oddershede, Chem. Phys. **153**, 189 (1991).
[63] C. J. Jameson, A. C. de Dios, and A. K. Jameson, J. Chem. Phys. **95**, 1069 (1991).
[64] J. Oddershede, I. Paidarová, and V. Špirko, J. Mol. Spectrosc. **152**, 342 (1992).
[65] I. Paidarová, V. Špirko, and J. Oddershede, J. Mol. Spectrosc. **160**, 311 (1993).
[66] J. Kowalewski and B. Roos, Chem. Phys. **11**, 123 (1975).
[67] P. Solomon and J. M. Schulman, J. Am. Chem. Soc. **99**, 7776 (1977).
[68] S. N. Yurchenko, W. Thiel, and P. Jensen, J. Mol. Spectrosc. **245**, 126 (2007).
[69] S. N. Yurchenko, J. Zheng, H. Lin, P. Jensen, and W. Thiel, J. Chem. Phys. **123**, 134308 (2005).
[70] C. Moler and C. Van Loan, SIAM Rev. **45**, 3 (2003).
[71] R. M. Gester, H. C. Georg, S. Canuto, M. C. Caputo, and P. F. Provasi, J. Phys. Chem. A **113**, 14936 (2010).
[72] A. Møgelhøj, K. Aidas, K. V. Mikkelsen, S. P. A. Sauer, and J. Kongsted, J. Chem. Phys. **130**, 134508 (2009).
[73] S. P. A. Sauer and M. J. Packer, in *Computational Molecular Spectroscopy*, edited by P. R. Bunker and P. Jensen (Wiley, London, 2000), Chap. 7, pp. 221–252.
[74] N. F. Ramsey, Phys. Rev. **91**, 303 (1953).
[75] J. Linderberg and Y. Öhrn, *Propagators in Quantum Chemistry* (Academic, London, 1973).
[76] E. S. Nielsen, P. Jørgensen, and J. Oddershede, J. Chem. Phys. **73**, 6238 (1980).
[77] J. Geertsen and J. Oddershede, Chem. Phys. **90**, 301 (1984).
[78] M. J. Packer, E. K. Dalskov, T. Enevoldsen, H. J. A. Jensen, and J. Oddershede, J. Chem. Phys. **105**, 5886 (1996).
[79] K. L. Bak, H. Koch, J. Oddershede, O. Christiansen, and S. P. A. Sauer, J. Chem. Phys. **112**, 4173 (2000).
[80] B. O. Roos, in *Ab Initio Methods in Quantum Chemistry—II. Advances in Chemical Physics*, edited by K. P. Lawley (Wiley, Chichester, 1987), pp. 399–445.
[81] J. Olsen, B. O. Roos, P. Jørgensen, and H. J. A. Jensen, J. Chem. Phys. **89**, 2185 (1988).
[82] H. J. A. Jensen, P. Jørgensen, H. Ågren, and J. Olsen, J. Chem. Phys. **88**, 3834 (1988).
[83] H. J. A. Jensen, P. Jørgensen, H. Ågren, and J. Olsen, J. Chem. Phys. **89**, 5354 (1988).
[84] S. P. A. Sauer, J. Chem. Phys. **98**, 9220 (1993).
[85] M. J. Packer, E. K. Dalskov, S. P. A. Sauer, and J. Oddershede, Theor. Chim. Acta **89**, 323 (1994).
[86] DALTON, a molecular electronic structure program, Release 2.0, http://www.kjemi.uio.no/software/dalton/dalton.html, 2005.
[87] H. Koch, O. Christiansen, R. Kobayashi, P. Jørgensen, and T. Helgaker, Chem. Phys. Lett. **228**, 233 (1994).
[88] H. Koch, A. S. de Merás, T. Helgaker, and O. Christiansen, J. Chem. Phys. **104**, 4157 (1996).
[89] F. B. van Duijneveldt, IBM Technical Report No. RJ945, 1971.
[90] T. H. Dunning, Jr., J. Chem. Phys. **90**, 1007 (1989).
[91] V. Galasso, J. Mol. Struct.: THEOCHEM **93**, 201 (1983).
[92] G. Fronzoni and V. Galasso, J. Mol. Struct.: THEOCHEM **122**, 327 (1985).
[93] H. Fukui, K. Miura, H. Matsuda, and T. Baba, J. Chem. Phys. **97**, 2299 (1992).
[94] T. Helgaker, M. Watson, and N. C. Handy, J. Chem. Phys. **113**, 9402 (2000).
[95] P. Lantto and J. Vaara, J. Chem. Phys. **114**, 5482 (2001).
[96] M. Pecul and J. Sadlej, Chem. Phys. Lett. **360**, 272 (2002).
[97] T. Janowski and M. Jaszunski, Int. J. Quantum Chem. **90**, 1083 (2002).
[98] W. S. Benedict and E. K. Plyler, Can. J. Phys. **35**, 1234 (1957).
[99] See supplementary material at http://dx.doi.org/10.1063/1.3359850 for a FORTRAN routine to evaluate the $^{1}\bar{J}^{N1}$ and $^{2}\bar{J}^{23}$ values at arbitrary geometries.
[100] S. P. A. Sauer, V. Špirko, I. Paidarová, and J. Oddershede, Chem. Phys. **184**, 1 (1994).
[101] S. N. Yurchenko, R. J. Barber, A. Yachmenev, W. Thiel, P. Jensen, and J. Tennyson, J. Phys. Chem. A **113**, 11845 (2009).
[102] P. R. Bunker and P. Jensen, *Molecular Symmetry and Spectroscopy*, 2nd ed. (NRC Research, Ottawa, 1998).
[103] P. Jensen and P. R. Bunker, Mol. Phys. **97**, 821 (1999).
[104] R. D. Wigglesworth, W. T. Raynes, J. Oddershede, and S. P. A. Sauer, Mol. Phys. **96**, 1595 (1999).
[105] R. D. Wigglesworth, W. T. Raynes, S. Kirpekar, J. Oddershede, and

S. P. A. Sauer, J. Chem. Phys. **112**, 736 (2000).
[106] R. A. Bernheim and H. Batiz-Hernandez, J. Chem. Phys. **40**, 3446 (1964).
[107] W. M. Litchman, M. Alei, Jr., and A. E. Florin, J. Chem. Phys. **50**, 1897 (1969).
[108] M. Alei, A. E. Florin, W. M. Litchman, and J. F. O'Brien, J. Phys. Chem. **75**, 932 (1971).
[109] R. E. Wasylishen and J. O. Friedrich, Can. J. Chem. **65**, 2238 (1987).

A theoretical spectroscopy, ab initio based study of the electronic ground state of $^{121}SbH_3$

S. N. Yurchenko, M. Carvajal, A. Yachmenev, W. Thiel, P. Jensen

J. Quant. Spec. Rad. Trans., **111**, 2279 (2010)

Journal of Quantitative Spectroscopy & Radiative Transfer 111 (2010) 2279–2290

Contents lists available at ScienceDirect

Journal of Quantitative Spectroscopy & Radiative Transfer

journal homepage: www.elsevier.com/locate/jqsrt

A theoretical-spectroscopy, *ab initio*-based study of the electronic ground state of $^{121}SbH_3$

Sergei N. Yurchenko [a,*], Miguel Carvajal [b], Andrey Yachmenev [c], Walter Thiel [c], Per Jensen [d]

[a] Technische Universität Dresden, Institut für Physikalische Chemie und Elektrochemie, D-01062 Dresden, Germany
[b] Departamento de Física Aplicada, Facultad de Ciencias Experimentales, Avenida de las Fuerzas Armadas s/n, Universidad de Huelva, E-21071 Huelva, Spain
[c] Max-Planck-Institut für Kohlenforschung, Kaiser-Wilhelm-Platz 1, D–45470 Mülheim an der Ruhr, Germany
[d] Theoretische Chemie, Bergische Universität, D-42097 Wuppertal, Germany

ARTICLE INFO

Article history:
Received 22 January 2010
Received in revised form
5 March 2010
Accepted 8 March 2010

Keywords:
Stibine
Rovibrational
Line list
Ab initio
Potential surface
Dipole moment surface

ABSTRACT

For the stibine isotopologue $^{121}SbH_3$, we report improved theoretical calculations of the vibrational energies below 8000 cm^{-1} and simulations of the rovibrational spectrum in the 0–8000 cm^{-1} region. The calculations are based on a refined *ab initio* potential energy surface and on a new dipole moment surface obtained at the coupled cluster CCSD(T) level. The theoretical results are compared with the available experimental data in order to validate the *ab initio* surfaces and the TROVE computational method [Yurchenko SN, Thiel W, Jensen P. J Mol Spectrosc 2007;245:126–40] for calculating rovibrational energies and simulating rovibrational spectra of arbitrary molecules in isolated electronic states. A number of predicted vibrational energies of $^{121}SbH_3$ are provided in order to stimulate new experimental investigations of stibine. The local-mode character of the vibrations in stibine is demonstrated through an analysis of the results in terms of local-mode theory.

1. Introduction

Over a period of several years we have developed theoretical models, of increasingly wider applicability, that describe the rotational and vibrational motion of polyatomic molecules in isolated electronic states. Our initial work was concerned with XY_3 ammonia-type molecules and led to the XY3 theoretical model and computer program for calculating the rotation–vibration energies [1–3], and simulating the rotation–vibration spectra [4–7] for such molecules. The XY3 approach is entirely variational in that the rotation–vibration energies and wavefunctions are obtained by diagonalization of a matrix representation of the rotation–vibration Hamiltonian, constructed in a suitable basis set. The rotation–vibration Hamiltonian employed is based on 'spectroscopic' ideas: Following the theory of Hougen et al. [8], small-amplitude vibrational motion is described in terms of displacements from a reference structure which follows the large-amplitude inversion (umbrella-flipping) motion of an NH_3-type molecule. The XY3 rotation–vibration Hamiltonian is expanded as a power series in the coordinates describing the small-amplitude vibrations.

More recently, we have implemented ideas similar to those of the XY3 approach in the more general program TROVE (Theoretical ROtation–Vibration Energies) [9] which, at least in principle, can calculate the rotation–vibration energies [9], and simulate the rotation–vibration spectra [10], for any molecule in an isolated electronic state. Also in the TROVE model, the rotation–vibration Hamiltonian is expanded as a power series in small-amplitude vibrational coordinates describing vibrational displacements from a reference configuration which can be rigid, as in customary, spectroscopic rotation–vibration theory [11] or flexible as in the Hougen–Bunker–Johns theory [8].

* Corresponding author. Tel.: +49 351 463 33635; fax: +49 351 463 35953.
E-mail address: s.yurchenko@chemie.tu-dresden.de (S.N. Yurchenko).

0022-4073/$ - see front matter © 2010 Elsevier Ltd. All rights reserved.
doi:10.1016/j.jqsrt.2010.03.008

We have applied the XY3 and TROVE programs to a series of XH_3 molecules (X=N,P,As,Sb,Bi) [1,2,5–7,10,12–17]. Also, TROVE has been used to predict and interpret the complicated torsional splittings of the HSOH molecule [18], to explain an intensity anomaly observed in this molecule [19,20] and to predict highly excited rotational energies in deuterated isotopologues of BiH_3, SbH_3, and AsH_3 [21]. The theoretical calculations of rotation–vibration energies and intensities are generally based on *ab initio* potential energy surfaces (PES) and dipole moment surfaces (DMS); in some instances we have refined the analytical representations of the PES in simultaneous least-squares fittings to experimentally derived vibrational energy spacings and *ab initio* data.

Our studies of the various XH_3 molecules (X=N, P, As, Sb, Bi) have had a different emphasis. For NH_3, the potential energy barrier to inversion is easily surmountable and energy splittings resulting from the inversion are readily observable. Thus, in the description of the vibrational motion of NH_3 it is imperative to account correctly for the strongly anharmonic inversion motion. NH_3 is an important molecule in astrophysical and atmospheric contexts and, to facilitate studies in these areas, there is interest in accurate predictions of its rotation–vibration spectra. Thus, our investigations of NH_3 have been generally focused on producing such predictions [1,4,5,13]; this work has culminated in a recent project aimed at the generation of a so-called line list (a database of NH_3 transition wavenumbers and line strengths to be used in astrophysical and atmospheric work) for NH_3 by means of the TROVE program [10]. The remaining molecules in the XH_3 series, PH_3, BiH_3, SbH_3, and AsH_3, are of less astrophysical importance than NH_3 (although PH_3 was observed in Jupiter and Saturn [22] and an intensive search of the interstellar and circumstellar medium is being carried out [23]). They have high potential energy barriers to inversion so that the inversion motion is effectively replaced by a small-amplitude bending motion. These molecules, however, show distinct local mode behavior [17,24,25] and we have predicted theoretically that, in consequence, they exhibit energy-cluster formation at high rotational excitation [6,12,15]. Our theoretical studies of these molecules have been generally aimed at providing predictions for laboratory spectroscopy with the hope of facilitating the experimental characterization of the energy cluster states. In particular, quite recently [21] we have carried out TROVE calculations for singly and di-deuterated isotopologues of PH_3, BiH_3, and SbH_3 (together with some effective-rotational-Hamiltonian calculations for AsH_2D and $AsHD_2$), demonstrating for the first time that some of these isotopologues have energy clusters.

In the present paper, we extend our previous work on stibine SbH_3 [15], in particular by computing values for the electric dipole transition moments based on a new *ab initio* DMS and on a 'spectroscopic' PES that is determined by least-squares fitting to available experimentally derived vibrational energies, using an *ab initio* PES [15,26,27] as starting point. To calculate the *ab initio* DMS we used the CCSD(T) method in conjunction with the pseudopotential ECP46MWB [28] and the SDB-aug-cc-pVTZ basis [29] to describe the Sb atom and the aug-cc-pVTZ basis set [30] to describe the hydrogen atoms. With the new DMS and the refined PES, we have carried out calculations of vibrational and rovibrational states for the $^{121}SbH_3$ isotopologue, and we have simulated the spectrum of this molecule in the wavenumber range 0–8000 cm^{-1}. In order to improve the agreement with experiment of the synthetic absorption spectrum, the empirical basis set correction (EBSC) was utilized [10], in which the vibrational energies were shifted to the experimental values in the rovibrational calculations (see the text below for details). In addition, the energy level pattern resulting from the cluster formation has been qualitatively analyzed in terms of local-mode theory.

The first experimental spectroscopic study of stibine was made in 1951 by Loomis et al. [31] who observed rotational spectra in the vibrational ground state of $^{121}SbH_2D$ and $^{123}SbH_2D$. Later on, microwave spectra were recorded for the ground vibrational states of $^{121}SbH_3$, $^{123}SbH_3$, $^{121}SbD_3$, and $^{123}SbD_3$ [32,33]. In the infrared region, spectra of different vibrational bands for $^{121}SbH_3$ and $^{123}SbH_3$ were subsequently measured and analyzed [34–40]; these works produced experimental values for vibrational term values up to 12 000 cm^{-1} above the vibrational ground state with the largest number of vibrational states being investigated for $^{121}SbH_3$. Halonen et al. [35] reported relative band intensities for stretching vibrational bands with up to four stretching quanta excited. Recently, the high-resolution infrared spectrum of $^{121}SbD_3$ was recorded and various fundamental levels were characterized by Canè et al. [27].

On the theoretical side, Halonen et al. [34,35,37] complemented their experimental studies of stibine by computing vibrational energies by means of local-mode models. Another local mode analysis of the vibrational energies of stibine was carried out by means of the creation and annihilation operators technique [41,42]. *Ab initio* studies [26,27] were performed to calculate the PES, the dipole moments, the equilibrium geometries, and effective rotation–vibration constants for $^{121}SbH_3$ and $^{123}SbH_3$, and $^{123}SbD_3$. Pluchart et al. [43] used their algebraic approach to describe vibrational modes of SbH_3. Liu et al. [44] reported an *ab initio* three-dimensional Sb–H stretching DMS of SbH_3 together with band intensities for stretching bands below 11 000 cm^{-1}.

Even the most recent *ab initio* PESs of stibine computed at state-of-the-art level of theory [27] are not sufficiently accurate for spectroscopic applications. This situation is usually resolved by adjusting the PES empirically in fits to experimental data. A number of 'spectroscopic' PESs of stibine [35,37,41,43] have been obtained by least-squares fitting to the available experimental band centers.

In the present work we report calculations that aim at an improved theoretical description of the vibration–rotation spectrum of stibine. We start from an *ab initio* PES of stibine [27] and refine it by fitting to the available experimental band centers. We also compute a new six-dimensional *ab initio* DMS of SbH_3, which is utilized for simulating the absorption spectrum at an absolute temperature of T=300 K.

The structure of this paper is as follows. In Section 2 we describe the variational procedure used for the nuclear-motion calculations; in Section 3 the refinement of the PES is presented; in Section 4 we report theoretical absorption intensities of $^{121}SbH_3$ (T=300 K); and a local mode analysis is performed in Section 5. In Section 6 we give some conclusions.

2. Computational details of the variational TROVE calculation

We have used the variational program TROVE [9] to calculate the rovibrational energies, eigenfunctions, and matrix elements of the electric dipole moment of $^{121}SbH_3$; these quantities are necessary for the simulation of the absorption spectrum. In the variational calculation, a matrix representation of the rotation–vibration Hamiltonian is diagonalized. This matrix is set up in terms of a symmetry-adapted contracted basis set constructed as follows. We prepare primitive basis functions as products of one-dimensional (1D) vibrational functions $\phi_{n_1}(r_1^\ell)$, $\phi_{n_2}(r_2^\ell)$, $\phi_{n_3}(r_3^\ell)$, $\phi_{n_4}(\alpha_1^\ell)$, $\phi_{n_5}(\alpha_2^\ell)$, and $\phi_{n_6}(\alpha_3^\ell)$. Here n_i are principal quantum numbers and the six coordinates $(r_1^\ell,r_2^\ell,r_3^\ell,\alpha_1^\ell,\alpha_2^\ell,\alpha_3^\ell)$, are linearized versions [45] of the coordinates r_1, r_2, r_3, α_1, α_2, and α_3. The coordinate r_i is the instantaneous value of the internuclear distance Sb–H_i, where H_i is the proton labeled i=1, 2, or 3, whilst the bond angles are given as $\alpha_1=\angle(H_2SbH_3)$, $\alpha_2=\angle(H_1SbH_3)$, and $\alpha_3=\angle(H_1SbH_2)$. Each set of $\phi_{n_i}(q_i)$ functions is obtained by solving, with the Numerov–Cooley technique [46,47], the one-dimensional (1D) Schrödinger equation [9] for the vibrational motion associated with the coordinate $q_i\in\{r_1^\ell,r_2^\ell,r_3^\ell,\alpha_1^\ell,\alpha_2^\ell,\alpha_3^\ell\}$, when the other coordinates are held fixed at their equilibrium values. The 1D functions could also be chosen so that they describe a 1D motion along a minimum energy path with all other coordinates relaxing so as to minimize the potential energy; such 1D functions are generated in the semi-rigid bender (SRB) approach first proposed by Bunker and Landsberg in 1977 [48]. The SRB-generated 1D functions may be slightly better approximations for the true wavefunctions than the 'rigid-bender-type' 1D functions [48] we use here. However, they are more complicated to generate and normally produce only a modest gain in computational efficiency for the total variational calculation. The basis set functions $\phi_{n_i}(q_i)$ are used in a variational solution of the J=0 vibrational problem:

$$\hat{H}_{\rm vib}|\Psi_{J=0,\gamma}^{\Gamma}\rangle=E_\gamma^{\rm vib}|\Psi_{J=0,\gamma}^{\Gamma}\rangle, \quad (1)$$

where $\hat{H}_{\rm vib}$ is the vibrational (J=0) Hamiltonian

$$\hat{H}_{\rm vib}=\frac{1}{2}\sum_{\lambda\mu}p_\lambda G_{\lambda\mu}p_\mu+V+U, \quad (2)$$

$E_\gamma^{\rm vib}$ and $\Psi_{J=0,\gamma}^{\Gamma}$ are the vibrational eigenvalues and eigenfunctions, respectively, and $\Gamma=A_1,A_2,E$ are the irreducible representations of the $\mathbf{C}_{3v}$(M) molecular symmetry group [45] to which SbH_3 belongs. In Eq. (2), p_λ and p_μ are generalized momenta conjugate to the coordinates q_λ and q_μ, respectively. The Hamiltonian $H_{\rm vib}$ is consistent with the volume element $dq_1\,dq_2\,dq_3\,dq_4\,dq_5\,dq_6$. In Eq. (2) the $G_{\lambda\mu}$ are kinetic energy factors (which depend on the vibrational coordinates), U is the pseudopotential, and V is the molecular potential energy function [9]. We use here the type of Hamiltonian where all vibrations are described as displacements from a rigid reference configuration, i.e., the Hamiltonian is given as an expansion around the equilibrium geometry (see below). In this case our $G_{\lambda\mu}$ matrix elements coincide with the Wilson G matrix elements [49]. Since the Hamiltonian is totally symmetric [45] in $\mathbf{C}_{3v}$(M), its eigenfunctions $\Psi_{J=0,\gamma}^{\Gamma}$ are automatically symmetrized, i.e., they must necessarily transform according to one of the irreducible representations of $\mathbf{C}_{3v}$(M). The details of our approach to recognizing and analyzing the symmetries of the $\Psi_{J=0,\gamma}^{\Gamma}$ functions will be reported elsewhere. In setting up the matrix representations of the rotation–vibration Hamiltonian for $J>0$ we use symmetrized basis functions $\Psi_{J,K,\gamma}^{\Gamma}$ obtained from the products $\Psi_{J=0,\gamma}^{\Gamma}|J,K,m,\tau_{\rm rot}\rangle$, where $|J,K,m,\tau_{\rm rot}\rangle$ is a symmetrized symmetric top rotational eigenfunction [3]. The quantum number $\tau_{\rm rot}$ (=0 or 1) determines the parity of the function [45] (the rotational parity) as $(-1)^{\tau_{\rm rot}}$ and $K\geq 0$ and m (where $-J\leq m\leq J$) are the projections, in units of $\hbar$, of the rotational angular momentum onto the molecule-fixed z-axis and the space-fixed Z-axis, respectively [45]. This basis set will be referred to as a (J=0)-contracted basis set [10].

The (J=0)-contraction offers a number of important advantages. The vibrational part $\hat{H}_{\rm vib}$ of the total Hamiltonian is diagonal in the (J=0)-basis set functions $\Psi_{J=0,\gamma}^{\Gamma}$ and thus its matrix elements are given completely by the eigenvalues $E_\gamma^{\rm vib}$ and do not need to be calculated. Another advantage is that for spectrum simulations the theoretical vibrational term values $E_\gamma^{\rm vib}$ can be substituted by the available experimental values [10]. This so-called empirical basis set correction (EBSC) scheme was introduced in Ref. [10], where it was used to improve the agreement with experiment for the synthetic spectra. We also employ the EBSC approach in the spectrum simulations of the present work.

In order to define the TROVE Hamiltonian we must define the expansion orders for its kinetic-energy and potential-energy parts. The expansions of $G_{\lambda\mu}$ and U in the coordinates $\{r_1^\ell, r_2^\ell, r_3^\ell, \alpha_1^\ell, \alpha_2^\ell, \alpha_3^\ell\}$, are truncated after the 6th-order terms while the expansion of V in the coordinates $\{\xi_1^\ell, \xi_2^\ell, \xi_3^\ell, \alpha_1^\ell, \alpha_2^\ell, \alpha_3^\ell\}$ is truncated after the 8th-order terms. Here $\xi_i^\ell=1-\exp[-a(r_i^\ell-r_e)]$ where a=1.4 Å^{-1} is a Morse parameter and r_e is the equilibrium bond length. In TROVE the size of the basis set, and therefore the size of the Hamiltonian matrix, is controlled by the polyad number defined as

$$P=2(n_1+n_2+n_3)+n_4+n_5+n_6, \quad (3)$$

where the local-mode quantum numbers n_i are defined in connection with the primitive basis functions ϕ_{n_i}. That is, we include in the primitive basis set only those combinations of ϕ_{n_i} for which $P\leq P_{\rm max}$. In present work we use $P_{\rm max}$=12 for the calculations of vibration energies J=0, including those made in connection with the empirical refinement of the PES, and $P_{\rm max}$=10 for the intensity simulations. The smaller $P_{\rm max}$-value used for the simulations helps to make the computation of

Table 1
Experimentally derived vibrational energies of $^{121}SbH_3$ (in cm^{-1}) compared with theoretical values.

State[a]	n_1[b]	n_2	n_3	n_4	n_5	n_6	Γ[c]	Obs.[d]	Calc. I[e]	Calc. II[f]
v_2	0	0	0	1	0	0	A_1	782.245[g]	799.04	782.18
v_4	0	0	0	1	0	0	E	827.855[g]	836.77	827.81
$2v_2$	0	0	0	1	1	0	A_1	1559.0	1594.21	1559.26
$2v_4$	0	0	0	2	0	0	A_1	1652.7	1669.03	1653.63
v_1	1	0	0	0	0	0	A_1	1890.503[g]	1894.24	1890.71
v_3	1	0	0	0	0	0	E	1894.497[g]	1899.65	1894.53
v_1+v_2	1	0	0	1	0	0	A_1	2661	2686.16	2661.61
v_1+v_4	1	0	0	1	0	0	E	2705	2719.80	2706.42
v_1+v_3	2	0	0	0	0	0	E	3719.860	3732.53	3719.67
$2v_3$	2	0	0	0	0	0	A_1	3719.933	3732.51	3719.96
$2v_3+v_4$	2	0	0	1	0	0	E	4513[h]	4541.89	4521.00[i]
$v_1+v_3+v_4$	1	1	0	1	0	0	A_1	4545[h]	4563.44	4539.19[j]
$2v_1+v_3$	3	0	0	0	0	0	E	5480.235	5506.41	5480.40
v_1+2v_3	3	0	0	0	0	0	A_1	5480.285	5506.52	5481.16
–	2	1	0	0	0	0	E	5607[h]	5632.72	5606.10
$3v_1$	2	1	0	0	0	0	A_1	5607[h]	5623.09	5609.20
v_1+3v_3	4	0	0	0	0	0	E	7173.783	7222.65	7178.35
$2v_1+2v_3$	4	0	0	0	0	0	A_1	7173.799	7222.67	7178.45

[a] Spectroscopic assignment of the vibrational state [42] when available.
[b] The local-mode quantum numbers n_i obtained presently as defined by the 1D basis functions ϕ_{n_i} (see text).
[c] Symmetry of the vibrational state in $\mathbf{C}_{3v}$(M).
[d] Experimentally derived vibrational term values from Ref. [37] unless otherwise indicated.
[e] Energies calculated with TROVE from the *ab initio* PES of Ref. [15].
[f] Energies calculated with TROVE from the refined PES (see Section 3).
[g] Experimental value from Ref. [40].
[h] Experimental value excluded from the fitting due to its low accuracy.
[i] Another energy with the same-local mode labels is calculated at 4525.70 cm^{-1}; for this state, the intensity of the transition from the vibrational ground state is comparable to that for the state given in the table.
[j] This is the calculated A_1 term value closest to the experimental value. Its local-mode labeling differs from the (2, 0, 0, 1, 0, 0; A_1) assignment in Refs. [37,42]. In the present work, an A_1 term value with this labeling is obtained at 4526.35 cm^{-1} but with a lower intensity for the transition from the vibrational ground state.

highly excited rotational states (with $J \leq 30$) feasible. The largest rotation–vibration matrix block to be diagonalized (J=30, P_{max}=10) had a dimension of 36 720 and was associated with the basis functions of E symmetry.

Recently a full-dimensional variational study of NH_3 based on the exact kinetic energy operator approach was reported by Mátyus et al. [50]. To confirm the consistency of their results with those obtained from the TROVE approach, we recalculated the vibrational term values of NH_3 using the same PES [51] as in Ref. [50] and tight convergence criteria. The basis set and truncation orders of the Hamiltonian were selected in such a way as to guarantee convergence to better than 0.1 cm^{-1}. For the 69 energies below 6000 cm^{-1} reported in Table V of Ref. [50] the root-mean-square (rms) deviation is 0.16 cm^{-1} with the largest deviation of 0.7 cm^{-1} for v_2+3v_4 at 5672.94 cm^{-1}[50].

In the case of SbH_3, we have checked that the effect of truncating the potential energy function (at 8th-order) is < 1 cm^{-1} for all vibrational term values below 8000 cm^{-1} and < 0.05 cm^{-1} for the values in Table 1. These deviations are significantly smaller than the deviations introduced by the inaccuracy of *ab initio* PES of SbH_3 used presently. The truncation of the kinetic energy operator (at 6th order) affects the vibrational term values by < 0.01 cm^{-1}.

3. Refinement of the *ab initio* potential energy surface

As starting point for the SbH_3 calculations of the present work we use the high-level *ab initio* PES by Breidung and Thiel, reported in the paper by Canè et al. [27]. Originally, this PES was given as a standard force constant expansion in terms of the symmetry-adapted coordinates [27]. In connection with recent XY3 calculations aimed at investigating the energy-cluster formation in SbH_3 [15], it was transformed to the expansion [3]

$$V(\xi_1,\xi_2,\xi_3,\xi_{4a},\xi_{4b};\sin\overline{\rho}) = V_e + V_0(\sin\overline{\rho}) + \sum_j F_j(\sin\overline{\rho})\xi_j + \sum_{j\leq k} F_{jk}(\sin\overline{\rho})\xi_j\xi_k + \sum_{j\leq k\leq l} F_{jkl}(\sin\overline{\rho})\xi_j\xi_k\xi_l + \sum_{j\leq k\leq l\leq m} F_{jklm}(\sin\overline{\rho})\xi_j\xi_k\xi_l\xi_m \quad (4)$$

in the coordinates ξ_k:

$$\xi_k = 1-\exp(-a(r_k-r_e)), \quad k=1,2,3, \quad (5)$$

$$\xi_{4a} = \frac{1}{\sqrt{6}}(2\alpha_1-\alpha_2-\alpha_3), \quad (6)$$

$$\xi_{4b} = \frac{1}{\sqrt{2}}(\alpha_2-\alpha_3), \quad (7)$$

$$\sin\overline{\rho} = \frac{2}{\sqrt{3}}\sin[(\alpha_1+\alpha_2+\alpha_3)/6], \quad (8)$$

where

$$V_0(\sin\overline{\rho}) = \sum_{s=1} f_0^{(s)}(\sin\rho_e - \sin\overline{\rho})^s \quad (9)$$

and

$$F_{jk\ldots}(\sin\overline{\rho}) = \sum_{s=0} f_{jk\ldots}^{(s)}(\sin\rho_e - \sin\overline{\rho})^s. \quad (10)$$

We also use this latter expansion in the present work.

In Table 1 we include the available, experimentally derived vibrational term values for $^{121}SbH_3$ (the column labeled 'Obs.') up to 8000 cm^{-1}. The table uses two labeling schemes for the molecular states, one based on the standard normal-mode, harmonic-oscillator quantum numbers and the other one based on local mode, Morse-oscillator quantum numbers [37,41,42]. Lemus et al. [41,42] demonstrated that the bending vibrations in stibine are predominantly of normal mode character, whereas the stretching vibrations are most appropriately described by local mode quantum numbers.

The *ab initio* PES, when used as input for TROVE, produces vibrational energies in rather modest agreement with the available experimental values as seen by comparing the columns labeled 'Obs.' and 'Calc. I' in Table 1. Thus, for the fundamental term values, deviations up to 17 cm^{-1} are found. This accuracy is too poor for most applications. We can improve the agreement with experiment by constructing a 'spectroscopic' PES. Towards this end, we refine the *ab initio* potential parameters [15] of SbH_3 in simultaneous least-squares fitting [2,14] to the available experimentally derived vibrational energy spacings [37,40] and to the *ab initio* data [26]. The fitting employs TROVE calculations of vibrational energies made with the P_{max} = 12 basis set. Following Lummila et al. [37] we discard from the fitting some experimentally derived vibrational energy spacings with high uncertainty (Table 1). Obviously, there are quite few experimentally derived vibrational energy spacings of acceptable accuracy and because of this, a fitting only to these data points would allow the determination of very few potential energy parameter values only. In practice, however, we have been able to obtain values for all relevant potential energy parameters by fitting not only to the experimentally derived vibrational term values but also to the *ab initio* data [26]. In the final fitting to 6455 *ab initio* energies and 14 experimental band center values we could usefully vary 48 potential energy parameters whose optimized values are given in Table 2. During the fitting, the *ab initio* data serve to define the potential energy function in coordinate regions not sampled by the wavefunctions of the experimentally characterized vibrational states.

The vibrational term values calculated with TROVE from the refined, spectroscopic PES are included in Table 1 (Column 'Calc. II') and can be compared with the experimental values. The rms error is 1.83 cm^{-1} for the 14 band centers in the table used in the fittings (0.59 for the term values below 7000 cm^{-1}). The improvement of the calculated vibrational term values of Calc. II with respect to the values of Calc. I is obvious. The local-mode labeling of the calculated states agrees with those given in Refs. [37,41,42] except for the experimental vibrational

Table 2
Parameters (in cm^{-1} unless otherwise indicated) defining the refined PES of SbH_3 in its electronic ground state.

Parameter	Value	Parameter	Value
r_e (Å)	1.700[a]	$f^{(1)}_{114}$	0.11898218331384 $\times 10^6$
α_e (deg)	91.557[a]	$f^{(0)}_{123}$	0.19017877159862 $\times 10^4$
a ($Å^{-1}$)	1.4[a]	$f^{(1)}_{123}$	−0.81887048961300 $\times 10^4$
$f^{(2)}$	0.26647619271542 $\times 10^6$	$f^{(0)}_{124}$	0.12617901283266 $\times 10^4$
$f^{(3)}$	−0.66702427305419 $\times 10^6$	$f^{(1)}_{124}$	0.12728050074026 $\times 10^4$
$f^{(4)}$	0.20692955884057 $\times 10^7$	$f^{(0)}_{144}$	−0.27263329498616 $\times 10^4$
$f^{(1)}_1$	−0.88777775084702 $\times 10^4$	$f^{(1)}_{144}$	−0.41042673137233 $\times 10^5$
$f^{(2)}_1$	−0.17244226542584 $\times 10^5$	$f^{(0)}_{155}$	−0.46758119412010 $\times 10^4$
$f^{(3)}_1$	−0.77196630858319 $\times 10^5$	$f^{(1)}_{155}$	−0.84171112194568 $\times 10^4$
$f^{(0)}_{11}$	0.29586000262748 $\times 10^5$	$f^{(0)}_{455}$	−0.69252855936919 $\times 10^4$
$f^{(1)}_{11}$	0.24713933006405 $\times 10^4$	$f^{(1)}_{455}$	−0.11306727106534 $\times 10^6$
$f^{(2)}_{11}$	−0.75317802775475 $\times 10^5$	$f^{(0)}_{1111}$	0.17507628819530 $\times 10^4$
$f^{(0)}_{12}$	−0.49400706456696 $\times 10^3$	$f^{(0)}_{1112}$	0.41596255026285 $\times 10^4$
$f^{(1)}_{12}$	0.48463297350027 $\times 10^4$	$f^{(0)}_{1114}$	0.10862778013817 $\times 10^5$
$f^{(2)}_{12}$	−0.21107725715571 $\times 10^5$	$f^{(0)}_{1122}$	0.13755090105555 $\times 10^4$
$f^{(0)}_{14}$	−0.10286969463684 $\times 10^4$	$f^{(0)}_{1123}$	−0.93872506047505 $\times 10^4$
$f^{(1)}_{14}$	−0.19498125653409 $\times 10^5$	$f^{(0)}_{1124}$	0.53668552250068 $\times 10^4$
$f^{(2)}_{14}$	0.79078897736870 $\times 10^5$	$f^{(0)}_{1125}$	−0.44737220254204 $\times 10^4$
$f^{(0)}_{44}$	0.15469244272597 $\times 10^5$	$f^{(0)}_{1144}$	−0.10723417778062 $\times 10^5$
$f^{(1)}_{44}$	0.34735788204833 $\times 10^5$	$f^{(0)}_{1155}$	−0.41428780667331 $\times 10^4$
$f^{(2)}_{44}$	−0.20464860777176 $\times 10^6$	$f^{(0)}_{1244}$	0.48983922855174 $\times 10^4$
$f^{(0)}_{111}$	−0.18866575310495 $\times 10^4$	$f^{(0)}_{1255}$	0.26202447614447 $\times 10^4$
$f^{(1)}_{111}$	−0.39885807692562 $\times 10^5$	$f^{(0)}_{1444}$	0.77940392092530 $\times 10^3$
$f^{(0)}_{112}$	0.42783722357650 $\times 10^2$	$f^{(0)}_{1455}$	−0.23334765139599 $\times 10^4$
$f^{(1)}_{112}$	0.29682625311639 $\times 10^5$	$f^{(0)}_{4444}$	0.30662189381386 $\times 10^4$
$f^{(0)}_{114}$	0.26089106317080 $\times 10^4$		

[a] Fixed in the least-squares fitting to the experimental values from Ref. [38].

Table 3
Experimentally derived rotational term values of $^{121}SbH_3$ in the ground vibrational state (in cm^{-1}) compared to the TROVE-calculated theoretical values.

Γ	J	K	τ_{rot}	Obs.	Calc.	Obs. − Calc.
A_1	0	0	0	0.000	0.000	0.000
E	1	1	0	5.725	5.724	0.002
A_2	1	0	1	5.873	5.868	0.005
E	2	2	0	17.027	17.025	0.002
E	2	1	0	17.470	17.459	0.012
A_1	2	0	0	17.618	17.603	0.015
A_2	3	3	1	33.903	33.903	0.001
A_1	3	3	0	33.903	33.903	0.001
E	3	2	0	34.642	34.626	0.017
E	3	1	0	35.084	35.058	0.026
A_2	3	0	1	35.231	35.202	0.029
E	4	4	0	56.350	56.352	−0.002
A_1	4	3	0	57.386	57.366	0.020
A_2	4	3	1	57.386	57.366	0.020
E	4	2	0	58.122	58.086	0.036
E	4	1	0	58.562	58.516	0.046
A_1	4	0	0	58.708	58.659	0.049
E	5	5	0	84.362	84.368	−0.006
E	5	4	0	85.698	85.675	0.022
A_2	5	3	1	86.729	86.684	0.045
A_1	5	3	0	86.729	86.684	0.045
E	5	2	0	87.461	87.400	0.061
E	5	1	0	87.898	87.828	0.070
A_2	5	0	1	88.044	87.970	0.074
A_1	6	6	0	117.932	117.944	−0.012
A_2	6	6	1	117.932	117.944	−0.012
E	6	5	0	119.571	119.548	0.023
E	6	4	0	120.899	120.847	0.052
A_1	6	3	0	121.923	121.849	0.074
A_2	6	3	1	121.923	121.849	0.074
E	6	2	0	122.650	122.560	0.090
E	6	1	0	123.085	122.985	0.100
A_1	6	0	0	123.229	123.126	0.103

energy of 4545 cm^{-1}. Following Lummila et al. [37] we include neither this level nor the level at 4513 cm^{-1} in the input for the fitting because of the uncertainties of the corresponding term values. In the spectral region around 4500 cm^{-1} there is a high density of vibrational states and so we 'assigned' the two uncertain levels to the theoretically calculated levels that are closest in energy and give rise to strong vibrational transitions from the vibrational ground state, the strength of these transitions being obtained from theoretically calculated intensities (see below).

It should be noted that the correct determination of the molecular equilibrium structure is of special importance for accurate spectrum simulations [10]. In the case of the rigid molecule SbH_3 it is fortunate that the experimental values [38] for the bond length r_e=1.70001 Å and the bond angle $\alpha_e = 91.5566^\circ$ are highly accurate. This is illustrated in Table 3, where we show the theoretical (TROVE) rotational term values of $^{121}SbH_3$ in its ground vibrational state compared to experiment. The corresponding 'experimental' term values were calculated with a Watsonian-type Hamiltonian (see Ref. [45, Section 13.2.4]) in conjunction with the spectroscopic constants reported by Harder et al. [39] without taking into account the hyperfine structure.

4. Electric dipole transition moments and intensities

As a prerequisite for the intensity simulations we have computed the *ab initio* dipole moment surface for SbH_3 employing CCSD(T) (coupled cluster theory with single and double excitations [52] augmented by a perturbational estimate of the effects of connected triple excitations [53]) as implemented in MOLPRO2002 [54,55]. We employed a level of *ab initio* theory similar to that of Ref. [27]. We used a large-core pseudopotential [28] (ECP46MWB) adjusted to quasi-relativistic Wood–Boring [56] all-electron energies to describe the Sb atom in conjunction with the SDB-aug-cc-pVTZ basis [29]. For the hydrogen atoms, we used the aug-cc-pVTZ basis set [30]. In order to account for core–valence correlation effects, the ECP46MWB pseudopotential was supplemented by a core-polarization potential (CPP) in the present CCSD(T) calculations (see also the discussion in Ref. [27]). Dipole moments were computed by a numerical finite-difference procedure with an added external dipole field of 0.001 a.u.

We initially use the *ab initio* dipole moment data to generate an analytical representation of the DMS. For this, we employ the molecular bond (MB) representation [4,5,57,58] as defined in Eq. (35) of Yurchenko et al. [4]. The MB representation is based on the dipole moment projections ($\overline{\boldsymbol{\mu}} \cdot \mathbf{e}_j$) (where $\mathbf{e}_j$ is a unit vector directed along the Sb–H_j bond and pointing from Sb towards H_j) onto the bonds of the molecule. It defines the DMS completely in terms of the instantaneous positions of the nuclei [4]. The three projections ($\overline{\boldsymbol{\mu}} \cdot \mathbf{e}_j$) are then expressed in terms of a single function $\overline{\mu}_0(r_1,r_2,r_3,\alpha_1,\alpha_2,\alpha_3)$ [4]:

$$\overline{\boldsymbol{\mu}} \cdot \mathbf{e}_1 = \overline{\mu}_0(r_1,r_2,r_3,\alpha_1,\alpha_2,\alpha_3) = \overline{\mu}_0(r_1,r_3,r_2,\alpha_1,\alpha_3,\alpha_2), \quad (11)$$

$$\overline{\boldsymbol{\mu}} \cdot \mathbf{e}_2 = \overline{\mu}_0(r_2,r_3,r_1,\alpha_2,\alpha_3,\alpha_1) = \overline{\mu}_0(r_2,r_1,r_3,\alpha_2,\alpha_1,\alpha_3), \quad (12)$$

$$\overline{\boldsymbol{\mu}} \cdot \mathbf{e}_3 = \overline{\mu}_0(r_3,r_1,r_2,\alpha_3,\alpha_1,\alpha_2) = \overline{\mu}_0(r_3,r_2,r_1,\alpha_3,\alpha_2,\alpha_1), \quad (13)$$

which is given by the expansion

$$\overline{\mu}_0 = \mu_0^{(0)} + \sum_k \mu_k^{(0)} \chi_k + \sum_{k,l} \mu_{kl}^{(0)} \chi_k \chi_l + \sum_{k,l,m} \mu_{klm}^{(0)} \chi_k \chi_l \chi_m + \sum_{k,l,m,n} \mu_{klmn}^{(0)} \chi_k \chi_l \chi_m \chi_n + \cdots \quad (14)$$

in the variables

$$\chi_k = (r_k - r_e)\exp(-\beta(r_k - r_e)^2), \quad k = 1,2,3, \quad (15)$$

$$\chi_l = \cos(\alpha_{l-3}) - \cos(\alpha_e), \quad l = 4,5,6. \quad (16)$$

In Table 4 the dipole moment parameters for the electronic ground state of SbH_3 are listed. Fitting Eq. (14) through 3×5000 *ab initio* data points, we obtained an rms error of 0.001 D by varying 112 parameters. Fortran routines for calculating the dipole moment components are provided as supplementary material. The new *ab initio* dipole moment function will be referred to as SDB-TZ.

Once the components of the electronically averaged dipole moment $\overline{\mu}_\alpha$ ($\alpha = x,y,z$) along the molecule-fixed axes *xyz* [3,9] are expressed as functions of the internal molecular coordinates, the matrix elements of the dipole moment components between the molecular eigenfunctions can be obtained. For intensity simulations of the

Table 4
The MB-representation dipole moment parameters [4,5] (in D unless otherwise indicated) for the electronic ground state of stibine.

Parameter	Value	Parameter	Value	Parameter	Value
β (Å^{-1})	1.0	$\mu^{(0)}_{246}$	0.09446641	$\mu^{(0)}_{1566}$	−0.18969200
$\mu^{(0)}_{0}$	−0.15382957	$\mu^{(0)}_{255}$	−0.08714483	$\mu^{(0)}_{1666}$	−0.27524468
$\mu^{(0)}_{1}$	−1.83611199	$\mu^{(0)}_{256}$	−0.12716119	$\mu^{(0)}_{2222}$	0.12706772
$\mu^{(0)}_{3}$	0.12683050	$\mu^{(0)}_{266}$	−0.12409425	$\mu^{(0)}_{2224}$	−0.11429074
$\mu^{(0)}_{4}$	0.09654568	$\mu^{(0)}_{333}$	0.04312205	$\mu^{(0)}_{2225}$	−0.09714754
$\mu^{(0)}_{5}$	−0.86510997	$\mu^{(0)}_{334}$	0.02113440	$\mu^{(0)}_{2244}$	−0.05649518
$\mu^{(0)}_{11}$	0.01993394	$\mu^{(0)}_{344}$	0.04912492	$\mu^{(0)}_{2245}$	−0.11936999
$\mu^{(0)}_{13}$	−0.04946879	$\mu^{(0)}_{444}$	0.06483608	$\mu^{(0)}_{2246}$	0.35605098
$\mu^{(0)}_{14}$	−0.14614088	$\mu^{(0)}_{445}$	0.45316260	$\mu^{(0)}_{2255}$	0.03419155
$\mu^{(0)}_{16}$	0.11984798	$\mu^{(0)}_{456}$	0.01943499	$\mu^{(0)}_{2256}$	−0.05172147
$\mu^{(0)}_{23}$	−0.04886949	$\mu^{(0)}_{466}$	0.08195234	$\mu^{(0)}_{2266}$	0.13911824
$\mu^{(0)}_{33}$	0.04278221	$\mu^{(0)}_{555}$	0.60263858	$\mu^{(0)}_{2333}$	−0.08426329
$\mu^{(0)}_{34}$	−0.12897179	$\mu^{(0)}_{556}$	0.17992418	$\mu^{(0)}_{2335}$	0.06212090
$\mu^{(0)}_{35}$	−0.72509985	$\mu^{(0)}_{1111}$	−0.38455475	$\mu^{(0)}_{2336}$	0.15794728
$\mu^{(0)}_{36}$	0.01665824	$\mu^{(0)}_{1112}$	0.06007596	$\mu^{(0)}_{2344}$	−0.07928812
$\mu^{(0)}_{44}$	−0.03760912	$\mu^{(0)}_{1114}$	−0.07969284	$\mu^{(0)}_{2345}$	0.23880925
$\mu^{(0)}_{46}$	−0.23400948	$\mu^{(0)}_{1115}$	0.35892869	$\mu^{(0)}_{2356}$	0.05479589
$\mu^{(0)}_{55}$	−0.02572926	$\mu^{(0)}_{1122}$	0.15639528	$\mu^{(0)}_{2366}$	0.03429291
$\mu^{(0)}_{56}$	0.09634099	$\mu^{(0)}_{1123}$	0.17820339	$\mu^{(0)}_{2444}$	−0.11772983
$\mu^{(0)}_{111}$	−1.43934622	$\mu^{(0)}_{1124}$	0.09074178	$\mu^{(0)}_{2445}$	−0.34369373
$\mu^{(0)}_{112}$	0.01202344	$\mu^{(0)}_{1126}$	−0.59561584	$\mu^{(0)}_{2456}$	0.33363574
$\mu^{(0)}_{114}$	0.05190559	$\mu^{(0)}_{1136}$	0.20513772	$\mu^{(0)}_{2466}$	0.29436052
$\mu^{(0)}_{115}$	0.51646355	$\mu^{(0)}_{1144}$	−0.03941277	$\mu^{(0)}_{3335}$	−0.54460774
$\mu^{(0)}_{123}$	−0.05792208	$\mu^{(0)}_{1146}$	−0.10634235	$\mu^{(0)}_{3445}$	0.02525874
$\mu^{(0)}_{124}$	0.14067552	$\mu^{(0)}_{1155}$	−0.08258537	$\mu^{(0)}_{3555}$	0.07766749
$\mu^{(0)}_{133}$	0.20671970	$\mu^{(0)}_{1233}$	−0.04666002	$\mu^{(0)}_{3556}$	0.15261861
$\mu^{(0)}_{135}$	0.23858808	$\mu^{(0)}_{1234}$	−0.06445876	$\mu^{(0)}_{3566}$	−0.01376070
$\mu^{(0)}_{136}$	0.01874878	$\mu^{(0)}_{1244}$	−0.13776673	$\mu^{(0)}_{3666}$	−0.04499354
$\mu^{(0)}_{144}$	0.18603743	$\mu^{(0)}_{1245}$	−0.05084070	$\mu^{(0)}_{4444}$	−0.04633795
$\mu^{(0)}_{146}$	0.23528044	$\mu^{(0)}_{1246}$	−0.18584935	$\mu^{(0)}_{4445}$	−0.04439568
$\mu^{(0)}_{155}$	0.67563925	$\mu^{(0)}_{1256}$	−0.26342756	$\mu^{(0)}_{4456}$	−0.40942554
$\mu^{(0)}_{156}$	0.44912683	$\mu^{(0)}_{1335}$	−0.14241433	$\mu^{(0)}_{4466}$	−0.12883163
$\mu^{(0)}_{223}$	0.01144244	$\mu^{(0)}_{1355}$	0.14154362	$\mu^{(0)}_{4555}$	−0.13254513
$\mu^{(0)}_{225}$	0.08900180	$\mu^{(0)}_{1366}$	−0.01688911	$\mu^{(0)}_{4556}$	−0.86386717
$\mu^{(0)}_{226}$	−0.18751441	$\mu^{(0)}_{1444}$	−0.10020889	$\mu^{(0)}_{5566}$	−0.01824977
$\mu^{(0)}_{234}$	0.11085087	$\mu^{(0)}_{1445}$	−0.25372629	$\mu^{(0)}_{5666}$	−0.02576928
$\mu^{(0)}_{235}$	0.04530505	$\mu^{(0)}_{1456}$	−1.32925498	$\mu^{(0)}_{6666}$	0.27677620
$\mu^{(0)}_{245}$	0.43081293	$\mu^{(0)}_{1466}$	−0.28429770		

[a] α_e and r_e were fixed in the least-squares fitting to the *ab initio* [27] equilibrium values of 91.76° and 1.702 Å, respectively.

absorption spectrum of $^{121}SbH_3$ we use the 'spectroscopic' PES and the *ab initio* SDB-TZ DMS in conjunction with the theory described by Yurchenko et al. [4]. We follow the procedures described in Ref. [4] and compute the line strengths (in units of D^2), and the integrated absorption coefficients (in units of cm/mol) for individual rotation–vibration transitions of $^{121}SbH_3$ at T=300 K. In the intensity simulations we considered all transitions within the wavenumber window 0…8000 cm^{-1} with lower states having term values $<$4000 cm above the ground state. It should be noted that the upper simulation limit (8000 cm^{-1}) is beyond the range in which our PES is optimized (to 7000 cm^{-1}). We have obtained 3 286 305 lines with absorption intensity $I(f\leftarrow i)>0.001$ cm/mol [corresponding to 4×10^{-8} cm^{-2} atm^{-1}] at T=300 K. The eigenfunctions and eigenvalues required for the spectrum simulations were computed with the $P_{\max}$=10 basis set. The EBSC [10] approach was used in order to improve empirically the agreement with experiment of the theoretical spectrum, in which we substituted the theoretical vibrational band centers $E_\gamma^{\rm vib}$ in Eq. (1) by the corresponding experimental values. For more details on the intensity calculations see Ref. [10].

For the calculation of the integrated absorption coefficients $I(f\leftarrow i)$ (see Ref. [4, Eq. (6)]) we require the partition function Q given by [45]

$$Q=\sum_i g_{\rm ns}(2J+1)e^{-E_i hc/kT}, \tag{17}$$

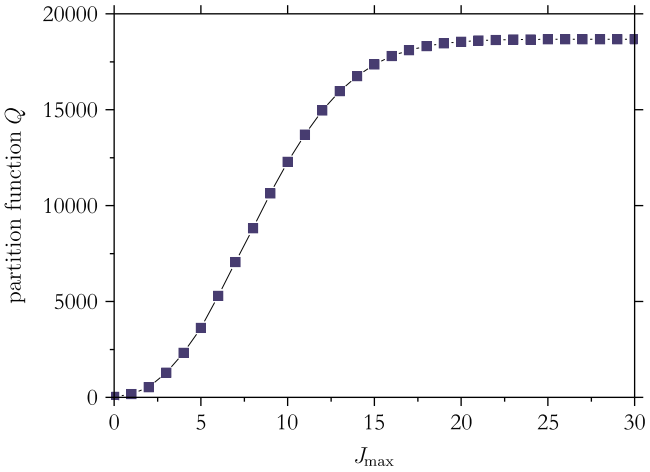

Fig. 1. The convergence of the partition function Q of $^{121}SbH_3$ with $J \leq J_{max}$; Q is calculated from all rovibrational states with $P \leq P_{max} = 10$ at T=300 K.

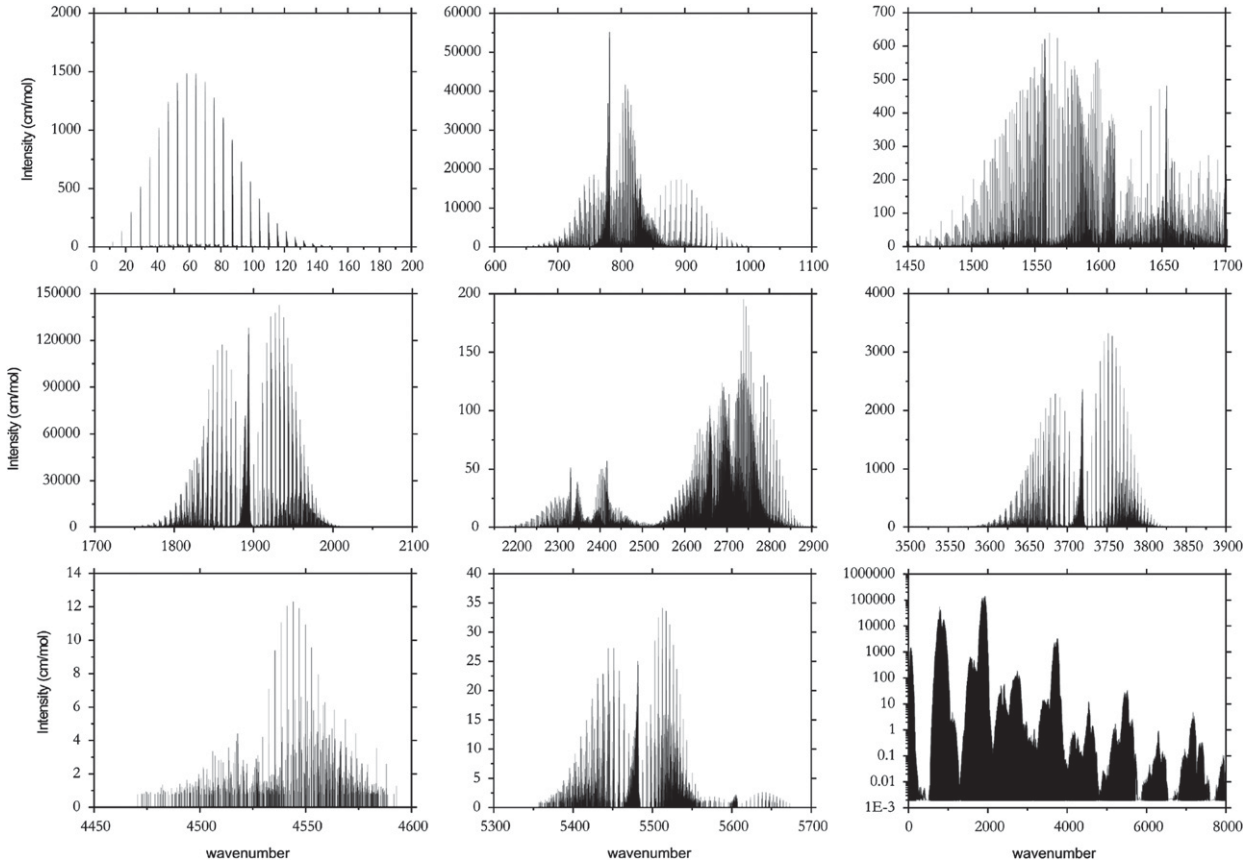

Fig. 2. Synthetic spectra of $^{121}SbH_3$ in the wavenumber range 0–8000 cm^{-1}, computed at an absolute temperature of 300 K.

where g_{ns} is the nuclear spin statistical weight, E_i is a rovibrational term value obtained through diagonalization of the Hamiltonian matrix, k is the Boltzmann constant, h is the Planck constant and c is the speed of light. For the $^{121}SbH_3$ molecule with the nuclear spins of 5/2 and 1/2 for ^{121}Sb and H, respectively, the statistical weight factors g_{ns} for all three symmetries A_1, A_2, and E [45] of $\mathbf{C}_{3v}(M)$ are equal to 24. Using all computed rovibrational term values with $J \leq 30$ (below 13 657 cm^{-1}, 442 998 levels) in Eq. (17), we obtained Q=18 702. The $^{121}SbH_3$ molecule is an oblate symmetric top with two rotational constants B and C. In the vibrational ground state, these constants have the values 2.937 and 2.789 cm^{-1}, respectively [38], and so we have

Table 5
Vibrational band centers $\tilde{\nu}_{fi}$ (in cm^{-1}), transition moments μ_{fi} (in D), and vibrational band strengths $S_{vib}(f \leftarrow i)$ (Eq. (19) in $cm^{-2}\,atm^{-1}$ at $T=300$ K) for a number of $^{121}SbH_3$ transitions.

Transition[a]		$\tilde{\nu}_{fi}$	E_f	E_i	μ_{fi}	$S_{vib}(f \leftarrow i)$
Upper state	Lower state					
(000;000;A_1)	(000;000;A_1)	0.00	0.00	0.00	0.331	1.119[b]
(000;120;E)	(000;110;E)	765.23	2422.29	1657.06	0.256	0.021
(000;300;E)	(000;002;E)	766.25	2366.89	1600.64	0.354	0.053
(000;111;A_1)	(000;011;A_1)	772.26	2331.52	1559.26	0.305	0.048
(000;002;E)	(000;001;E)	772.83	1600.64	827.81	0.257	1.147
(000;011;A_1)	(000;001;A_1)	777.08	1559.26	782.18	0.255	1.409
(000;001;A_1)	(000;000;A_1)	782.18	782.18	0.00	0.184	31.534
(000;002;E)	(000;001;A_1)	818.46	1600.64	782.18	0.137	0.431
(000;002;A_1)	(000;001;E)	825.82	1653.63	827.81	0.136	0.346
(000;001;E)	(000;000;A_1)	827.81	827.81	0.00	0.141	19.593
(000;110;E)	(000;001;E)	829.25	1657.06	827.81	0.198	0.733
(000;002;A_1)	(000;001;A_1)	871.45	1653.63	782.18	0.031	0.023
(000;111;A_1)	(000;001;A_1)	1549.34	2331.52	782.18	0.021	0.020
(000;011;A_1)	(000;000;A_1)	1559.26	1559.26	0.00	0.014	0.356
(000;300;E)	(000;001;A_1)	1584.71	2366.89	782.18	0.025	0.029
(000;120;E)	(000;001;E)	1594.48	2422.29	827.81	0.025	0.024
(000;002;E)	(000;000;A_1)	1600.64	1600.64	0.00	0.018	0.618
(000;210;E)	(000;001;E)	1652.79	2480.60	827.81	0.025	0.024
(000;002;A_1)	(000;000;A_1)	1653.63	1653.63	0.00	0.012	0.281
(000;110;E)	(000;000;A_1)	1657.06	1657.06	0.00	0.008	0.134
(100;001;A_1)	(000;001;E)	1833.80	2661.61	827.81	0.041	0.071
(100;001;E)	(000;001;E)	1836.38	2664.19	827.81	0.051	0.112
(100;110;A_2)	(000;110;E)	1862.20	3519.26	1657.06	0.175	0.025
(100;002;E)	(000;002;A_1)	1863.50	3517.13	1653.63	0.221	0.040
(100;110;E)	(000;110;E)	1865.93	3522.99	1657.06	0.224	0.040
(100;011;A_1)	(000;011;A_1)	1866.13	3425.38	1559.26	0.130	0.022
(100;002;A_1)	(000;002;E)	1866.17	3466.81	1600.64	0.158	0.026
(100;011;E)	(000;011;A_1)	1867.73	3426.98	1559.26	0.231	0.069
(100;002;E)	(000;002;E)	1868.43	3469.07	1600.64	0.231	0.057
(100;002;E)	(000;002;E)	1870.58	3471.22	1600.64	0.195	0.040
(100;110;E)	(000;110;E)	1871.73	3528.79	1657.06	0.204	0.034
(100;002;A_2)	(000;002;E)	1871.83	3472.47	1600.64	0.175	0.032
(100;001;E)	(000;001;E)	1878.61	2706.42	827.81	0.239	2.470
(100;001;A_1)	(000;001;E)	1878.68	2706.49	827.81	0.173	1.296
(100;001;A_1)	(000;001;A_1)	1879.43	2661.61	782.18	0.140	1.055
(100;001;A_2)	(000;001;E)	1881.52	2709.33	827.81	0.178	1.377
(100;001;E)	(000;001;E)	1881.86	2709.67	827.81	0.214	1.992
(100;001;E)	(000;001;A_1)	1882.01	2664.19	782.18	0.244	3.223
(100;000;A_1)	(000;000;A_1)	1890.71	1890.71	0.00	0.146	48.931
(100;000;E)	(000;000;A_1)	1894.53	1894.53	0.00	0.251	146.160
(100;001;A_1)	(000;001;A_1)	1924.31	2706.49	782.18	0.031	0.054
(100;001;E)	(000;001;A_1)	1927.50	2709.67	782.18	0.053	0.155
(000;111;A_1)	(000;000;A_1)	2331.52	2331.52	0.00	0.004	0.042
(000;111;A_1)	(000;000;A_1)	2417.89	2417.89	0.00	0.004	0.039
(100;001;A_1)	(000;000;A_1)	2661.61	2661.61	0.00	0.005	0.079
(100;001;E)	(000;000;A_1)	2664.19	2664.19	0.00	0.006	0.127
(100;001;E)	(000;000;A_1)	2706.42	2706.42	0.00	0.007	0.173
(100;001;A_1)	(000;000;A_1)	2706.49	2706.49	0.00	0.005	0.082
(100;001;E)	(000;000;A_1)	2709.67	2709.67	0.00	0.003	0.031
(100;002;E)	(000;000;A_1)	3471.22	3471.22	0.00	0.002	0.024
(200;001;E)	(000;001;A_1)	3690.29	4472.46	782.18	0.023	0.058
(020;001;A_1)	(000;001;A_1)	3690.36	4472.54	782.18	0.015	0.024
(200;001;A_2)	(000;001;E)	3692.60	4520.41	827.81	0.018	0.029
(200;001;E)	000;001;E)	3693.19	4521.00	827.81	0.025	0.053
(020;001;E)	(000;001;E)	3697.89	4525.70	827.81	0.022	0.043
(200;001;A_1)	(000;001;E)	3698.54	4526.35	827.81	0.017	0.023
(200;000;E)	(000;000;A_1)	3719.67	3719.67	0.00	0.026	3.022
(020;000;A_1)	(000;000;A_1)	3719.96	3719.96	0.00	0.017	1.270
(110;000;E)	(000;000;A_1)	3794.30	3794.30	0.00	0.002	0.021
(300;000;E)	(000;000;A_1)	5480.40	5480.40	0.00	0.002	0.029
(003;000;A_1)	(000;000;A_1)	5481.16	5481.16	0.00	0.002	0.026

The threshold for the vibrational line strengths was taken to be $0.02\,cm^{-2}\,atm^{-1}$ at $T=300$ K.
[a] Spectroscopic assignment of the vibrational band.
[b] Calculated using a fictitious value of $\tilde{\nu}_{fi}=50.0\,cm^{-1}$ in Eq. (19) in order to estimate S_{vib} for the ground-state rotational spectrum.

$B \approx C$. Consequently, we can view $^{121}SbH_3$ as a quasi-spherical top. The constants B and C are sufficiently large that only states with moderate values of J (up to around 20) are populated at T=300 K, and we can thus generate a converged value of the partition function Q considering this range of J values in the calculation of Q. This is illustrated in Fig. 1. We estimate that in terms of the vibrational basis set (i.e., P_{max}=10), Q is converged to better than 0.1%.

The results of the simulations (line strengths, Einstein coefficients, and absorption intensities) are included in the supporting information along with a Fortran program to generate a synthetic spectrum. As an illustration, we show in Fig. 2 the strongest absorption bands from the chosen wavenumber window. In the same figure the complete spectrum (with wavenumbers from 0 to 8000 cm^{-1}) is also depicted with a logarithmic ordinate scale. The complete SbH_3 list is also available electronically in compressed form at http://www.spectrove.org.

In Table 5 the vibrational transition moments

$$\mu_{fi} = \sqrt{\sum_{\alpha=x,y,z} |\langle \Psi^{\Gamma_f}_{J=0,f} | \overline{\mu}_\alpha | \Psi^{\Gamma_i}_{J=0,i} \rangle|^2} \quad (18)$$

for a number of selected transition lines are given. In Eq. (18), $\Psi^{\Gamma_w}_{J=0,w}$ (w=i or f) are the vibrational wavefunctions. The electronically averaged dipole moment functions $\overline{\mu}_\alpha$ in Eq. (18) are derived from the *ab initio* dipole moment surface SDB-TZ (Table 4). We have computed the transition moments in Eq. (18) for all vibrational transitions that are relevant for the T=300 K absorption spectrum. The strength of the vibrational band at a given temperature [59,60] is

$$S_{vib}(f \leftarrow i) = \frac{8\pi^3 \tilde{\nu}_{fi}}{3hc} \frac{LT_0}{Q_{vib}(T)T} e^{-E_i/kT} [1 - e^{-(E_f - E_i)/kT}] \mu^2_{fi}, \quad (19)$$

Table 6
Experimental and calculated relative intensities of $^{121}SbH_3$ for transitions from the vibrational ground state to pure stretching states.

State[a]	I_{obs}[b]	I_{Hal}[c]	I_{Liu}[d]	$I_{calc.}$[e]
(100;000;A_1/E)	1.0	1.0	1.0	1.0[f]
(200;000;A_1/E)	0.022	0.021	0.021	0.022[f]
(110;000;A_1)[g]		0.20×10^{-4}		0.15×10^{-4}
(110;000;E)		0.98×10^{-5}		0.11×10^{-3}
(300;000;A_1/E)	0.32×10^{-3}	0.47×10^{-3}	0.20×10^{-3}	0.28×10^{-3}[f]
(210;000;A_1)	0.11×10^{-4}	0.82×10^{-7}	0.11×10^{-5}	0.51×10^{-5}
(210;000;E)[h]		0.79×10^{-7}		0.15×10^{-4}
(210;000;E)[i]				0.1×10^{-10}
(400;000;A_1/E)	0.14×10^{-4}	0.78×10^{-5}	0.28×10^{-5}	0.36×10^{-4}[f]

[a] Spectroscopic local-mode assignment of the vibrational band. The calculated energies are given in Tables 1 and 5 unless otherwise indicated.
[b] Observed relative intensities [35].
[c] Calculated relative intensities [35].
[d] Calculated relative intensities [44].
[e] Relative intensities calculated in the present work from the $S_{vib}(f \leftarrow i)$ values in Table 5.
[f] Obtained by adding the A_1 and E intensities.
[g] Calculated energy is 3777.34 cm^{-1}.
[h] Calculated energy is 5606.10 cm^{-1}.
[i] Calculated energy is 5639.07 cm^{-1}.

where E_i and E_f are the band centers of the initial and final states, respectively, and $hc\tilde{\nu}_{fi} = E_f - E_i$, h is the Planck constant, c is the speed of light in vacuum, k is the Boltzmann constant, $L = 2.68675 \times 10^{19}$ mol cm^{-3} atm^{-1} is the Loschmidt constant for 1 atm pressure at the reference temperature of T_0=273.15 K, and T=300 K. In the calculation of the vibrational strength $S_{vib}(f \leftarrow i)$, Q_{vib}=8.34. In Table 5 we have compiled the transition moments of stibine that correspond to band strengths $S_{vib}(f \leftarrow i) > 0.02$ cm^{-2} atm^{-1}. The complete list of computed transition moments and band strengths is given in the supporting information.

In Table 6 we list relative vibrational intensities for a number of vibrational bands and compare them with the corresponding experimental values from Ref. [35] and with other theoretical values [35,44]. For all transitions with available, experimentally derived intensity values (Table 6), the present work has improved the agreement with experiment significantly relative to the previous calculations [35,44].

5. Local mode analysis: comparison of SbH_3 and PH_3

It is well known that the local-mode character of molecules such as phosphine and stibine manifests itself in their geometries, energy level patterns, potential energy and dipole moment surfaces as well in their transition moments (see, for example, Refs. [24,25] and our recent local mode analysis of PH_3 in Ref. [17]). It is also generally accepted that for molecules with local-mode character, the local-mode quantum numbers represent a more adequate labeling scheme for the molecular states, especially for the stretching modes. In the case of stibine this has been shown in Refs. [34,35,37,42].

Here, we compare the local-mode characters of phosphine PH_3 and stibine $^{121}SbH_3$. We expect that stibine exhibits a stronger local-mode character than phosphine, due to the very large mass of the central atom in stibine. Besides, the equilibrium interbond angles of $^{121}SbH_3$ are 91.6° [38] and so they are closer to 90° than the corresponding angles of PH_3 which are 93.4° [61]. In Fig. 3 the vibrational stretching energy patterns for stibine and phosphine are compared up to the polyad 4, where the pure stretching term values are plotted relative to the lowest state in each polyad and labeled according to the local-mode scheme. The theoretical PH_3 energies are taken from Ref. [17], while the stibine energies are from the present work.

The local mode effects become stronger with increasing stretching excitation. This is visible in Fig. 3, where the local-mode degeneracies (for example, of the lowest two levels in each polyad) generally get more pronounced as the polyad number increases. The lowest energy in the polyad has the local-mode label (n,0,0); it is the 'most local' level in the polyad. The higher energies in the polyad correspond to states with a higher degree of mixing between local-mode basis states; these states are less local. However, this energy pattern can be perturbed by the presence of bending levels, especially in the high

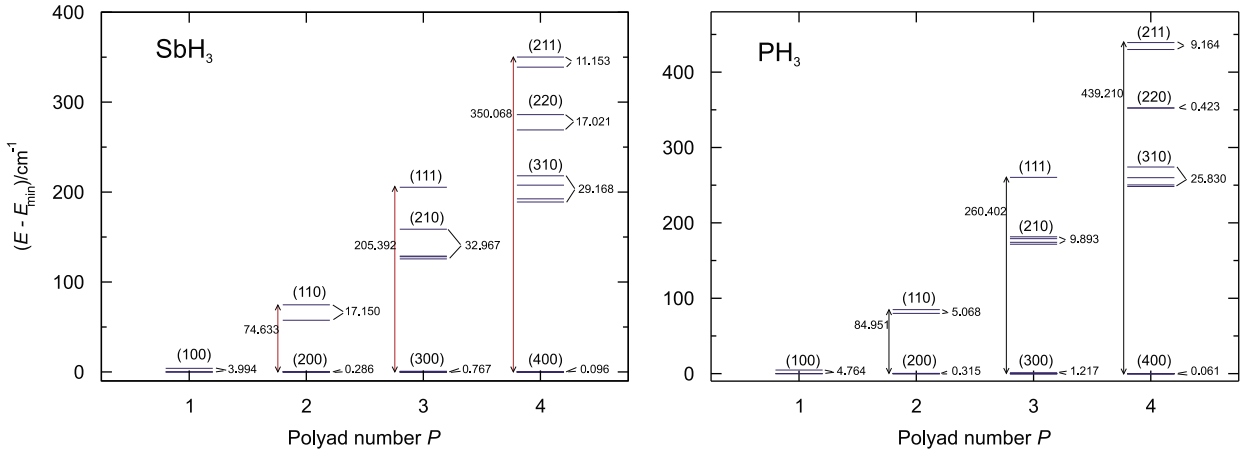

Fig. 3. Comparison between the term value diagrams for the $P \leq 4$ vibrational polyads of PH_3 and $^{121}SbH_3$. The term values (in cm^{-1}) are plotted relative to the lowest state in each polyad. The stretching states are labeled by the local-mode labels (n_1, n_2, n_3).

energy regions with a high density of states. For more details see, for example, the review [25]. Comparing the energy differences of (n,0,0) states in the local mode diagrams of stibine and phosphine in Fig. 3, stibine shows a more pronounced local mode character than phosphine. We also note that in stibine, the stretching vibrations are more harmonic than in phosphine. This is manifest in the smaller energy spread of each polyad.

It was shown in Ref. [17] that according to local-mode theory, the vibrational transition moments for the pure stretching states obey the following simple rule:

$$|\langle n00; E|\boldsymbol{\mu}|000; A_1\rangle| = 2|\langle n00; A_1|\boldsymbol{\mu}|000; A_1\rangle|, \tag{20}$$

where n is the stretching local quantum number and $|\langle n00; \Gamma|\boldsymbol{\mu}|000; \Gamma'\rangle|$ denotes the transition moment μ_{fi} from Eq. (18) between the $|n00; \Gamma\rangle$ and $|000; \Gamma'\rangle$ states. This can be readily verified by inspecting Table 5. For the transition moments μ_{fi} that couple the ground state with the stretching states (100) and (200) we obtain

$$\frac{|\langle 100; E|\boldsymbol{\mu}|000; A_1\rangle|}{2|\langle 100; A_1|\boldsymbol{\mu}|000; A_1\rangle|} = \frac{0.251386}{0.291202} \approx 0.86 \tag{21}$$

and

$$\frac{|\langle 200; E|\boldsymbol{\mu}|000; A_1\rangle|}{2|\langle 200; A_1|\boldsymbol{\mu}|000; A_1\rangle|} = \frac{0.025799}{0.033452} \approx 0.77. \tag{22}$$

That is, Eq. (20) is fairly well satisfied for SbH_3. For PH_3, the corresponding ratios were 0.99 and 0.91 [17], respectively, so that in this case we obtained better agreement with Eq. (20) than for SbH_3.

Finally, in Ref. [17] it was shown that the local mode transition moments $\langle 0|\boldsymbol{\mu}|200; A_1\rangle$ and $\langle 0|\mu|100; A_1\rangle$ satisfy the following condition:

$$\frac{|\langle 0|r|2\rangle|}{|\langle 0|r|1\rangle|} \approx \frac{|\langle 0|\boldsymbol{\mu}|200; A_1\rangle|}{|\langle 0|\boldsymbol{\mu}|100; A_1\rangle|}, \tag{23}$$

where $|\langle 0|r|2\rangle$ is the matrix element of one of the stretching coordinate r_i (i=1,2,3) on the corresponding 1D stretching function represented by the Morse oscillator. For $^{121}SbH_3$ we obtain

$$\frac{|\langle 0|r|2\rangle|}{|\langle 0|r|1\rangle|} \approx 0.09 \quad \text{and} \quad \frac{|\langle 0|\boldsymbol{\mu}|200; A_1\rangle|}{|\langle 0|\boldsymbol{\mu}|100; A_1\rangle|} \approx 0.11, \tag{24}$$

so that the relation in Eq. (23) is better obeyed than in the case of PH_3, where the corresponding quantities were 0.05 and 0.11, respectively.

6. Summary and conclusion

We have reported here a new PES for SbH_3, obtained by empirical refinement of an *ab initio* PES [27], together with a new *ab initio* DMS, computed with the CCSD(T) method as described in Section 4. The new PES and DMS have been used as input for the program TROVE [9] to compute the vibrational energies of $^{121}SbH_3$ up to 8000 cm^{-1} and to simulate the rovibrational spectrum of this molecule in this wavenumber region.

Initially, we calculated the vibrational energies using the high-level *ab initio* PES reported by Canè et al. [27]. The resulting energy values were too large and still far from spectroscopic accuracy. Consequently, an empirical refinement of the PES was performed through a simultaneous fit to the *ab initio* data from Ref. [27] and the available vibrational term values [2]. With the refined PES, we obtained vibrational term values in good agreement with the experimental values. The energies and intensities obtained with the resulting PES and the new DMS were used in a local-mode analysis of $^{121}SbH_3$ whose local-mode behavior was compared to that of phosphine [17].

For stibine, only very limited experimental spectroscopic data is available which do not suffice to determine uniquely the PES in an appreciable volume of configuration space. In particular, there is a paucity of experimentally characterized excited bending levels and levels involving simultaneous excitation of bending and stretching. Therefore, it is impossible to derive a suitable spectroscopic PES purely from experimental data so that a simultaneous fitting to *ab initio* data and the available experimentally derived vibrational energies is inevitable.

In view of the good agreement with the available experimental data obtained with the refined PES and the new *ab initio* DMS, we are confident that we can accurately predict the energies and the intensities of transitions not yet observed, for example those involved in $^{121}SbH_3$ polyads at higher energies as well as the missing bending and bend-stretch levels at lower energies, in particular if we use the CVBS extrapolation method for this purpose [16]. Also, we can make predictions for other isotopologues such as $^{123}SbH_3$, for which there is a dramatic lack of experimental data (see Ref. [27]) and only limited theoretical information [27,35]. We hope that the predictions of the present work will encourage new experimental investigations of $^{121}SbH_3$ and its isotopologues.

Acknowledgments

We acknowledge support from the European Commission through Contract no. MRTN-CT-2004-512202 'Quantitative Spectroscopy for Atmospheric and Astrophysical Research' (QUASAAR). The work of P.J. is supported in part by the Fonds der Chemischen Industrie and that of M.C. by the Andalusian Government (Spain) under the project Contract number P07-FQM-03014.

Appendix A. Supplementary data

Supplementary data associated with this article can be found in the online version at doi:10.1016/j.jqsrt.2010.03.008.

References

[1] Lin H, Thiel W, Yurchenko SN, Carvajal M, Jensen P. J Chem Phys 2002;117:11265–76.
[2] Yurchenko SN, Carvajal M, Jensen P, Herregodts F, Huet TR. Chem Phys 2003;290:59–67.
[3] Yurchenko SN, Carvajal M, Jensen P, Lin H, Zheng JJ, Thiel W. Mol Phys 2005;103:359–78.
[4] Yurchenko SN, Carvajal M, Thiel W, Lin H, Jensen P. Adv Quant Chem 2005;48:209–38.
[5] Yurchenko SN, Carvajal M, Lin H, Zheng JJ, Thiel W, Jensen P. J Chem Phys 2005;122:104317 [14pp.].
[6] Yurchenko SN, Carvajal M, Thiel W, Jensen P. J Mol Spectrosc 2006;239:71–87.
[7] Yurchenko SN, Thiel W, Carvajal M, Jensen P. Chem Phys 2008;346:146–59.
[8] Hougen JT, Bunker PR, Johns JWC. J Mol Spectrosc 1970;34:136–72.
[9] Yurchenko SN, Thiel W, Jensen P. J Mol Spectrosc 2007;245:126–40.
[10] Yurchenko SN, Barber RJ, Yachmenev A, Thiel W, Jensen P, Tennyson J. J Phys Chem A 2009;113:11845–55.
[11] Papoušek D, Aliev MR. Molecular vibrational–rotational spectra. Amsterdam: Elsevier; 1982.
[12] Yurchenko SN, Thiel W, Patchkovskii S, Jensen P. Phys Chem Chem Phys 2005;7:573–82.
[13] Yurchenko SN, Zheng J, Lin H, Jensen P, Thiel W. J Chem Phys 2005;123:134308 [14pp.].
[14] Yurchenko SN, Breidung J, Thiel W. Theor Chem Acc 2005;114: 333–40.
[15] Yurchenko SN, Thiel W, Jensen P. J Mol Spectr 2006;240:174–87.
[16] Ovsyannikov RI, Thiel W, Yurchenko SN, Carvajal M, Jensen P. J Chem Phys 2008;129:044309 [8pp.].
[17] Ovsyannikov RI, Thiel W, Yurchenko SN, Carvajal M, Jensen P. J Mol Spectrosc 2008;252:121–8.
[18] Ovsyannikov RI, Melnikov VV, Thiel W, Jensen P, Baum O, Giesen TF, et al. J Chem Phys 2008;129:044309 [8pp.].
[19] Yurchenko SN, Yachmenev A, Thiel W, Baum O, Giesen TF, Melnikov VV, et al. J Mol Spectrosc 2009;257:57–65.
[20] Yachmenev A, Yurchenko SN, Jensen P, Melnikov VV, Baum O, Giesen TF, et al. to be published.
[21] Yurchenko S, Ovsyannikov RI, Thiel W, Jensen P. J Mol Spectrosc 2009;256:119–27.
[22] Burgdorf MJ, Orton GS, Encrenaz T, Davis GR, Lellouch E, Sidher SD, et al. Adv Space Res 2004;34:2247–50.
[23] Agúndez M, Cernicharo J, Pardo JR, Guélin M, Phillips TG. Astron Astrophys 2008;485:33–6.
[24] Child MS, Halonen L. Adv Chem Phys 1984;57:1–57.
[25] Jensen P. Mol Phys 2000;98:1253–85.
[26] Breidung J, Thiel W. J Mol Spectrosc 1995;169:166–80.
[27] Canè E, Di Lonardo G, Fusina L, Jerzembeck W, Bürger H, Breidung J, et al. Mol Phys 2005;103:557–77.
[28] Bergner A, Dolg M, Küchle W, Stoll H, Preuss H. Mol Phys 1993;80:1431–41.
[29] Martin J, Sundermann A. J Chem Phys 2001;114:3408–20.
[30] Kendall RA, Dunning TH, Harrison RJ. J Chem Phys 1992;96:6796–806.
[31] Loomis CC, Strandberg MWP. Phys Rev 1951;81:798–807.
[32] Jache AW, Blevins GS, Gordy W. Phys Rev 1955;97:680–3.
[33] Helminger P, Beeson Jr. EL, Gordy W. Phys Rev A 1971;3:122–6.
[34] Halonen M, Halonen L, Bürger H, Moritz P. J Chem Phys 1991;95:7099–107.
[35] Halonen M, Halonen L, Bürger H, Moritz P. J Phys Chem 1992;96:4225–31.
[36] Dinelli BM, Corbelli G, Fantoni AC, Scappini F, Di Lonardo G, Fusina L. J Mol Spectrosc 1992;153:307–15.
[37] Lummila J, Lukka T, Halonen L, Bürger H, Polanz O. J Chem Phys 1996;104:488–98.
[38] Fusina L, Di Lonardo G, De Natale P. J Chem Phys 1998;109:997–1003.
[39] Harder H, Gerke C, Fusina L. J Chem Phys 2001;114:3508–23.
[40] Fusina L, Di Lonardo G. J Mol Spectrosc 2002;216:493–500.
[41] Amezcua-Eccius CA, Álvarez-Bajo O, Sánchez-Castellanos M, Lemus R. J Mol Spectrosc 2006;240:164–73.
[42] Sánchez-Castellanos M, Amezcua-Eccius CA, Álvarez-Bajo O, Lemus R. J Mol Spectrosc 2008;247:140–59.
[43] Pluchart L, Leroy C, Sanzharov N, Michelot F, Bekhtereva E, Ulenikov O. J Mol Spectrosc 2005;232:119–36.
[44] Liu A-W, Hu S-M, Ding Y, Zhu Q-S. Chin Phys 2005;14:1946–53.
[45] Bunker PR, Jensen P. Molecular symmetry and spectroscopy, second ed.. Ottawa: NRC Research Press; 1998.
[46] Numerov B. Mon Not R Astron Soc 1924;84:592–602.
[47] Cooley JW. Math Comput 1961;15:363–74.
[48] Bunker PR, Landsberg BM. J Mol Spectrosc 1977;67:374–85.
[49] Wilson EB, Decius JC, Cross PC. Molecular vibrations. New York: McGraw-Hill; 1955.
[50] Mátyus E, Czakó G, Császár AG. J Chem Phys 2009;130:134112.
[51] Yurchenko SN, Zheng JJ, Lin H, Jensen P, Thiel W. J Chem Phys 2005;123:134308.
[52] Purvis GD, Bartlett RJ. J Chem Phys 1982;76:1910–8.
[53] Raghavachari K, Trucks GW, Pople JA, Head-Gordon M. Chem Phys Lett 1989;157:479–83.
[54] Werner HJ, Knowles PJ, Bernhardsson A, Berning A, et al., with contributions from Amos RD, MOLPRO, version 2002.3 and 2002.6, a package of *ab initio* programs; 2002.
[55] Hampel C, Peterson K, Werner HJ. Chem Phys Lett 1992;190:1–12.
[56] Wood J, Boring A. Phys Rev B 1978;18:2701–11.
[57] Mecke R. Z Electrochem 1950;54:38–42.
[58] Marquardt R, Quack M, Thanopulos I, Luckhaus D. J Chem Phys 2003;119:10724–32.
[59] Zare RN. Angular momentum. New York: Wiley; 1988 [section 6.5].
[60] Cottaz C, Tarrago G, Kleiner I, Brown LR. J Mol Spectrosc 2001;209:30–49.
[61] Kijima K, Tanaka T. J Mol Spectrosc 1981;89:62–75.

Theoretical rotation-torsion spectra of HSOH

A. Yachmenev, S. N. Yurchenko, P. Jensen, O. Baum, T. F. Giesen, W. Thiel

Phys. Chem. Chem. Phys., **12**, 8387 (2010)

Theoretical rotation–torsion spectra of HSOH†

Andrey Yachmenev,[a] Sergei N. Yurchenko,[b] Per Jensen,*[c] Oliver Baum,[d] Thomas F. Giesen[d] and Walter Thiel[a]

Received 9th February 2010, Accepted 17th May 2010
First published as an Advance Article on the web 5th June 2010
DOI: 10.1039/c002803g

Rotation–torsion spectra of HSOH, involving the vibrational ground state and the fundamental torsional state, have been simulated at $T = 300$ K. The simulations are carried out with the variational computer program TROVE in conjunction with recently reported *ab initio* potential energy and electric dipole moment surfaces. HSOH is a near-prolate-symmetric top at equilibrium and the simulated spectra are of perpendicular-band-type with strong *R*-branch and *Q*-branch transitions. Recently, an anomalous (*b*-type-transition)/(*c*-type-transition) intensity ratio in the vibrational-ground-state ${}^rQ_{K_a}$-branches of HSOH has been experimentally observed. Our calculations reproduce correctly the anomaly and show that it originates in the large-amplitude torsional motion of HSOH. We analyze our theoretical results in order to explain the effect and to provide unambiguous (*b*/*c*)-type-transition assignments.

I. Introduction

Sulfur compounds play important roles in biochemistry,[1] in atmospheric processes,[2–4] and in combustion chemistry.[5] In particular, there is evidence[2–4] that oxadisulfane HSOH is involved in the formation of pollutants in the upper layers of the terrestrial atmosphere. Consequently, the study of HSOH becomes a prerequisite for understanding atmospheric sulfur chemistry. In addition, HSOH is the first example of a skew-chain molecule with two different internal-rotor moieties (OH and SH) to be spectroscopically characterized at high resolution.[6–13] The rotation–vibration energies of HSOH exhibit splittings caused by the large-amplitude internal rotation of the OH and SH moieties about the OS bond. Already in the initial spectroscopic characterization of HSOH,[6] it became apparent that the variation of the splittings with rotational excitation was very different from, and much more complicated than, the splitting pattern previously observed for the related molecules HOOH and HSSH (see, for example, ref. 14 and the references therein). We have previously made theoretical analyses[14–17] of the HSOH splitting pattern, thus explaining the spectroscopic observations, and in the present work we extend the theoretical description of HSOH to the simulation of rotation–torsion spectra with the aim of explaining recently observed 'anomalous' intensities.[12] Since HSOH can be considered a prototype skew-chain molecule with two different internal rotors, we believe that the theoretical study of the torsional energy splittings reported in ref. 14–17, together with the intensity analyses of the present work, will assist future experimental investigations of molecules of this type.

In ref. 16, we have reported the *ab initio* potential energy and dipole moment surfaces for the electronic ground state of HSOH used in the present work. These surfaces were calculated by the CCSD(T) method (coupled-cluster theory with single and double excitations[18] and a perturbative treatment of triple excitations)[19] with the aug-cc-pV(T + *d*)Z and aug-cc-pV(Q + *d*)Z (augmented correlation-consistent triple- and quadruple-zeta) bases.[20–23] We used in ref. 16 the *ab initio* data and the program TROVE[24] to determine theoretical values for the fundamental vibrational band centers and the vibrational transition moments of HSOH. Prior to publication of the potential energy surface (PES), we had already applied it[15] for calculating with TROVE the rotation–torsion term values of HSOH for $J \leq 40$. As mentioned above, with the results of ref. 15 we could explain the initially unexpected variation of the torsional splittings with rotational excitation (ref. 14, 17).

The very recent ref. 12 reported accurate spectral data of $H^{32}SOH$ recorded at 1.3 THz. These spectra exhibited an unexpected effect in that for $H^{32}SOH$, no *b*-type transitions were observed in the ${}^rQ_3$-branch of the vibrational ground state. This effect was not explained in ref. 12 and the primary aim of the present paper is to provide an explanation. Towards this end, we simulate the rotation–torsion spectrum of $H^{32}SOH$ (henceforth referred to as HSOH) by means of the program suite TROVE. The term values and eigenfunctions needed for constructing the spectra are generated in the so-called *reaction path* Hamiltonian (RPH) approach[25] (also known as the *semirigid bender* (SRB) approach),[26,27] the TROVE version of which is based on the integration along the minimum energy path (MEP). We use the MEP of HSOH reported in ref. 15. We can explain the intensity anomaly observed for HSOH in terms of our theoretical results, and by analyzing the intensity results we can provide unambiguous (*b*/*c*)-type-transition assignments.

[a] *Max-Planck-Institut für Kohlenforschung, Kaiser-Wilhelm-Platz 1, D–45470 Mülheim an der Ruhr, Germany*
[b] *Technische Universität Dresden, Institut für Physikalische Chemie und Elektrochemie, D-01062 Dresden, Germany*
[c] *FB C – Theoretische Chemie, Bergische Universität, D–42097 Wuppertal, Germany. E-mail: jensen@uni-wuppertal.de*
[d] *I. Physikalisches Institut, Universität zu Köln, Zülpicher Straße 77, D-50937 Köln, Germany*

† Electronic supplementary information (ESI) available: Line lists for all transitions discussed in the paper. See DOI: 10.1039/c002803g

The paper is structured as follows. In section II the variational TROVE method is described. The theoretical rotation–torsion spectrum is presented and discussed in section III, where the intensity anomaly of the $^{r}Q_3$ branch is analyzed. In this section we also predict the fundamental and hot torsional bands. Some conclusions are presented in section IV.

II. Details of the TROVE calculation

For the calculation of the rotation–torsion energies of HSOH together with the eigenfunctions necessary for the intensity calculations we employ the variational method as implemented in the program TROVE.[24] In the calculations we use the computational setup applied in ref. 15 for the analysis of the torsional energy-level splittings of HSOH. Consequently, the reader is referred to ref. 15 for the details of the basis set, the Hamiltonian and the computational method. It suffices to say here that, as mentioned above, we employ the RPH/SRB approach[25–27] in which the rotation–vibration Hamiltonian is expanded around the torsional minimum energy path of HSOH.[15] The RPH/SRB calculations are based on the MEP from ref. 15 which, in turn, is obtained from the *ab initio* PES of ref. 16. In order to improve the agreement with experiment we have performed an empirical adjustment of the MEP from ref. 15 by adjusting the value of a_0^{OS} (the new value is 1.68712 Å), which defines the OS-bond length at the planar *trans* configuration of the molecule.

The basis set employed in the RPH/SRB calculations is identical to that of ref. 15. The basis functions are given by products

$$|\phi_{\mathrm{rv}}\rangle = |v_{\mathrm{OS}}\rangle|v_{\mathrm{SH}}\rangle|v_{\mathrm{OH}}\rangle|v_{\mathrm{OSH}}\rangle|v_{\mathrm{SOH}}\rangle|v_{\mathrm{HSOH}},\tau_{\mathrm{tor}}\rangle|J,\, K,\, \tau_{\mathrm{rot}}\rangle, \quad (1)$$

where v_{X} is the principal quantum number for the vibrational mode ν_{X} (X = OS, SH, OH, OSH, and SOH in an obvious notation; ν_{HSOH} is the torsional mode), $\tau_{\mathrm{tor}} = 0$ or 1 determines the torsional parity[28] as $(-1)^{\tau_{\mathrm{tor}}}$, and $\tau_{\mathrm{rot}} = 0$ or 1 determines the rotational parity[28] as $(-1)^{\tau_{\mathrm{rot}}}$. The total parity of the basis state $|\phi_{\mathrm{rv}}\rangle$ is consequently $(-1)^{\tau_{\mathrm{tor}}+\tau_{\mathrm{rot}}}$. We label the rotational states by quantum numbers $\{J, K, \tau_{\mathrm{rot}}\}$ that correlate with the customary ones J_{K_a,K_c} according to

$$K_a = K,\ K_c = J - K_a + \tau_{\mathrm{rot}}. \quad (2)$$

The one-dimensional small-amplitude vibrational basis functions $|v_{\mathrm{X}}\rangle$ and the torsional basis functions $|v_{\mathrm{HSOH}},\ \tau_{\mathrm{tor}}\rangle$ are generated by means of the Numerov–Cooley method.[29]

In the RPH/SRB calculations, we follow ref. 15 in setting $v_{\mathrm{OS}} = v_{\mathrm{SH}} = v_{\mathrm{OH}} = v_{\mathrm{OSH}} = v_{\mathrm{SOH}} = 0$. Consequently, the rotation–torsion eigenfunctions $\Psi_{J,\Gamma,i}$ are obtained as the variational solution

$$\Psi_{J,\Gamma,i} = |0\rangle \sum_{v_{\mathrm{HSOH}},\tau_{\mathrm{tor}},K,\tau_{\mathrm{rot}}} C_{J,\Gamma,i}^{(K,\tau_{\mathrm{rot}},v_{\mathrm{HSOH}},\tau_{\mathrm{tor}})} |v_{\mathrm{HSOH}},\tau_{\mathrm{tor}}\rangle|J,K,\tau_{\mathrm{rot}}\rangle, \quad (3)$$

to the rotation–torsion Schrödinger equation. Here, the $C_{J,\Gamma,i}^{(K,\tau_{\mathrm{rot}},v_{\mathrm{HSOH}},\tau_{\mathrm{tor}})}$ are expansion coefficients and '$|0\rangle$' is a shorthand notation for $|0\rangle|0\rangle|0\rangle|0\rangle|0\rangle$ where each zero is the value of one of the vibrational quantum numbers v_{X}, X = OS, SH, OH, OSH, and SOH. We have introduced Γ (= A' or A'') to denote an irreducible representation of the molecular symmetry group C_s(M) (see Table A-2 of ref. 28) generated by the eigenfunction $\Psi_{J,\Gamma,i}$. The running index i labels eigenstates with the same values of J and Γ.

The approach to simulate absorption spectra implemented in TROVE is based on the theory described in detail in ref. 30. This theory was developed in connection with the program XY3,[31] a fore-runner program for TROVE, and the modifications related to the specifics of the TROVE program have been reported in ref. 32. The expression for the line strength $S(f \leftarrow i)$ is given in Appendix A. In all spectrum simulations, we have assumed the HSOH molecules to be in thermal equilibrium at an absolute temperature of $T = 300$ K. In order to reduce the computation time we have applied a pre-screening procedure to truncate the wavefunction expansions in eqn (3): All terms with $|C_{J,\Gamma,i}^{(K,\tau_{\mathrm{rot}},v_{\mathrm{HSOH}},\tau_{\mathrm{tor}})}|^2 < 10^{-14}$ are neglected in the computation of $S(f \leftarrow i)$.

In the present study we employ the HSOH dipole moment surface denoted as ACV(T + *d*) in ref. 16. We expand it as a Taylor series in the internal coordinates similar to the expansion of the potential energy function (see section 4 of ref. 24). The expansion coefficients are determined as partial derivatives of the *ab initio* dipole moment components. These components are evaluated numerically by the finite-difference method. The expansions of the dipole moment components are truncated after the fourth order terms.

The expression for the intensity of an absorption line for the transition from the state i with energy E_i, in thermal equilibrium at the temperature T, to the state f with energy E_f is given by ref. 28,

$$I(f \leftarrow i) = \int_{\mathrm{Line}} \epsilon(\tilde{\nu})\mathrm{d}\tilde{\nu} = \frac{8\pi^3 N_{\mathrm{A}} \tilde{\nu}_{if}}{(4\pi\varepsilon_0)3hc} \frac{e^{-E_i/kT}}{Q}[1 - \exp(-hc\tilde{\nu}_{if}/kT)]S(f \leftarrow i), \quad (4)$$

where $hc\tilde{\nu}_{if} = E_f - E_i$, N_{A} is the Avogadro constant, h is Planck's constant, c is the speed of light in vacuum, k is the Boltzmann constant, ε_0 is the permittivity of free space, and $S(f \leftarrow i)$ is the line strength defined in eqn (26) of Appendix A. The partition function Q is given by

$$Q = \sum_j g_j\, \mathrm{e}^{-E_j/kT}, \quad (5)$$

where g_j is the total degeneracy of the state with energy E_j and the sum runs over all energy levels of the molecule. Because of the constraints in the specification of the RPH/SRB basis set [eqn (3)], we cannot proceed in the usual manner and evaluate Q in eqn (5) by summing over all energy levels obtained in the TROVE variational calculation; the levels with excited quanta of the small-amplitude vibrational modes ν_{X} (X = OS, SH, OH, OSH, and SOH) would then be missing from the sum. In order to circumvent this problem we employ the theoretical vibrational term values from ref. 16 and approximate $Q \approx Q_{\mathrm{vib}} \times Q_{\mathrm{rot}}$, where Q_{vib} and Q_{rot} are vibrational and rotational partition functions, respectively. This approximation for Q is equivalent to the neglect of rotation–vibration

interaction. The rotational partition function Q_{rot} is taken to have the rigid-rotor value[33]

$$Q_{rot} = g_{ns}\frac{\sqrt{\pi}}{\sigma\sqrt{ABC}}\left(\frac{kT}{hc}\right)^{3/2}, \qquad (6)$$

where the symmetry number $\sigma = 1$ for HSOH and the values of the rotational constants A, B, and C are from ref. 12. In eqn (6), we have included the effect of nuclear spin degeneracies through the nuclear spin statistical weight factor g_{ns} ($g_{ns} = 4$ for all rovibrational states of HSOH). For $T = 300$ K we obtain $Q_{rot} = 16368.12$. The vibrational partition function Q_{vib} is computed from the vibrational term values of ref. 16 with the summation limited to vibrational levels below 10 000 cm^{-1}. We obtain $Q_{vib} = 2.37$ and so the total partition function for HSOH, $Q = Q_{vib} \times Q_{rot} = 38792.48$ at $T = 300$ K. The approximation $Q = Q_{vib} \times Q_{rot}$ is probably not highly accurate but we expect that it produces a Q value of the correct order of magnitude. It should be emphasized that a more accurate Q value would not alter any of the conclusions drawn in the present work. We discuss here relative intensities which are not dependent on the value of Q. A change of the Q value employed in the calculations has the effect of multiplying all computed intensities by a common factor [eqn (4)].

III. The theoretical rotation–torsion absorption spectrum of HSOH at $T = 300$ K

Fig. 1 shows the $J \leq 40$ simulated rotational spectrum (in the vibrational ground state) of HSOH below 180 cm^{-1}. Owing to the torsional tunneling between two minima on the potential energy surface, each transition is split into a doublet.[14,17] Line lists for the transitions in the Figure and for all transitions discussed in the remainder of the paper are available as ESI.† In the stick diagram of Fig. 1, the height of a stick represents the integrated absorption coefficient computed from eqn (4). When the wavenumbers of two or more transitions coincide, the intensities of these transitions are added to give the height of the stick. The most prominent features of the spectrum in the figure are the wide $^rR_{K_a}$ branches whose transitions are drawn as grey sticks. These branches start abruptly on the low-wavenumber side with the transition $J = K_a+1 \leftarrow K_a$; the other transitions in a given branch correspond to higher J values and fall at higher wavenumber values. The narrow $^rQ_{K_a}$ branches are marked by asterisks, and the $^rP_{K_a}$ branches (marked by arrows) are comparatively weak.

Each low-lying rovibrational energy level of HSOH is split into two torsional components of symmetry A' or A'', respectively, in the molecular symmetry group $\boldsymbol{C}_s$(M). This fact, in conjunction with the electric-dipole-transition selection rule[28] of $A' \leftrightarrow A''$ (or, equivalently, $|\Delta(\tau_{tor} + \tau_{rot})| = 1$), causes each rotational transition to split into a doublet (see also ref. 15).

Along the entire torsional MEP of HSOH, the dipole moment is almost perpendicular to the SO bond. The principal axis of least moment of inertia a is approximately parallel to the SO bond and so HSOH has a relatively small 'parallel' dipole moment component $\bar{\mu}_a$, (see Fig. 2 in ref. 16) and large 'perpendicular' components $\bar{\mu}_b$ and $\bar{\mu}_c$. Since we associate the a axis with the molecule-fixed z axis[28] for the near-prolate-symmetric top HSOH, the strong transitions in the rotational spectrum have $|\Delta K_a| \neq 0$ as shown in Fig. 1 (see also ref. 12). Customarily, these strong transitions are further classified as being of b-type (c-type) if their intensity originates predominantly in the dipole moment component $\bar{\mu}_b$ ($\bar{\mu}_c$). A b-type transition has $\Delta\tau_{tor} = 0$ (and $|\Delta\tau_{rot}| > 0$) because $\bar{\mu}_b$ has A' symmetry in $\boldsymbol{C}_s$(M). Conversely, a c-type transition has $|\Delta\tau_{tor}| > 0$ (and $\Delta\tau_{rot} = 0$) because $\bar{\mu}_c$ has A'' symmetry. This normally allows observed lines to be identified according to their intensities: In the first approximation the ratio between the intensities of the b- and c-type transitions is roughly equal to the ratio between the squares of $\bar{\mu}_b$ and $\bar{\mu}_c$:

$$\frac{I_b}{I_c} \approx \frac{\bar{\mu}_b^2}{\bar{\mu}_c^2}. \qquad (7)$$

If this relation is satisfied, the structures of the observed spectrum can be recognized as being of b-type or c-type. This effect is general for (semi-)rigid symmetric tops[28,34] with a small $\bar{\mu}_a$-value and has been observed in HSOH spectra.[6]

From the equilibrium values of the HSOH *ab initio* dipole moment components,[16] $\bar{\mu}_b^{eq} = 0.744$ D and $\bar{\mu}_c^{eq} = 1.399$ D, we obtain from eqn (7) $I_b/I_c \approx 0.28$. The corresponding vibrationally averaged values for the vibrational ground state are $\bar{\mu}_b^{eq} = 0.699$ D and $\bar{\mu}_c^{eq} = 1.297$ D;[16] these values produce $I_b/I_c \approx 0.29$. The experimentally derived intensity ratio for the $^rQ_0$ and $^rQ_1$ branches of the HSOH rotational spectrum has been reported to be very close to this value; $I_b/I_c \approx 0.22(4)$ for the $^rQ_0$ branch and 0.23(2) for $^rQ_1$ where the quantities in parentheses are quoted uncertainties in units of the last decimal given (see also ref. 12). For the $^rQ_2$ and $^rQ_3$ branches, however, eqn (7) is not satisfied: I_b/I_c is experimentally determined to be 0.58(11) for the $^rQ_2$ branch, and for the $^rQ_3$ branch the ratio was found to be below 0.02. In ref. 12, this 'intensity anomaly' was attributed to mixing of basis states. It is illustrated in Fig. 2 which shows the $^rQ_2$ and $^rQ_3$ branches from ref. 12. The $^rQ_2$ branch has been recorded with the Cologne THz spectrometer[35] whereas for the $^rQ_3$ branch measurements at 1.3 THz, a synthesizer-based multiplier spectrometer was employed. In this Figure, the assigned transitions of the stick

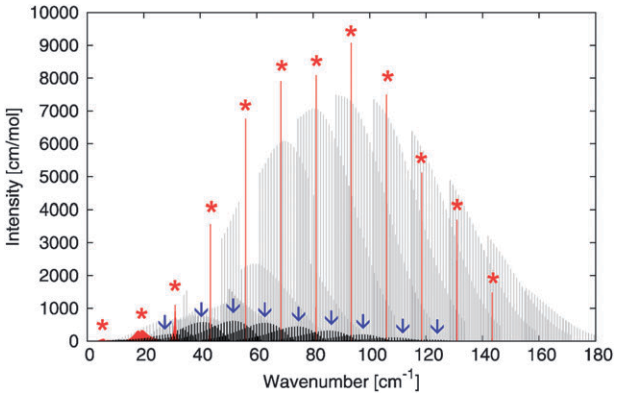

Fig. 1 Simulated rotational spectrum of HSOH at $T = 300$ K. All prominent transitions have $\Delta K_a = 1$. The ^rP and ^rQ branches are indicated by arrows and asterisks, respectively. The strongest transitions are found in the ^rR-branches.

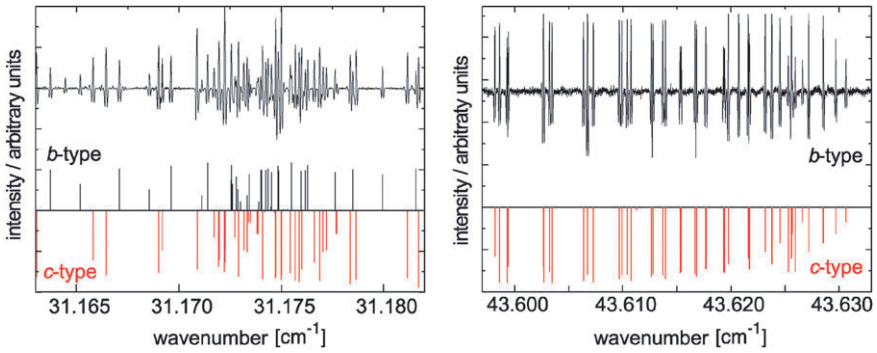

Fig. 2 Band heads of the ${}^{r}Q_2$ and ${}^{r}Q_3$ branches[12] of HSOH in the vibrational ground state. Below the experimental spectra, the assignments to *b*-type and *c*-type transitions are indicated by stick spectra drawn in black and red, respectively.

spectrum are colour-coded: *c*-type transitions are drawn in red and *b*-type transitions are drawn in black.

In Fig. 3, we plot simulated stick spectra of the ${}^{r}Q_{K_a}$ ($K_a = 0, 1, 2, 3$) branches in the vibrational-ground-state rotational spectrum of HSOH. The colour-coding is the same as in Fig. 2 and the *b*-type transitions are drawn upside-down so as to distinguish them better from the *c*-type transitions. The ${}^{r}Q_0$, ${}^{r}Q_1$, and ${}^{r}Q_2$ branches all have an appreciable number of both *b*-type and *c*-type transitions with an intensity ratio $I_b/I_c \approx 1/3$ in agreement with eqn (7). However, in agreement with the experimental findings, the ${}^{r}Q_3$ branch hardly has *b*-type transitions at all.

In order to understand the intensity anomaly of the ${}^{r}Q_{K_a}$ branches we analyze the eigenfunctions in eqn (3) for the rotation–torsion states involved. Recently[15] we have shown that the rotational quantum number K_a for HSOH is a nearly-good quantum number even for high J. This is in agreement with the experimental observations[6] and typical for this type of molecule (*e.g.*, HOOH[36] and HSSH[37]). Therefore we can safely use K_a to assign the rotational states being analyzed. Each rotation–torsion state characterized by the quantum numbers J, K_a is torsionally and rotationally split into four components (see Fig. 4). These states span the representation $2A' \oplus 2A''$ of $\boldsymbol{C}_s$(M) and, in consequence, the corresponding eigenfunctions can be denoted as $\Psi^{A',(1)}_{J,K_a,i}$, $\Psi^{A',(2)}_{J,K_a,i}$, $\Psi^{A'',(1)}_{J,K_a,i}$, and $\Psi^{A'',(2)}_{J,K_a,i}$, where the index i determines the torsional excitation. For the states considered, the torsional splitting varies in the range 0.0005–0.00025 cm^{-1} and shows a strong dependence on K_a.[12,15] The rotational (asymmetry) splitting for the asymmetric (but near-prolate-symmetric) top HSOH is apparent only for low K_a[34] and cannot be resolved experimentally at $K_a \geq 4$[12,15] (see the top-right display of Fig. 4). Analyzing the expansion coefficients of eqn (3) we find that in a good approximation, the four eigenfunctions associated with given values of J, K_a ($K_a > 0$) can be modeled by the expressions

$$\Psi^{A',(1)}_{J,K_a,i} \approx c_{J,K_a}|J,K_a,0\rangle\phi^{(\mathrm{vib})}_{K_a,0} + s_{J,K_a}|J,K_a,1\rangle\phi^{(\mathrm{vib})}_{K_a,1}, \quad (8)$$

$$\Psi^{A',(2)}_{J,K_a,i} \approx -s_{J,K_a}|J,K_a,0\rangle\phi^{(\mathrm{vib})}_{K_a,0} + c_{J,K_a}|J,K_a,1\rangle\phi^{(\mathrm{vib})}_{K_a,1}, \quad (9)$$

$$\Psi^{A'',(1)}_{J,K_a,i} \approx c_{J,K_a}|J,K_a,0\rangle\phi^{(\mathrm{vib})}_{K_a,1} + s_{J,K_a}|J,K_a,1\rangle\phi^{(\mathrm{vib})}_{K_a,0}, \quad (10)$$

$$\Psi^{A'',(2)}_{J,K_a,i} \approx -s_{J,K_a}|J,K_a,0\rangle\phi^{(\mathrm{vib})}_{K_a,1} + c_{J,K_a}|J,K_a,1\rangle\phi^{(\mathrm{vib})}_{K_a,0}, \quad (11)$$

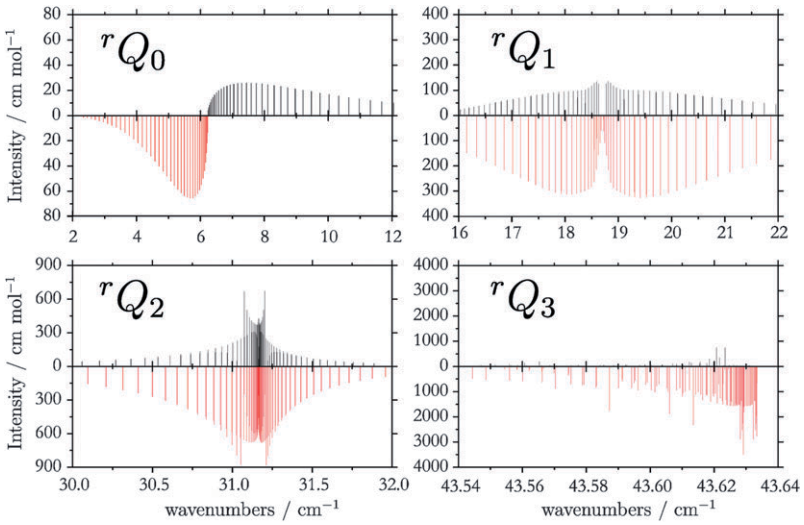

Fig. 3 ${}^{r}Q_{K_a}$ ($K_a = 0, 1, 2, 3$) branches in the rotational spectrum of HSOH, simulated at an absolute temperature of $T = 300$ K. Transitions assigned as *b*-type transitions are drawn in black, and *c*-type transitions are drawn upside-down in red. The *b*/*c*-type assignment is made by comparing the $|T^{\mathrm{if}}_b|$ and $|T^{\mathrm{if}}_c|$ contributions in eqn (25) (see text).

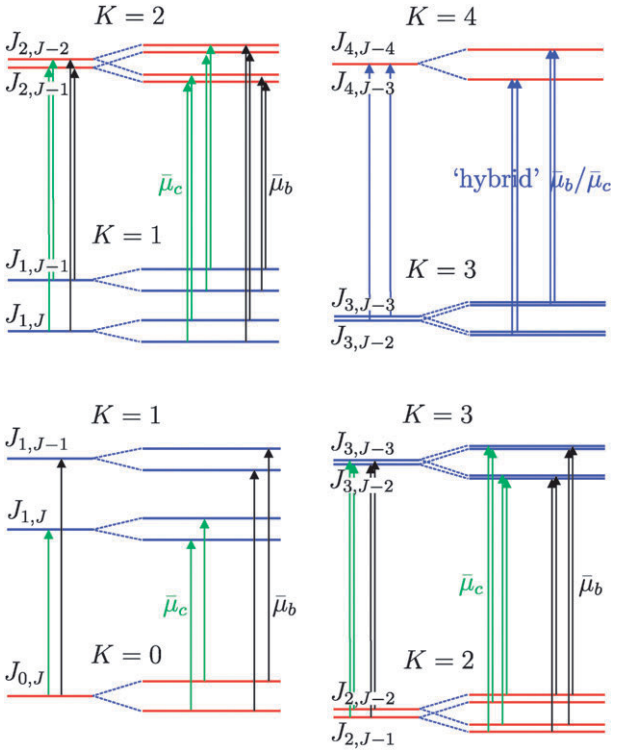

Fig. 4 Term level diagram showing the ${}^{r}Q_{K_a}$ ($K_a \leq 3$) transitions of HSOH. The 'experimental' quantum numbers are indicated as given by eqn (2).

where $c_{J,K_a} = \cos(\theta_{J,K_a})$ and $s_{J,K_a} = \sin(\theta_{J,K_a})$ with the mixing angle $\theta_{J,K_a} \in [0, \pi/4]$ so that $c_{J,K_a} \geq s_{J,K_a}$. Further, in eqn (8)–(11)

$$\phi^{(\mathrm{vib})}_{K_a,\tau_{\mathrm{tor}}} \approx |0\rangle \sum_{v_{\mathrm{HSOH}}} C^{(K_a,\tau_{\mathrm{rot}},v_{\mathrm{HSOH}},\tau_{\mathrm{tor}})}_{J,\Gamma,i} |v_{\mathrm{HSOH}}, \tau_{\mathrm{tor}}\rangle, \qquad (12)$$

where the expansion coefficients $C^{(K_a,\tau_{\mathrm{rot}},v_{\mathrm{HSOH}},\tau_{\mathrm{tor}})}_{J,\Gamma,i}$ are defined in eqn (3). Our previous analyses of the torsion–rotation wavefunctions[15] suggest, together with our experience with semi-empirical models[14,17] for explaining the rotation–torsion splittings in HSOH, that as indicated in eqn (12) (the right hand side can be evaluated for any τ_{rot}-value available) the vibrational basis functions $\phi^{(\mathrm{vib})}_{K_a,\tau_{\mathrm{tor}}}$ are largely independent of τ_{rot}.

We aim at calculating the line strengths for the ${}^{r}Q_{K_a}$ transitions originating in one four-member manifold of states with wavefunctions defined by eqn (8)–(11) and ending in another such manifold. In principle, there are 16 possible transitions but owing to the symmetry selection rule $\Gamma = A' \leftrightarrow A''$ only eight of these have a nonvanishing intensity.

We now insert eqn (8)–(11) in the general expression for the line strength $S(f \leftarrow i)$ (see Appendix A) to obtain the desired line strengths. We employ the fact that because of symmetry, non-vanishing vibrational matrix elements of $\bar{\mu}_b$ are diagonal in τ_{tor} while non-vanishing vibrational matrix elements of $\bar{\mu}_c$ are off-diagonal in τ_{tor}. It is known from experience that vibrational dipole-moment matrix elements involving symmetrized vibrational basis functions normally depend weakly on parity labels, and so we initially assume that the non-vanishing vibrational matrix elements of the dipole moment components are independent of τ_{tor}:

$$\langle\phi^{(\mathrm{vib})}_{K_a,0}|\bar{\mu}_b|\phi^{(\mathrm{vib})}_{K_a+1,0}\rangle = \langle\phi^{(\mathrm{vib})}_{K_a,1}|\bar{\mu}_b|\phi^{(\mathrm{vib})}_{K_a+1,1}\rangle \qquad (13)$$

and

$$\langle\phi^{(\mathrm{vib})}_{K_a,0}|\bar{\mu}_c|\phi^{(\mathrm{vib})}_{K_a+1,1}\rangle = \langle\phi^{(\mathrm{vib})}_{K_a,1}|\bar{\mu}_c|\phi^{(\mathrm{vib})}_{K_a+1,0}\rangle. \qquad (14)$$

With these simplifications, we obtain for the eight non-vanishing transitions for a given J value in an ${}^{r}Q_{K_a}$ branch:

$$\begin{aligned} S_{A'(1)\leftrightarrow A''(1)} = S_{A'(2)\leftrightarrow A''(2)} &= g_{\mathrm{ns}} A(J,K_a) \\ &\times [\cos^2(\theta_{J,K_a+1} - \theta_{J,K_a})\langle\phi^{(\mathrm{vib})}_{K_a,0}|\bar{\mu}_b|\phi^{(\mathrm{vib})}_{K_a+1,0}\rangle^2 \\ &+ \sin^2(\theta_{J,K_a+1} + \theta_{J,K_a})\langle\phi^{(\mathrm{vib})}_{K_a,0}|\bar{\mu}_c|\phi^{(\mathrm{vib})}_{K_a+1,1}\rangle^2] \end{aligned} \qquad (15)$$

and

$$\begin{aligned} S_{A'(1)\leftrightarrow A''(2)} = S_{A'(2)\leftrightarrow A''(1)} &= g_{\mathrm{ns}} A(J,K_a) \\ &\times [\cos^2(\theta_{J,K_a+1} + \theta_{J,K_a})\langle\phi^{(\mathrm{vib})}_{K_a,0}|\bar{\mu}_c|\phi^{(\mathrm{vib})}_{K_a+1,1}\rangle^2 \\ &+ \sin^2(\theta_{J,K_a+1} - \theta_{J,K_a})\langle\phi^{(\mathrm{vib})}_{K_a,0}|\bar{\mu}_b|\phi^{(\mathrm{vib})}_{K_a+1,0}\rangle^2]. \end{aligned} \qquad (16)$$

Each symbol $S_{\Gamma_1(i_1)\leftrightarrow\Gamma_2(i_2)}$ in eqn (15) and (16) represents the line strength of two transitions, $\Gamma_1(i_1) \leftarrow \Gamma_2(i_2)$ and $\Gamma_2(i_2) \leftarrow \Gamma_1(i_1)$. $A(J, K_a)$ is a Hönl–London-type factor (see, for example, Chapter 12 of ref. 38) common to all ${}^{r}Q_{K_a}$ transitions with given values of J and K_a.

For $K_a = 0$, there is only one rotational basis function $|J, 0, \tau_{\mathrm{rot}}\rangle$ with $\tau_{\mathrm{rot}} = J \bmod 2$, and thus the two corresponding torsion–rotation eigenfunctions are defined by:

$$\Psi^{A'(1)}_{J,K_a=0,i} \approx |J,0,0\rangle\phi^{(\mathrm{vib})}_{K_a,0}, \qquad (17)$$

$$\Psi^{A''(1)}_{J,K_a=0,i} \approx |J,0,0\rangle\phi^{(\mathrm{vib})}_{K_a,1} \qquad (18)$$

for J even and

$$\Psi^{A'(2)}_{J,K_a=0,i} \approx |J,0,1\rangle\phi^{(\mathrm{vib})}_{K_a,1}, \qquad (19)$$

$$\Psi^{A''(2)}_{J,K_a=0,i} \approx |J,0,1\rangle\phi^{(\mathrm{vib})}_{K_a,0} \qquad (20)$$

for J odd. In applying eqn (15) and (16) to ${}^{r}Q_0$ transitions we can set $\theta_{J,0} = 0$.

Furthermore, for small $K_a > 0$ (in practice, $K_a = 1,2$) analyses of the TROVE calculations show that $\theta_{J,K_a} \approx 0$. For example, with $(J, K_a) = (10, 1)$ we have $c^2_{J,K_a} = 0.95$ and $s^2_{J,K_a} = 0.05$ corresponding to $\theta_{J,K_a} \approx 0.23$ rad (or 13°). That is, for $K_a = 0, 1, 2$ we can approximate $\theta_{J,K_a} = 0$ and so for the ${}^{r}Q_0$ and ${}^{r}Q_1$ transitions, $\theta_{J,K_a} = \theta_{J,K_a+1} = 0$ in eqn (15) and (16). These equations then simplify to

$$\begin{aligned} S_{A'(1)\leftrightarrow A''(1)} &= S_{A'(2)\leftrightarrow A''(2)} \\ &= g_{\mathrm{ns}} A(J,K_a)\langle\phi^{(\mathrm{vib})}_{K_a,0}|\bar{\mu}_b|\phi^{(\mathrm{vib})}_{K_a+1,0}\rangle^2 \end{aligned} \qquad (21)$$

and

$$\begin{aligned} S_{A'(1)\leftrightarrow A''(2)} &= S_{A'(2)\leftrightarrow A''(1)} \\ &= g_{\mathrm{ns}} A(J,K_a)\langle\phi^{(\mathrm{vib})}_{K_a,0}|\bar{\mu}_c|\phi^{(\mathrm{vib})}_{K_a+1,1}\rangle^2 \end{aligned} \qquad (22)$$

and the resulting relations are consistent with eqn (7). Eqn (21) defines a *b*-type transition, while eqn (22) defines a *c*-type transition. Obviously, the simplified theory presented here explains the experimentally derived intensity ratios of $I_b/I_c \approx 0.22$ for the ${}^rQ_0$ branch and 0.23 for ${}^rQ_1$ (ref. 12).

In ref. 15 we found that at higher K_a-values, the rotation–torsion wavefunctions become equal mixtures of the $|J, K_a, \tau_{\rm rot} = 0\rangle$ and $|J, K_a, \tau_{\rm rot} = 1\rangle$ basis functions (see Fig. 8 of ref. 15 and the associated discussion). For example, for $J = 10$, $K_a = 5$ the TROVE calculation yields $c^2_{J,K_a} = 0.48$ and $s^2_{J,K_a} = 0.52$ [eqn (8)–(11)], corresponding to $\theta_{J,K_a} \approx 0.81$ rad (or 46°). We have $\lim_{K_a\to\infty}\theta_{J,K_a} = \pi/4$ (or 45°). In this limit, eqn (15) and (16) simplify to

$$S_{A'(1)\leftrightarrow A''(1)} = S_{A'(2)\leftrightarrow A''(2)} = g_{\rm ns}A(J,K_a)[\langle\phi^{(\rm vib)}_{K_a,0}|\bar{\mu}_b|\phi^{(\rm vib)}_{K_a+1,0}\rangle^2 + \langle\phi^{(\rm vib)}_{K_a,0}|\bar{\mu}_c|\phi^{(\rm vib)}_{K_a+1,1}\rangle^2]$$

and

$$S_{A'(1)\leftrightarrow A''(2)} = S_{A'(2)\leftrightarrow A''(1)} = 0. \qquad (24)$$

It is obviously meaningless to assign transitions as being *b*-type or *c*-type in this situation, but we see that for large K_a, we obtain half as many ${}^rQ_{K_a}$ transitions as for, say, $K_a = 1$. This is consistent with the fact that for the ${}^rQ_3$ branch I_b/I_c is experimentally determined[12] to be below 0.02.

Fig. 5 shows values of $\theta_{J,K_a} = \arccos c_{J,K_a}$ computed from TROVE values of c_{J,K_a} for different values of K_a and $J = 10$. It is evident that the limiting value of $\lim_{K_a\to\infty}\theta_{J,K_a} = \pi/4$ (or 45°) is reached rather slowly as K_a increases. For the ${}^rQ_2$ branch, I_b/I_c is experimentally determined[12] to be 0.58. This value corresponds neither to the low-K_a limit of $\theta_{J,K_a} = \theta_{J,K_{a+1}} = 0$ nor to the high-K_a limit of $\theta_{J,K_a} = \theta_{J,K_{a+1}} = \pi/4$. The value of $\theta_{J,3} \approx 38°$ (Fig. 5) is intermediate between 0 and 45°.

To illustrate in greater detail how the intensities of the ${}^rQ_{K_a}$ transitions vary with K_a for HSOH, we collect in Table 1 information about these transitions for $J = 8$. We include in the Table the initial and final term values E_i and E_f, respectively, the transition wavenumbers ν_{if}, and absorption intensities $I(f \leftarrow i)$ [eqn (4)]. As discussed above in terms of the basis functions, for $K_a = 0$ there are two non-degenerate eigenstates, shown in Table 1 to be separated by 0.0022 cm^{-1}.

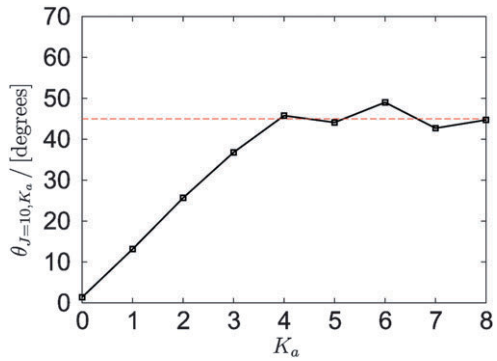

Fig. 5 Values of the angle $\theta_{J,K_a} = \arccos c_{J,K_a}$ [see eqn (8)–(11)] for different values of K_a and $J = 10$. The limiting value of $\theta_{J,K_a} = 45°$ is indicated by a horizontal dashed line.

For $K_a > 0$ there are always four eigenstates and when $K_a = 1$ or $K_a = 2$, these are all non-degenerate to an extent that with the four decimal places given in Table 1, four different energies ensue. For $K_a \geq 3$ the rotational (asymmetry) splittings become so small (see Table 3 of ref. 15 and the associated discussion) that the four eigenstates appear as two energy doublets (where, for each doublet, the member energies are equal to at least four decimal places). This is the *symmetric top limit* described in Fig. 9 of ref. 14. In Table 1, only two energies are given in these cases, and the effect of the double degeneracy on the transition intensities is indicated by a factor of ×2 [whilst non-degeneracy is indicated by a factor of ×1]. Owing to the general symmetry selection rule of $\Gamma = A' \leftrightarrow A''$, each J value gives rise to four ${}^rQ_{K_a} = 0$ transitions, eight ${}^rQ_{K_a} = 1$ transitions, eight ${}^rQ_{K_a} = 2$ transitions, and four resolved ${}^rQ_{K_a} \geq 3$ transitions as seen in Table 1.

Table 1 shows that for $J = 8$ (and also for all other J values) in the ${}^rQ_{K_a} = 0$ branch, there are two 'doublet' transitions, the members of each doublet being closely spaced (display ${}^rQ_0$ of Fig. 4). When, for $J = 8$, we take $I^{(b)}(f \leftarrow i)$ to be the sum of the intensities of the two doublet lines near 6.50 cm^{-1} and $I^{(c)}(f \leftarrow i)$ to be the sum of the intensities of the two doublet lines near 5.97 cm^{-1}, we have $I^{(b)}(f \leftarrow i)/I^{(c)}(f \leftarrow i) \approx 0.3 \approx I_b/I_c$ from eqn (7). Obviously, the two transitions near 6.50 cm^{-1} are *b*-type transitions while those near 5.97 cm^{-1} are *c*-type transitions.

The structure of the ${}^rQ_1$ branch is less apparent, but clearly we can separate the eight transitions (display ${}^rQ_1$ of Fig. 4) for $J = 8$ into a set of four 'weak' transitions (with $I(f \leftarrow i) < 110$ cm mol^{-1}) and a set of four 'strong' transitions (with $I(f \leftarrow i) > 210$ cm mol^{-1}). When we take $I^{(b)}(f \leftarrow i)$ to be the sum of the intensities of the four weak transitions and $I^{(c)}(f \leftarrow i)$ to be the sum of the intensities of the four strong transitions, we have again $I^{(b)}(f \leftarrow i)/I^{(c)}(f \leftarrow i) \approx 0.3 \approx I_b/I_c$ from eqn (7). Here, it is evident that the four weak transitions are of the *b*-type while the four strong transitions are of the *c*-type.

To investigate the ${}^rQ_{K_a}$ branches with $K_a \geq 2$ (see for example displays ${}^rQ_2$ and ${}^rQ_3$ of Fig. 4) we have found it instructive to analyze the TROVE values for the line strength $S(f \leftarrow i)$, calculated from the general expression in eqn (A1), in terms of the contributions from $\bar{\mu}_a$, $\bar{\mu}_b$, and $\bar{\mu}_c$:

$$S(f \leftarrow i) = g_{\rm ns}(2J+1)^2|T^{(\rm if)}(\bar{\mu}_a) + T^{(\rm if)}(\bar{\mu}_b) + T^{(\rm if)}(\bar{\mu}_c)|^2, \qquad (25)$$

where $J = J'' = J'$ and $T^{(\rm if)}(\bar{\mu}_\alpha)$ ($\alpha = a, b, c$) represent terms in the expression for $S(f \leftarrow i)$ involving the $\bar{\mu}_\alpha$ component only. The contributions $T^{(\rm if)}_b = T^{(\rm if)}(\bar{\mu}_b)$ and $T^{(\rm if)}_c = T^{(\rm if)}(\bar{\mu}_c)$ are included in Table 1; the corresponding $T^{(\rm if)}_a$ values are all found to be negligibly small. Now we can assign a transition as the *b*-type if $|T^{\rm if}_b| > |T^{\rm if}_c|$ in Table 1 and as the *c*-type if $|T^{\rm if}_c| > |T^{\rm if}_b|$. We immediately find that our *b*-type/*c*-type assignment of the ${}^rQ_0$ and ${}^rQ_1$ transitions is correct. We also find that it would be incorrect to base the assignment of ${}^rQ_2$ transitions on the individual transition intensities only: not all *b*-type transitions are weaker than all *c*-type transitions. When we now take $I^{(b)}(f \leftarrow i)$ to be the sum of the $I(f \leftarrow i)$ values for all ${}^rQ_2$ transitions, with $|T^{\rm if}_b| > |T^{\rm if}_c|$ and $I^{(c)}(f \leftarrow i)$ to be the analogous sum for all transitions with $|T^{\rm if}_c| > |T^{\rm if}_b|$, we obtain

Table 1 Initial and final term values E_i and E_f (in cm^{-1}), transition wavenumbers ν_{if} (in cm^{-1}), $\bar{\mu}_\alpha$-contribution T_α^{if} (in D, $\alpha = b, c$) to the line strength, and intensities $I(i \leftarrow f)$ (in cm mol^{-1}) for $J = 8$ transitions in the ${}^rQ_{K_a}$ branches of the HSOH rotational spectrum in the vibrational ground state. For each ${}^rQ_{K_a}$ branch, the theoretical value of the intensity ratio I_b/I_c is given (see text)

Branch	Γ_i	E_i	E_f	ν_{if}	T_b^{if}	T_c^{if}	$I(i \leftarrow f)$	I_b/I_c
${}^rQ_0$	A''	36.1484	42.1182	5.9698	0.021	0.217	59.0 × 1	
	A'	36.1462	42.1195	5.9732	−0.021	−0.217	58.9 × 1	
	A''	36.1484	42.6510	6.5026	0.119	0.003	18.1 × 1	
	A'	36.1462	42.6497	6.5035	−0.119	−0.003	18.3 × 1	0.3
${}^rQ_1$	A'	42.6510	61.0845	18.4335	0.028	0.149	291.7 × 1	
	A''	42.6497	61.0838	18.4341	0.004	0.149	216.7 × 1	
	A'	42.6510	61.0897	18.4387	0.081	−0.022	33.1 × 1	
	A''	42.6497	61.0903	18.4406	0.086	0.022	108.1 × 1	
	A''	42.1195	61.0838	18.9643	0.084	0.021	109.7 × 1	
	A'	42.1182	61.0845	18.9662	0.080	−0.021	33.6 × 1	
	A''	42.1195	61.0903	18.9708	−0.004	−0.146	220.2 × 1	
	A'	42.1182	61.0897	18.9715	−0.028	−0.146	296.4 × 1	0.3
${}^rQ_2$	A'	61.0903	92.2501	31.1598	0.013	0.145	589.1 × 1	
	A''	61.0897	92.2501	31.1604	0.082	0.046	388.3 × 1	
	A'	61.0903	92.2522	31.1619	−0.082	−0.005	175.1 × 1	
	A''	61.0897	92.2522	31.1625	0.011	−0.137	375.9 × 1	
	A''	61.0845	92.2501	31.1656	0.011	−0.137	376.0 × 1	
	A'	61.0838	92.2501	31.1663	0.082	0.005	175.1 × 1	
	A''	61.0845	92.2522	31.1677	−0.082	−0.046	388.4 × 1	
	A'	61.0838	92.2522	31.1684	0.013	0.145	589.4 × 1	0.6
${}^rQ_3$	A''	92.2522	135.8812	43.6290	0.042	0.129	1132.0 × 2	
	A''	92.2522	135.8832	43.6309	−0.066	0.051	8.5 × 2	
	A'	92.2501	135.8812	43.6311	0.066	−0.052	8.1 × 2	
	A'	92.2501	135.8832	43.6331	0.043	0.128	1132.6 × 2	0.007
${}^rQ_4$	A'	135.8832	191.9786	56.0955	0.048	0.112	1284.1 × 2	
	A'	135.8832	191.9804	56.0972	0.055	−0.065	4.5 × 2	
	A''	135.8812	191.9786	56.0974	−0.055	0.065	4.5 × 2	
	A''	135.8812	191.9804	56.0992	0.048	0.112	1284.3 × 2	0.003
${}^rQ_5$	A'	191.9804	260.5419	68.5616	−0.040	−0.103	1155.0 × 2	
	A''	191.9786	260.5419	68.5633	−0.052	0.052	0.0 × 2	
	A'	191.9804	260.5440	68.5636	0.052	−0.052	0.0 × 2	
	A''	191.9786	260.5440	68.5654	−0.040	−0.103	1155.2 × 2	1.2×10^{-6}
${}^rQ_6$	A''	260.5440	341.5716	81.0276	0.030	0.091	799.7 × 2	
	A''	260.5419	341.5716	81.0296	−0.047	0.036	6.9 × 2	
	A'	260.5440	341.5736	81.0296	−0.047	0.036	6.9 × 2	
	A'	260.5419	341.5736	81.0317	−0.030	−0.091	799.8 × 2	0.009

$I^{(b)}(f \leftarrow i)/I^{(c)}(f \leftarrow i) \approx 0.6$, in perfect agreement with the experimental value[12] of 0.58.

By comparing $|T_b^{if}|$ and $|T_c^{if}|$, we have been able to make b/c-type assignments for the ${}^rQ_{K_a}$ transitions with $K_a \leq 6$ and $J = 8$ (Table 1). We determine $I^{(b)}(f \leftarrow i)$ $[I^{(c)}(f \leftarrow i)]$ by adding the intensities of the b-type [c-type] transitions found in the given branch and compute $I^{(b)}(f \leftarrow i)/I^{(c)}(f \leftarrow i)$. The resulting values are included in Table 1 for each ${}^rQ_{K_a}$ -branch. For the branches ${}^rQ_3$, ${}^rQ_4$, ${}^rQ_5$, and ${}^rQ_6$, very small values of $I^{(b)}(f \leftarrow i)/I^{(c)}(f \leftarrow i)$ ensue. The ratio drops from 0.007 for $K_a = 3$ to 0.003 for $K_a = 4$ and further to a minimum of 1.2×10^{-6} at $K_a = 5$. For $K_a = 6$ it increases again to a value of 0.009. The value of 0.007 obtained theoretically for the $J = 8$ transitions in the ${}^rQ_3$ branch is in agreement with the experimental determination[12] of $I^{(b)}(f \leftarrow i)/I^{(c)}(f \leftarrow i) < 0.02$.

Closer inspection of the T_b^{if} and T_c^{if} values in Table 1 allows us to make two observations: (i) b/c-type assignments become ambiguous for $K_a \geq 3$ since for many transitions in the corresponding ${}^rQ_{K_a}$ branches, $|T_b^{if}| \approx |T_c^{if}|$, and (ii) we have already discussed in connection with eqn (24) that in the limit of $K_a \rightarrow \infty$, the line strengths $S_{A'(1)\leftrightarrow A'(2)}$ and $S_{A'(2)\leftrightarrow A'(1)}$ vanish. This is borne out by the TROVE results in Table 1 where we recognize that for these very weak transitions, $T_b^{if} \approx -T_c^{if}$. That is, b-type and c-type contributions to the line strength cancel. This initially unexpected behaviour of the b/c-type intensity ratio was first noted experimentally for the ${}^rQ_3$ branch of HSOH[12] in that $I^{(b)}(f \leftarrow i)/I^{(c)}(f \leftarrow i)$ was determined to be less than 0.02, and it has been satisfactorily explained by theory in the present work (see Fig. 3). That is, the limit of $K_a \rightarrow \infty$ (which, for HSOH, in practice means $K_a \geq 3$) we find transitions for which the b-type and c-type intensity contributions cancel according to eqn (24). We also find 'hybrid' transitions for which the two contributions interfere constructively as described by eqn (23). As already noted, for hybrid transitions b/c-type assignments are meaningless. The ${}^rQ_3$-display in Fig. 4 shows examples of allowed hybrid transitions.

In deriving eqn (15) and (16) we have assumed that the vibrational matrix elements $\left\langle \phi^{(vib)}_{K_a,\tau_{tor}} | \bar{\mu}_b | \phi^{(vib)}_{K'_a,\tau_{tor}} \right\rangle$ and $\left\langle \phi^{(vib)}_{K_a,\tau_{tor}} | \bar{\mu}_c | \phi^{(vib)}_{K'_a,\tau'_{tor}} \right\rangle$, which occur in these equations for $K'_a = K_a + 1$, are independent of τ_{tor} and τ'_{tor}. This condition is relatively well satisfied in the actual TROVE calculations. If we are to describe accurately the intensities of the HSOH transitions, however, it is not permissible to approximate these matrix elements by the values of the dipole moment components at equilibrium, $\bar{\mu}_b{}^e$ and $\bar{\mu}_c{}^e$. The actual values for $\left\langle \phi^{(vib)}_{K_a,\tau_{tor}} | \bar{\mu}_b | \phi^{(vib)}_{K'_a,\tau_{tor}} \right\rangle$ and $\left\langle \phi^{(vib)}_{K_a,\tau_{tor}} | \bar{\mu}_c | \phi^{(vib)}_{K'_a,\tau'_{tor}} \right\rangle$ obtained by

TROVE differ substantially from $\bar{\mu}_b^e$ and $\bar{\mu}_c^e$. Thus, we must calculate the matrix elements numerically and, in particular, take into account the dependence of these matrix elements on K_a and K_a' which arises from the dependence of the torsional wavefunctions $\phi^{(\mathrm{vib})}_{K_a,\tau_{\mathrm{tor}}}$ on K_a. This is illustrated in Fig. 6 where we show the torsional wavefunctions $\phi^{(\mathrm{vib})}_{K_a,\tau_{\mathrm{tor}}=0}$ computed for $K_a = 2$ and $K_a = 8$, as a function of τ_{HSOH}, the dihedral angle between the HSO and SOH planes.[16] We also include in Fig. 6 the two dipole moment components $\bar{\mu}_b(\tau_{\mathrm{HSOH}})$ and $\bar{\mu}_c(\tau_{\mathrm{HSOH}})$, calculated along the torsional MEP of HSOH.[15] The wavefunction $\phi^{(\mathrm{vib})}_{K_a=2,\tau=0}(\tau_{\mathrm{HSOH}})$ has its maximum amplitude near the equilibrium τ_{HSOH}-value, $\tau_{\mathrm{eq}} = 91.4°$, whereas the maximum amplitude of $\phi^{(\mathrm{vib})}_{K_a=8,\tau=0}(\tau_{\mathrm{HSOH}})$ occurs at $\tau_{\mathrm{HSOH}} = 126.3°$. That is, relative to $\phi^{(\mathrm{vib})}_{K_a=2,\tau=0}(\tau_{\mathrm{HSOH}})$, the wavefunction $\phi^{(\mathrm{vib})}_{K_a=8,\tau=0}(\tau_{\mathrm{HSOH}})$ has its maximum amplitude shifted towards the *trans*-planar configuration at $\tau_{\mathrm{HSOH}} = 180°$. The quantum number K_a is the projection, in units of $\hbar$, of the total angular momentum onto the molecule-fixed a axis which almost coincides with the SO bond in HSOH. That is, K_a measures how the entire molecule rotates about the SO bond which is also the axis that defines the torsional motion. Because of this, there is a strong coupling between the torsion and the K_a-type rotation and this coupling manifests itself in the wavefunctions included in Fig. 6: When the molecule rotates faster, centrifugal effects cause the dihedral angle τ_{HSOH} to open. The shift of the maximum amplitude of the wavefunctions towards $\tau_{\mathrm{HSOH}} = 180°$ causes the matrix elements $\left\langle \phi^{(\mathrm{vib})}_{K_a,\tau_{\mathrm{tor}}} | \bar{\mu}_b | \phi^{(\mathrm{vib})}_{K_a'\tau_{\mathrm{tor}}} \right\rangle$ and $\left\langle \phi^{(\mathrm{vib})}_{K_a,\tau_{\mathrm{tor}}} | \bar{\mu}_c | \phi^{(\mathrm{vib})}_{K_a'\tau_{\mathrm{tor}}'} \right\rangle$ to decrease, since the dipole moment components $\bar{\mu}_b(\tau_{\mathrm{HSOH}})$ and $\bar{\mu}_b(\tau_{\mathrm{HSOH}})$ both decrease when τ_{HSOH} approaches 180°. Thus the strong variation of $\bar{\mu}_b(\tau_{\mathrm{HSOH}})$ and $\bar{\mu}_c(\tau_{\mathrm{HSOH}})$ with τ_{HSOH}, and the strong dependence of the wavefunctions $\left|\phi^{(\mathrm{vib})}_{K_a,\tau_{\mathrm{tor}}}\right\rangle$ on K_a, both lead to a strong dependence of T_b^{if} and T_c^{if} on K_a (see Table 1), and to a strong variation of the ratio I_b/I_c with K_a.

Along with the rotational spectrum of HSOH shown in Fig. 1, we have also simulated the rotational spectrum

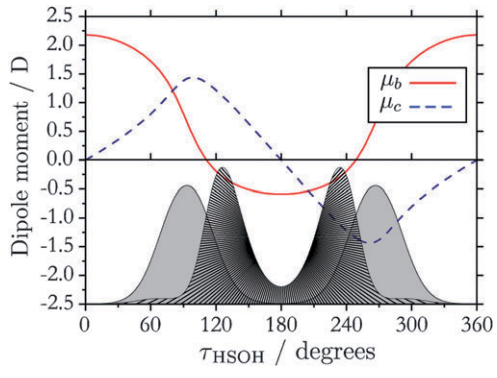

Fig. 6 Upper part: The two dipole moment components $\bar{\mu}_b(\tau_{\mathrm{HSOH}})$ (solid curve) and $\bar{\mu}_c(\tau_{\mathrm{HSOH}})$ (dashed curve), calculated along the torsional MEP of HSOH shown in Fig. 1 of ref. 15. Lower part: The torsional wavefunctions $\phi^{(\mathrm{vib})}_{K_a=2,\tau_{\mathrm{tor}}=0}(\tau_{\mathrm{HSOH}})$ (area under curve uniformly semi-transparent grey) and $\phi^{(\mathrm{vib})}_{K_a=8,\tau_{\mathrm{tor}}=0}(\tau_{\mathrm{HSOH}})$ (area under curve inhomogeneously shaded) for HSOH, drawn in arbitrary units. All functions in the figure depend on τ_{HSOH}, the dihedral angle between the HSO and SOH planes.[16]

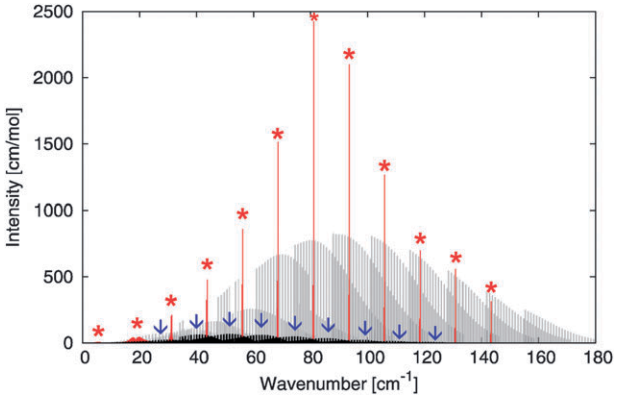

Fig. 7 The rotational spectrum of HSOH associated with the fundamental torsional state at 440 cm^{-1}, simulated theoretically at $T = 300$ K. ^rP- and ^rQ-branch transitions are indicated by arrows and asterisks, respectively.

associated with the first excited torsional state ν_{HSOH} located at 440 cm^{-1}. The transitions in this spectrum all originate and end in the ν_{HSOH} fundamental state. The RPH/SRB approach[25–27] used for the nuclear-motion calculations of the present work is also valid for the ν_{HSOH} state which is well below the lowest small-amplitude vibrational state, the SO stretch fundamental state near 760 cm^{-1} (see ref. 16). In fact even higher torsionally excited states are well described by the RPH/SRB approach, see ref. 15. The simulated ν_{HSOH}-state rotational spectrum ($T = 300$ K, $J \leq 40$) is shown in Fig. 7. The 'hot' spectrum is very similar to the ground-state rotational spectrum of Fig. 1, but the intensities are reduced by a factor of four.

We have also analyzed the calculated torsional splittings Δ_{tor} ($v_{\mathrm{HSOH}} = 1, J, K_a, \tau_{\mathrm{rot}}$) associated with the ν_{HSOH} state. In Fig. 8 we plot for each K_a-value the splittings calculated for $J = K_a, \ldots, 40$. We find that the main pattern of the ground state splittings[15] are reproduced here: the irregular K_a-variation of the splittings for the lowest K_a-values and the period-of-three variation as K_a increases.[15] Relative to the ground state, the splittings in Fig. 8 are larger by two orders of magnitude.

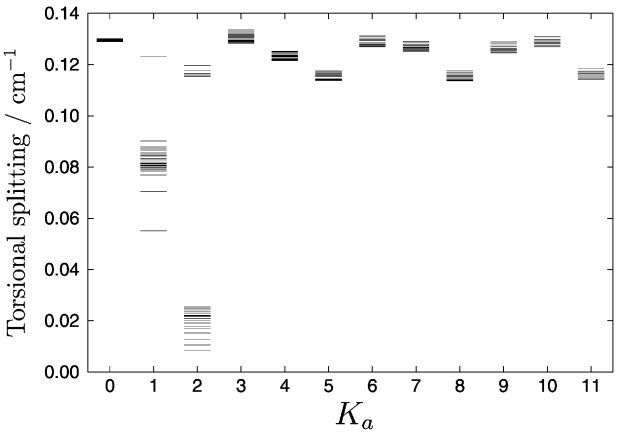

Fig. 8 The theoretical values of the torsional splittings Δ_{tor} ($v_{\mathrm{HSOH}} = 1, J, K_a, \tau_{\mathrm{rot}}$) (in cm^{-1}), plotted against the rotational quantum number K_a. For each K_a-value, we plot splittings calculated for $J = K_a, \ldots, 40$ and $\tau_{\mathrm{rot}} = 0$ and 1.

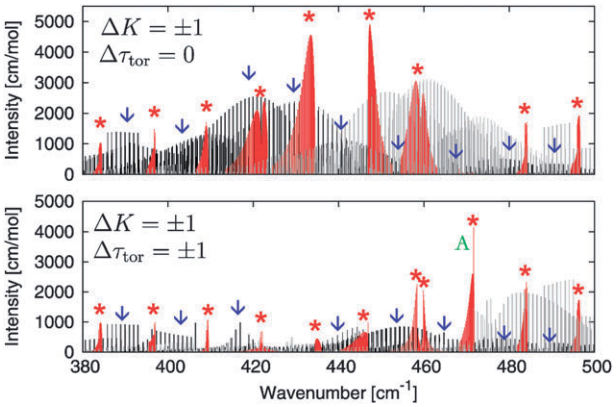

Fig. 9 The fundamental torsional band of HSOH, simulated theoretically at $T = 300$ K. The transitions are separated into a $\Delta\tau_{tor} = 0$ spectrum in the upper display and a $\Delta\tau_{tor} = \pm 1$ spectrum in the lower display (see text). The *P*- and *Q*-branch transitions are indicated by arrows and asterisks, respectively.

Finally, we report the simulation of the ν_{HSOH} fundamental band of HSOH (Fig. 9). The calculations are done for $T = 300$ K, taking into account transitions between states with $J \leq 40$. Only transitions with $\Delta K_a = \pm 1$ are plotted in Fig. 9 since the $K_a = 0$ transitions are vanishingly weak in comparison with the $K_a = \pm 1$ ones. We separate the spectrum into a $\Delta\tau_{tor} = 0$ spectrum (which, in the case of separable rotation–torsion wavefunctions, consists of *b*-type transitions) and a $\Delta\tau_{tor} = \pm 1$ spectrum (which, in the case of separable rotation–torsion wavefunctions, consists of *c*-type transitions). For the assignment of the transitions in the Figure, we used an automatic procedure which assigns to a given state the K_a and τ_{tor} values of the basis function with the largest contribution to the state, *i.e.* the basis function with the largest absolute value of the expansion coefficients in eqn (3). Because of the strong torsion–rotation interaction (see discussion above) this approach occasionally leads to 'unsystematic' assignments. As an example of this, it is surprising that all transitions in the sub-band marked 'A' in the lower display of Fig. 9 are assigned as belonging to the $\Delta\tau_{tor} = \pm 1$ spectrum. Clearly this sub-band, or at least some of the transitions in it, could reasonably be assigned as belonging to the $\Delta\tau_{tor} = 0$ spectrum (top display).

IV. Summary and discussion

The program suite TROVE[24] for calculating the rotation–vibration energies of an arbitrary molecule in an isolated electronic state has recently been extended[32] by modules to compute the intensities of rotation–vibration transitions such that rotation–vibration spectra can be simulated. The present simulations of the rotation–torsion spectrum of $H^{32}SOH$ are based on *ab initio* potential energy and dipole moment surfaces for the electronic ground state of HSOH, calculated at the CCSD(T) level of theory using the aug-cc-pV(T+*d*)Z and aug-cc-pV(Q+*d*)Z basis sets.[20–23]

The current work is mainly motivated by the recent experimental observation of intensity anomalies in some of the ${}^rQ_{K_a}$-branches of the HSOH rotational spectrum recorded at 1.3 THz with a synthesizer-based multiplier spectrometer.[12] An experimentally observed ${}^rQ_{K_a}$-branch in the HSOH spectrum is customarily assigned in a pattern-recognition process which attempts to separate the transitions of the ${}^rQ_{K_a}$-branch into two sets of *b*-type and *c*-type transitions. The dipole moment of HSOH is approximately perpendicular to the SO bond which almost coincides with the *a* principal axis. Consequently, the dipole moment component $\bar{\mu}_a$ along the *a* axis is small whereas the *b* and *c* components, $\bar{\mu}_b$ and $\bar{\mu}_c$, are comparatively large. Conventional spectroscopic wisdom assumes that a *b*-type (*c*-type) transition predominantly derives its intensity from $\bar{\mu}_b$ ($\bar{\mu}_c$), and that the ratio of typical *b*-type and *c*-type transition intensities, I_b/I_c, is roughly given by eqn (7) which predicts $I_b/I_c \approx 0.3$ for HSOH.

Experimentally[12] it has been found that transitions of the ${}^rQ_0$ and ${}^rQ_1$ branches of HSOH can be straightforwardly separated into *b*-type and *c*-type transitions with a value of $I_b/I_c \approx 0.3$. That is, these two branches behave according to the conventional spectroscopic wisdom. The transitions of the ${}^rQ_2$ branch of HSOH can also be assigned as *b*-type or *c*-type but here $I_b/I_c \approx 0.6$, twice as large as the value predicted by eqn (7). In contrast, for the ${}^rQ_3$ branch the *b*-type transitions are very weak compared to the *c*-type ones and experiment yields $I_b/I_c < 0.02$.

The present theoretical calculations produce intensity values for the ${}^rQ_{K_a}$-branch transitions in perfect agreement with the experimental findings (see Table 1). Our analysis of the theoretical results (Section III) shows that eqn (7) applies when the rotation–torsion wavefunctions for the states involved in the transitions, $\Psi^{\Gamma,i)}_{J,K_a,i}$, are separable as $\Psi^{\Gamma,i)}_{J,K_a,i} \approx |J, K_a, \tau_{rot}\rangle \phi^{(vib)}_{K_a,\tau_{tor}}$ As mentioned in connection with eqn (1), the parity[28] of the rotational basis function $|J,K_a,\tau_{rot}\rangle$ is $(-1)^{\tau_{rot}}$, and the parity of the torsional basis function $\phi^{(vib)}_{K_a,\tau_{tor}}$ is $(-1)^{\tau_{tor}}$. We have shown in section III [see, in particular, eqn (15) and (16)], that for HSOH, separable wavefunctions [*i.e.*, $\theta_{J,K_a} \approx 0$ in eqn (8)–(11)] are obtained for $K_a = 0$, 1, and 2. This explains the experimental result[12] that eqn (7) is well satisfied for the ${}^rQ_0$ and ${}^rQ_1$ branches of HSOH.

As K_a increases, HSOH approaches the so-called symmetric top limit. In this limit, $\theta_{J,K_a} \approx 45^\circ$ in eqn (8)–(11) and the rotation–torsion wavefunctions $\Psi^{\Gamma,i)}_{J,K_a,i}$ become fifty–fifty mixtures of products $|J, K_a, \tau_{rot}\rangle \phi^{(vib)}_{K_a,\tau_{tor}}$ with a common value of $(\tau_{rot} + \tau_{tor})$ mod 2 (=0 or 1). With $\theta_{J,K_a} \approx 45^\circ$ in eqn (8)–(11), the intensities of the ${}^rQ_{K_a}$ transitions are given by eqn (23) and (24) which, at least formally, are consistent with $I_b/I_c = 0$, in keeping with the experimental result[12] of $I_b/I_c < 0.02$ for the ${}^rQ_3$ branch of HSOH.

The ${}^rQ_2$ branch of HSOH is neither described by the limiting case $\theta_{J,K_a} \approx 0$ nor by the other limiting case, the symmetric top limit with $\theta_{J,K_a} \approx 45^\circ$. The TROVE calculations give a theoretical value of $I_b/I_c = 0.6$ for this branch (Table 1), in perfect agreement with the experimental value[12] of 0.58. Hence they also remain reliable in the intermediate range between the low-K_a and high-K_a limits. Closer inspection of the TROVE results indicates that the expected limiting behaviour of a symmetric top is not fully reached with increasing K_a, since the computed I_b/I_c values do not vanish completely as implied by eqn (24). These ratios drop from

0.007 for $K_a = 3$ to 0.004 for $K_a = 4$ and further to a minimum of 2.5×10^{-6} at $K_a = 5$, but increase again to 0.009 for $K_a = 6$. Such deviations from the symmetric-top limit are not too surprising since the underlying qualitative model neglects a number of factors that are taken into account in the actual TROVE calculations, including the actual degree of wavefunction mixing (with θ_{J,K_a} somewhat different from 45°) as well the vibrational dependence of the dipole moment components and the variation of the vibrational dipole-moment matrix elements with K_a and K_a'.

In summary, the present study demonstrates that the variational TROVE approach provides a realistic description of the large amplitude torsional motion of HSOH. The simulations provide rotation–torsion spectra of HSOH that reproduce the observed intensity patterns very well, including the intensity anomalies in the ${}^rQ_{K_a}$-branches which are caused by the large-amplitude torsional motion; these anomalies can be understood qualitatively by an analysis of the TROVE results.

Appendix A: The line strength

The line strength $S(f \leftarrow i)$ of an individual rovibrational transition $f \leftarrow i$ is used in eqn (4). It is initially expressed in terms of the matrix elements of the dipole moment function between the rotation–torsion wavefunctions in eqn (3). For the calculations of the present work, we use

$$S(f \leftarrow i) = g_{\rm ns}(2J'+1)(2J''+1) \times \left| \sum_{v'_{\rm HSOH},K',\tau'_{\rm rot}} \sum_{v''_{\rm HSOH},K'',\tau''_{\rm rot}} (-1)^{\sigma'_{\rm rot}+\sigma''_{\rm rot}+K''} \times C_{J,\Gamma',f}^{(K',\tau'_{\rm rot},v'_{\rm HSOH},\tau'_{\rm tor})} C_{J,\Gamma'',i}^{(K'',\tau''_{\rm rot},v''_{\rm HSOH},\tau''_{\rm tor})} \times \begin{pmatrix} J'' & 1 & J' \\ K'' & K''-K' & -K' \end{pmatrix} F_{v',K',\tau'_{\rm rot};v'',K'',\tau''_{\rm rot}} \right|^2, \quad \text{(A1)}$$

where the quantum numbers

$$(J', K', \tau'_{\rm rot}, \tau'_{\rm tor}, v'_{\rm HSOH}, \sigma'_{\rm rot})$$

apply to the final state of the transition and

$$(J'', K'', \tau''_{\rm rot}, \tau''_{\rm tor}, v''_{\rm HSOH}, \sigma''_{\rm rot})$$

to the initial state. The expansion coefficients $C_{J,\Gamma',f}^{(K',\tau'_{\rm rot},v'_{\rm HSOH},\tau'_{\rm tor})}$ and $C_{J,\Gamma'',i}^{(K'',\tau''_{\rm rot},v''_{\rm HSOH},\tau''_{\rm tor})}$ are defined in eqn (3). Furthermore,

$$F_{v',K',\tau'_{\rm rot};v'',K'',\tau''_{\rm rot}} = \begin{cases} (\tau''_{\rm rot} - \tau'_{\rm rot})\langle v'|\bar{\mu}_z|v''\rangle, & K' = K'', \tau'_{\rm rot} \neq \tau''_{\rm rot} \\ f_{K',K''}(\tau'_{\rm rot} - \tau''_{\rm rot})(K''-K')\langle v'|\bar{\mu}_x|v''\rangle, & K''-K' = 1, \tau'_{\rm rot} \neq \tau''_{\rm rot} \\ -f_{K',K''}\langle v'|\bar{\mu}_y|v''\rangle, & |K''-K'| = 1, \tau'_{\rm rot} = \tau''_{\rm rot} \end{cases} . \quad \text{(A2)}$$

These expressions have been derived by following the procedure described in Chapter 14 of ref. 28 and in ref. 30. They are given in terms of the symmetrized rotational basis functions in eqn (73) and (74) of ref. 24. In eqn (A2), $\begin{pmatrix} J'' & 1 & J' \\ K'' & K''-K' & -K' \end{pmatrix}$ is a standard 3*j*-symbol (see, for example) ref. 28,

$$f_{K',K''} = \begin{cases} \frac{1}{\sqrt{2}} & \text{for } K' + K'' \neq 1 \\ 1 & \text{otherwise} \end{cases} \quad \text{(A3)}$$

$$\sigma_{\rm rot} = \begin{cases} K \bmod 3 & \text{for } \tau_{\rm rot} = 1 \\ 0 & \text{otherwise,} \end{cases} \quad \text{(A4)}$$

and

$$|v\rangle = |v_{\rm OS}\rangle\ |v_{\rm SH}\rangle\ |v_{\rm OH}\rangle\ |v_{\rm OSH}\rangle\ |v_{\rm SOH}\rangle\ |v_{\rm HSOH},\tau_{\rm tor}\rangle \quad \text{(A5)}$$

is a vibrational basis function as introduced in eqn (1). In eqn (A1) and (A2) $\bar{\mu}_\alpha$ ($\alpha = a, b, c$) are electronically averaged dipole moment components $\langle\Phi_{\rm elec}|\mu_\alpha|\Phi_{\rm elec}\rangle$ expressed in the molecule-fixed axis system *xyz* defined by Eckart–Sayvetz conditions.[24]

Acknowledgements

We acknowledge support from the European Commission (contract no. MRTN-CT-2004-512202 "Quantitative Spectroscopy for Atmospheric and Astrophysical Research" (QUASAAR)).

References

1 R. J. Huxtable, *Biochemistry of Sulphur*, Plenum Press, New York, 1986.
2 C. F. Cullis and M. M. Hirschler, *Atmos. Environ.*, 1980, **14**, 1263–1278.
3 N. S. Wang and C. J. Howard, *J. Phys. Chem.*, 1990, **94**, 8787–8794.
4 G. S. Tyndal and A. R. Ravishankara, *Int. J. Chem. Kinet.*, 1991, **23**, 483–527.
5 L. Vervisch, B. Labegorre and J. Réveillon, *Fuel*, 2004, **83**, 605–614.
6 G. Winnewisser, F. Lewen, S. Thorwirth, M. Behnke, J. Hahn, J. Gauss and E. Herbst, *Chem.–Eur. J.*, 2003, **9**, 5501–5510.
7 M. Behnke, J. Suhr, S. Thorwirth, F. Lewen, H. Lichau, J. Hahn, J. Gauss, K. M. T. Yamada and G. Winnewisser, *J. Mol. Spectrosc.*, 2003, **221**, 121–126.
8 S. Brünken, M. Behnke, S. Thorwirth, K. M. T. Yamada, T. F. Giesen, F. Lewen, J. Hahn and G. Winnewisser, *J. Mol. Struct.*, 2005, **742**, 237–242.
9 O. Baum, S. Esser, N. Gierse, S. Brünken, F. Lewen, J. Hahn, J. Gauss, S. Schlemmer and T. F. Giesen, *J. Mol. Struct.*, 2006, **795**, 256–262.
10 H. Beckers, S. Esser, T. Metzroth, M. Behnke, H. Willner, J. Gauss and J. Hahn, *Chem.–Eur. J.*, 2006, **12**, 832–844.
11 O. Baum, T. F. Giesen and S. Schlemmer, *J. Mol. Spectrosc.*, 2008, **247**, 25–29.
12 O. Baum, M. Koerber, O. Ricken, G. Winnewisser, S. N. Yurchenko, S. Schlemmer, K. M. T. Yamada and T. F. Giesen, *J. Chem. Phys.*, 2008, **129**, 224312.
13 O. Baum, *PhD dissertation*, University of Cologne, 2008.
14 K. M. T. Yamada, G. Winnewisser and P. Jensen, *J. Mol. Struct.*, 2004, **695–696**, 323–337.
15 R. I. Ovsyannikov, V. V. Melnikov, W. Thiel, P. Jensen, O. Baum, T. F. Giesen and S. N. Yurchenko, *J. Chem. Phys.*, 2008, **129**, 154314.

16 S. N. Yurchenko, A. Yachmenev, W. Thiel, O. Baum, T. F. Giesen, V. V. Melnikov and P. Jensen, *J. Mol. Spectrosc.*, 2009, **257**, 57–65.
17 K. M. T. Yamada, P. Jensen, S. C. Ross, O. Baum, T. F. Giesen and S. Schlemmer, *J. Mol. Struct.*, 2009, **927**, 96–100.
18 G. D. Purvis and R. J. Bartlett, *J. Chem. Phys.*, 1982, **76**, 1910–1918.
19 K. Raghavachari, G. W. Trucks, J. A. Pople and M. Head-Gordon, *Chem. Phys. Lett.*, 1989, **157**, 479–483.
20 T. H. Dunning, *J. Chem. Phys.*, 1989, **90**, 1007–1023.
21 R. A. Kendall, T. H. Dunning and R. J. Harrison, *J. Chem. Phys.*, 1992, **96**, 6796–6806.
22 D. E. Woon and T. H. Dunning, *J. Chem. Phys.*, 1993, **98**, 1358–1371.
23 A. K. Wilson and T. H. Dunning, *J. Chem. Phys.*, 2003, **119**, 11712–11714.
24 S. N. Yurchenko, W. Thiel and P. Jensen, *J. Mol. Spectrosc.*, 2007, **245**, 126–140.
25 W. H. Miller, N. C. Handy and J. A. Adams, *J. Chem. Phys.*, 1980, **72**, 99–112.
26 J. T. Hougen, P. R. Bunker and J. W. C. Johns, *J. Mol. Spectrosc.*, 1970, **34**, 136–172.
27 P. R. Bunker and B. M. Landsberg, *J. Mol. Spectrosc.*, 1977, **67**, 374–385.
28 P. R. Bunker and P. Jensen, *Molecular Symmetry and Spectroscopy*, NRC Research Press, Ottawa, 2nd edn, 1998.
29 J. W. Cooley, *Math. Comput.*, 1961, **15**, 363–374.
30 S. N. Yurchenko, M. Carvajal, W. Thiel, H. Lin and P. Jensen, *Adv. Quantum Chem.*, 2005, **48**, 209–238.
31 S. N. Yurchenko, M. Carvajal, P. Jensen, H. Lin, J. J. Zheng and W. Thiel, *Mol. Phys.*, 2005, **103**, 359–378.
32 S. N. Yurchenko, R. J. Barber, A. Yachmenev, W. Thiel, P. Jensen and J. Tennyson, *J. Phys. Chem. A*, 2009, **113**, 11845–11855.
33 E. A. Desloge, *Am. J. Phys.*, 1984, **52**, 261–262.
34 D. Papoušek and M. R. Aliev, *Molecular Vibrational/Rotational Spectra*, Elsevier, Amsterdam, 1982.
35 G. Winnewisser, *Vib. Spectrosc.*, 1995, **8**, 241–253.
36 G. Winnewisser and K. M. T. Yamada, *Vib. Spectrosc.*, 1991, **1**, 263–272.
37 G. Pelz, K. M. T. Yamada and G. Winnewisser, *J. Mol. Spectrosc.*, 1993, **159**, 507–520.
38 P. R. Bunker and P. Jensen, *Fundamentals of Molecular Symmetry*, IOP Publishing, Bristol, 2004.

A new 'spectroscopic' potential energy surface for formaldehyde in its ground electronic state

A. Yachmenev, S. N. Yurchenko, P. Jensen, W. Thiel,

J. Chem. Phys., submitted for publication (2011)

A new 'spectroscopic' potential energy surface for formaldehyde in its ground electronic state

Andrey Yachmenev,[1] Sergei N. Yurchenko,[2] Per Jensen,[3] and Walter Thiel*[1]

[1]*Max-Planck-Institut für Kohlenforschung, Kaiser-Wilhelm-Platz 1, D–45470 Mülheim an der Ruhr, Germany*

[2]*Technische Universität Dresden, Physikalische Chemie, D-01062 Dresden, Germany.*

[3]*FB C – Physikalische und Theoretische Chemie, Bergische Universität, D–42097 Wuppertal, Germany.*

(Dated: March 2, 2011)

Abstract

We report a new 'spectroscopic' potential energy surface (PES) of formaldehyde ($H_2{}^{12}C^{16}O$) in its ground electronic state, obtained by refining an *ab initio* PES in a least-squares fitting to the experimental spectroscopic data for formaldehyde currently available in the literature. The *ab initio* PES was computed using the CCSD(T)/aug-cc-pVQZ method at 30 840 geometries that cover the energy range up to 44 000 cm^{-1} above equilibrium. Ro-vibrational energies of formaldehyde were determined variationally for this *ab initio* PES by means of the program TROVE. The parameter values in the analytical representation of the PES were optimized in fittings to 319 ro-vibrational energies with $J = 0, 1, 2, 5$. The initial parameter values in the fittings were those of the *ab initio* PES, the ro-vibrational eigenfunctions obtained from this PES served as basis set during the fitting process, and constraints were imposed to ensure that the refined PES does not deviate unphysically from the *ab initio* one in regions of configuration space not sampled by the experimental data. The resulting refined PES, referred to as H2CO-2011, reproduces the available experimental $J \leq 5$ data with a root-mean-square error of 0.04 cm^{-1}.

* Corresponding author. E-mail: thiel@mpi-muelheim.mpg.de.

I. INTRODUCTION

An important goal of theoretical spectroscopy is the generation of accurate ground-state potential energy surfaces (PESs) for small polyatomic molecules. The PESs obtained are intended to serve as input for variational computations of highly accurate ro-vibrational term values with deviations from experiment typically below 0.1 cm^{-1}. In order to achieve this accuracy, an 'empirical' approach is required in which an *ab initio* PES is refined in least-squares fittings to experimentally derived energies or observed wavenumbers. The PESs determined in this manner are generally referred to as 'spectroscopic' potentials. The semi-empirical PESs of H_3^+, H_2O, H_2Te, H_2S, O_3, CO_2, and NH_3[1–8] are successful examples of this strategy being employed towards approaching spectroscopic accuracy in the theoretical calculation of rotation-vibration energy levels.

Recently we have implemented a new procedure[9] in the program suite TROVE[10] for the refinement of an *ab initio* PES of a polyatomic molecule through least-squares fitting to experimental ro-vibrational energies. We have already applied this approach to construct 'spectroscopic' PESs for $^{121}SbH_3$ and $^{14}NH_3$.[9,11] In the present work we generate an accurate 'spectroscopic' PES for $H_2{}^{12}C{}^{16}O$ (henceforth referred to as formaldehyde or H_2CO). We first compute a six-dimensional *ab initio* PES for ground-state H_2CO by means of standard coupled cluster theory CCSD(T)[12–14] in conjunction with the augmented correlation-consistent atomic basis set aug-cc-pVQZ.[15,16] When we use this *ab initio* PES for variational TROVE[10] calculations of the vibrational energies, the resulting energies typically deviate from the experimentally derived values by up to several wavenumbers. As we are aiming for a 'spectroscopic accuracy' of better than 0.1 cm^{-1}, we refine the *ab initio* PES in a least-squares fitting to the available experimental ro-vibrational energies for $J = 0, 1, 2$ and 5. The resulting 'spectroscopic' PES reproduces the experimentally determined term values of formaldehyde for $J \leq 5$ with a root-mean-square (rms) error of 0.04 cm^{-1}.

The spectrum of H_2CO is important in diverse applications, including atmospheric, interstellar, and combustion chemistry. A number of *ab initio* PESs for H_2CO, computed at various levels of theory, are available. Martin *et al.*[17] determined the *ab initio* quartic force field using the CCSD(T)/cc-pVTZ and CCSD(T)/cc-pVQZ methods, and reported theoretical values for structural and spectroscopic parameters. A set of multiresolution PESs were recently computed by Yagi *et al.*[18] by combining B3LYP/cc-pVDZ, CCSD/cc-

pVDZ, and CCSD(T)/cc-pVTZ results. Global ground-state PESs were constructed for formaldehyde by Jalbout and Chang[19] on the basis of combined *ab initio* and DFT results and by Zhang *et al.*[20] in purely *ab initio* calculations at the CCSD(T)/aug-cc-pVTZ and MR-CI/aug-cc-pVTZ levels of theory.

No available theoretical PES of H_2CO is capable of providing the accuracy that we target in the present work. An empirical adjustment of the force field from Ref. 17, aimed at improving the agreement with experimentally derived vibrational energies, was made by Carter *et al.*[21] The rms deviation attained was 1.1 cm^{-1}. In Ref. 22, Carter *et al.* improved their PES by including the term values of rotationally excited states (with $J \leq 3$) of H_2CO and D_2CO in the refinement, which led to a fitting with rms deviations of 1.1 cm^{-1} ($J = 0$), 0.002 cm^{-1} ($J = 1$), 0.005 cm^{-1} ($J = 2$), and 0.009 cm^{-1} ($J = 3$) for the ground and fundamental vibrational states. Burleigh *et al.*[23] obtained a 'spectroscopic' force field by refining the force constants from Ref. 17 in fittings (with an rms deviation of 1.5 cm^{-1}) to the vibrational band centers from Ref. 24. Similar fittings have been carried out by Mardis and Sibert[25] (rms deviation: 1.5 cm^{-1} for 139 term values) and by Bernal and Lemus[26] (rms deviation: 2.39 cm^{-1} for 260 states) who employed an algebraic local-mode model for the vibrational motion. Bekhtereva[27] and Ulenikov *et al.*[28] generated empirically adjusted force constant values in global fittings to the vibrational band centers of H_2CO, HDCO, and D_2CO (rms deviation: 0.97 cm^{-1} for 254 levels).

A detailed review of the experimentally available spectroscopic data for H_2CO is given in Ref. 29. In the PES fittings of the present work, input data derived from the following vibrational transitions have been employed: The 5.7 μm and 3.6 μm band systems[30]; the 3.5 μm band system[31]; the hot transitions $\nu_4 - \nu_4$, $\nu_1 + \nu_4 - \nu_4$, $\nu_4 + \nu_5 - \nu_4$[32]; and the band centers reported in Refs. 24,31,33,34. The band centers obtained from dispersed fluorescence spectra[24] are of special importance in the present work. Despite their relatively low resolution, these data are associated with an extensive set of vibrationally excited states. Thus, they sample large portions of vibrational configuration space and are essential for the accurate determination of the PES at high energies. In the PES refinement of the present work, we did not use as input the H_2CO data compiled in the databases HITRAN[35] and GEISA[36] because of the well-documented deficiencies of these data (see, for example, the discussion in Ref. 29).

The paper is structured as follows. The *ab initio* calculations and the analytical repre-

TABLE I: Equilibrium structures of H_2CO (bond lengths in Å, angle in degrees).

Method	r^e_{CO}	r^e_{CH}	θ^e_{OCH}	Ref.
CCSD(T)/aug-cc-pVQZ	1.20754	1.10222	121.693	this work
Refined PES-2010	1.20367	1.10290	121.781	this work
CCSD(T)/cc-pVQZ	1.2066	1.1022	121.78	17
CCSD(T)/cc-pVTZ	1.2115	1.1031	121.7	20
Refined	1.20312(50)	1.10034(50)	121.62(5)	39
Refined	1.20296	1.10064	121.648	22
Experiment	1.2033(10)	1.1005(20)	121.91(15)	40

sentation of the PES are described in Section II. The computational procedure is outlined in Section III. The selection of the experimental data for the refinement is discussed in Section IV. The results of the refinement are presented in Section V which also offers conclusions.

II. THE *AB INITIO* POTENTIAL ENERGY SURFACE

The six-dimensional *ab initio* PES of H_2CO was computed at 30 840 geometries with energies ranging up to 44 000 cm^{-1} above equilibrium. The quantum-chemical calculations were done at the CCSD(T) (coupled cluster theory involving single and double excitations, with a quasi-perturbative treatment of triple excitations[12–14]) level of theory using the frozen-core approximation and the augmented correlation-consistent aug-cc-pVQZ basis.[15,16] The CCSD(T) calculations were performed with the MOLPRO2006 package[37,38] using the default thresholds. The equilibrium structural parameters of H_2CO obtained from the *ab initio* results are listed in Table I, where they are compared with experimental and theoretical literature values.

In order to represent analytically the *ab initio* PES, we employ a Taylor-like expansion around the minimum energy path (MEP):

$$V(r_1, r_2, r_3, \theta_1, \theta_2, \tau) =$$

$$\sum_{ijklmn} f_{ijklmn} \left(1 - e^{-\Delta r_1}\right)^i \left(1 - e^{-\Delta r_2}\right)^j \left(1 - e^{-\Delta r_3}\right)^k (\Delta\theta_1)^l (\Delta\theta_2)^m (\cos\tau + 1)^n, \quad (1)$$

with the maximum expansion order $i + j + k + l + m + n = 6$.

In Eq. (1) we use the three stretching coordinates

$$\Delta r_1 = r_{\rm CO} - r_{\rm CO}^{\rm ref}(\tau), \quad (2)$$

$$\Delta r_2 = r_{\rm CH_1} - r_{\rm CH}^{\rm ref}(\tau), \quad (3)$$

$$\Delta r_3 = r_{\rm CH_2} - r_{\rm CH}^{\rm ref}(\tau), \quad (4)$$

the two bending coordinates

$$\Delta\theta_1 = \theta_{\rm OCH_1} - \theta_{\rm OCH}^{\rm ref}(\tau), \quad (5)$$

$$\Delta\theta_2 = \theta_{\rm OCH_2} - \theta_{\rm OCH}^{\rm ref}(\tau), \quad (6)$$

and the out-of-plane bending coordinate τ. Here, $r_{\rm CO}$, $r_{\rm CH_1}$, and $r_{\rm CH_2}$ are the bond lengths, $\theta_{\rm OCH_1}$ and $\theta_{\rm OCH_2}$ are the bond angles, and τ is the dihedral angle between the OCH_1 and OCH_2 planes. The sign of τ is chosen such that an observer on the O nucleus, who is looking towards the C nucleus, will see the rotation by τ from the CH_1 bond to the CH_2 bond as an anti-clockwise rotation.

Formaldehyde has the molecular symmetry (MS) group $\boldsymbol{C}_{2\rm v}$(M),[41] and so the potential function of H_2CO is invariant to the interchange to the two protons. This imposes the condition $f_{i(jk)(lm)n} = f_{i(kj)(ml)n}$ for the expansion coefficients in Eq. (1). The coordinates $r_{\rm CO}$, $r_{\rm CH_1}$, and $r_{\rm CH_2}$, $\theta_{\rm OCH_1}$ and $\theta_{\rm OCH_2}$ are all invariant under the spatial inversion operator E^*,[41] while $E^*\,\tau = 360^\circ - \tau$. However, $E^*\,\cos\tau = \cos\tau$ and the expression for V in Eq. (1) is invariant under E^* as required by symmetry. When the molecule is planar, $\tau = 180^\circ$, and the quantity $(\cos\tau + 1)$ in Eq. (1) vanishes. The reference structural parameters $r_{\rm CO}^{\rm ref}(\tau)$, $r_{\rm CH}^{\rm ref}(\tau)$, and $\theta_{\rm OCH}^{\rm ref}(\tau)$ defining the MEP of H_2CO were determined *ab initio* at the CCSD(T)/aug-cc-pVQZ level in geometry optimizations at 10 values of τ equidistantly distributed between $\tau = 80^\circ$ and $\tau = 180^\circ$. They were then expanded in terms of $(\cos\tau + 1)$ as follows:

$$r_{\rm CO}^{\rm ref}(\tau) = \sum_{n=0}^{4} a_n^{\rm CO} (\cos\tau + 1)^n, \quad (7)$$

$$r_{\rm CH}^{\rm ref}(\tau) = \sum_{n=0}^{3} a_n^{\rm CH} (\cos\tau + 1)^n, \quad (8)$$

$$\theta_{\rm OCH}^{\rm ref}(\tau) = \sum_{n=0}^{2} a_n^{\rm OCH} (\cos\tau + 1)^n. \quad (9)$$

TABLE II: Expansion parameters $a_n^{\rm X}$ (X=CO,CH,OCH) defining the reference structure of H_2CO (bond lengths in Å, angle in rad).

	CO	CH	OCH
a_0	1.2075443	1.10221709	2.123948763
a_1	0.0162744135	0.0208797432	−0.103629709
a_2	0.0059211995	0.0079106055	−0.0066300781
a_3	−0.0041248571	0.0034126562	
a_4	0.0049473990		

The computed MEP is shown in Fig. 1. The expansion parameters $a_n^{\rm X}$ (X=CO, CH, OCH), obtained in separate fittings to the 10 chosen data points are listed in Table II; the rms deviations of these fittings are 10^{-5} Å, 2×10^{-6} Å, and 3×10^{-5} radian for the CO, CH, and OCH parameters, respectively. The global minimum is found at $r_{\rm CO}^{\rm e}$ =1.20754 Å, $r_{\rm CH}^{\rm e}$ = 1.10222 Å, and $\theta_{\rm OCH}^{\rm e}$ = 121.693°. These values are in keeping with the equilibrium parameters from the literature (see Table I).

With the MEP defined by Eqs. (7-9) in conjunction with Table II, we have determined the remaining potential parameter values in a least-squares fitting to the complete set of computed *ab initio* energies. In this fitting, we could usefully vary 110 parameters f_{ijklmn} in Eq. (1) to get an overall root-mean-square (rms) error of 1.05 cm^{-1} (0.56 cm^{-1} for the points with energies below 5 000 cm^{-1}). We used weight factors of the form suggested by Partridge and Schwenke[42]:

$$w_i = \frac{\tanh\left[-0.0006 \text{ cm} \times (V_i - 16\,000 \text{ cm}^{-1})\right] + 1.002\,002\,002}{2.002\,002\,002 \text{ cm} \times V_i^{(w)}}, \qquad (10)$$

where $V_i^{(w)} = \max(16\,000 \text{ cm}^{-1}, V_i)$, and V_i is the *ab initio* energy at the ith geometry (in cm^{-1}), measured relative to the equilibrium energy. The *ab initio* energy V_i is weighted by the factor w_i in the PES fitting; these weight factors favor the energies below 16 000 cm^{-1}. The optimized values of the parameters f_{ijklmn} are given in the supplementary material to the present paper.[43] The analytical representation of the H_2CO PES [Eq. (1)] corresponding to these parameter values will be referred to as AVQZ as this reflects the underlying level of *ab initio* theory, CCSD(T)/aug-cc-pVQZ.

To assess the quality of the AVQZ PES of H_2CO, we have calculated a set of vibrational band centers associated with it by means of the TROVE approach[10] (see Section III for the

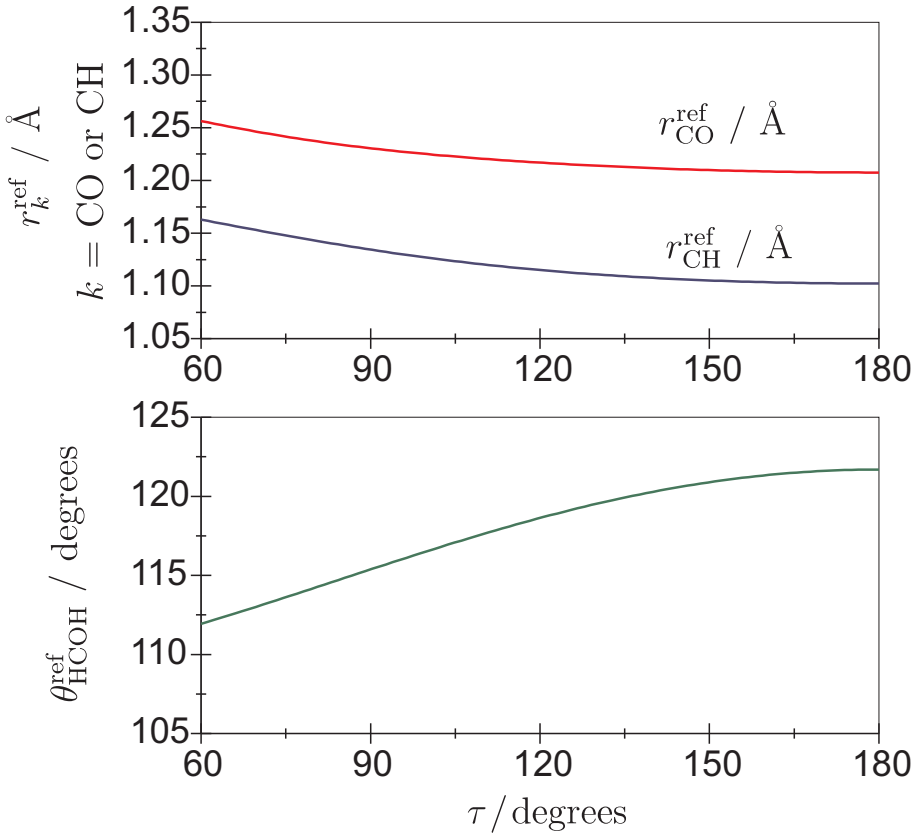

FIG. 1: Variation of the reference bond length values $r_{\rm CO}^{\rm ref}$ and $r_{\rm CH}^{\rm ref}$ (top panel) and of the reference bond angle value $\theta_{\rm OCH}^{\rm ref}$ (bottom panel) along the minimum energy path (see text) of H_2CO.

computational details). Tables III–VI include the calculated band center values (relative to the calculated zero point energy of 5769.78 cm^{-1}) and compare them with the available experimental values from the literature (see Section IV for the corresponding references). The rms deviation between theory and experiment is 4.0 cm^{-1} for all term values below 7 200 cm^{-1}. The fundamental term values are accurate to better than 1.4 cm^{-1}, except for the asymmetric bending mode ν_6 for which the fundamental term value deviates by 3.5 cm^{-1} from experiment. In view of the fact that at the CCSD(T)/aug-cc-pVQZ level of *ab initio* theory, we neglect for example higher-order coupled cluster excitations, core-valence correlation, basis set incompleteness, and relativistic effects, the agreement with experiment achieved with the AVQZ PES is better than expected. We also note that the purely rotational term values for $J \leq 5$ (see Table VIII below) are reproduced very well, with an rms error of 0.094 cm^{-1}. This indicates that the AVQZ equilibrium geometry is quite accurate. In summary, the new AVQZ PES of H_2CO appears to be of high quality and

should thus provide a good starting point for refinement of the PES in least-squares fittings to experimental data.

III. TROVE: COMPUTATIONAL DETAILS

We compute the ro-vibrational energies of H_2CO by means of the variational program suite TROVE.[10] In the variational calculations, we generate the matrix representation of the rotation-vibration Hamiltonian in terms of a symmetry-adapted basis set constructed as follows: The primitive vibrational basis functions are given by products of one-dimensional (1D) vibrational functions $\phi_{n_1}(r_1^\ell)$, $\phi_{n_2}(r_2^\ell)$, $\phi_{n_3}(r_3^\ell)$, $\phi_{n_4}(\theta_1^\ell)$, $\phi_{n_5}(\theta_2^\ell)$, and $\phi_{n_6}(\tau)$. Here, $(r_1^\ell, r_2^\ell, r_3^\ell, \theta_1^\ell, \theta_2^\ell)$ are linearized versions[10,41] of the coordinates $r_{\rm CO}, r_{\rm CH_1}, r_{\rm CH_2}, \theta_{\rm OCH_1}$, and $\theta_{\rm OCH_2}$, respectively. We use the Numerov-Cooley technique[44,45] to determine the functions $\phi_{n_i}(q_i)$ (where n_i denotes the principal quantum number) by solving the 1D Schrödinger equation[10] for the vibrational motion associated with the corresponding coordinate $q_i \in \{r_1^\ell, r_2^\ell, r_3^\ell, \theta_1^\ell, \theta_2^\ell, \tau\}$, with the other coordinates held fixed at their equilibrium values.

The basis functions $\phi_{n_i}(q_i)$ are then utilized to solve variationally the $J = 0$ problem:

$$\hat{H}_{\rm vib}|\Psi^\Gamma_{J=0,\gamma}\rangle = E^{\rm vib}_\gamma|\Psi^\Gamma_{J=0,\gamma}\rangle, \tag{11}$$

where $\hat{H}_{\rm vib}$ is the vibrational ($J = 0$) Hamiltonian

$$\hat{H}_{\rm vib} = \frac{1}{2}\sum_{\lambda\mu} p_\lambda G_{\lambda\mu} p_\mu + V + U, \tag{12}$$

Here, $E^{\rm vib}_\gamma$ and $\Psi^\Gamma_{J=0,\gamma}$ are the vibrational eigenvalues and eigenfunctions, respectively, and $\Gamma = A_1$, A_2, B_1, and B_2 are the irreducible representations of the $\boldsymbol{C}_{2\rm v}$(M) molecular symmetry group[41] to which H_2CO belongs. In Eq. (12), p_λ and p_μ are generalized momenta conjugate to the coordinates q_λ and q_μ, respectively. The kinetic energy factors $G_{\lambda\mu}$ and the pseudo-potential U are represented as 8th-order expansions in the displacement coordinates $\Delta r_i^\ell = r_i^\ell - r_i^{\rm e}$ ($i = 1, 2, 3$) and $\Delta\theta_j^\ell = \theta_j^\ell - \theta^{\rm e}$ ($j = 1, 2$) with $r_i^{\rm e}$ and $\theta^{\rm e}$ representing the equilibrium bond lengths and bond angle of H_2CO in the ground electronic state. For consistency, the molecular potential energy function V in (1) is also expanded in terms of linearized coordinates $\{\xi_1^\ell, \xi_2^\ell, \xi_3^\ell, \theta_1^\ell, \theta_2^\ell\}$, where $\xi_i^\ell = 1 - \exp(-\Delta r_i^\ell)$; this expansion is also truncated after the 8th-order terms.

The pure vibrational eigenfunctions $\Psi^\Gamma_{J=0,\gamma}$ of the $J = 0$ Hamiltonian [Eq. (11)] are multiplied by the symmetrized symmetric-top rotational eigenfunction[10,46] $|J, K, m, \tau_{\rm rot}\rangle$ in

TABLE III: Residuals (Obs.−Calc.; in cm^{-1}) for selected $J = 0$, $\Gamma = A_1$ energy levels of H_2CO, computed with TROVE from the *ab initio* AVQZ (A) and refined H2CO-2010 (R) PESs. The 'observed' values are from Ref. 24 unless indicated.

State	Obs.	Calc. (A)	Obs.-(A)	Calc.(R)	Obs.-(R)
ν_3	1500.1747[a]	1499.11	1.07	1500.19	−0.01
ν_2	1746.0093[b]	1744.63	1.38	1746.03	−0.02
$2\nu_4$	2327.5239[b]	2325.18	2.34	2327.54	−0.01
$\nu_3 + \nu_6$	2494.3543[b]	2487.74	6.61	2494.34	0.01
ν_1	2782.4575[b]	2781.76	0.70	2782.46	0.00
$\nu_3 + \nu_6$	2998.9873[b]	2997.28	1.71	2998.94	0.04
$\nu_2 + \nu_3$	3238.4548[b]	3236.24	2.22	3238.36	0.09
$2\nu_2$	3471.6	3469.61	1.99	3471.23	0.37
$\nu_3 + 2\nu_4$	3825.3	3822.46	2.84	3825.94	−0.64
$3\nu_6$	3937.4	3929.96	7.44	3936.02	1.38
$\nu_2 + 2\nu_4$	4058.3	4054.72	3.58	4058.53	−0.23
$\nu_5 + \nu_6$	4083.1	4078.96	4.14	4083.21	−0.11
$\nu_2 + \nu_3 + \nu_6$	4248.7	4241.25	7.45	4247.13	1.57
$\nu_1 + \nu_3$	4253.8	4253.93	−0.13	4254.58	−0.78
$\nu_1 + \nu_2$	4529.5025[c]	4527.77	1.73	4529.82	−0.31
$4\nu_4$	4629.0	4625.16	3.84	4628.59	0.41
$\nu_2 + \nu_3 + \nu_6$	4730.8	4726.68	4.12	4732.59	−1.79
$\nu_3 + 2\nu_4 + \nu_6$	4842.0	4834.75	7.25	4840.93	1.07
$2\nu_2 + \nu_3$	4955.2	4953.98	1.22	4954.65	0.55
$\nu_1 + 2\nu_4$	5092.4	5090.03	2.37	5092.32	0.08
$3\nu_2$	5177.7595[c]	5176.89	0.87	5177.82	−0.06
$\nu_3 + 2\nu_4 + \nu_6$	5325.6	5317.75	7.85	5324.51	1.09
$4\nu_6$	5389.4	5380.89	8.51	5386.16	3.24
$2\nu_1$	5462.7	5460.57	2.13	5462.94	−0.24
$\nu_2 + \nu_3 + 2\nu_4$	5546.5	5541.02	5.48	5545.43	1.07
$\nu_2 + \nu_3 + 2\nu_4$	5551.3	5549.22	2.08	5553.13	−1.83
$\nu_1 + \nu_5$	5651.1904[d]	5650.38	0.81	5651.38	−0.19
$\nu_2 + 3\nu_6$	5687.9	5683.16	4.74	5688.20	−0.30
$\nu_1 + \nu_3 + \nu_6$	5729.2	5728.12	1.08	5729.86	−0.66
$2\nu_2 + \nu_3 + \nu_6$	5809.5	5805.36	4.14	5810.02	−0.52
$2\nu_3 + 2\nu_6$	5986.2	5980.71	5.49	5984.48	1.72
$\nu_3 + 4\nu_4$	6123.6	6119.36	4.24	6123.36	0.24
$\nu_1 + 2\nu_2$	6254.7	6255.18	−0.48	6253.93	0.77
$2\nu_4 + 3\nu_6$	6263.1	6259.19	3.91	6262.05	1.05
$4\nu_3 + \nu_6$	6373.4	6358.21	15.19	6372.06	1.34
$2\nu_4 + \nu_5 + \nu_6$	6401.2	6395.34	5.86	6399.83	1.37
$2\nu_2 + \nu_3 + \nu_6$	6447.6	6439.16	8.44	6445.83	1.77
$\nu_2 + 2\nu_3 + 2\nu_6$	6553.1	6541.30	11.80	6550.09	3.01
$\nu_1 + \nu_3 + 2\nu_4$	6562.7	6561.96	0.74	6565.39	−2.69
$\nu_2 + \nu_3 + 2\nu_4 + \nu_6$	6578.8	6571.98	6.82	6575.74	3.06
$2\nu_5 + \nu_6$	6635.7	6627.72	7.98	6633.85	1.85
$3\nu_2 + \nu_3$	6652.2	6657.86	−5.66	6655.34	−3.14
$2\nu_5 + \nu_6$	6777.6	6765.10	12.50	6772.28	5.32
$2\nu_3 + 2\nu_4 + \nu_6$	6815.2	6809.97	5.23	6816.11	−0.91
$\nu_1 + \nu_2 + 2\nu_4$	6825.5	6823.02	2.48	6823.88	1.62
$6\nu_4$	6910.7	6903.45	7.25	6910.15	0.55
$2\nu_1 + \nu_3$	6921.3	6914.03	7.27	6919.35	1.95
$\nu_2 + 2\nu_3 + \nu_5$	7137.4	7141.02	−3.62	7140.25	−2.85

[a]Ref. 30; [b]Ref. 31; [c]Ref. 33; [d]Ref. 34.

TABLE IV: Residuals (Obs.−Calc.; in cm^{-1}) for selected $J = 0$, $\Gamma = A_2$ energy levels of H_2CO, computed with TROVE from the *ab initio* AVQZ (A) and refined H2CO-2010 (R) PESs. The 'observed' values are from Ref. 24 unless indicated.

State	Obs.	Calc. (A)	Obs.-(A)	Calc.(R)	Obs.-(R)
$\nu_4+\nu_6$	2422.9701[a]	2418.44	4.53	2422.69	0.28
$2\nu_3+\nu_4$	3886.5	3883.42	3.08	3886.47	0.03
$\nu_4+\nu_5$	3996.5180[b]	3994.78	1.74	3996.54	−0.03
$\nu_2+\nu_4+\nu_6$	4163.2890[c]	4159.50	3.79	4164.12	−0.83
$3\nu_4+\nu_6$	4741.9	4736.27	5.63	4742.10	−0.20
$3\nu_3+\nu_4$	5353.2	5354.86	−1.66	5356.66	−3.46
$\nu_2+2\nu_3+\nu_4$	5625.5	5622.27	3.23	5624.72	0.78
$\nu_2+\nu_4+\nu_5$	5717.7	5715.79	1.91	5718.18	−0.48
$2\nu_2+\nu_4+\nu_6$	5887.5	5884.78	2.72	5888.43	−0.93
$2\nu_3+3\nu_4$	6189.1	6184.65	4.45	6190.55	−1.45
$3\nu_4+\nu_5$	6281.9	6279.20	2.70	6281.68	0.22
$\nu_2+3\nu_4+\nu_6$	6465.2	6459.86	5.34	6464.58	0.62
$\nu_3+\nu_4+\nu_5+\nu_6$	6492.1	6488.38	3.72	6491.50	0.60
$5\nu_4+\nu_6$	7030.7	7027.34	3.36	7032.38	−1.68
$\nu_2+3\nu_3+\nu_4$	7088.6	7091.58	−2.98	7094.70	−6.10

[a]Ref. 31; [b]Ref. 32; [c]Ref. 33.

order to generate the final symmetrized basis functions $\Psi^{\Gamma}_{J,K,\gamma}$. In terms of the quantum number $\tau_{\rm rot}$ (= 0 or 1), the rotational parity is defined as $(-1)^{\tau_{\rm rot}}$,[41] and $K = |k|$ with k and m (where $-J \le k, m \le J$) specifying the projections, in units of $\hbar$, of the rotational angular momentum onto the molecule-fixed z axis and the space-fixed Z-axis, respectively.[41] In this so-called (J=0)-contracted basis set[47] of products $\Psi^{\Gamma}_{J=0,\gamma}\,|J,K,m,\tau_{\rm rot}\rangle$, the vibrational part $\hat{H}_{\rm vib}$ of the total Hamiltonian is diagonal with diagonal matrix elements given by eigenvalues $E^{\rm vib}_{\gamma}$.

In TROVE calculations, the size of the basis set, and therefore the size of the Hamiltonian matrix blocks, can be controlled by the polyad number P, which in the present case is given by

$$P = 2(n_1 + n_2 + n_3) + n_4 + n_5 + n_6, \tag{13}$$

where the local-mode quantum numbers n_i are defined in connection with the primitive basis functions ϕ_{n_i}. Hence, we can choose a maximum value $P_{\rm max}$ of the polyad quantum number and then include in the primitive basis set only those combinations of ϕ_{n_i} for which $P \le P_{\rm max}$. In the present work we use $P_{\rm max} = 14$. The largest rotation-vibration matrix blocks that had to be diagonalized for H_2CO ($J = 5$) had dimensions of about 21 000. Routines from the LAPACK and ARPACK[48] libraries were employed for the diagonalizations.

TABLE V: Residuals (Obs.−Calc.; in cm^{-1}) for selected $J = 0$, $\Gamma = B_1$ energy levels of H_2CO, computed with TROVE from the *ab initio* AVQZ (A) and refined H2CO-2010 (R) PESs. The 'observed' values are from Ref. 24 unless indicated.

State	Obs.	Calc. (A)	Obs.-(A)	Calc.(R)	Obs.-(R)
ν_4	1167.2563[a]	1166.10	1.16	1167.30	−0.05
$\nu_3+\nu_4$	2667.0481[b]	2664.66	2.39	2667.03	0.02
$\nu_2+\nu_4$	2905.9685[b]	2903.41	2.56	2905.97	−0.01
$3\nu_4$	3480.7	3478.06	2.64	3481.03	−0.33
$\nu_3+\nu_4+\nu_6$	3673.5	3668.92	4.58	3675.07	−1.57
$\nu_1+\nu_4$	3941.5295[c]	3939.88	1.65	3941.52	0.01
$\nu_2+\nu_3+\nu_4$	4397.5	4394.30	3.20	4397.14	0.36
$2\nu_2+\nu_4$	4624.3	4621.21	3.09	4623.37	0.93
$\nu_3+3\nu_4$	4977.1	4973.84	3.26	4977.71	−0.61
$\nu_4+3\nu_6$	5104.0	5104.22	−0.22	5106.65	−2.65
$\nu_2+3\nu_4$	5205.2	5201.08	4.12	5205.09	0.11
$\nu_4+\nu_5+\nu_6$	5244.1	5242.10	2.00	5245.34	−1.24
$\nu_2+\nu_3+\nu_4+\nu_6$	5417.6	5413.30	4.30	5417.35	0.25
$\nu_1+\nu_2+\nu_4$	5680.0	5679.10	0.90	5681.15	−1.15
$5\nu_4$	5771.0	5766.87	4.13	5771.29	−0.29
$\nu_3+3\nu_4+\nu_6$	5996.0	5992.61	3.39	5997.11	−1.11
$2\nu_2+\nu_3+\nu_4$	6106.2	6105.77	0.43	6106.04	0.16
$\nu_1+3\nu_4$	6235.2	6233.39	1.81	6235.44	−0.24
$3\nu_2+\nu_4$	6321.7	6322.30	−0.60	6322.30	−0.60
$2\nu_3+\nu_4+\nu_5$	6553.3	6548.69	4.61	6549.82	3.48
$2\nu_1+\nu_4$	6611.6	6609.65	1.95	6611.27	0.33
$\nu_2+\nu_3+3\nu_4$	6693.4	6689.57	3.83	6693.34	0.06
$\nu_1+\nu_4+\nu_5$	6710.0	6705.04	4.96	6708.68	1.32
$\nu_1+\nu_4+\nu_5$	6795.1	6794.27	0.83	6794.14	0.96
$\nu_2+\nu_4+3\nu_6$	6849.7	6846.65	3.05	6848.88	0.82
$\nu_1+\nu_3+\nu_4+\nu_6$	6894.6	6886.94	7.66	6892.96	1.64
$2\nu_2+\nu_3+\nu_4+\nu_6$	6964.1	6962.61	1.49	6965.32	−1.22

[a]Ref. 30; [b]Ref. 31; [c]Ref. 32.

The TROVE program automatically labels the eigenvalues and eigenvectors with quantum numbers, based on an analysis of which basis functions contribute most to the corresponding eigenfunctions. As explained above, the basis functions are in turn associated with the quantum numbers $K, \tau_{\rm rot}$, $\Gamma_{\rm vib}$, n_1, n_2, n_3, n_4, n_5, and n_6. Here n_1, n_2, n_3 are stretching local mode quantum numbers,[49] describing the C-O, C-H_1, and C-H_2 modes, respectively, n_4 and n_5 represent the two bending modes, and n_6 is the out-of-plane bending quantum number. These quantum numbers can be straightforwardly mapped onto the normal mode quantum numbers v_1, v_2, v_3, v_4, v_5, and v_6 conventionally used in most spectroscopic studies. In the normal mode notation, the H_2CO vibrational states are labelled as $v_1\nu_1 + v_2\nu_2 + v_3\nu_3 + v_4\nu_4 + v_5\nu_5 + v_6\nu_6$. The normal modes are defined as follows. A_1

TABLE VI: Residuals (Obs.−Calc.; in cm^{-1}) for selected $J = 0$, $\Gamma = B_2$ energy levels of H_2CO, computed with TROVE from the *ab initio* AVQZ (A) and refined H2CO-2010 (R) PESs. The 'observed' values are from Ref. 24 unless indicated.

State	Obs.	Calc. (A)	Obs.-(A)	Calc.(R)	Obs.-(R)
ν_6	1249.0948[a]	1245.61	3.49	1249.07	0.03
$2\nu_3$	2719.1550[b]	2715.26	3.89	2719.15	0.01
ν_5	2843.3256[b]	2842.40	0.93	2843.31	0.01
$\nu_2 + \nu_6$	3000.0659[b]	2996.01	4.05	3000.08	−0.01
$2\nu_4 + \nu_6$	3586.6	3581.12	5.48	3586.55	0.05
$\nu_1 + \nu_6$	4021.0807[c]	4017.76	3.32	4021.26	−0.18
$3\nu_3$	4192.3816[c]	4189.71	2.67	4192.62	−0.24
$\nu_3 + \nu_5$	4335.0971[c]	4334.88	0.22	4334.97	0.13
$\nu_2 + 2\nu_3$	4466.8	4462.77	4.03	4466.04	0.76
$\nu_2 + \nu_5$	4571.6947[c]	4568.81	2.89	4571.31	0.39
$2\nu_2 + \nu_6$	4734.2078[c]	4730.45	3.76	4734.27	−0.07
$2\nu_3 + 2\nu_4$	5043.7	5038.33	5.37	5042.49	1.21
$2\nu_4 + \nu_5$	5140.1	5137.31	2.79	5141.13	−1.03
$4\nu_3$	5151.0	5146.24	4.76	5154.61	−3.61
$\nu_2 + 2\nu_4 + \nu_6$	5312.2	5306.43	5.77	5313.16	−0.96
$\nu_2 + 2\nu_4 + \nu_6$	5321.3	5319.30	2.00	5324.12	−2.82
$2\nu_5$	5433.4	5429.53	3.87	5433.41	−0.01
$\nu_2 + \nu_3 + 2\nu_6$	5489.0	5482.42	6.58	5490.40	−1.40
$2\nu_5$	5530.5	5528.78	1.72	5532.12	−1.62
$\nu_1 + \nu_2 + \nu_6$	5768.8	5762.21	6.59	5767.72	1.08
$4\nu_4 + \nu_6$	5891.8	5884.81	6.99	5890.37	1.43
$\nu_2 + \nu_3 + \nu_5$	6051.7	6052.30	−0.60	6053.30	−1.60
$2\nu_2 + 2\nu_3$	6194.8	6194.65	0.15	6195.37	−0.57
$2\nu_2 + \nu_5$	6276.4	6274.25	2.15	6276.02	0.38
$\nu_1 + 2\nu_4 + \nu_6$	6346.2	6335.70	10.50	6346.55	−0.35
$3\nu_3 + 2\nu_4$	6508.8	6505.94	2.86	6509.15	−0.35
$\nu_5 + 3\nu_6$	6582.3	6577.82	4.48	6586.45	−4.15
$2\nu_1 + \nu_6$	6683.7	6681.75	1.95	6686.22	−2.52
$\nu_1 + \nu_5 + \nu_6$	6759.0	6756.45	2.55	6761.01	−2.01
$\nu_2 + 2\nu_4 + \nu_5$	6856.3	6853.77	2.53	6857.17	−0.87
$\nu_3 + 2\nu_5$	6864.3	6864.02	0.28	6865.22	−0.92
$\nu_2 + 4\nu_3$	6909.0	6902.11	6.89	6909.20	−0.20

[a]Ref. 30; [b]Ref. 31; [c]Ref. 33.

symmetry: ν_1 is the symmetric C-H stretching mode ($E_{\nu_1} = 2782.46$ cm^{-1}), ν_2 is the C-O stretching mode ($E_{\nu_2} = 1746.01$ cm^{-1}), ν_3 is the symmetric O-C-H bending mode ($E_{\nu_3} = 1500.18$ cm^{-1}); B_1 symmetry: ν_4 is the out-of-plane bending mode associated with the coordinate τ ($E_{\nu_4} = 1167.26$ cm^{-1}); B_2 symmetry: ν_5 is the asymmetric C-H stretching C-H mode ($E_{\nu_5} = 2843.30$ cm^{-1}), and ν_6 is the asymmetric bending O-C-H mode ($E_{\nu_6} = 1249.09$ cm^{-1}). The values given above in parentheses are the experimental fundamental term values from Refs. 31,35. The quantum numbers v_1, v_2, v_3, v_4, v_5, and v_6 count the excitations of the corresponding modes.

IV. THE REFINED POTENTIAL ENERGY SURFACE

We have extended the program TROVE to allow for the direct fitting of the potential energy surface to experimental ro-vibrational term values. Details of the procedure are given in Ref. 9. The basic idea is to describe the refinement in terms of a correction ΔV to the initial *ab initio* PES V. That is, the refined PES V' can be written as $V' = V + \Delta V$, and now the eigenfunctions of the initial Hamiltonian H are used as basis functions for the diagonalization of the extended Hamiltonian $H' = H + \Delta V$. In this basis set, the only off-diagonal Hamiltonian term is ΔV, which we expand in analogy to Eq. (1), that is, by the expansion of the form already used for V. The corresponding expansion coefficients Δf_{ijklmn} are obtained by least-squares fitting starting from $\Delta V = 0$.

In the PES fittings, we use as input data 'experimental' energies derived from the corresponding experimental transition wavenumbers or frequencies. In order to determine from experimental wavenumber data, for example, the upper state energy of an absorption transition for inclusion in our PES-fitting input data set, we must know the assignment of the transition and the energy of the lower state. The accuracy of the determined upper state energy will reflect both the accuracy of the experimental wavenumber and that of the lower state energy. Correct assignments of the experimentally observed transitions are required in order that we can identify the upper and lower state energies involved in a given observed transition and correlate each experimentally derived energy with a calculated energy. In the present work on H_2CO it was straightforward to correlate the theoretically calculated and the experimentally derived energies because, as mentioned above, using the initial *ab initio* PES AVQZ we obtained theoretical energies in very good agreement with the experimentally derived ones. That is, the pattern of ro-vibrational energies obtained in the initial theoretical calculation could immediately be identified with the pattern of experimentally derived energies. All we had to do was to verify that each ro-vibrational level was assigned experimentally as belonging to a state with values of the good quantum numbers J and Γ (where Γ is the ro-vibrational symmetry in the MS group) that match the values for the correlating theoretically calculated level.

We include in the input data set for the PES fitting all experimentally known term values of H_2CO with $J \leq 5$. Table VII gives various statistical information about the selected input data. We outline briefly the sources of these data. The current (2008) version of

TABLE VII: Number N of experimentally determined energy levels of H_2CO included in the input data set for the PES fitting.[a]

J	N	rms (cm^{-1})	Refs.	Comment
0	18	0.073	29,30,32	
1	45	0.018	29,30,32	
2	75	0.017	29,30,32	
3	94	0.024	29,30,32	Not used in fittings
4	118	0.040	29,30,32	Not used in fittings
5	142	0.055	29,30,32	A_1, B_2 not used in fittings
total	492	0.040		Excluding band centers from Refs. 24,31,33,34
0	107	1.653	24,31,33,34	Below 7 500 cm^{-1}

[a]For each set of energy levels we give the angular momentum quantum number J, the rms error attained in the fitting of the H2CO-2010 PES (see below), and the references to the experimental data.

the HITRAN database contains experimentally derived energies for H_2CO in three regions: the pure rotational term values, the term values of the ν_2 state around 1740 cm^{-1}, and the term values for the states ν_1, $\nu_2+\nu_4$, $2\nu_3$, $\nu_2+\nu_6$, $\nu_3+\nu_6$, $\nu_3+\nu_4$, ν_5, and $2\nu_6$ between 2 600 cm^{-1} and 3 000 cm^{-1}. It is known that the H_2CO data in HITRAN are far from being complete and so we decided not to use HITRAN data as input for our PES fitting. Instead, we have explored other, more up-to-data sources of experimental information. Recently, Tchana *et al.*[30] reported an experimental line list for the ν_2, ν_3, ν_4, and ν_6 transitions of formaldehyde. Perrin *et al.*[29] published a very accurate synthetic line list covering the band systems $(\nu_2, \nu_3, \nu_4, \nu_6)$ and $(\nu_1,\ \nu_2+\nu_3,\ \nu_2+\nu_4,\ \nu_2+\nu_6,\ 2\nu_3,\ \nu_3+\nu_4,\ \nu_3+\nu_6,\ 2\nu_4,\ \nu_4+\nu_6,\ \nu_5,\ 2\nu_6)$ in the 5.7 μm and 3.6 μm regions, respectively. Perez *et al.*[32] measured a set of hot transitions belonging to the bands $\nu_4-\nu_4$, $\nu_1+\nu_4-\nu_4$, and $\nu_4+\nu_5-\nu_4$. These transitions involve states not present in the line compilations of Tchana *et al.*[30] and Perrin *et al.*[29] For our input data set we selected 492 energy levels with $J \leq 5$ from Refs. 29,30,32. In the fitting, we assigned weights of $w_i = 100.0$ to the purely rotational energy levels and $w_i = 1.0$ to levels in excited vibrational states. We chose higher weights for the rotational energies in order to ensure an accurate determination of the equilibrium structure, since accurate structural parameter values are important for the reliable prediction of ro-vibrational term values at high J values.

Energies of vibrationally excited states are important for the determination of the PES since increasing vibrational excitation causes increasing vibrational amplitudes. Consequently, when the input data set for the fitting involves highly excited vibrational states, the high-energy part of the PES is sampled by the corresponding data. For this reason, we included in the input data set the vibrational band centers of H_2CO from the dispersed fluorescence study by Bouwens *et al.*[24] in spite of their relatively low accuracy (standard deviation of 1.7 cm^{-1}). We selected the term values below 7 500 cm^{-1} and weighted them by 0.1. Some of the 3.5 μm-region band centers of Ref. 24 corresponding to the states (ν_1, $\nu_2 + \nu_3$, $\nu_2 + \nu_4$, $\nu_2 + \nu_6$, $2\nu_3$, $\nu_3 + \nu_4$, $\nu_3 + \nu_6$, $2\nu_4$, $\nu_4 + \nu_6$, ν_5, and $2\nu_6$) were recently re-determined at a higher accuracy by Perrin *et al.*[31] Similar improvements were made by Flaud *et al.*[33] for the ($\nu_1+\nu_2$, $\nu_1+\nu_6$, $3\nu_2$, $\nu_2+\nu_5$, $2\nu_2+\nu_6$, $\nu_2+\nu_4+\nu_6$, $\nu_3+\nu_5$, and $2\nu_3+\nu_6$) states in the 1.9 – 2.56 μm region. In addition, the $2\nu_5$ band was re-investigated by Saha *et al.*[34] These recent band center values[31,33,34] were used in place of the corresponding $J = 0$ energies from Ref. 24.

In total, our input data set comprised 599 energies. For the actual refinement, we used only 319 energies with $J = 0, 1, 2$ (all symmetries) and $J = 5$ (A_2 and B_1 symmetry) in order to speed up the fitting procedure. The comparison of theoretical and experimental energies with ensuing statistical analysis was carried out for all 599 experimental energies.

In the refinement, we constrain the fitted PES to follow roughly the shape of the initial AVQZ PES of H_2CO. This is achieved by simultaneously fitting the f_{ijklmn} parameters to the *ab initio* points V_i and to the experimental energy levels.[50] The simultaneous fitting has a dual purpose: firstly, it ensures that the PES retain a physically acceptable shape and secondly, it allows all potential parameters to be varied irrespective of the amount of the experimental data available for particular vibrational excitations.[50] The refined parameter values characterizing the new 'spectroscopic' PES of H_2CO (which we refer to as H2CO-2010) are given in the supplementary material to the present paper,[43] together with a Fortran 90 routine that generates values of the potential energy function. It should be noted that we do not vary the structural parameters a_i^{ref} in our fitting procedure. Instead, the equilibrium geometry is adjusted by varying the linear expansion constants f_{10000}, f_{01000} ($= f_{00100}$), and f_{00100} ($= f_{00010}$), which are zero in the case of the *ab initio* PES. The PES refinement thus results in a new semi-empirical equilibrium structure with $r_{\mathrm{CO}}^{\mathrm{e}}$ =1.20367 Å, $r_{\mathrm{CH}}^{\mathrm{e}}$ =1.10290 Å, and $\theta^{\mathrm{e}} = 121.781°$. These values are very similar to the *ab initio* AVQZ

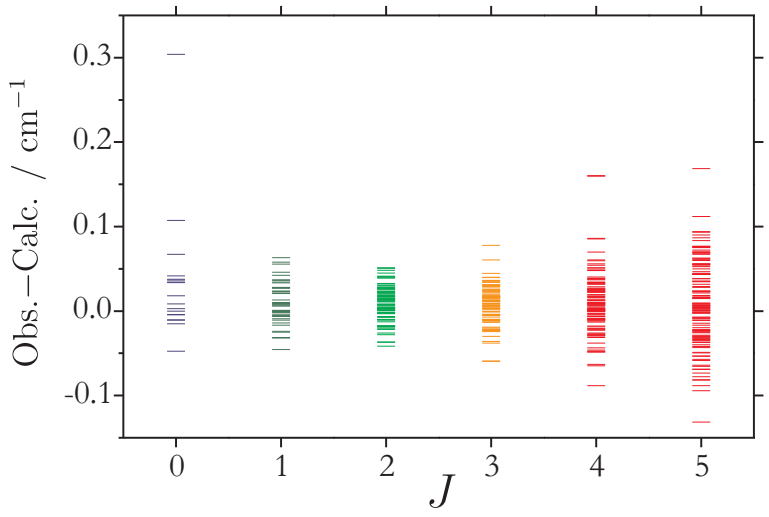

FIG. 2: Residuals (Obs.−Calc.) for the $J \geq 0$ term values of H_2CO, obtained with TROVE and the refined PES H2CO-2010 (see text). The residuals associated with the vibrational band centers from Refs. 24,31,33,34 are excluded.

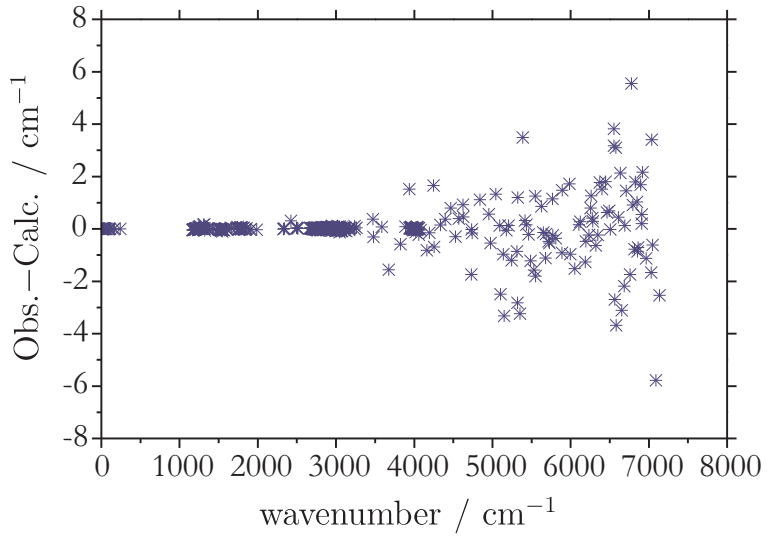

FIG. 3: Residuals (Obs.−Calc.) for the $J = 0$ term values of H_2CO, obtained with TROVE and the refined PES PES H2CO-2010 (see text).

equilibrium parameters (see Table I).

TABLE VIII: Residuals (Obs.−Calc.; in cm^{-1}) for pure rotational term values with $J \leq 5$, computed with TROVE from the *ab initio* AVQZ (A) and refined H2CO-2010 (R) PESs. The corresponding rms errors are 0.094 cm^{-1} and 0.004 cm^{-1}, respectively. The 'observed' ground state energy levels are from Ref. 30 obtained there using the spectroscopic parameters from Ref. 51.

J	K_a	K_b	τ	Γ	Obs.	Calc.(A)	Obs.-Calc.(A)	Calc.(R)	Obs.-Calc.(R)
0	0	0	0	A_1	0.0000	0.0000	0.0000	0.0000	0.0000
1	0	1	1	A_2	2.4296	2.4182	0.0114	2.4291	0.0005
1	1	1	0	B_1	10.5390	10.5316	0.0074	10.5396	−0.0006
1	1	0	1	B_2	10.7001	10.6916	0.0085	10.7009	−0.0008
2	0	2	0	A_1	7.2864	7.2523	0.0341	7.2848	0.0016
2	2	2	0	A_1	40.0428	40.0219	0.0209	40.0454	−0.0026
2	2	1	1	A_2	40.0404	40.0195	0.0209	40.0430	−0.0026
2	1	2	0	B_1	15.7202	15.6878	0.0324	15.7202	0.0000
2	1	2	1	B_2	15.2369	15.2078	0.0291	15.2361	0.0008
3	2	3	0	A_1	47.3278	47.2730	0.0548	47.3289	−0.0011
3	0	3	1	A_2	14.5655	14.4975	0.0680	14.5623	0.0032
3	2	1	1	A_2	47.3397	47.2847	0.0550	47.3408	−0.0011
3	1	3	0	B_1	22.2822	22.2206	0.0616	22.2794	0.0028
3	3	3	0	B_1	88.2382	88.2004	0.0378	88.2434	−0.0052
3	1	2	1	B_2	23.2487	23.1805	0.0682	23.2474	0.0013
3	3	0	1	B_2	88.2382	88.2005	0.0377	88.2434	−0.0052
4	0	4	0	A_1	24.2597	24.1465	0.1132	24.2542	0.0055
4	2	4	0	A_1	57.0780	56.9773	0.1007	57.0771	0.0009
4	4	4	0	A_1	155.1694	155.1105	0.0589	155.1752	−0.0058
4	2	3	1	A_2	57.0425	56.9422	0.1003	57.0414	0.0011
4	4	1	1	A_2	155.1694	155.1105	0.0589	155.1752	−0.0058
4	1	4	0	B_1	33.2835	33.1678	0.1157	33.2807	0.0028
4	3	4	0	B_1	97.9578	97.8745	0.0833	97.9608	−0.0030
4	1	4	1	B_2	31.6729	31.5682	0.1047	31.6674	0.0055
4	3	2	1	B_2	97.9577	97.8743	0.0834	97.9606	−0.0029
5	2	5	0	A_1	69.1825	69.0254	0.1571	69.1787	0.0038
5	4	5	0	A_1	167.3247	167.1988	0.1259	167.3177	0.0070
5	0	5	1	A_2	36.3592	36.1899	0.1693	36.3510	0.0082
5	2	3	1	A_2	69.2653	69.1071	0.1582	69.2618	0.0035
5	4	1	1	A_2	167.3247	167.1988	0.1259	167.3177	0.0070
5	1	5	0	B_1	43.4067	43.2480	0.1587	43.3978	0.0089
5	3	5	0	B_1	110.1086	109.9683	0.1403	110.1088	−0.0002
5	5	5	0	B_1	240.7771	240.6934	0.0837	240.7792	−0.0021
5	1	4	1	B_2	45.8219	45.6468	0.1751	45.8171	0.0048
5	3	2	1	B_2	110.1104	109.9689	0.1415	110.1095	0.0010
5	5	0	1	B_2	240.7771	240.6934	0.0837	240.7792	−0.0021

TABLE IX: Residuals (Obs.−Calc.; in cm^{-1}) for selected $J = 2$ ($\Gamma = A_1, A_2$) and $J = 4$ (A_1) energy levels of H_2CO, computed with TROVE from the refined H2CO-2010 PES. See the supplementary material for a complete list.[43] The 'observed' energy levels are from Refs. 29,30,32.

J	Γ	K	State	Obs.	Calc.	Obs.-Calc.	J	Γ	K	State	Obs.	Calc.	Obs.-Calc.
2	A_1	0	g.s.	7.286	7.285	0.002	4	A_1	0		24.260	24.254	0.005
2	A_1	2	g.s.	40.043	40.045	−0.003	4	A_1	2		57.078	57.077	0.001
2	A_1	1	ν_4	1181.584	1181.612	−0.028	4	A_1	4		155.169	155.175	−0.006
2	A_1	1	ν_6	1265.614	1265.594	0.020	4	A_1	1	ν_4	1198.999	1199.010	−0.012
2	A_1	0	ν_3	1507.483	1507.508	−0.025	4	A_1	3	ν_4	1254.369	1254.290	0.079
2	A_1	2	ν_3	1540.469	1540.475	−0.006	4	A_1	1	ν_6	1282.007	1281.991	0.016
2	A_1	0	ν_2	1753.247	1753.250	−0.003	4	A_1	3	ν_6	1357.492	1357.496	−0.004
2	A_1	2	ν_2	1786.013	1786.033	−0.019	4	A_1	0	ν_3	1524.504	1524.557	−0.054
2	A_1	0	$\nu_3 + \nu_6$	2501.618	2501.608	0.010	4	A_1	2	ν_3	1557.564	1557.603	−0.038
2	A_1	1	$\nu_3 + \nu_4$	2680.851	2680.853	−0.002	4	A_1	4	ν_3	1656.329	1656.303	0.026
2	A_1	1	$2\nu_3$	2736.240	2736.234	0.006	4	A_1	0	ν_2	1770.105	1770.078	0.027
2	A_1	0	ν_1	2789.742	2789.747	−0.006	4	A_1	2	ν_2	1802.935	1802.921	0.013
2	A_1	2	ν_1	2821.865	2821.861	0.004	4	A_1	4	ν_2	1901.055	1901.085	−0.030
2	A_1	1	ν_5	2858.367	2858.359	0.008	4	A_1	1	$\nu_3 + \nu_4$	2698.307	2698.323	−0.017
2	A_1	1	$\nu_2 + \nu_4$	2920.755	2920.749	0.006	4	A_1	3	$\nu_3 + \nu_4$	2751.225	2751.272	−0.047
2	A_1	0	$\nu_3 + \nu_6$	3006.318	3006.303	0.016	4	A_1	1	$2\nu_3$	2752.706	2752.720	−0.014
2	A_1	1	$\nu_2 + \nu_6$	3016.219	3016.227	−0.008	4	A_1	0	ν_1	2806.711	2806.717	−0.006
2	A_1	2	$\nu_3 + \nu_6$	3039.511	3039.492	0.019	4	A_1	3	$2\nu_3$	2830.592	2830.562	0.030
2	A_1	1	$\nu_1 + \nu_4$	3955.706	3955.712	−0.007	4	A_1	2	ν_1	2838.930	2838.957	−0.027
2	A_1	2	$\nu_4 + \nu_5$	4030.369	4030.410	−0.041	4	A_1	1	ν_5	2874.756	2874.731	0.025
2	A_2	2	g.s.	40.040	40.043	−0.003	4	A_1	4	ν_1	2935.100	2935.056	0.044
2	A_2	1	ν_4	1181.160	1181.190	−0.030	4	A_1	1	$\nu_2 + \nu_4$	2938.072	2938.003	0.068
2	A_2	1	ν_6	1266.111	1266.093	0.019	4	A_1	3	ν_5	2939.626	2939.687	−0.061
2	A_2	2	ν_3	1540.466	1540.472	−0.007	4	A_1	3	$\nu_2 + \nu_4$	2996.977	2996.972	0.005
2	A_2	2	ν_2	1786.012	1786.030	−0.019	4	A_1	0	$\nu_3 + \nu_6$	3023.382	3023.431	−0.048
2	A_2	1	$\nu_3 + \nu_4$	2680.424	2680.423	0.001	4	A_1	1	$\nu_2 + \nu_6$	3032.507	3032.496	0.011
2	A_2	1	$2\nu_3$	2736.757	2736.764	−0.007	4	A_1	2	$\nu_3 + \nu_6$	3056.667	3056.721	−0.053
2	A_2	2	ν_1	2821.867	2821.858	0.009	4	A_1	3	$\nu_2 + \nu_6$	3106.050	3106.043	0.008
2	A_2	1	ν_5	2858.856	2858.847	0.009	4	A_1	4	$\nu_3 + \nu_6$	3156.042	3156.063	−0.021
2	A_2	1	$\nu_2 + \nu_4$	2920.322	2920.327	−0.005	4	A_1	1	$\nu_1 + \nu_4$	3973.122	3973.134	−0.012
2	A_2	1	$\nu_2 + \nu_6$	3016.724	3016.721	0.003	4	A_1	2	$\nu_4 + \nu_5$	4047.248	4047.252	−0.003
2	A_2	2	$\nu_3 + \nu_6$	3039.511	3039.489	0.022							
2	A_2	1	$\nu_1 + \nu_4$	3955.272	3955.275	−0.003							
2	A_2	0	$\nu_4 + \nu_5$	4003.754	4003.765	−0.011							
2	A_2	2	$\nu_4 + \nu_5$	4030.371	4030.413	−0.042							

TABLE X: Residuals (Obs.−Calc.; in cm^{-1}) for selected $J = 5$ energy levels of H_2CO, computed with TROVE from the refined H2CO-2010 PES. See the supplementary material for a complete list.[43] The 'observed' energy levels are from Refs. 29,30,32.

J	Γ	K	State	Obs.	Calc.	Obs.-Calc.	J	Γ	K	State	Obs.	Calc.	Obs.-Calc.
5	A_1	2	g.s.	69.182	69.179	0.004	5	B_1	1		43.407	43.398	0.009
5	A_1	4	g.s.	167.325	167.318	0.007	5	B_1	3		110.109	110.109	0.000
5	A_1	1	ν_4	1209.313	1209.325	−0.012	5	B_1	5		240.777	240.779	−0.002
5	A_1	3	ν_4	1266.466	1266.379	0.087	5	B_1	2	ν_4	1231.188	1231.157	0.032
5	A_1	1	ν_6	1296.198	1296.190	0.007	5	B_1	0	ν_6	1285.408	1285.392	0.015
5	A_1	3	ν_6	1369.614	1369.620	−0.007	5	B_1	4	ν_4	1316.675	1316.516	0.158
5	A_1	5	ν_6	1514.745	1514.723	0.022	5	B_1	2	ν_6	1323.189	1323.264	−0.075
5	A_1	2	ν_3	1569.702	1569.760	−0.058	5	B_1	4	ν_6	1433.619	1433.621	−0.002
5	A_1	4	ν_3	1668.521	1668.517	0.004	5	B_1	1	ν_3	1543.659	1543.700	−0.042
5	A_1	2	ν_2	1814.957	1814.922	0.035	5	B_1	3	ν_3	1610.920	1610.954	−0.034
5	A_1	4	ν_2	1913.119	1913.125	−0.006	5	B_1	5	ν_3	1742.477	1742.420	0.058
5	A_1	1	$\nu_3 + \nu_4$	2708.628	2708.642	−0.015	5	B_1	1	ν_2	1789.164	1789.137	0.027
5	A_1	3	$\nu_3 + \nu_4$	2763.354	2763.413	−0.059	5	B_1	3	ν_2	1855.896	1855.879	0.017
5	A_1	1	$2\nu_3$	2767.034	2767.125	−0.091	5	B_1	5	ν_2	1986.603	1986.634	−0.031
5	A_1	3	$2\nu_3$	2842.751	2842.720	0.031	5	B_1	2	$\nu_3 + \nu_4$	2729.309	2729.351	−0.042
5	A_1	2	ν_1	2851.050	2851.099	−0.049	5	B_1	0	$2\nu_3$	2755.631	2755.695	−0.064
5	A_1	5	$\nu_3 + \nu_4$	2877.620	2877.678	−0.058	5	B_1	5	$\nu_3 + \nu_6$	2791.651	2791.631	0.020
5	A_1	1	ν_5	2888.900	2888.856	0.044	5	B_1	2	$2\nu_3$	2795.228	2795.261	−0.033
5	A_1	4	ν_1	2947.231	2947.178	0.053	5	B_1	4	$\nu_3 + \nu_4$	2812.663	2812.730	−0.068
5	A_1	1	$\nu_2 + \nu_4$	2948.280	2948.219	0.061	5	B_1	1	ν_1	2825.676	2825.668	0.008
5	A_1	3	ν_5	2951.745	2951.792	−0.047	5	B_1	0	ν_5	2879.596	2879.543	0.053
5	A_1	5	$2\nu_3$	2989.064	2989.131	−0.067	5	B_1	3	ν_1	2891.108	2891.052	0.056
5	A_1	3	$\nu_2 + \nu_4$	3009.004	3008.964	0.040	5	B_1	4	$2\nu_3$	2907.673	2907.733	−0.060
5	A_1	1	$\nu_2 + \nu_6$	3046.646	3046.577	0.068	5	B_1	2	ν_5	2911.800	2911.796	0.004
5	A_1	2	$\nu_3 + \nu_6$	3068.840	3068.937	−0.097	5	B_1	2	$\nu_2 + \nu_4$	2971.601	2971.530	0.070
5	A_1	5	ν_5	3079.477	3079.581	−0.104	5	B_1	4	ν_5	3007.671	3007.762	−0.091
5	A_1	3	$\nu_2 + \nu_6$	3118.100	3118.071	0.029	5	B_1	5	ν_1	3019.289	3019.216	0.073
5	A_1	5	$\nu_2 + \nu_4$	3130.633	3130.731	−0.098	5	B_1	0	$\nu_2 + \nu_6$	3036.146	3036.091	0.055
5	A_1	4	$\nu_3 + \nu_6$	3168.285	3168.354	−0.069	5	B_1	1	$\nu_3 + \nu_6$	3042.557	3042.608	−0.050
5	A_1	5	$\nu_2 + \nu_6$	3260.950	3260.922	0.028	5	B_1	4	$\nu_2 + \nu_4$	3061.890	3061.903	−0.013
5	A_1	0	$\nu_4 + \nu_5$	4032.623	4032.585	0.038	5	B_1	2	$\nu_2 + \nu_6$	3072.862	3072.821	0.040
5	A_1	3	$\nu_1 + \nu_4$	4038.166	4038.128	0.038	5	B_1	3	$\nu_3 + \nu_6$	3110.325	3110.412	−0.087
5	A_1	2	$\nu_4 + \nu_5$	4059.382	4059.365	0.017	5	B_1	4	$\nu_2 + \nu_6$	3180.935	3180.912	0.023

TABLE XI: (Continued) Residuals (Obs.−Calc.; in cm^{-1}) for selected $J = 5$ energy levels of H_2CO, computed with TROVE from the refined H2CO-2010 PES. See the supplementary material for a complete list.[43] The 'observed' energy levels are from Refs. 29,30,32.

J	Γ	K	State	Obs.	Calc.	Obs.-Calc.	J	Γ	K	State	Obs.	Calc.	Obs.-Calc.
5	A_2	0	g.s.	36.359	36.351	0.008	5	B_1	5	$\nu_3+\nu_6$	3242.685	3242.728	−0.043
5	A_2	2	g.s.	69.265	69.262	0.004	5	B_1	2	$\nu_4+\nu_5$	4004.845	4004.887	−0.042
5	A_2	4	g.s.	167.325	167.318	0.007	5	B_1	1	$\nu_1+\nu_4$	4040.305	4040.262	0.042
5	A_2	1	ν_4	1211.431	1211.432	0.000	5	B_2	1	g.s.	45.822	45.817	0.005
5	A_2	3	ν_4	1266.466	1266.380	0.087	5	B_2	3	g.s.	110.110	110.109	0.001
5	A_2	1	ν_6	1293.712	1293.699	0.013	5	B_2	5	g.s.	240.777	240.779	−0.002
5	A_2	3	ν_6	1369.614	1369.620	−0.006	5	B_2	0	ν_4	1203.449	1203.469	−0.020
5	A_2	5	ν_6	1514.745	1514.723	0.022	5	B_2	2	ν_4	1231.267	1231.236	0.032
5	A_2	0	ν_3	1536.634	1536.707	−0.073	5	B_2	4	ν_4	1316.675	1316.516	0.158
5	A_2	2	ν_3	1569.797	1569.860	−0.063	5	B_2	2	ν_6	1323.189	1323.188	0.000
5	A_2	4	ν_3	1668.521	1668.517	0.004	5	B_2	4	ν_6	1433.619	1433.621	−0.002
5	A_2	0	ν_2	1782.122	1782.074	0.048	5	B_2	1	ν_3	1546.255	1546.358	−0.103
5	A_2	2	ν_2	1815.041	1815.003	0.038	5	B_2	3	ν_3	1610.920	1610.955	−0.035
5	A_2	4	ν_2	1913.119	1913.125	−0.006	5	B_2	5	ν_3	1742.477	1742.420	0.057
5	A_2	1	$\nu_3+\nu_4$	2710.766	2710.794	−0.028	5	B_2	1	ν_2	1791.598	1791.532	0.066
5	A_2	3	$\nu_3+\nu_4$	2763.301	2763.352	−0.052	5	B_2	3	ν_2	1855.896	1855.879	0.016
5	A_2	1	$2\nu_3$	2764.503	2764.536	−0.033	5	B_2	5	ν_2	1986.603	1986.634	−0.031
5	A_2	0	ν_5	2818.805	2818.811	−0.006	5	B_2	0	$\nu_3+\nu_4$	2703.300	2703.314	−0.013
5	A_2	3	$2\nu_3$	2842.751	2842.721	0.030	5	B_2	2	$\nu_3+\nu_4$	2729.408	2729.452	−0.044
5	A_2	2	ν_5	2851.138	2851.189	−0.051	5	B_2	5	$\nu_3+\nu_6$	2791.651	2791.631	0.020
5	A_2	5	$\nu_3+\nu_4$	2877.620	2877.678	−0.058	5	B_2	2	$2\nu_3$	2795.151	2795.181	−0.030
5	A_2	1	ν_1	2886.456	2886.419	0.037	5	B_2	4	$\nu_3+\nu_4$	2812.662	2812.730	−0.068
5	A_2	4	ν_5	2947.231	2947.178	0.053	5	B_2	1	ν_5	2828.148	2828.175	−0.027
5	A_2	1	$\nu_2+\nu_4$	2950.430	2950.319	0.111	5	B_2	3	ν_5	2891.108	2891.052	0.055
5	A_2	3	ν_1	2951.745	2951.797	−0.051	5	B_2	4	$2\nu_3$	2907.672	2907.733	−0.062
5	A_2	5	$2\nu_3$	2989.064	2989.131	−0.067	5	B_2	2	ν_1	2911.713	2911.709	0.003
5	A_2	3	$\nu_2+\nu_4$	3009.004	3008.964	0.040	5	B_2	0	$\nu_2+\nu_4$	2941.927	2941.842	0.085
5	A_2	0	$\nu_3+\nu_6$	3035.539	3035.630	−0.091	5	B_2	2	$\nu_2+\nu_4$	2971.676	2971.602	0.074
5	A_2	1	$\nu_2+\nu_6$	3044.133	3044.113	0.020	5	B_2	4	ν_1	3007.671	3007.762	−0.091
5	A_2	2	$\nu_3+\nu_6$	3068.947	3069.053	−0.106	5	B_2	5	ν_5	3019.289	3019.216	0.073
5	A_2	5	ν_1	3079.477	3079.581	−0.104	5	B_2	1	$\nu_3+\nu_6$	3045.316	3045.475	−0.159
5	A_2	3	$\nu_2+\nu_6$	3118.100	3118.071	0.030	5	B_2	4	$\nu_2+\nu_4$	3061.890	3061.903	−0.013
5	A_2	5	$\nu_2+\nu_4$	3130.633	3130.731	−0.098	5	B_2	2	$\nu_2+\nu_6$	3072.782	3072.744	0.038
5	A_2	4	$\nu_3+\nu_6$	3168.285	3168.354	−0.069	5	B_2	3	$\nu_3+\nu_6$	3110.325	3110.413	−0.088
5	A_2	5	$\nu_2+\nu_6$	3260.950	3260.922	0.028	5	B_2	4	$\nu_2+\nu_6$	3180.935	3180.912	0.023
5	A_2	1	$\nu_4+\nu_5$	3985.538	3985.569	−0.031	5	B_2	5	$\nu_3+\nu_6$	3242.685	3242.728	−0.043
5	A_2	3	$\nu_4+\nu_5$	4038.166	4038.128	0.038	5	B_2	0	$\nu_4+\nu_5$	3977.681	3977.653	0.028
5	A_2	2	$\nu_1+\nu_4$	4059.300	4059.274	0.026	5	B_2	2	$\nu_4+\nu_5$	4004.929	4004.973	−0.045

V. RESULTS AND CONCLUSIONS

The TROVE-calculated vibrational term values obtained with the H2CO-2010 PES are included in Tables III–VI (relative to the calculated zero point energy of 5774.05 cm^{-1}) and compared with the corresponding experimental data and the *ab initio* AQVZ values from this work. Tables IX–XI give the residuals (Obs.−Calc.) for selected states; a complete list is given in the supplementary material.[43] Graphical representations of the agreement between theoretical and experimental energies are shown in Figs. 2 and 3, where the residuals are displayed for all $J = 0, 1, 2, 3, 4, 5$ term values that have experimental counterparts, including those not considered in the fitting. The total rms error for all energy levels except the $J = 0$ set from Bouwens *et al.*[24] is 0.040 cm^{-1} (for further details see Table VII). The largest deviation of 0.3 cm^{-1} (see Fig. 2) is found for the $\nu_4 + \nu_6$ band center ($J = 0$). We suspect the corresponding 'experimental' value from Ref. 31 to be an outlier since all other experimental ro-vibrational term values from this band[29] are reproduced to better than to 0.05 cm^{-1}. The band centers from Bouwens *et al.*[24] (below 7 500 cm^{-1}) are reproduced with an rms error of 1.65 cm^{-1}, close to the quoted accuracy of the experimental data (see above).

It should be noted that the variational TROVE calculations employed in the PES fitting of the present work are not fully converged because of the basis set truncation at $P_{\max} = 14$ and the internal use of Taylor-type expansions of the Hamiltonian operator truncated after the 8th order terms (see Section III). Therefore, our refined PES H2CO-2010 is 'effective' in the sense that the stated accuracy of 0.04 cm^{-1} can only be guaranteed when the H2CO-2010 PES is used in conjunction with the same calculation setup as described in Section III.

We have generated a 'spectroscopic' PES of H_2CO which reproduces the available experimental ro-vibrational energies of this molecule with unprecedented accuracy. We are planning to use this PES in comprehensive line list calculations. Another future application is the detailed assignment of the experimental transitions in the 1.5 μm region, which have been extensively investigated by high-resolution spectroscopy owing to the development of monochromatic diode lasers operating near this wavelength (see, for example, Refs. 52,53).

[1] B. M. Dinelli, S. Miller, and J. Tennyson, J. Mol. Spectrosc. **163**, 71 (1994).

[2] B. M. Dinelli, C. R. Le Sueur, J. Tennyson, and R. D. Amos, Chem. Phys. Lett. **232**, 295 (1995).

[3] S. V. Shirin, O. L. Polyansky, N. F. Zobov, P. Barletta, and J. Tennyson, J. Chem. Phys. **118**, 2124 (2003).

[4] P. Gomez and P. Jensen, J. Mol. Spectrosc. **185**, 282 (1997).

[5] V. Tyuterev, S. Tashkun, and D. Schwenke, Chem. Phys. Lett. **348**, 223 (2001).

[6] V. Tyuterev, S. Tashkun, P. Jensen, A. Barbe, and T. Cours, J. Mol. Spectrosc. **198**, 57 (1999).

[7] J. Zunga, M. Alacid, A. Bastida, F. Carvajal, and A. Requena, J. Mol. Spectrosc. **195**, 137 (1999).

[8] X. Huang, D. W. Schwenke, and T. J. Lee, J. Chem. Phys. **134**, 044320 (2011).

[9] S. Yurchenko, R. J. Barber, J. Tennyson, W. Thiel, and P. Jensen, J. Mol. Spectrosc., submitted for publication (2011).

[10] S. N. Yurchenko, W. Thiel, and P. Jensen, J. Mol. Spectrosc. **245**, 126 (2007).

[11] S. Yurchenko, M. Carvajal, A. Yachmenev, W. Thiel, and P. Jensen, J. Quant. Spectrosc. Rad. Transf. **111**, 2279 (2010).

[12] G. D. Purvis and R. J. Bartlett, J. Chem. Phys. **76**, 1910 (1982).

[13] M. Urban, J. Noga, S. J. Cole, and R. J. Bartlett, J. Chem. Phys. **83**, 4041 (1985).

[14] K. Raghavachari, G. W. Trucks, J. A. Pople, and M. Head-Gordon, Chem. Phys. Lett. **157**, 479 (1989).

[15] T. H. Dunning, J. Chem. Phys. **90**, 1007 (1989).

[16] D. E. Woon and T. H. Dunning, J. Chem. Phys. **98**, 1358 (1993).

[17] J. Martin, T. Lee, and P. Taylor, J. Mol. Spectrosc. **160**, 105 (1993).

[18] K. Yagi, S. Hirata, and K. Hirao, Theor. Chem. Acc. **118**, 681 (2007).

[19] A. Jalbout and C. Chang, J. Mol. Struct. **634**, 127 (2003).

[20] X. Zhang, S. Zou, L. Harding, and J. Bowman, J. Phys. Chem. A **108**, 8980 (2004).

[21] S. Carter, N. Pinnavaia, and N. Handy, Chem. Phys. Lett. **240**, 400 (1995).

[22] S. Carter, N. Handy, and J. Demaison, Mol. Phys. **90**, 729 (1997).

[23] D. Burleigh, A. McCoy, and E. Sibert, J. Chem. Phys. **104**, 480 (1996).

[24] R. Bouwens, J. Hammerschmidt, M. Grzeskowiak, T. Stegink, P. Yorba, and W. Polik, J. Chem. Phys. **104**, 460 (1996).

[25] K. Mardis and E. Sibert, J. Mol. Spectrosc. **187**, 167 (1998).

[26] R. Bernal and R. Lemus, J. Mol. Spectrosc. **235**, 218 (2006).

[27] E. S. Bekhtereva, Russ. Phys. J. **51**, 175 (2008).

[28] O. N. Ulenikov, E. S. Bekhtereva, C. Leroy, O. V. Gromova, and A. L. Fomchenko, J. Mol. Spectrosc. **255**, 88 (2009).

[29] A. Perrin, D. Jacquemart, F. K. Tchana, and N. Lacome, J. Quant. Spectrosc. Radiat. Transf. **110**, 700 (2009).

[30] F. K. Tchana, A. Perrin, and N. Lacome, J. Mol. Spectrosc. **245**, 141 (2007).

[31] A. Perrin, A. Valentin, and L. Daumont, J. Mol. Struct. **780-81**, 28 (2006).

[32] R. Perez, J. Brown, Y. Utkin, J. Han, and R. Curl, J. Mol. Spectrosc. **236**, 151 (2006).

[33] J. Flaud, W. Lafferty, R. Sams, and S. Sharpe, Mol. Phys. **104**, 1891 (2006).

[34] S. Saha, H. Barry, G. Hancock, G. A. D. Ritchie, and C. M. Western, Mol. Phys. **105**, 797 (2007).

[35] L. S. Rothman, I. E. Gordon, A. Barbe, D. C. Benner, P. E. Bernath, M. Birk, V. Boudon, L. R. Brown, A. Campargue, J. P. Champion, et al., J. Quant. Spectrosc. Radiat. Transf. **110**, 533 (2009).

[36] N. Jacquinet-Husson, N. A. Scott, A. Chedina, L. Crepeau, R. Armante, V. Capelle, J. Orphal, A. Coustenis, C. Boonne, N. Poulet-Crovisier, et al., J. Quant. Spectrosc. Radiat. Transf. **109**, 1043 (2008).

[37] H.-J. Werner, P. J. Knowles, R. Lindh, F. R. Manby, M. Schütz, et al., *Molpro, version 2006.1, a package of ab initio programs* (2006), see http://www.molpro.net.

[38] C. Hampel, K. Peterson, and H. J. Werner, Chem. Phys. Lett. **190**, 1 (1992).

[39] S. Carter and N. Handy, J. Mol. Spectrosc. **179**, 65 (1996).

[40] J. Duncan, Mol. Phys. **28**, 1177 (1974).

[41] P. R. Bunker and P. Jensen, *Molecular Symmetry and Spectroscopy* (NRC Research Press, Ottawa, 1998), 2nd ed.

[42] H. Partridge and D. Schwenke, J. Chem. Phys. **106**, 4618 (1997).

[43] See EPAPS document No.E-JCP-xxx-xxx-xxx. A direct link to this document may be found in the online article's html reference section. The document may also be reached via the

EPAPS homepage http://www.aip.org/pubservs/epaps.html or from ftp.aip.org in the directory /EPAPS/. See the EPAPS homepage for more information.

[44] B. Numerov, Mon. Not. R. Astron. Soc. **84**, 592 (1924).

[45] J. W. Cooley, Math. Comp. **15**, 363 (1961).

[46] S. N. Yurchenko, M. Carvajal, P. Jensen, H. Lin, J. J. Zheng, and W. Thiel, Mol. Phys. **103**, 359 (2005).

[47] S. N. Yurchenko, R. J. Barber, A. Yachmenev, W. Thiel, P. Jensen, and J. Tennyson, J. Phys. Chem. A **113**, 11845 (2009).

[48] R. B. Lehoucq, D. C. Sorensen, and C. Yang, *ARPACK Users' Guide: Solution of Large-scale Eigenvalue Problems with Implicitly Restarted Arnoldi Methods (Software, Environments and Tools)* (Society for Industrial & Applied Mathematics, U.S., http://www.caam.rice.edu/software/ARPACK/, 1998).

[49] I. Mills and A. Robiette, Mol. Phys. **56**, 743 (1985).

[50] S. N. Yurchenko, M. Carvajal, P. Jensen, F. Herregodts, and T. R. Huet, Chem. Phys. **290**, 59 (2003).

[51] H. Müller, G. Winnewisser, J. Demaison, A. Perrin, and A. Valentin, J. Mol. Spectrosc. **200**, 143 (2000).

[52] M. Staak, E. Gash, D. Venables, and A. Ruth, J. Mol. Spectrosc. **229**, 115 (2005).

[53] W. Zhao, X. Gao, L. Deng, T. Huang, T. Wu, and W. Zhang, J. Quant. Spectrosc. Radiat. Transf. **107**, 331 (2007).

High level ab initio potential energy surface and vibrational energies of H_2CS

A. Yachmenev, S. N. Yurchenko, T. Ribeyre, W. Thiel

J. Chem. *Phys.*, submitted for publication (2011)

High-level *ab initio* potential energy surfaces and vibrational energies of H_2CS

Andrey Yachmenev

Max-Planck-Institut für Kohlenforschung, Kaiser-Wilhelm-Platz 1, D–45470 Mülheim an der Ruhr, Germany

Sergei N. Yurchenko

Physikalische Chemie, Technische Universität Dresden, Mommsenstr. 13, D-01062 Dresden, Germany

Tristan Ribeyre

Département Chimie, Ecole Normale Supérieure de Cachan, 61 Avenue du Président Wilson, 94235 Cachan Cedex, France

Walter Thiel*

Max-Planck-Institut für Kohlenforschung, Kaiser-Wilhelm-Platz 1, D-45470 Mülheim an der Ruhr, Germany

(Dated: March 31, 2011)

Abstract

Six-dimensional (6D) potential energy surfaces (PESs) of H_2CS have been generated *ab initio* using the recently proposed explicitly correlated (F12) singles and doubles coupled cluster method including a perturbational estimate of connected triple excitations, CCSD(T)-F12b [T. B. Adler, G. Knizia, and H.-J. Werner, *J. Chem. Phys.*, **127**, 221106 (2007)] in conjunction with F12-optimized correlation consistent basis sets. Core-electron correlation, high-order correlation, scalar relativistic, and diagonal Born-Oppenheimer terms were included as additive high-level (HL) corrections. The resulting 6D PESs were represented by analytical functions which were used in variational calculations of the vibrational term values below 5000 cm^{-1}. The best PESs obtained with and without the HL corrections, VQZ-F12^{*HL} and VQZ-F12*, reproduce the fundamental vibrational wavenumbers with mean absolute deviations of 1.35 and 1.42, cm^{-1} respectively. A detailed analysis of the effects of the HL corrections shows how the VQZ-F12 results benefit from error cancellation. The present purely *ab initio* PESs will be useful as starting points for empirical refinements towards an accurate 'spectroscopic' PES of H_2CS.

I. INTRODUCTION

Thioformaldehyde plays an important role in the photochemical evolution of sulfur-containing species in atmospheric and astrophysical chemistry (see, for example, Refs. 1–7). It was first detected in the laboratory by Johnson and Powell.[1] Soon thereafter, an interstellar search was carried out by Evans *et al.*,[2] which was followed by the first interstellar detection of H_2CS by Sinclair *et al.*[3] Woodney *et al.*[4] were the first to report the presence of H_2CS in the atmosphere of the comet Hale-Bopp. Recently H_2CS was also identified in the Orion KL Nebula.[5–7]

Experimentally, there are only rather few high-resolution spectroscopic data on $H_2^{12}C^{32}S$ (henceforth referred to as thioformaldehyde or H_2CS). Recently, Flaud *et al.*[8] reported a high-resolution Fourier transform study of the infrared ro-vibrational spectrum of H_2CS at 10 μm, covering the ν_3, ν_4, and ν_6 vibrational bands. Maeda *et al.*[9] presented new laboratory measurements of the pure rotational spectrum of H_2CS together with a global analysis of all available experimental data on the rotational transitions. For the other three fundamental bands ν_1, ν_2, and ν_5, as well as for the overtone $2\nu_2$ and combination $\nu_2 + \nu_3$ bands, only low-resolution data have been published so far. Experimental work on H_2CS prior to 1983 has been reviewed by Clouthier and Ramsay.[10] A detailed up-to-date collection of the available experimental microwave, millimeter-wave, and far-infrared data on this molecule can also be found in the Cologne Database for Molecular Spectroscopy.[11,12] Concerning the electronic spectroscopy of H_2CS, experimental studies in the visible and ultraviolet regions were reported in Refs. 10,13–18.

On the theoretical side, the quartic force field for H_2CS was first calculated *ab initio* by Martin *et al.*[19] using the coupled cluster CCSD(T) method with a correlation-consistent triple-zeta basis set in the frozen core (FC) approximation: the vibrational fundamental term values (obtained perturbationally) agreed with experiment to within 10 cm^{-1}, while overtones were off by almost twice as much.[19] The force field of Martin *et al.* was later refined by Carter and Handy[20] by fitting to the eight known vibrational ($J = 0$) and the corresponding ro-vibrational ($J = 1$) energy levels of H_2CS and D_2CS using their variational approach,[21] in which both the *ab initio* equilibrium geometry and force constants were adjusted. The corresponding root-mean-square (rms) errors for the $J = 0$ and $J = 1$ energy levels were 0.4 and 0.0044 cm^{-1}, respectively.[20] This refined PES was recently employed

in simulations of ro-vibrational spectra ($J \leq 20$) for H_2CS covering the pure rotational transitions as well as the ν_3, ν_4, and ν_6 bands;[22] the intensities were computed using a DFT dipole moment surface.[23]

The quality of an *ab initio* PES can usually be improved through fittings to accurate experimental energies or transition wavenumbers. The resulting so-called 'spectroscopic' PES has the potential to approach experimental accuracy when used in variational (ro-)vibrational calculations. However, the scarcity of high-resolution spectroscopic data on H_2CS hinders the construction of a globally accurate 'spectroscopic' PES for this molecule. For instance, the refined force constants from Carter and Handy[20] provide good accuracy for their fitting set (covering the pure rotational, fundamental, $2\nu_2$, and $\nu_2 + \nu_3$ bands), but cannot be expected to deliver the same accuracy for transitions beyond this set. In such a situation, accurate *ab initio* calculations are the only resort. Therefore it is the goal of this paper to generate *ab initio* PESs for H_2CS by combining the highest level of modern *ab initio* theory with variational calculations of the vibrational energies for this molecule. Towards this end we employ the recently proposed explicitly correlated F12 singles and doubles coupled cluster method including a perturbational estimate of connected triple excitations, CCSD(T)-F12b,[24] in conjunction with the corresponding F12-optimized correlation consistent basis sets. The F12 methods have the advantage to provide near-basis-set-limit accuracy already with basis sets of moderate size.[25] We also include high-level (HL) additive corrections for core-valence (CV) correlation, high-order electron correlation (HO), and scalar relativistic (SR) effects as well as diagonal Born-Oppenheimer corrections (DBOC). It has been shown in the case of diatomic closed-shell molecules that potential curves obtained from valence-only CCSD(T) calculations at the one-particle basis set limit can be improved by adding these HL corrections (even when evaluated with rather small basis sets) such that the desired spectroscopic accuracy is reached.[26–33] The importance of these corrections for accurate construction of multidimensional PESs of polyatomic molecules has also been recognized (see, for example, Refs. 34–39). We analyze in some detail the effect of the individual HL corrections on the vibrational term values of H_2CS below 5000 cm^{-1}.

The paper is organized as follows. The *ab initio* calculations are presented in Section II A. The analytical representations of the individual HL contributions and of the total PES of H_2CS are described in Section II B. Section II C gives details on the variational calculations. The recommended PESs, their analysis, and comparisons with experiment are presented in

Section III. Section IV offers some conclusions.

II. COMPUTATIONAL DETAILS

A. Electronic structure calculations

We use the following expression to represent the total electronic energy

$$E_{\rm tot} = E_{\rm fcCCSD(T)-F12} + \Delta E_{\rm CV} + \Delta E_{\rm HO} + \Delta E_{\rm SR} + \Delta E_{\rm DBOC}, \quad (1)$$

where $E_{\rm fcCCSD(T)-F12}$ is the valence-only explicitly correlated coupled cluster CCSD(T)-F12 energy, $\Delta E_{\rm CV}$ is the correction arising from core-valence correlation, $\Delta E_{\rm HO}$ is the correction for electron correlation effects from higher-order coupled cluster terms [beyond CCSD(T)], $\Delta E_{\rm SR}$ accounts for scalar relativistic effects, and $\Delta E_{\rm DBOC}$ is the diagonal Born-Oppenheimer correction. The energies from explicitly correlated CCSD(T) calculations, $E_{\rm fcCCSD(T)-F12}$, are known to converge much faster towards the basis set limit than those from the canonical CCSD(T) treatment. It has been shown, for example, that the accuracy of vibrational frequencies obtained from CCSD(T)-F12 in conjunction with triple-zeta basis sets matches the quality of the conventional CCSD(T) results with pentuple-zeta basis sets.[25]

To obtain the $E_{\rm fcCCSD(T)-F12}$ energies we employed the recently proposed approximate explicitly correlated coupled cluster CCSD(T)-F12b[24] method in conjunction with the diagonal fixed amplitude ansatz 3C(FIX)[40] as implemented in the MOLPRO package of *ab initio* programs.[41] In this ansatz the explicitly correlated amplitudes are determined utilizing the wave function cusp conditions. The method is orbital invariant, size consistent, and free from geminal basis set superposition errors.[40] For the efficient evaluation of the many-electron integrals in F12 theory, the resolution-of-identity (RI) approximation is combined with density fitting (DF). Therefore, the F12 calculations require three different basis sets for (i) orbitals, (ii) DF, and (iii) RI. In the present study we employ the orbital basis sets specifically optimized for the F12 methods, namely the valence correlation-consistent basis sets cc-pVTZ-F12 and cc-pVQZ-F12.[42] Henceforth the corresponding explicitly correlated coupled cluster calculations as well as the resulting energies $E_{\rm fcCCSD(T)-F12}$ will be referred to as VTZ-F12 and VQZ-F12, respectively. We also utilized the OptRI,[43] cc-pV5Z/JKFIT,[44] and aug-cc-pwCV5Z/MP2FIT[45] auxiliary basis sets for evaluating the many-electron integrals (RI), the exchange and Fock operators (DF), and the remaining electron repulsion

integrals (DF), respectively. The value of the geminal Slater exponent β was chosen as 1.0 both for VTZ-F12 and VQZ-F12, as recommended in Ref. 42.

In some calculations we extrapolated the correlation part CCSD-F12b of $E_{\mathrm{fcCCSD(T)-F12}}$ to the complete basis set (CBS) limit utilizing the proposed X^{-7} and X^{-4} formulas, where $X = 3, 4$ denotes the cardinal quantum number of the basis sets VTZ-F12 and VQZ-F12, respectively. The choice of the X^{-7} extrapolating function is motivated by the formal convergence properties of explicitly correlated methods,[46,47] while the X^{-4} dependence conforms to the CBS extrapolation of the MP2-F12 correlation energies in a benchmark study for molecules containing first-row and some second-row atoms.[42] Since the perturbative triples (T) contributions to the correlation energies $E_{\mathrm{fcCCSD(T)-F12}}$ are not treated in an explicitly correlated manner in the current MOLPRO[41] implementation, they were extrapolated using the standard X^{-3} expression.[48] We shall use the label VQZ-F12* for the results obtained by incorporating this CBS extrapolation for the (T) contributions on top of the VQZ-F12 results. In addition, the CBS extrapolation for the CCSD-F12b part is in some cases also included on top of the VQZ-F12* results, which leads to results denoted as CBS(7)-F12 and CBS(4)-F12, respectively, for the two types of extrapolating functions considered (see above). These latter two extrapolations for the CCSD-F12b part usually have only very minor effects (see below), and in the absence of further validation, it is not clear which one to prefer. Therefore we adopt VQZ-F12* as our best approximation to the CCSD(T)/CBS limit.

The VTZ-F12 and VQZ-F12 energies were computed in the frozen-core (FC) approximation. To estimate the effect of core-valence correlation ΔE_{CV}, we performed all-electron (AE) calculations, in which the $1s$ electrons of carbon and the $2s$ and $2p$ electrons of sulfur were correlated. The CCSD(T)-F12b method was used in conjunction with the core-valence basis sets cc-pCVTZ-F12 and cc-pCVQZ-F12 and the corresponding new compact RI auxiliary basis sets.[49] These CV calculations and the resulting energies will be referred to as $\mathrm{CV_{TZ-F12}}$ and $\mathrm{CV_{QZ-F12}}$, respectively, while CV will be used to label the correction irrespective of the basis set. We utilized the same DF auxiliary basis sets as in the FC calculations. The geminal Slater exponents β were selected as recommended in Ref. 49, namely 1.4 ($\mathrm{CV_{TZ-F12}}$) and 1.5 ($\mathrm{CV_{QZ-F12}}$) both for the valence-only and all-electron calculations. In some calculations the $\mathrm{CV_{TZ-F12}}$ and $\mathrm{CV_{QZ-F12}}$ energies were extrapolated to the CBS limit (denoted as $\mathrm{CV_{CBS(4)-F12}}$ and $\mathrm{CV_{CBS(7)-F12}}$) using the same approach as in the extrapolation of the

FC correlation energies (see above).

The SR corrections were computed using either the Cowan-Griffin perturbation theory[50] [including the one-electron Darwin and mass-velocity terms (MVD1)] or the second-order Douglas-Kroll-Hess (DKH2) approach.[51,52] The MVD1 corrections were calculated at the AE CCSD(T) level of theory[53] employing the augmented core-valence aug-cc-pCVTZ basis set[54–57] as implemented in the program package CFOUR.[58] The DKH2 calculations were done with MOLPRO[41] at the FC CCSD(T)/cc-pVQZ-DK level.[59] The DBOC corrections were determined using the aug-cc-pCVTZ basis set and the AE CCSD method[60] as implemented in CFOUR.[58]

The HO corrections were obtained from CCSDT, CCSDT(Q), CCSDTQ, and CCSDTQ(P) calculations that were performed with the general coupled cluster approach implemented in the MRCC code[61] interfaced to CFOUR.[58] In these calculations, we employed the cc-pVDZ, aug-cc-pVnZ, and aug-cc-pV(n+d)Z (n=D,T) basis sets[54,55,62,63] [abbreviated as VDZ, AVnZ, and AV(n+d)Z, respectively] and the FC approximation. The corrections from the full triples [CCSDT-CCSD(T)] and the perturbative quadruples [CCSDT(Q)-CCSDT] were computed employing the AVTZ, AV(T+d)Z, and AVDZ, AV(D+d)Z basis sets, respectively. For the corrections from the full quadruples [CCSDTQ-CCSDT(Q)] and the perturbative pentuples [CCSDTQ(P)-CCSDTQ] the VDZ basis set was used.

B. Analytical representation of the potential energy surface

To generate an accurate multidimensional PES for a tetratomic molecule, a very large number of single-point *ab initio* calculations is required (several thousands at least). In our case, each *ab initio* point is constructed from five independent terms, see Eq. (1), each of which computationally very demanding. Our procedure of PES generation consists of the following three steps. (i) The first term, $E_{\mathrm{fcCCSD(T)-F12}}$, is evaluated on the complete global grid of geometries (24 640 points). (ii) The other terms, i.e., the HL corrections, are computed on individually chosen (smaller) grids of geometries and described by suitable analytical functions that are usually rather simple, because the HL corrections are generally small and smooth (see below). (iii) The total energies are generated on the complete global grid of geometries by adding all terms, see Eq. (1), with the proviso that HL terms missing at any given grid point are determined by interpolation employing the corresponding analytical

function from step (ii).

For the purpose of analysis, we compute not only a set of total energies according to Eq. (1), but in an analogous manner also sets of reduced energies, in which only individual HL terms are included (for example, VQZ-F12+CV, VQZ-F12+CV+HO, etc.); these are then used to investigate how different HL corrections and their combinations affect the vibrational energies. For each set of energies on the complete global grid, an analytical PES representation is constructed by fitting (see below) which serves as input for the variational calculation of the vibrational energies.

To make the required HL calculations feasible we adjusted the number of points in the corresponding grid depending on the target term E_{X} in Eq. (1) (X = CV, HO, SR, or DBOC). Towards this end we set up four reduced grids designed to provide a reasonable description of each given term with minimum effort. Each of them was then interpolated independently by fitting to an appropriate analytical function. In fact, the HL corrections in Eq. (1) are quite distinct in terms of their dependence on the internal coordinates of the molecule. This is illustrated in Figs. 1 and 2, where one-dimensional (1D) cuts are shown for different HL terms. In general, the CV and particularly the HO terms appear to be larger than the MVD1 and DBOC terms, and their variation is usually more pronounced along the stretching modes (especially CS) than along the bending modes. Most of the HL corrections show a rather simple polynomial-type dependence along the cuts. Thus we could reduce the number of required expansion parameters (force constants) as well as the number of the corresponding *ab initio* data points by individually selecting an appropriate analytical form for each HL term. Towards this end we tested different types of vibrational coordinates and found that the valence coordinates (see the definition below) provide the highest degree of inter-mode separation, at least in the energy range below 20 000 cm^{-1}.

To construct a 6D analytical representation for the HL correction energies E_{X} (X = CV, HO, MVD1, and DBOC) in Eq. (1), the following n-mode expansion was used

$$\mathcal{F} = \mathcal{F}^{(0)} + \sum_{i}^{6} \mathcal{F}_{i}^{(1)}(\xi_i) + \sum_{i}^{6}\sum_{i>j}^{6} \mathcal{F}_{ij}^{(2)}(\xi_i,\xi_j) + \sum_{i}^{6}\sum_{i>j}^{6}\sum_{i>j>k}^{6} \mathcal{F}_{ijk}^{(3)}(\xi_i,\xi_j,\xi_k) + \ldots \qquad (2)$$

where $\mathcal{F}_{ijk\ldots}^{(n)}(\xi_i,\xi_j,\xi_k,\ldots)$ is a n-dimensional cut ($n = 1,\ldots,6$) through the corresponding six-dimensional surface E_{X} along the $\xi_i,\xi_j,\xi_k,\ldots$ coordinates, with all other coordinates

FIG. 1. One-dimensional cuts of the CV_{QZ-F12} and HO corrections given by the solid and dashed lines, respectively. The ranges for the coordinates are selected such that the total energy is always below 25 000 cm^{-1}. Please note the different energy scales.

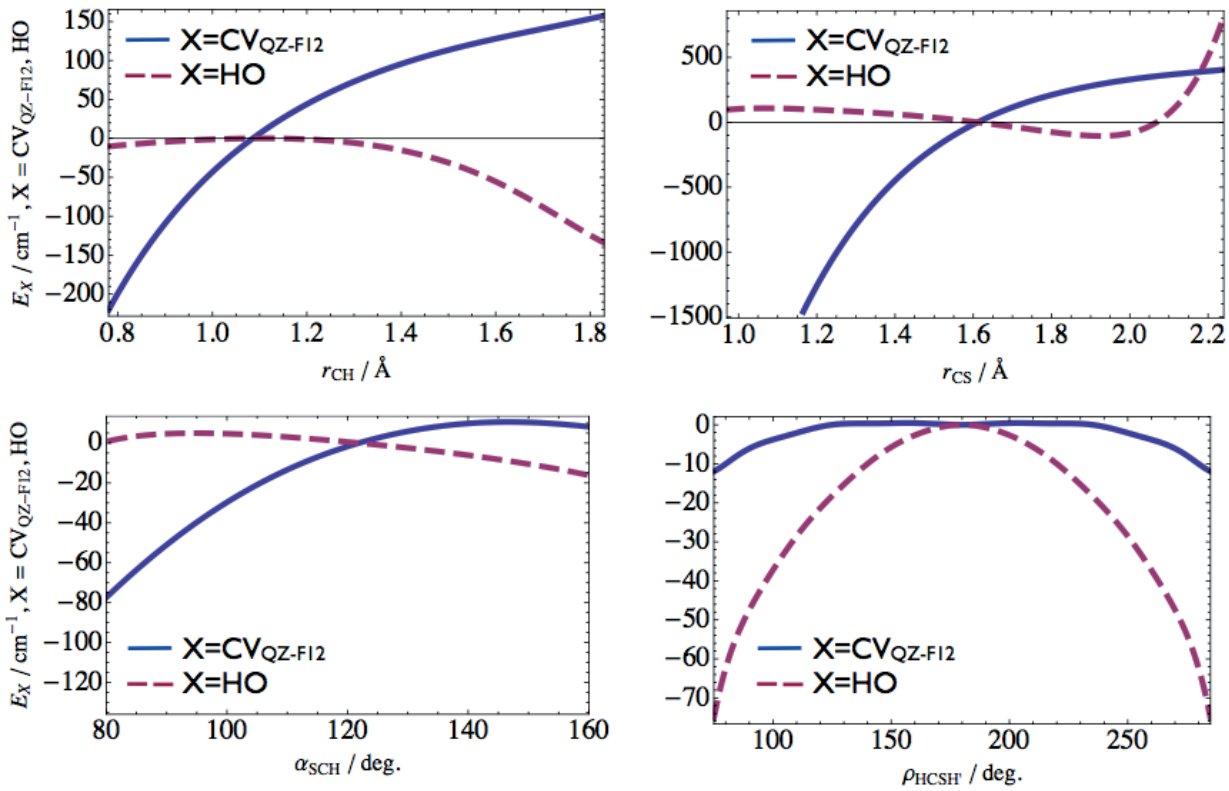

fixed to zero. In turn, each n-mode term in Eq. (2) is given by the polynomial expansion

$$\mathcal{F}^{(n)}_{ij..}(\xi_i, \xi_j, ...) = \sum_{s>0,t>0,...} F^{(ij...)}_{st...} \xi_i^s \xi_j^t ... \tag{3}$$

in terms of the variables

$$\xi_i = r_i - r_i^{(\mathrm{eq})}, \; i = \mathrm{CS}, \; \mathrm{CH_1}, \; \text{or} \; \mathrm{CH_2}, \tag{4}$$

$$\xi_j = \alpha_j - \alpha_j^{(\mathrm{eq})}, \; j = \mathrm{SCH_1} \; \text{or} \; \mathrm{SCH_2}, \tag{5}$$

$$\xi_6 = 1 + \cos\rho. \tag{6}$$

Here, r_{CS}, r_{CH_1}, and r_{CH_2} are the bond lengths, α_{SCH_1} and α_{SCH_2} are the bond angles, and ρ is the dihedral angle between the SCH_1 and SCH_2 planes. The expansion coefficients $F^{(ij...)}_{st...}$

FIG. 2. One-dimensional cuts of the MVD1 and DBOC corrections given by the solid and dashed lines, respectively. The ranges for the coordinates are selected such that the total energy is always below 25 000 cm^{-1}. Please note the different energy scales.

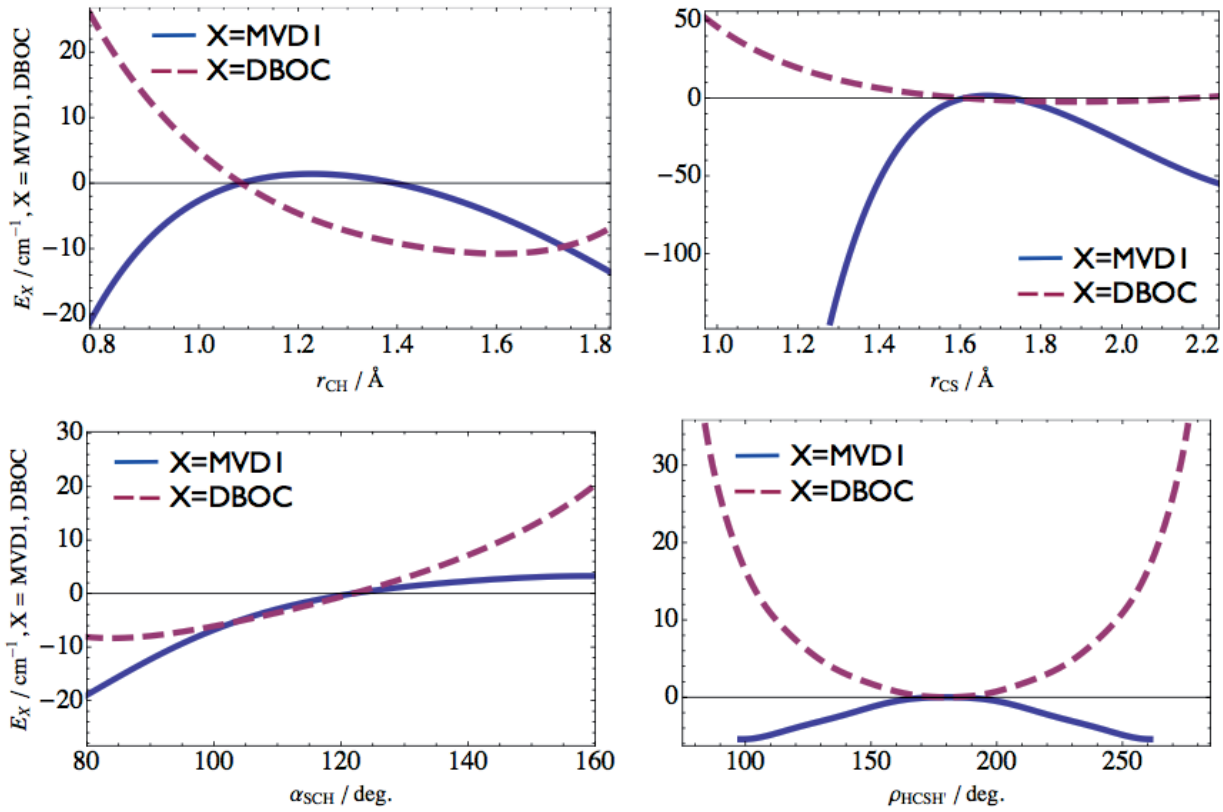

in Eq. (3) obey the permutation rule

$$F_{st\ldots}^{(i'j'\ldots)} = F_{st\ldots}^{(ij\ldots)} \tag{7}$$

where the indices $i', j' \ldots$ are obtained from $i, j \ldots$ by replacing all indices 2 by 3, all indices 3 by 2, all indices 4 by 5, and all indices 5 by 4.

The linear expansion coefficients $F_{st\ldots}^{(ij\ldots)}$ in Eq. (3) were determined for each HL term independently by a least-squares fit (LSQ) to the corresponding *ab initio* data points. The GESVD routine from LAPACK was used to solve the corresponding (ill-conditioned) LSQ system of linear equations by the singular value decomposition technique. For each HL term we determined two to three interpolating polynomials, depending on the truncation order ($n_{\max} = 2$, 3, or 4) in the n-mode expansion (2). The maximum expansion order

in Eq. (3) was restricted to six. For different HL terms the number of *ab initio* points varied between 700 and 5000 depending on $n_{\max}$. In case of the 2-mode expansions we could usefully vary 143, 135, 138, 193, 68, and 97 parameters for the $\mathrm{CV_{TZ-F12}}$, $\mathrm{CV_{QZ-F12}}$, HO, DKH2, MVD1, and DBOC terms, respectively, whilst 196, 187, 194, 230, 134, and 200 parameters were used for the 3-mode expansions. The 4-mode expansion was employed only for the $\mathrm{CV_{TZ-F12}}$, $\mathrm{CV_{QZ-F12}}$, DKH2, and MVD1 corrections, utilizing 221, 214, 315, and 96 parameters, respectively. The rms errors in all these fittings were less than 0.1 $\mathrm{cm^{-1}}$.

The VQZ-F12 total energies and the various types of CBS corrections to the FC correlation energies were calculated on a grid containing 7647 geometries. The energy differences $E_{\mathrm{VQZ-F12}} - E_{\mathrm{VTZ-F12}}$ and the CBS corrections ($E_{\mathrm{VQZ-F12^*}} - E_{\mathrm{VQZ-F12}}$ or $E_{\mathrm{CBS-F12}} - E_{\mathrm{VQZ-F12}}$) were represented by the same kind of n-mode expansion that was also used for the HL corrections, Eq. (2). The 4-mode expansion was employed to fit the $E_{\mathrm{VQZ-F12}} - E_{\mathrm{VTZ-F12}}$, $E_{\mathrm{VQZ-F12^*}} - E_{\mathrm{VQZ-F12}}$, $E_{\mathrm{CBS(7)-F12}} - E_{\mathrm{VQZ-F12}}$, and $E_{\mathrm{CBS(4)-F12}} - E_{\mathrm{VQZ-F12}}$ basis set corrections utilizing 485, 493, 73, and 166 parameters, respectively. The rms errors in these fittings were less than 0.15 $\mathrm{cm^{-1}}$.

The CCSD(T) energies $E_{\mathrm{fcCCSD(T)-F12}}$ [first term in Eq. (1)] were generated as follows: the VTZ-F12 energies were calculated directly on the global grid for each of the 24 640 points (up to 40 000 $\mathrm{cm^{-1}}$), the VQZ-F12 energies were then obtained by adding the energy differences $E_{\mathrm{VQZ-F12}} - E_{\mathrm{VTZ-F12}}$ as evaluated at each grid point from the corresponding n-mode expansion, and the CBS corrections were included in the same manner. The total energies E_{tot}, see Eq. (1), were computed for each grid point likewise, by including the HL corrections represented by their n-mode expansions (2).

The convergence of the HL terms with respect to the expansion order $n_{\max}$ in the n-mode expansion (2) is illustrated in Fig. 3, where we show the following rms deviations as a function of the total energy $E = E_{\mathrm{tot}}$:

$$\sigma_{\mathrm{X}}(E) = \sqrt{\sum_{i}^{N} [E_{\mathrm{X}}^{(n_{\max}+1)}(i) - E_{\mathrm{X}}^{(n_{\max})}(i)]^2 / N}. \tag{8}$$

Here i runs over all 24 640 geometries of the global grid, and X = $\mathrm{CV_{QZ-F12}}$, HO, MVD1, and DBOC. The main features in the plots for $\mathrm{CV_{TZ-F12}}$ and DKH2 resemble those for $\mathrm{CV_{QZ-F12}}$ and MVD1, respectively, and are thus not shown. As can be seen from Fig. 3, the differences between the interpolated energies $E_{\mathrm{X}}^{(4)}$ and $E_{\mathrm{X}}^{(3)}$ are small for X = $\mathrm{CV_{QZ-F12}}$ and

MVD1, of the order of 0.1 cm^{-1} (circles). For X = HO and DBOC, where only the 2- and 3-mode expansions were feasible computationally, the differences between the interpolated energies $E_X^{(3)}$ and $E_X^{(2)}$ are of similar magnitude as those for X = CV_{QZ-F12} and MVD1 (squares), and one may thus assume an analogous convergence behavior. Hence, the use of 3- or 4-mode expansions in Eq. (2) should be sufficient to obtain well-converged energies for all HL corrections. In the energy region above 14 000 cm^{-1}, the CCSD(T) energies of H_2CS start to become non-smooth which leads to a step-like increase (of up to 0.5 cm^{-1}) in all rms plots in Fig. 3. The apparent convergence of the rms errors above 20 000 cm^{-1} is due to the limited number of calculated *ab initio* data at high energies.

We have also investigated how the different HL corrections as well as their analytical representations affect the vibrational energies. Towards this end we have generated a number of PESs resulting from different n-mode expansions in combination with different HL terms (thirteen in total), such as VQZ-F12+$X^{(n_{max}=2)}$, VQZ-F12+$X^{(n_{max}=3)}$, VQZ-F12+$X^{(n_{max}=4)}$, etc (X = CV, HO, SR, and DBOC). The vibrational energies were then computed variationally using the program TROVE[64] (see below). The convergence of the vibrational term values with respect to the expansion order n_{max} in Eq. (2) is illustrated in Figs. 4 and 5, which show the differences between the vibrational energies obtained with the 2- and 3-mode expansions (bars) and with the 3- and 4-mode expansions (circles), respectively. We conclude that the 3-mode expansion is sufficient to obtain vibrational term values converged to better than 0.1 cm^{-1}.

To construct an accurate analytical representation for the total energy, Eq. (1), we follow Ref. 38 and divide the PES into short-range and long-range terms:

$$V = V_{short} f_{damp} + V_{long}. \tag{9}$$

The long-range part V_{long} is given by a simple Morse potential in terms of the three stretching coordinates

$$V_{long} = \sum_{i=1}^{3} D_e^{(i)} \left[1 - \exp\left(-a_i \Delta r_i\right)\right]^2, \tag{10}$$

where $\Delta r_i = r_i - r_i^{(ref)}$ and i = CS, CH_1, or CH_2. The parameters $D_e^{(i)}$ and a_i are selected to provide the correct asymptotic behavior of the potential energy in the corresponding dissociation channel. The f_{damp} function which 'damps' the short-range potential at large

FIG. 3. Estimates of rms fitting errors, Eq. (8), for the HL corrections as function of the total energy: n-mode expansions for $n_{\max} = 2$ (squares) and $n_{\max} = 3$ (circles). Please note the different energy scales.

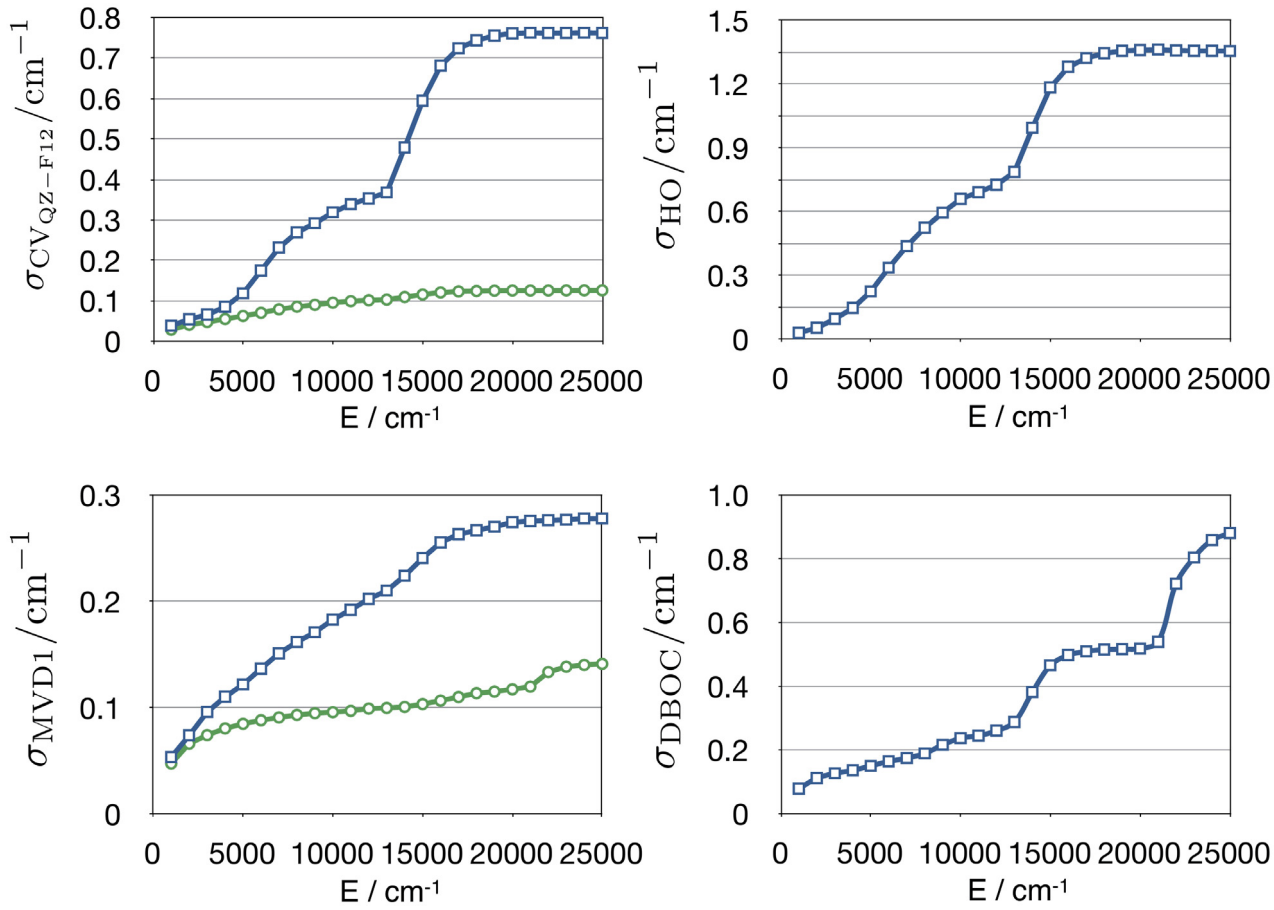

displacements of the nuclei is given by

$$f_{\mathrm{damp}} = \exp\left(\sum_{i=1}^{3} -d_i \Delta r_i^4\right). \tag{11}$$

The criteria used for choosing the damping parameters d_i are (i) small rms errors and (ii) smooth behavior of the resulting potential function along each 1D dissociation cut. The short-range part of the PES is represented by a six-mode eight-order expansion, as given in Eqs. (2) and (3). To investigate the effects of the individual HL correction terms on the equilibrium constants and vibrational energies we have constructed several six-dimensional

FIG. 4. Convergence of the vibrational term values (see Table III) of H_2CS with respect to the truncation order in the n-mode expansions of different HL corrections: $\Delta\nu_X = \nu_X^{(n_{max}+1)} - \nu_X^{(n_{max})}$ (X = CV and HO) for $n_{max} = 2$ (bars) and $n_{max} = 3$ (circles). Please note the different energy scales.

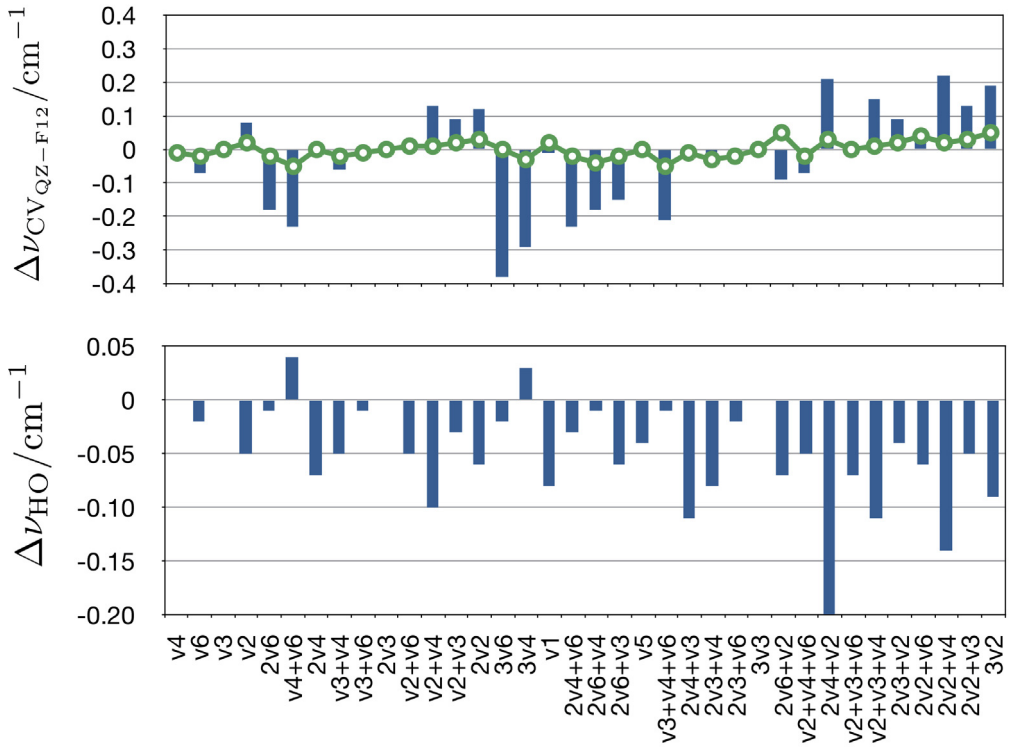

PESs with different HL contributions (see above). The expansion parameters were determined by a LSQ fit to the 24 640 energies calculated in accordance with Eq. (1). The number of parameters varied between 800 and 900 depending on the individual case. The rms errors were less than 0.2 cm^{-1} in all these fittings. In case of the total energy, E_{tot}, we used the weighting function suggested by Partridge and Schwenke[65]

$$w_i = \left\{1/E_i^{(w)} \tanh\left[-0.0006\,(E_i - 40\,000)\right] + 1.002\,002\,002\right\}/2.002\,002\,002, \qquad (12)$$

where $E_i^{(w)} = \max(20\,000, E_i)$ and E_i is the energy at the i-th geometry (all values in cm^{-1}). Thus points below 20 000 cm^{-1} are weighted more heavily. The optimized parameters for several choices of the energy being fitted are given in the supplementary material.

FIG. 5. Convergence of the vibrational term values (see Table III) of H_2CS with respect to the truncation order in the n-mode expansions of different HL corrections: $\Delta\nu_X = \nu_X^{(n_{max}+1)} - \nu_X^{(n_{max})}$ (X = MVD1 and DBOC) for $n_{max} = 2$ (bars) and $n_{max} = 3$ (circles).

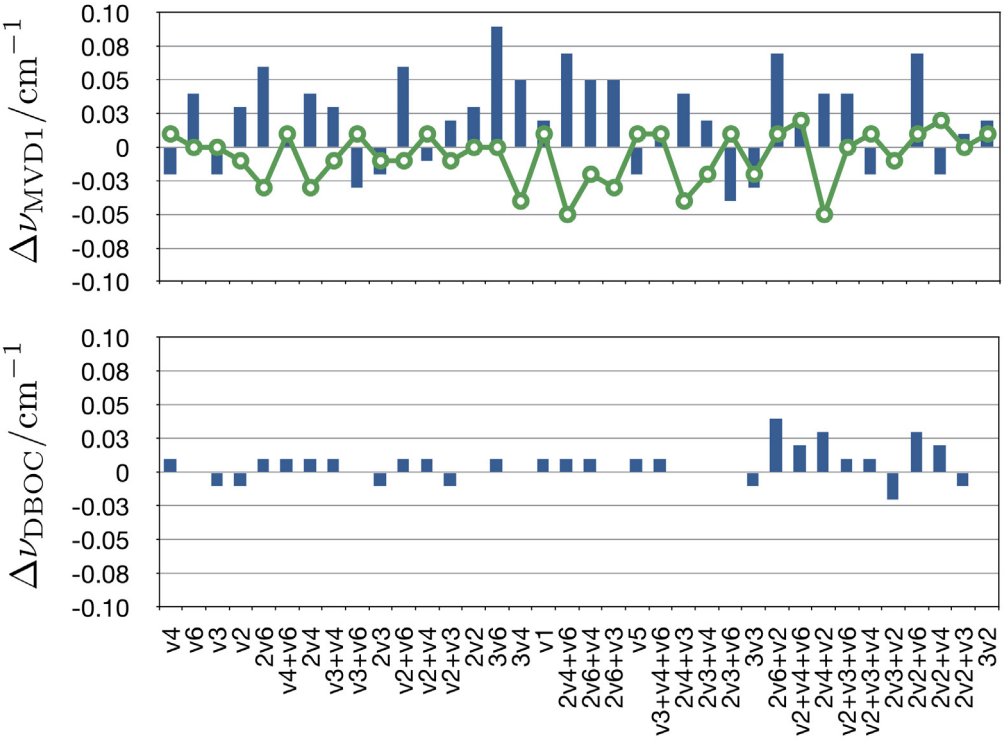

C. Variational calculations of vibrational energies

We computed the vibrational energies of H_2CS employing the variational program TROVE.[64] In TROVE the kinetic energy and potential energy operators are represented by Taylor series expansions of the Xth and Yth order, respectively, in coordinates ξ_i^ℓ. The HL effects on the vibrational energies as well as their n-mode convergence were studied employing X=6 and Y=8, while our best estimates for vibrational energies were obtained with X=8 and Y=12. The coordinates ξ_i^ℓ $(i = 1, \ldots, 5)$ are linearized versions[66] of the coordinates ξ_i defined in Eqs. (4,5). The dihedral angle ρ is treated as a nonrigid mode, i.e., it is evaluated explicitly on a grid of equidistantly spaced values.[64] The size of the vibrational basis set, and therefore the size of the Hamiltonian matrix, is controlled by the

polyad number P, which in the present case is given by

$$P = n_1 + 2(n_2 + n_3) + n_4 + n_5 + n_6, \tag{13}$$

where the local-mode quantum numbers n_i are defined in connection with the primitive basis functions ϕ_{n_i} (see Ref. 64 for details). Hence, we include in the primitive basis set only those combinations of ϕ_{n_i} for which $P \leq P_{\max}$. In the present work we use $P_{\max} = 18$, which ensures convergence to better than 0.1 cm^{-1} for vibrational energies below 5000 cm^{-1}.

We use the normal mode quantum numbers v_1, v_2, v_3, v_4, v_5, and v_6 to label the vibrational states of H_2CS as $v_1\nu_1 + v_2\nu_2 + v_3\nu_3 + v_4\nu_4 + v_5\nu_5 + v_6\nu_6$. The normal modes are defined as follows. ν_1 is the symmetric C-H stretching mode (2971.03 cm^{-1}), ν_2 is the symmetric S-C-H bending mode (1455.50 cm^{-1}), ν_3 is the C-S stretching mode (1059.21 cm^{-1}), ν_4 is the out-of-plane bending mode (990.18 cm^{-1}), ν_5 is the asymmetric C-H stretching mode (3024.62 cm^{-1}), and ν_6 is the asymmetric S-C-H bending mode (991.02 cm^{-1}). The values given in parentheses are the experimental fundamental frequencies from Ref. 10.

III. RESULTS

Here we first analyze how different levels of *ab initio* theory affect the calculated equilibrium geometry and harmonic frequencies of H_2CS. The results of this analysis are summarized in Tables I and II, where our calculated values are compared with the published experimental data and previous theoretical results.

The equilibrium geometry of H_2CS obtained at the VQZ-F12 level of theory is in good agreement with experiment: the theoretical CS and CH equilibrium bond distances of 161.21 and 108.67 pm are only slightly larger, by 0.11 pm, than the experimentally derived equilibrium values.[67] The basis set convergence of the equilibrium parameters is very fast: going from VTZ-F12 to VQZ-F12 changes their values by only -0.04 pm (CS), -0.02 pm (CH), and 0.0005 deg (HCS). The corresponding effect on the harmonic frequencies is less than 1.4 cm^{-1} in all cases. Further extrapolation to the CBS limit results in very small variations both in the equilibrium bond lengths (within 0.02 pm) and harmonic frequencies (within 1 cm^{-1}). Therefore, both VQZ-F12 and VQZ-F12* can serve as reference methods that provide results of essentially CCSD(T)/CBS quality.

Regarding the contributions from the HL corrections, the largest effect is observed for

TABLE I. Equilibrium constants of H_2CS (see text for notation). Increments from basis set extension and high-level corrections are given with respect to the VTZ-F12 reference structure.

	CS, pm	CH, pm	HCS, deg.
VTZ-F12	161.25	108.69	121.79
VQZ-F12	-0.04	-0.02	0.00
VQZ-F12*	-0.02	-0.02	0.00
CBS(7)-F12	-0.04	-0.02	0.00
CBS(4)-F12	-0.05	-0.02	0.00
CV_{TZ-F12}	-0.42	-0.15	0.00
CV_{QZ-F12}	-0.44	-0.15	0.00
$CV_{CBS(7)-F12}$	-0.44	-0.15	0.00
$CV_{CBS(4)-F12}$	-0.45	-0.15	0.00
HO	0.12	0.00	0.00
DKH2	-0.02	-0.01	-0.01
MVD1	-0.02	-0.01	-0.01
DBOC	0.01	0.02	-0.01
Our best estimate[a]	160.90	108.53	121.77
Refined PES[20]	161.10	108.56	121.88
Experiment[67]	161.10(8)	108.56(21)	

[a] VQZ-F12*+CV_{QZ-F12}+HO+MVD1+DBOC

CV. For example, the CS equilibrium bond is shortened by about 0.44 pm, and the harmonic frequencies ω_1 and ω_5 are increased by 6.2 cm^{-1}, when the CV terms are taken into account. The CV correction exhibits very fast convergence in terms of the basis set (VTZ-F12⟶VQZ-F12): the maximum changes in the equilibrium distances and harmonic frequencies are found for $r_{CS}^{(eq)}$ (0.02 pm) and ω_3 (0.3 cm^{-1}), respectively. The CBS extrapolation leads to negligible modifications both of the equilibrium distances (less than 0.01 pm) and harmonic frequencies (less than 0.1 cm^{-1}).

In H_2CS, the effect of the CV correction on the harmonic frequencies is largely compen-

TABLE II. Harmonic frequencies (in cm^{-1}) of H_2CS (see text for notation). Increments from basis set extension and high-level corrections are given with respect to the VTZ-F12 reference value.

	ω_1	ω_2	ω_3	ω_4	ω_5	ω_6
VTZ-F12	3083.26	1495.91	1076.42	1002.36	3175.09	1004.48
VQZ-F12	1.18	-0.69	0.60	1.18	1.40	-0.75
VQZ-F12*	0.83	-1.48	0.29	0.64	1.17	-1.08
CBS(7)-F12	1.01	-1.42	0.47	0.72	1.35	-1.13
CBS(4)-F12	1.40	-1.50	0.82	0.74	1.83	-0.70
CV_{TZ-F12}	6.05	2.75	4.67	3.87	6.07	2.64
CV_{QZ-F12}	6.21	2.95	4.93	3.85	6.17	2.84
$CV_{CBS(7)-F12}$	6.21	2.98	4.93	3.77	6.17	2.85
$CV_{CBS(4)-F12}$	6.26	3.05	5.03	3.80	6.22	2.92
HO	-0.89	-1.05	-4.58	-3.43	-1.01	-1.05
DKH2	-0.45	-0.21	-1.46	-0.43	-0.31	-0.43
MVD1	-0.52	-0.17	-1.47	-0.33	-0.34	-0.34
DBOC	-0.65	-0.26	-0.07	-0.21	-0.40	0.07
Total correction[a]	4.15	1.47	-1.19	-0.12	4.42	1.52
Our best estimate[b]	3088.24	1495.90	1075.52	1002.88	3180.68	1004.92

[a] CV_{QZ-F12}+HO+MVD1+DBOC

[b] VQZ-F12*+CV_{QZ-F12}+HO+MVD1+DBOC

sated by the effects of the other three HL corrections considered presently (i.e., HO+SR+DBOC with SR = MVD1 or DKH2). While the CV correction affects mainly the CH stretching modes, the HO and SR corrections influence especially the CS stretching mode.

The formally highest *ab initio* level in the present work is reached by supplementing the VQZ-F12* energies with all HL corrections (i.e., VQZ-F12*+CV_{QZ-F12}+HO+MVD1+DBOC). At this VQZ-F12^{*HL} level, the equilibrium constants deviate from the experimentally derived values by -0.20 pm, -0.03 pm, and -0.11 deg for r_{CS}, r_{CH}, and α_{SCH}, respectively; these deviations are comparable to those at the VQZ-F12* level (+0.13 pm, +0.11 pm, and -0.09 deg). For the harmonic frequencies of H_2CS, there are no reliable experimental

values for comparison. Inclusion of all HL corrections increases the harmonic CH stretching wavenumbers ω_1 and ω_5 by 4.2 and 4.4 cm^{-1}, respectively, while the changes for the other fundamental modes range between 0.1 and 1.5 cm^{-1}.

We now turn to a discussion of the variational results for the vibrational term values below 5000 cm^{-1}. We first address their convergence with regard to the basis set used in the CCSD(T) calculations [first term in Eq. (1)]. Figure 6 shows the changes in the computed term values upon basis set extension or extrapolation. Generally speaking, these changes are rather small, typically of the order of 1–2 cm^{-1}, so that basis set convergence is fast. At the CCSD(T)-F12b level, the differences between VQZ-F12 and VTZ-F12 (columns) tend to be most notable for modes involving ν_3 – they exceed 2.0 cm^{-1} for two such modes. Going beyond VQZ-F12, there is a well-validated extrapolation strategy for the perturbative triples (T) energy contributions in canonical CCSD(T) calculations.[48] The resulting (T) CBS corrections relative to VQZ-F12 (grey area in Fig. 6) generally lower the term values slightly, by about 1 cm^{-1}. Since they come from an established procedure, we have included them in our final CCSD(T) energies (labeled as VQZ-F12*). They are also incorporated in the remaining two curves that indicate the additional changes in the CCSD-F12b contributions arising from the X^{-7} and X^{-4} extrapolations (squares and circles, respectively, in Fig. 6). These two curves follow the same pattern, but they often differ appreciably, and it is not clear which one to prefer. The shifts due to the X^{-7} extrapolation for the CCSD part are tiny (squares vs. grey curve) whereas those due to the X^{-4} extrapolation are slightly larger (circles vs. grey curve), but mostly still small on an absolute scale. Since none of these two extrapolation procedures for the CCSD part is firmly established, we have decided against incorporating either of these two corrections. For the CCSD contribution to our PES, we thus adopt the VQZ-F12 energies, which have previously been shown to yield results of nearly benchmark quality.[25,32]

Table III lists the corresponding VQZ-F12* results, the changes resulting from the different HL corrections, and the total changes upon inclusion of all four HL corrections. The CV terms cause a substantial increase in the computed wavenumbers, up to 15 cm^{-1} in overtone and combination bands, and up to 6–7 cm^{-1} in the fundamental bands (CH stretching modes). This increase is largely compensated by the strong decrease coming mainly from the HO terms, up to -14 cm^{-1} in overtone and combination bands, and up to -5 cm^{-1} in the fundamental bands (CS stretching mode), with further smaller negative contributions from

TABLE III. The effect of the high-level *ab initio* corrections on the vibrational term values (in cm^{-1}) of H_2CS.

mode	$\Gamma^{(\mathbf{C}_{2v})}$	VQZ-F12*	CV_{QZ-F12}	HO	MVD1	DKH2	DBOC	Total[a]
ν_6	B_2	989.59	2.71	-1.19	-0.35	-0.43	0.09	1.26
ν_4	B_1	990.59	3.64	-3.01	-0.56	-0.51	-0.03	0.04
ν_3	A_1	1061.81	4.94	-4.61	-1.48	-1.46	-0.05	-1.20
ν_2	A_1	1454.50	2.89	-1.28	-0.19	-0.24	-0.20	1.22
$2\nu_6$	A_1	1965.56	6.03	-3.84	-0.89	-0.91	0.10	1.40
$\nu_4+\nu_6$	A_2	1988.41	6.33	-4.22	-0.92	-0.93	0.08	1.27
$2\nu_4$	A_1	1991.73	6.50	-4.45	-0.93	-0.92	0.01	1.13
$\nu_3+\nu_4$	B_1	2047.29	7.65	-6.15	-2.03	-1.96	-0.09	-0.62
$\nu_3+\nu_6$	B_2	2047.92	8.63	-7.43	-1.84	-1.90	0.04	-0.60
$2\nu_3$	A_1	2113.97	9.88	-9.25	-2.95	-2.90	-0.12	-2.44
$\nu_2+\nu_6$	B_2	2429.00	5.49	-2.45	-0.54	-0.66	-0.12	2.38
$\nu_2+\nu_4$	B_1	2438.82	6.63	-4.47	-0.79	-0.78	-0.23	1.14
$\nu_2+\nu_3$	A_1	2511.92	7.84	-5.92	-1.66	-1.69	-0.26	0.00
$2\nu_2$	A_1	2875.24	5.71	-2.25	-0.46	-0.51	-0.44	2.56
$3\nu_6$	B_2	2946.96	8.40	-4.52	-1.12	-1.28	0.26	3.02
$3\nu_4$	B_1	2954.65	9.94	-7.55	-1.52	-1.39	0.02	0.89
ν_1	A_1	2969.47	6.11	-2.04	-0.52	-0.50	-0.56	2.99
$2\nu_4+\nu_6$	B_2	2997.92	9.32	-6.06	-1.35	-1.34	0.06	1.97
$2\nu_6+\nu_4$	B_1	3000.08	9.70	-6.66	-1.40	-1.39	0.04	1.68
$2\nu_6+\nu_3$	A_1	3018.97	10.69	-8.30	-2.38	-2.38	0.05	0.06
ν_5	B_2	3024.32	6.54	-2.28	-0.50	-0.46	-0.34	3.42
$\nu_3+\nu_4+\nu_6$	A_2	3041.58	11.32	-8.99	-2.40	-2.40	0.03	-0.04
$2\nu_4+\nu_3$	A_1	3044.92	11.47	-9.18	-2.42	-2.39	-0.03	-0.16
$2\nu_3+\nu_6$	B_2	3095.45	13.60	-11.61	-3.31	-3.41	-0.02	-1.34
$2\nu_3+\nu_4$	B_1	3095.51	12.56	-11.36	-3.51	-3.34	-0.14	-2.45
$3\nu_3$	A_1	3156.42	14.81	-13.89	-4.42	-4.34	-0.16	-3.66
$2\nu_6+\nu_2$	A_1	3393.66	8.42	-4.35	-0.95	-1.09	-0.06	3.06
$\nu_2+\nu_4+\nu_6$	A_2	3422.46	9.23	-5.64	-1.16	-1.20	-0.12	2.31
$2\nu_4+\nu_2$	A_1	3429.48	9.92	-6.82	-1.31	-1.25	-0.24	1.55
$\nu_2+\nu_3+\nu_6$	B_2	3482.65	10.43	-7.15	-2.02	-2.12	-0.17	1.09
$\nu_2+\nu_3+\nu_4$	B_1	3491.57	11.62	-9.20	-2.28	-2.24	-0.29	-0.15
$2\nu_3+\nu_2$	A_1	3559.70	12.77	-10.58	-3.13	-3.13	-0.32	-1.26
$2\nu_2+\nu_6$	B_2	3839.77	8.26	-3.52	-0.78	-0.91	-0.34	3.62
$2\nu_2+\nu_4$	B_1	3855.66	9.50	-5.56	-1.07	-1.07	-0.46	2.41
$2\nu_2+\nu_3$	A_1	3930.76	10.64	-6.92	-1.93	-1.96	-0.49	1.30
$3\nu_2$	A_1	4283.46	8.50	-3.43	-0.70	-0.78	-0.63	3.74

[a] CV_{QZ-F12}+HO+MVD1+DBOC

FIG. 6. Basis set convergence of the CCSD(T)-F12b vibrational term values (in cm^{-1}) of H_2CS. The grey area shows the changes due to the CBS extrapolation of the perturbative triples (T) contributions relative to VQZ-F12 (see text).

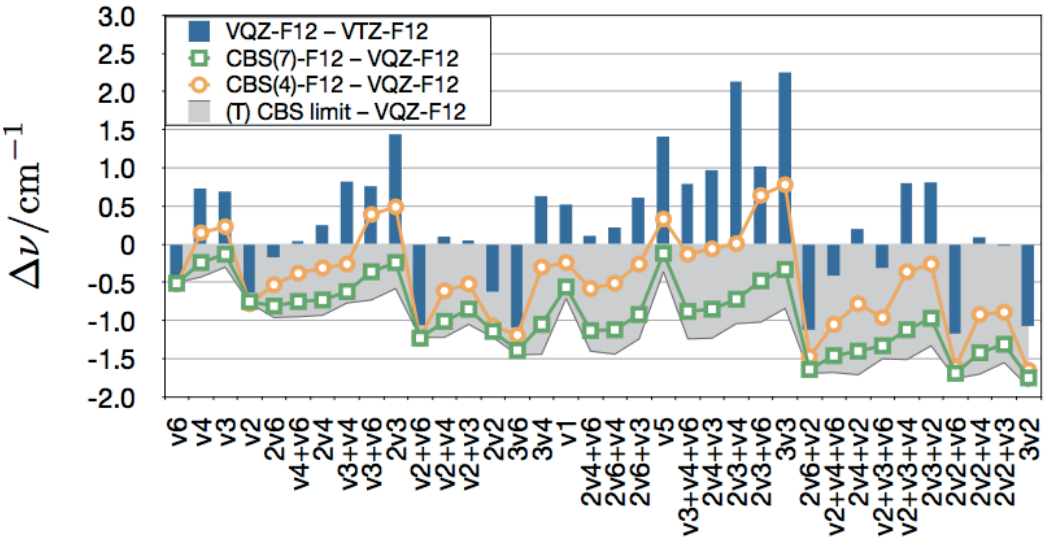

the relativistic terms, up to -4.4 cm^{-1}. The two alternative approaches for computing the relativistic effects (MVD1 and DKH2) yield quite similar results: they lower the computed wavenumbers typically by 1–2 cm^{-1}, with somewhat larger effects on modes that involve CS stretching (ν_3 and its overtone and combination bands). The DBOC correction affects mostly only the ν_1 and ν_5 modes, but its influence is generally small (normally less than 0.5 cm^{-1}). Because of cancellation effects, the HL corrections cause only a rather small overall shift in the calculated wavenumbers, with a maximum shift of 3.7 cm^{-1} in the $3\nu_2$ overtone. The fundamental CH stretching modes are among the few examples where this compensation is fairly incomplete, since the large positive CV contributions outweigh the negative HO and SR contributions, leading to overall shifts of 3.0 cm^{-1} for ν_5 and 3.4 cm^{-1} for ν_5. For the other four fundamentals, the overall shifts are small and do not exceed 1.3 cm^{-1}.

We have also checked the basis set dependence for the largest HL correction, i.e., the CV contribution (see Figure 7). The basis set extension TZ→QZ causes the computed vibrational term values to change by less than 1 cm^{-1} (with a maximum value of 0.7 cm^{-1} for $3\nu_3$). The CBS extrapolation of the CV_{QZ-F12} energies only leads to tiny modifications of the

FIG. 7. Basis set convergence of the CV effects on the vibrational term values (in cm^{-1}) of H_2CS.

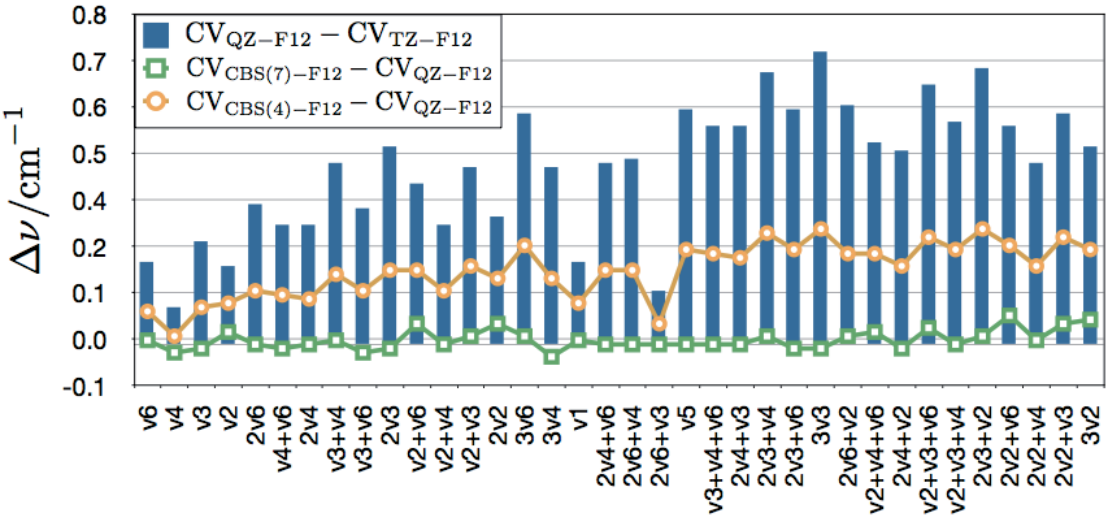

vibrational term values, less than 0.2 cm^{-1} for $CV_{CBS(4)-F12}$ and 0.1 cm^{-1} for $CV_{CBS(7)-F12}$.

We now focus on our two recommended global *ab initio* PESs of H_2CS, obtained without (VQZ-F12*) and with (VQZ-F12*^{HL}) the HL corrections. Both PESs are of similar quality because the HL corrections compensate each other to a large extent (see above). Table IV lists the fundamental term values obtained with these two PESs and compares them to the available experimental data.[8,10] The VQZ-F12* surface provides vibrational term values in fairly good agreement with experiment: the maximum error is 2.60 cm^{-1} for ν_3, the deviations are less than 2 cm^{-1} for the other fundamentals, and the mean absolute deviation for all six fundamentals amounts to 1.42 cm^{-1} (the latter is even lower for the VQZ-F12 surface, 1.28 cm^{-1}). In spite of the significantly higher computational effort, the VQZ-F12*^{HL} surface yields slightly larger errors: the wavenumbers of the C-H stretching modes ν_1 and ν_5 are overestimated by 1.43 and 3.12 cm^{-1}, respectively, the description of ν_3 is slightly improved (overestimate of 1.40 rather than 2.60 cm^{-1}), and the mean absolute deviation for all six fundamentals is 1.35 cm^{-1}. These data indicate that it is very difficult to get beyond wavenumber accuracy by a purely *ab initio* approach for molecules such as H_2CS, in spite of a dedicated attempt to include the dominant HL corrections in a converged manner.

To put the present results into perspective, we compare the vibrational term values obtained with the present *ab initio* PESs to those obtained with the refined PES of Carter

TABLE IV. Best theoretical estimates of the vibrational wavenumbers of H_2CS (in cm^{-1}) compared with the available experimental data.

Mode	$\Gamma^{(C_{2v})}$	VQZ-F12*	VQZ-F12*^{HL}	Exp.[10]	VQZ-F12*–Exp.	VQZ-F12*^{HL}–Exp.
ν_1	A_1	2969.47	2972.46	2971.03	-1.56	1.43
ν_2	A_1	1454.50	1455.72	1455.50	-1.00	0.22
ν_3	A_1	1061.81	1060.61	1059.21	2.60	1.40
ν_4	B_1	990.59	990.63	990.18	0.41	0.45
ν_5	B_2	3024.32	3027.74	3024.62	-0.30	3.12
ν_6	B_2	989.59	990.85	991.02	-1.43	-0.17
$2\nu_2$	A_1	2875.24	2877.80	2877.11	-1.87	0.69
$\nu_2+\nu_3$	A_1	2511.92	2511.92	2511.60	0.32	0.32

et al.[20] (Table V). Since the VQZ-F12* results have already been presented in Table III, we employ the VQZ-F12 and VQZ-F12*^{HL} results for these comparisons. All three surfaces considered perform equally well for the fundamental term values, but the results from the previous PES[20] start to deviate greatly already for the first overtones, with a maximum deviation of 53 cm^{-1} for $2\nu_4$, and even more so for the higher combination bands with a maximum deviation of 152 cm^{-1} for $2\nu_2+\nu_4$. Since the present PESs are fully *ab initio*, we expect them to be more reliable in terms of predicting energies for higher excitations. By contrast, the previously refined PES[20] was obtained by fitting a quartic force field to the rotational, fundamental, $2\nu_2$, and $\nu_2+\nu_3$ bands of H_2CS, and it thus seems likely that this PES will not guarantee high accuracy beyond this training set of states: judging from the present comparisons, it appears to have deficiencies in the description of C-S stretching and out-of-plane bending motions.

IV. CONCLUSIONS

In this work we present two *ab initio* potential energy surfaces for the ground electronic state of H_2CS. They have been calculated purely *ab initio* in an attempt of pushing the

TABLE V. Best theoretical estimates of the vibrational term values of H_2CS (in cm^{-1}) from the *ab initio* VQZ-F12 and VQZ-F12^{*HL} PESs (see text) compared with the results obtained using the refined PES of Carter *et. al.*[20]

Mode	$\Gamma^{(\mathbf{C}_{2v})}$	VQZ-F12	VQZ-F12^{*HL}	Carter	VQZ-F12–Carter	VQZ-F12^{*HL}–Carter
ν_6	B_2	990.09	990.85	990.88	-0.79	-0.03
ν_4	B_1	991.02	990.63	990.55	0.47	0.08
ν_3	A_1	1062.11	1060.61	1058.86	3.25	1.75
ν_2	A_1	1455.27	1455.72	1457.34	-2.07	-1.62
$2\nu_6$	A_1	1966.52	1966.96	1978.70	-12.18	-11.74
$\nu_4+\nu_6$	A_2	1989.36	1989.68	2009.26	-19.90	-19.58
$2\nu_4$	A_1	1992.66	1992.86	1939.58	53.08	53.28
$\nu_3+\nu_4$	B_1	2048.06	2046.67	2045.00	3.06	1.67
$\nu_3+\nu_6$	B_2	2048.65	2047.32	2045.49	3.16	1.83
$2\nu_3$	A_1	2114.55	2111.53	2101.79	12.76	9.74
$\nu_2+\nu_6$	B_2	2430.22	2431.38	2430.56	-0.34	0.82
$\nu_2+\nu_4$	B_1	2440.04	2439.96	2484.39	-44.35	-44.43
$\nu_2+\nu_3$	A_1	2512.97	2511.92	2510.68	2.29	1.24
$2\nu_2$	A_1	2876.46	2877.80	2875.77	0.69	2.03
$3\nu_6$	B_2	2948.41	2949.98	2956.84	-8.43	-6.86
$3\nu_4$	B_1	2956.09	2955.54	2863.36	92.73	92.18
ν_1	A_1	2970.18	2972.46	2969.90	0.28	2.56
$2\nu_4+\nu_6$	B_2	2999.32	2999.89	2981.01	18.31	18.88
$2\nu_6+\nu_4$	B_1	3001.52	3001.76	3024.75	-23.23	-22.99
$2\nu_6+\nu_3$	A_1	3020.21	3019.03	3028.99	-8.78	-9.96
ν_5	B_2	3024.68	3027.74	3024.50	0.18	3.24
$\nu_3+\nu_4+\nu_6$	A_2	3042.82	3041.54	3059.33	-16.51	-17.79
$2\nu_4+\nu_3$	A_1	3046.15	3044.76	2991.83	54.32	52.93
$2\nu_3+\nu_4$	B_1	3096.49	3094.11	3083.10	13.39	11.01
$2\nu_3+\nu_6$	B_2	3096.53	3093.06	3084.18	12.35	8.88
$3\nu_3$	A_1	3157.26	3152.76	3128.33	28.93	24.43
$2\nu_6+\nu_2$	A_1	3395.35	3396.72	3399.95	-4.60	-3.23
$\nu_2+\nu_4+\nu_6$	A_2	3424.14	3424.77	3491.53	-67.39	-66.76
$2\nu_4+\nu_2$	A_1	3431.19	3431.03	3460.53	-29.34	-29.50
$\nu_2+\nu_3+\nu_6$	B_2	3484.15	3483.74	3480.46	3.69	3.28
$\nu_2+\nu_3+\nu_4$	B_1	3493.08	3491.42	3533.13	-40.05	-41.71
$2\nu_3+\nu_2$	A_1	3561.03	3558.44	3548.11	12.92	10.33
$2\nu_2+\nu_6$	B_2	3841.53	3843.39	3838.53	3.00	4.86
$2\nu_2+\nu_4$	B_1	3857.36	3858.07	4009.80	-152.44	-151.73
$2\nu_2+\nu_3$	A_1	3932.31	3932.06	3926.66	5.65	5.40
$3\nu_2$	A_1	4285.33	4287.20	4283.67	1.66	3.53

accuracy towards the currently feasible limit. The first surface is generated at the VQZ-F12* level (i.e., CCSD(T) near the CBS limit), while the second one incorporates additive high-level corrections for core-valence correlation, higher-order correlation effects beyond CCSD(T), and relativistic effects as well as diagonal Born-Oppenheimer corrections. Special care has been taken to obtain converged values for all these terms. Both surfaces provide reasonable descriptions of the vibrational term values of H_2CS (Table IV). The two sets of variationally calculated results are similar because the effects of the different high-level corrections compensate each other to a large extent and in an apparently systematic manner. In particular, the large positive shifts in the computed wavenumbers caused by the core-valence correlation terms (up to +15 cm^{-1}) are counteracted by similarly large negative shifts from the higher-order correlation terms (up to -14 cm^{-1}).

On the basis of the current results, we believe that it is difficult to go beyond wavenumber accuracy in a purely *ab initio* fashion for a molecule such as H_2CS. In the future, we therefore plan to perform an empirical optimization of the current *ab initio* surfaces by a slight adjustment through least-squares fittings to the few accurate experimental energies of H_2CS that are available. Such a refined surface should allow us to approach experimental accuracy in simulations of rotational-vibrational spectra. We believe that each of our current *ab initio* surfaces can be used successfully as initial guess for the refinement process: their documented accuracy is essential for this purpose, since the amount of available experimental data is very limited in the case of H_2CS.

V. ACKNOWLEDGMENTS

We thank Jürgen Breidung for valuable discussions.

* Corresponding author. E-mail: thiel@mpi-muelheim.mpg.de

[1] D. R. Johnson and F. X. Powell, Science **169**, 679 (1970).

[2] N. J. Evans, C. H. Townes, H. F. Weaver, and D. R. Williams, Science **169**, 680 (1970).

[3] M. W. Sinclair, N. Fourikis, J. C. Ribes, B. J. Robinson, R. D. Brown, and P. D. Godfrey, Aust. J. Phys. **26**, 85 (1973).

[4] L. M. Woodney, M. F. A'Hearn, J. McMullin, and N. Samarasinha, Earth Moon Plan. **78**, 69 (1997).

[5] P. Schilke, T. D. Groesbeck, G. A. Blake, and T. G. Phillips, Astrophys. J. Suppl. Ser. **108**, 301 (1997).

[6] P. Schilke, D. J. Benford, T. R. Hunter, D. C. Lis, and T. G. Phillips, Astrophys. J. Suppl. Ser. **132**, 281 (2001).

[7] C. Comito, P. Schilke, T. G. Phillips, D. C. Lis, F. Motte, and D. Mehringer, Astrophys. J. Suppl. Ser. **156**, 127 (2005).

[8] J.-M. Flaud, W. J. Lafferty, A. Perrin, Y. S. Kim, H. Beckers, and H. Willner, J. Quant. Spectr. Rad. Trans. **109**, 995 (2008).

[9] A. Maeda, I. R. Medvedev, M. Winnewisser, F. C. De Lucia, E. Herbst, H. S. P. Mueller, M. Koerber, C. P. Endres, and S. Schlemmer, Astrophys. J. Suppl. Ser. **176**, 543 (2008).

[10] D. J. Clouthier and D. A. Ramsay, Ann. Rev. Phys. Chem. **34**, 31 (1983).

[11] H. S. P. Müller, S. Thorwirth, D. A. Roth, and G. Winnewisser, Astronom. Astrophys. **370**, L49 (2001).

[12] H. S. P. Müller, F. Schlöder, J. Stutzki, and G. Winnewisser, J. Mol. Struct. **742**, 215 (2005).

[13] M. Kawasaki, K. Kasatani, and H. Sato, Chem. Phys. **94**, 179 (1985).

[14] T. Suzuki, S. Saito, and E. Hirota, J. Molec. Spectrosc. **111**, 54 (1985).

[15] J. R. Dunlop, J. Karolczak, D. J. Clouthier, and S. C. Ross, J. Phys. Chem. **95**, 3063 (1991).

[16] J. R. Dunlop, J. Karolczak, D. J. Clouthier, and S. C. Ross, J. Phys. Chem. **95**, 3045 (1991).

[17] K. Kasatani, M. Kawasaki, and H. Sato, Chem. Letters **1**, 62 (2001).

[18] S. Y. Chiang and I. F. Lin, J. Chem. Phys. **122**, 94301 (2005).

[19] J. M. L. Martin, J. P. Francois, and R. Gijebels, J. Molec. Spectrosc. **168**, 363 (1994).

[20] S. Carter and N. C. Handy, J. Molec. Spectrocs. **192**, 263 (1998).

[21] S. Carter, J. M. Bowman, and N. C. Handy, Theor. Chem. Acc. **100**, 191 (1998).

[22] S. Carter, A. Sharma, J. Bowman, P. Rosmus, and R. Tarroni, J. Chem. Phys. **131**, 224106 (2009).

[23] C. Léonard, G. Chambaud, P. Rosmus, S. Carter, and N. C. Handy, Phys. Chem. Chem. Phys. **3**, 508 (2001).

[24] T. Adler, G. Knizia, and H.-J. Werner, J. Chem. Phys. **127**, 221106 (2007).

[25] G. Rauhut, G. Knizia, and H.-J. Werner, J. Chem. Phys. **130**, 054105 (2009).

[26] T. A. Ruden, T. Helgaker, P. Jørgensen, and J. Olsen, J. Chem. Phys. **121**, 5874 (2004).

[27] M. H. Cortez, N. R. Brinkmann, W. F. Polik, P. R. Taylor, Y. J. Bomble, and J. F. Stanton, J. Chem. Theory Comput. **3**, 1267 (2007).

[28] D. P. Tew, W. Klopper, M. Heckert, and J. Gauss, J. Phys. Chem. A **111**, 11242 (2007).

[29] D. Feller and K. Peterson, J. Chem. Phys. **131**, 154306 (2009).

[30] C. Puzzarini, J. F. Stanton, and J. Gauss, Int. Rev. Phys. Chem. **29**, 273 (2010).

[31] W. Klopper, R. A. Bachorz, C. Hättig, and D. P. Tew, Theor. Chem. Acc. **126**, 289 (2010).

[32] K. Kahn, B. Kirtman, J. Noga, and S. Ten-no, J. Chem. Phys. **133**, 74106 (2010).

[33] A. Karton and J. M. L. Martin, J. Chem. Phys. **133**, 144102 (2010).

[34] O. L. Polyansky, A. G. Császár, S. V. Shirin, N. F. Zobov, P. Barletta, J. Tennyson, D. W. Schwenke, and P. J. Knowles, Science **299**, 539 (2003).

[35] T. Rajamäki, A. Miani, and L. Halonen, J. Chem. Phys. **118**, 6358 (2003).

[36] T. Rajamäki, A. Miani, and L. Halonen, J. Chem. Phys. **118**, 10929 (2003).

[37] X. Huang and T. J. Lee, J. Chem. Phys. **129**, 44312 (2008).

[38] X. Huang, D. W. Schwenke, and T. J. Lee, J. Chem. Phys. **129**, 214304 (2008).

[39] X. Huang, D. W. Schwenke, and T. J. Lee, J. Chem. Phys. **134**, 044320 (2011).

[40] S. Ten-No, Chem. Phys. Lett. **398**, 56 (2004).

[41] H.-J. Werner, P. J. Knowles, F. R. Manby, M. Schütz, P. Celani, G. Knizia, T. Korona, R. Lindh, A. Mitrushenkov, G. Rauhut, T. B. Adler, R. D. Amos, A. Bernhardsson, A. Berning, D. L. Cooper, M. J. O. Deegan, A. J. Dobbyn, F. Eckert, E. Goll, C. Hampel, A. Hesselmann, G. Hetzer, T. Hrenar, G. Jansen, C. Köppl, Y. Liu, A. W. Lloyd, R. A. Mata, A. J. May, S. J. McNicholas, W. Meyer, M. E. Mura, A. Nicklass, P. Palmieri, K. Pflüger, R. Pitzer, M. Reiher, T. Shiozaki, H. Stoll, A. J. Stone, R. Tarroni, T. Thorsteinsson, M. Wang, and A. Wolf, "Molpro, version 2010.1, a package of ab initio programs," (2010), see http://www.molpro.net.

[42] K. Peterson, T. Adler, and H.-J. Werner, J. Chem. Phys. **128**, 084102 (2008).

[43] K. Yousaf and K. Peterson, J. Chem. Phys. **129**, 184108 (7 pp.) (2008).

[44] F. Weigend, Phys. Chem. Chem. Phys. **4**, 4285 (2002).

[45] C. Hättig, Phys. Chem. Chem. Phys. **7**, 59 (2005).

[46] W. Kutzelnigg and W. Klopper, J. Chem. Phys. **94**, 1985 (1991).

[47] W. Klopper and C. C. M. Samson, J. Chem. Phys. **116**, 6397 (2002).

[48] T. Helgaker, W. Klopper, H. Koch, and J. Noga, J. Chem. Phys. **106**, 9639 (1997).

[49] J. Hill, S. Mazumder, and K. Peterson, J. Chem. Phys. **132**, 054108 (2010).

[50] R. D. Cowan and D. C. Griffin, J. Opt. Soc. Am. **66**, 1010 (1976).

[51] M. Douglas and N. M. Kroll, Ann. Phys. **82**, 89 (1974).

[52] B. A. Heß, Phys. Rev. A **33**, 3742 (1986).

[53] W. Klopper, J. Comp. Chem. **18**, 20 (1997).

[54] R. A. Kendall, T. H. Dunning, Jr., and R. J. Harrison, J. Chem. Phys. **96**, 6796 (1992).

[55] D. E. Woon and T. H. Dunning, Jr., J. Chem. Phys. **98**, 1358 (1993).

[56] D. E. Woon and T. H. Dunning, Jr., J. Chem. Phys. **103**, 4572 (1995).

[57] K. A. Peterson and T. H. Dunning, Jr., J. Chem. Phys. **117**, 10548 (2002).

[58] J. F. Stanton, J. Gauss, M. E. Harding, P. G. Szalay, *et al.*, "CFOUR, a quantum chemical program package," for the current version, see http://www.cfour.de.

[59] W. A. de Jong, R. J. Harrison, and D. A. Dixon, J. Chem. Phys. **114**, 48 (2001).

[60] J. Gauss, A. Tajti, M. Kállay, J. F. Stanton, and P. G. Szalay, J. Chem. Phys. **125**, 144111 (2006).

[61] M. Kállay, "MRCC, a string-based quantum chemical program suite," see also M. Kállay, P. R. Surján, J. Chem. Phys. 115 2945 (2001) as well as: http://www.mrcc.hu.

[62] T. H. Dunning, Jr., J. Chem. Phys. **90**, 1007 (1989).

[63] T. H. Dunning, Jr., K. A. Peterson, and A. K. Wilson, J. Chem. Phys. **114**, 9244 (2001).

[64] S. N. Yurchenko, W. Thiel, and P. Jensen, J. Mol. Spectrosc. **245**, 126 (2007).

[65] H. Partridge and D. Schwenke, J. Chem. Phys. **106**, 4618 (1997).

[66] P. R. Bunker and P. Jensen, *Molecular Symmetry and Spectroscopy*, 2nd ed. (NRC Research Press, Ottawa, 1998).

[67] P. H. Turner, L. Halonen, and I. M. Mills, J. Molec. Spectrosc. **88**, 402 (1981).